UNIVERSITÀ
DEGLI STUDI
FIRENZE

DOTTORATO DI RICERCA IN
FISICA E ASTRONOMIA

CICLO XXX
COORDINATORE Prof. Raffaello D'Alessandro

Assessing the chemical evolution of galaxies with large spectral surveys and spatially resolved observations

Settore scientifico disciplinare: FIS/05 Astronomia e Astrofisica

Dottorando	**Tutori**
Dott. Mirko Curti	Prof. Filippo Mannucci Dott. Simone Esposito

Anni 2014 / 2017

Quanti progetti in mente,
poi finire a guardare il cielo

Pino Daniele

Contents

Summary

Galaxies continuously undergo chemical enrichment. Heavy elements are produced in stars during their lifetime and then dispersed by means of stellar winds and supernovae, contributing to the enrichment of the surrounding interstellar medium (ISM). Gas flows, including inflows from the cosmic web and supernovae- or AGN-driven outflows, also play a crucial role in the definition of the chemical enrichment level by acting as regulators of both the gas content and the amount of metals that galaxies are capable to retain in the gas-phase of the ISM. Therefore, the gas-phase metallicity represents a fossil record of the recent star formation history of a galaxy and is strongly sensitive to all the physical processes which shape and drive the baryon-cycle in the Universe. Indeed, this mutual correlation between stellar activity, mass growth, metal production and gas flows gives rise to the well established scaling relations between mass, metallicity and star formation rate observed and thoroughly investigated both in the local Universe and at higher redshifts, whose characterization can provide crucial constraints on models and simulations aimed at describing how galaxies evolve across the epochs.

In this thesis we address some of the currently most debated topics related to the chemical evolution of star forming galaxies, by means of statistically robust analysis of large samples of local objects from the Sloan Digital Sky Survey (SDSS) and of near-infrared, spatially resolved spectroscopy of high-redshift sources, obtained from new generation instruments like KMOS on the Very Large Telescope and ARGOS on the Large Binocular Telescope. A broad overview on the instrumentation and data used in this work is given in Chapter 2.

In the first part of the dissertation, we focus on the methods for chemical abundances measurements in galaxies, trying to address the long-standing issue related to the lack of an absolute metallicity scale based on global galaxy spectra. In Chapter 3, therefore, we revisit some of the most common methods for metallicity determination based on strong emission lines, exploiting a novel approach based on stacking the spectra of SDSS star-forming galaxies according to their position on the [O III]λ5007/Hβ vs [O III]λ3727/Hβ diagram, thus assuming that galaxies with such similar line ratios have similar metallicities. This stacking procedure allows us to detect the extremely faint, metallicity-sensitive auroral lines required to apply the T_e method to measure the oxygen abundances from our composite spectra. In this way, we can provide a new calibration of the strong-line metallicity diagnostics which is fully based on the T_e abundance scale and covers the entire metallicity range spanned by the SDSS galaxies. The new set of calibrated diagnostics is then used to explore the relations between mass, metallicity and star formation rate in the local Universe.

In the second part of the thesis, we move to study the high redshift Universe in order to investigate the ISM properties in high-redshift galaxies and how their metal content is linked to their star formation history.

Chapter 4 is dedicated to the analysis of a sample of high-redshift galaxies in the framework of the KLEVER survey. Combining integral field spectroscopy from KMOS with the increased sensitivity and resolution provided by gravitational lensing, we can investigate in detail the physical properties of the ionized gas in our sample on spatially resolved scales. In particular, we focus on assessing the properties and the cosmic evolution of metallicity gradients. The large majority of analyzed galaxies present azimuthally-averaged radial metallicity gradients fully consistent with being flat, with no clear evidence of redshit evolution, consistently with a theoretical scenario where efficient mixing and feedback processes are in place in redistributing a significant amount of gas over large scales. However, given the presence of irregular patterns in the full, resolved metallicity maps, we warn against the use of azimuthally-averaged radial gradients as the only observable benchmark to compare predictions from chemical evolution models and simulations. We also investigate the possible correlations between the metallicity gradients and intrinsic galaxy properties. We report a tentative correlation between the shape of the gradients and the star formation activity in galaxies, as parametrized by the sSFR, as well as a qualitative evidence of a general spatial anti-correlation on local scales between metallicity and the SFR surface density, as previously claimed also by different studies conducted on samples of high-redshift sources. This suggests that, on local scales, smooth inflow of gas is active in diluting the metal content and boost star formation episodes. Moreover, we investigated the processes responsible for the observed offset in the position of high-z galaxies in the classical BPT diagrams, trying to disentangle the different physical contributions at the origin of the observed evolution in the emission line ratios.

The study of galaxy properties at high redshift conducted with ground-based spectroscopy can largely benefit from the increased spatial resolution provided by the adaptive optics correction of the atmospheric turbulence, thus representing a strong scientific case for the development of new AO-facilities. In Chapter 5 we present the first spectroscopic observations conducted at the Large Binocular Telescope with the near-infrared imager and spectrograph LUCI assisted by the laser guide stars ground-layer adaptive optics system ARGOS. In particular, we focus on a small sample of $z \sim 2$ strongly lensed objects, observed by means of a curved-slit multi-object spectroscopy technique that allows us to cover the full extension of the arc-like shapes of these systems on the sky. The increased spatial and spectral resolution achievable thanks to the AO-correction provides us with clear information on the kinematic properties of our sources, allowing us to detect the presence of possible star formation driven outflows. From the analysis of the ionized gas properties we can reasonably exclude any evidence for AGN activity in these systems, which are characterized by metallicities consistent with those generally observed in low-mass galaxies at these epochs, fully in agreement with the predictions of the fundamental metallicity relation defined in the local Universe.

1

Introduction

A few moments after the Big Bang, the expanding Universe reached the right temperature and density conditions to start a nucleosynthesis which lasted about 3 minutes. Within this short period of time, nuclear reactions was responsible for the formation of most of the helium and of small amounts of deuterium and lithium isotopes which, in addition to the very abundant hydrogen, constituted the chemical composition of the primordial Universe. The totality of all the other elements were, are and will be produced by nuclear reactions occurring in stars during their lifetimes or in the dramatic events following their deaths.

In the widely accepted ΛCDM cosmological framework, baryons, dark matter and dark energy are the three main energy components of the Universe, shaping the geometry of the space and the distribution of the structures we observe nowadays. The process of structure formation is driven by gravity, acting on small inhomogeneities in the (dark) matter distribution of an otherwise completely homogeneous Universe. These perturbations grow until they reach a given size (which depends on the cosmological parameters), to form then a gravitationally bound structure known as dark matter halo. The growth of these halos then proceed hierarchically by further accretion of matter or merging of smaller structures into larger ones. As gas cools into these halos, it may reach conditions compatible with triggering the process of star formation. This brought to the formation of the first, massive and completely metal-free stars (population III stars), which quickly consumed their supply of fuel and started releasing the first metals[1] into the interstellar medium. Then, larger systems of stars, interstellar gas, dust, and dark matter began to form: the detailed process driving the formation of these early galaxies is one the open questions for the astrophysical community.

Once they are formed, galaxies continuously undergo chemical enrichment. As metals are produced in stars, they are released into the interstellar medium by means of stellar winds and supernovae. Accretion of pristine gas or outflows due to stellar or

---

[1] in astronomy, the word *metals* is usually referred to all the chemical elements heavier than helium

black holes activity also largely contribute in regulating the fraction of the heavy elements (called *metallicity*) in the interstellar gas and in generating the scaling relations with stellar mass and star formation rate observed both in the local Universe as well as at earlier cosmic epochs. The study of metal abundances within galaxies represents, therefore, the *Rosetta Stone* which enable to decipher the history of the chemical evolution of our Universe.

In this Chapter we provide an overview of the main processes related to the chemical evolution of star forming galaxies, with particular emphasis on their observational probes, aimed at highlighting the global scientific context in which the work discussed in this dissertation have been conducted. After a brief introduction on global galaxy properties (Sec. 1.1), we move on giving a description of the nature of the interstellar gas, mainly focusing on its ionized component and on the principles that can be used to get insight into the mechanisms regulating its physics (Sec. 1.2). Finally, we describe the methods for measuring chemical abundances in star forming galaxies and present the main observational evidences of the mutual relation between galaxy properties and their metal content, highlighting how their detailed comprehension can be used to constrain the role of star formation and gas flows in driving galaxy evolution.

1.1 Global properties of star forming galaxies

In this Section we provide a brief description of galaxy properties and their classification relative to their star formation activity and sources of ionization. The work presented in this thesis will only focus on studying the chemical properties of galaxies characterized by an appreciable level of current star formation, according to the criteria that will be discussed in the following.

1.1.1 Galaxy bimodality

In the last decades, large imaging and spectroscopic surveys like the Sloan Digital Sky Survey (SDSS, York et al. (2000)) revolutionized the study of the physical properties of galaxies in terms of data quality and statistical significance. For example, the analysis of the distribution of galaxies in the color- absolute magnitude (or color-stellar mass) diagram allowed to clearly identify the existence of two distinct populations (Fig 1.1), classified according to their color indices, a quantity strictly related to their recent star formation activity :

- highly star forming galaxies, typically low mass spiral galaxies dominated by young stellar populations, which define the *blue cloud*;

- high-mass spheroidal galaxies with poor star formation activity, which define the *red sequence.*

Roughly speaking, this bimodality that characterize galaxy populations can be explained assuming the following, simple evolutionary path. As a prototypical galaxy forms, it is characterized by elevated star formation and takes its place in the blue cloud; it then evolves along the star-forming sequence, increasing mass through the accretion of cold gas from the cosmic web and through merger events with other galaxies. At a given point (usually when reaching a certain threshold in stellar mass) some process intervenes in strongly suppressing (*quenching*) the current level of star formation and preventing new episodes, by directly or indirectly removing the supply of gas: the galaxy then moves into the passive population. Different mechanisms can be invoked to induce the star formation quenching, from feedback driven by AGN activity (Cicone et al., 2014; Carniani et al., 2016), to the consumption of the available gas reservoir (i.e. strangulation, Peng et al. 2015), to processes related to the large scale environment embedding the galaxy (e.g. ram pressure stripping, Fumagalli et al. 2014; Poggianti et al. 2016).

A Deeper analysis of the diagram reveals the presence of an intermediate area of the diagram, the so-called *green valley*, occupied by galaxies which are experiencing the transition between the two sequences at the time at which they are observed; these sources could provide key insights on the relative contribution played by different mechanisms in triggering the migration from the active to the passive galaxy population. This bimodal distribution of the population can be found also when considering different structural properties of galaxies (e.g. their Sersic indices, Blanton & Moustakas 2009).

1.1.2 Star formation and Galaxy Main Sequence

Observationally, the probe of the level of star formation currently in place in a galaxy is quantified by the star formation rate (SFR), defined as the mass of stars formed in a given interval of time, which is usually measured in units of solar masses per year ($M_\odot$ yr^{-1}). It critically depends both on the amount of gas available to be converted into stars and on the efficiency of the conversion mechanism[2].

Deep multi-wavelength surveys conducted both from ground and space based facilities have revealed that the level of star formation activity evolves with cosmic time, reaching its peak during the epoch between $1 < z < 3$ (i.e. the so called *cosmic noon*)

---

[2] Observations demonstrate that the efficiency of star formation (the fraction of gas eventually converted into stars) is closer to just a few percent. How to explain this observed low efficiency in star formation processes represents one the fundamental theoretical problems in astronomy.

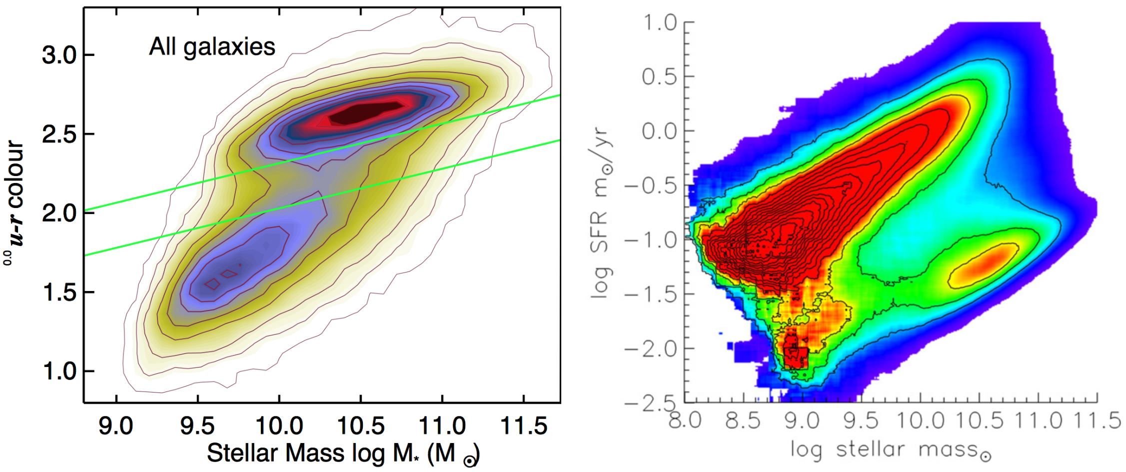

Figure 1.1: *Left Panel*: Distribution of the SDSS galaxies in the *u-r* color vs stellar mass diagram. Galaxies in the upper region represent the more luminous, more massive, and redder objects that constitutes the *red sequence*, while in the bottom part lie the less massive, highly star forming galaxies of the *blue cloud.* The *green valley* area is enclosed by the green straight lines. From Schawinski et al. (2014). *Right Panel*: Distribution of SDSS galaxies in the stellar mass vs star formation rate plane, revealing the existence of a Main Sequence of star forming galaxies; regions of high number density of galaxies are color coded in red. Stellar masses and star formation rates have been computed by the MPA-JHU group (Brinchmann et al. 2004). From Renzini & Peng (2015).

where the maximum star formation density of the Universe is reached and almost half of the total stellar mass is assembled in galaxies (Madau & Dickinson, 2014). The SFR density then slowly decline when moving both to earlier epochs and towards the present day. Different observational tracers are commonly exploited to measure the galaxy SFR. The most widely used include near-UV emission, which trace directly the emission of young stars, Hα emission, tracing the gas photoionized by massive stars in regions of recent star formation (i.e. HII regions), and far-infrared (FIR) emission, tracing the radiation absorbed and reprocessed by dust (Kennicutt 1998; Kennicutt & Evans 2012). In the context of nebular studies, a widely used functional form for the relationship between Hα and SFR, is given by Kennicutt (1998). Assuming a certain parametrization of the initial mass function[3] (IMF, Salpeter 1955) the SFR is given by

$$\mathrm{SFR} = 7.9 \cdot 10^{-42} L_{\mathrm{H}\alpha} \ , \tag{1.1}$$

where the Hα luminosity is measured in erg s^{-1} and the resulting SFR is then expressed in units of $\mathrm{M}_{\odot}\mathrm{yr}^{-1}$.

By investigating the level of star formation in different galaxies, it has been assessed

---

[3] the initial mass function is the mass distribution of newborn stars. Based on stellar counts in the solar neighborhood, Salpeter suggested the IMF to be a power law of the form dN/dM= $\Phi_{\mathrm{IMF}}(M) \propto M^{-\alpha}$, where dN/dM is the number of stars formed per unit mass, and the slope $\alpha = 2.55$. The exact shape of the IMF in the high-mass end of the distribution, as well as its cosmic universality, are still hotly debated.

that a tight correlation exists in the local Universe between the SFR and the stellar mass ($M_\star$) of star forming galaxies (Noeske et al., 2007; Renzini & Peng, 2015). This relation, known as the Star Forming Main Sequence (SFMR), is usually parametrized as a linear relation between SFR and $M_\star$ of the form

$$\mathrm{SFR} = \alpha \mathrm{M}_\star^\beta \; ; \tag{1.2}$$

the typical scatter around the relation is only of the order of $0.2 - 0.3$ dex (Speagle et al., 2014), suggesting that galaxies lying on this sequence follow a smooth, secular evolution driven by gas accretion. Several works have then verified that this relation holds across the epochs, while its slope and normalization evolves with redshift (Noeske et al. 2007; Daddi et al. 2007; Rodighiero et al. 2011); the evolution of the cosmic SFR is such that between z~ 2 and z$= 0$ the SFR (at fixed stellar mass) has decreased by a factor of ~ 30 (Daddi et al., 2007). A certain amount of galaxies appear to be forming stars at a much more elevated rate with respect to the average SFMS population: these *starburst* galaxies lie thus well above the SFMS locus. Their enhanced star formation activity is mainly triggered by interactions and merger events that fuel large amount of gas and dramatically reduce the depletion timescale, rather than secular processes.

Dividing the SFR by the stellar mass $M_\star$ we can define the specific star formation rate (sSFR), a useful quantity to account for the current level of star formation with respect to the average of that occurred in the past (which is encompassed in $M_\star$); the sSFR, therefore, can be considered as a rough estimate of the evolutionary status of a galaxy. Observations in the local Universe show that the sSFR decreases with increasing stellar mass, which implies that massive galaxies evolved first and formed their stars in the past, whereas less massive galaxies are still actively forming stars and are in a earlier stage of their evolution.

1.1.3 BPT diagrams and excitation mechanisms in galaxies

In 1981, Baldwin et al. (1981) suggested that some line intensity ratios could be used as spectroscopic diagnostics to discriminate the dominant ionization mechanism of the gas. The idea was to compare the level of ionization of collisionally excited lines and recombination lines to obtain information about the nature of the ionizing continuum. They first proposed a bi-dimensional diagram based on the [O III]$\lambda 5007$/Hβ vs [N II]$\lambda 6584$/Hα line ratios, which is even nowdays commonly referred to as the BPT diagram (named after Baldwin, Phillips & Terlevich). This approach turned out to be both easy and powerful since the required lines lie in the optical spectral range and their proximity in wavelength makes the diagram reddening insensitive. From the analysis of the distribution of a large sample of local galaxies (e.g. from the SDSS), it became

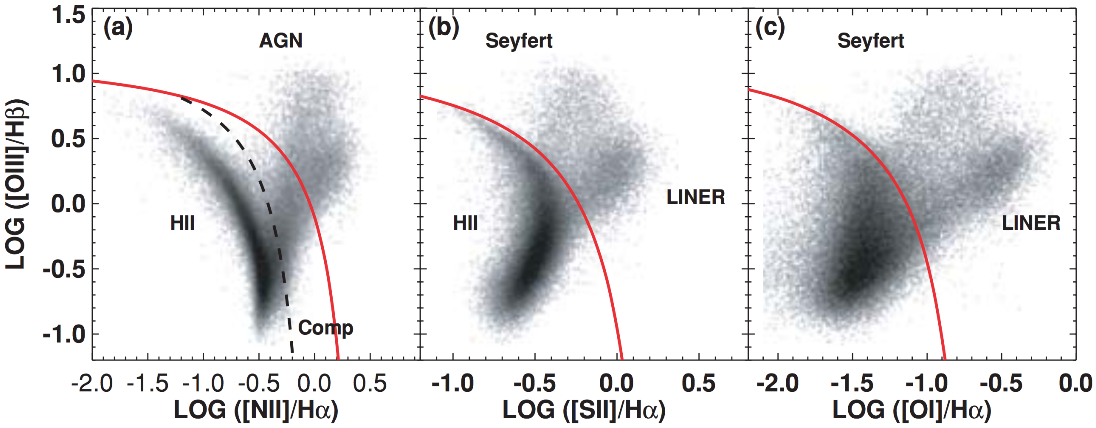

Figure 1.2: BPT diagnostic diagrams for SDSS galaxies involving [O III]/Hβ vs [N II]/Hα (*left*), [S II]/Hα (*middle*) and [O I]/Hα (*right*) line ratios respectively. The theoretical maximum starburst line by Kewley et al. 2001 is shown in red in all panels, while the revised diving line by Kauffmann et al. 2003b is shown as the dashed black line in the [N II]-based BPT panel. Figure from Kewley et al. 2006.

immediately clear that the overall population separates in two distinct groups which occupy different regions of the diagram, assuming a characteristic double-wing shape (Fig. 1.2). A large number of galaxies appear to lie on a tight sequence characterized by lower values of [O III]/Hβ and [N II]/Hα with respect to the rest of the sample (i.e. the left-wing): these are star forming galaxies, whose ionising continuum is mostly due to O-B type massive stars in H II regions. On the other hand, galaxies associated with different ionization mechanisms (like those hosting an AGN in their center and thus subject to a harder radiation field), are characterized by increased collisionally excited lines over recombination lines ratios, and mostly occupy the upper right region of the diagram. The [O III]/Hβ vs [N II]/Hα diagram proves to be very efficient in separating AGN from star-forming galaxies; the heating by an AGN in fact boosts the [N II] line and creates the clear separation of the two populations. Based on photoionisation and stellar population synthesis models, Kewley et al. (2001) defined an upper boundary for the locus occupied by star forming galaxies in the BPT diagram, to aid the classification between star forming and AGN objects; this theoretical upper bound has been then empirically revised by Kauffmann et al. (2003b) to better match the locus occupied by the star forming population, and can be also used in conjunction with the Kewley et al. (2001) line to separate the pure non-SF region from the *composite* region of the diagram occupied by galaxies with a mixed contribution in ionization.

Veilleux & Osterbrock (1987) proposed two more diagrams, based on [S II]/Hα and [O I]/Hα ratios, valuable to discriminate between Seyfert galaxies and LINERs, which are characterized by higher fluxes in low ionization lines (like [S II] and [N II]) but low [O III]/Hβ. Originally ascribed to a relatively flat power-law ionizing spectrum, which could be attributed to the presence of a low-luminosity AGN in the central region of the galaxy (Kauffmann et al., 2003b; Kewley et al., 2006), or by shock-heating ionization (Filippenko & Terlevich, 1992; Dopita et al., 1996), it has recently been proposed that their photoionisation is due to evolved (post-AGB) hot stars, which become the main contributors to the ionization flux once O and B stars die (Cid Fernandes et al., 2011; Belfiore et al., 2016).

Early observations of small samples of high-redshift galaxies (e.g., Shapley et al. 2005; Erb 2006; Liu et al. 2008) suggested that the situation at high-z might be radically different, with galaxies exhibiting nebular line ratios inconsistent with observations of the majority of local galaxies. With the advent of new generation, multiobject spectrographs like KMOS on VLT (Sharples et al., 2013), MOSFIRE on Keck (McLean et al., 2012) and FMOS on Subaru (Kimura et al., 2010) the number of high-quality rest-frame optical spectra from the high-redshift Universe has increased dramatically, in particular at the epoch between z$\sim 1.5-3$, where the rest-frame optical lines are shifted into the near-infrared. Large surveys conducted in the last years confirmed that high-redshift star forming galaxies show a clear offset in the position on the classical N2-BPT diagram with respect to the tight sequence in which their local counterparts lie (Steidel et al., 2014; Shapley et al., 2015; Kashino et al., 2016; Strom et al., 2017). Understanding the physical drivers of the observed differences has proven to be challenging, particularly due to the clear degeneracy affecting many of the proposed explanations.

Some works based on different galaxy samples at similar redshifts (Masters et al., 2014, 2016; Shapley et al., 2015; Cowie et al., 2015; Sanders et al., 2016) has argued that the offset observed in high-redshift objects could be mainly due to an enhancement of nitrogen with respect to oxygen (i.e. higher N/O) at a given metallicity (O/H); in this picture, the N2-BPT offset is primarily a shift towards higher [N II]/Hα, affecting in particular low mass galaxies. This would justify the fact that the same shift is much less evident in the [S II]/Hα BPT. Other recent works concluded that the high-redshift locus of galaxies in the N2-BPT plane is most easily explained by a hardening of the stellar ionizing radiation field produced by young Fe-poor stellar populations, together with a slightly increase in ionization parameter and electron density (Steidel et al., 2014; Strom et al., 2017). Predictions from such photoionization models (Steidel et al., 2016) could also reproduce the apparent absence of appreciable offset in the S2-BPT without invoking an increased N/O at fixed O/H. However, larger samples and more direct observational probes of the physical quantities involved are needed to fully address the issue. In Chapter 5 we present and discuss recent observational efforts conducted on this topic.

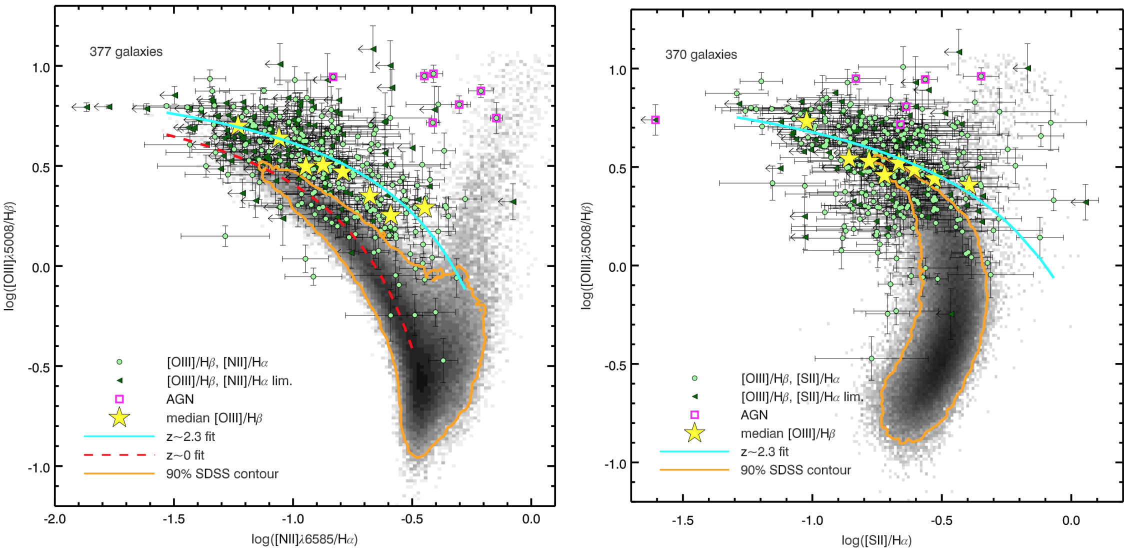

Figure 1.3: *Left panel*: High-redshift galaxies from the KBSS-MOSFIRE Survey on the N2-BPT. In greyscale the position of local SDSS galaxies is reported, with the orange contour enclosing the 90% of the total sample. Magenta squares denote objects identified as AGNs. The average position occupied by the high-z sources appears clearly shifted with respect to the the 90% SDSS contour, as shown both by the location of the median log([O III]/Hβ) values in bins of log([N II]/Hα) represented by the yellow stars, and also by the fit to the distribution of individual KBSS galaxies (the cyan curve). *Right Panel*: High-redshift galaxies from the KBSS-MOSFIRE Survey on the S2-BPT. Symbols and colors are the same as in the *left* panel. In this case the average observed offset in less prominent, as the the log([O III]/Hβ) medians (yellow stars) and the fit to the KBSS sample (cyan curve) coincide with the upper envelope of the orange contour enclosing SDSS galaxies. From Strom et al. 2017.

1.2 The Interstellar Medium

The interstellar medium (ISM) is the mix of diffuse matter and radiation that fill the space between stars in a galaxy. Its matter component is constituted by multiple phases characterized by different physical properties in terms of temperature, density and ionization state, which coexist in rough equilibrium provided by thermal pressure, magnetic fields and turbulence support.

In this Section the nature of the ISM is briefly described, and particular relevance is given to the warm gas residing in ionized nebulae (H II regions), to its line-emission spectrum and associated physical diagnostics, upon which a large part of this dissertation is based. In fact, because emission-line spectra can be detected relatively easily even at faint levels (the bright emission lines contrast with the fainter continuum level), we can measure the spectra of ionized gas nebulae in other galaxies, even at high redshifts. The emergent spectrum of H II regions thus gives us the principal probe of the physical conditions and gas-phase abundances in other galaxies. Observations of H II regions are thus crucial in working out the chemical enrichment history of the ISM throughout the epochs.

1.2.1 A multi-phase medium

The gas component in the ISM exists in a number of different thermal phases depending upon the local conditions and the established balance between heating and cooling processes. From a theoretical point of view, in the classic work by Field et al. (1969) (usually known as "FGH") the ISM is described as constituted by two stable phases, warm and cold, as driven by the stability of clouds in local thermal pressure equilibrium against isobaric perturbations. Later work by McKee & Ostriker (1977) expanded this to consider the role of supernova remnants in contributing a hot, low-density "third phase" to the cold and warm phases identified by FGH. However, to fit all the observational pieces in a coherent theoretical framework has proven to be challenging and providing a self-consistent global model of the ISM represent a subject of current research .

Observationally, the interstellar gas can be probed in, at least, five different phases. Hydrogen molecular clouds are the densest and coolest component of the ISM, with temperatures of $10 - 20$ K and densities $> 10^{-3}$ particles per cm^{-3}. These clouds typically comprise $\sim 30\%$ of the mass of the ISM, but occupy only $\sim 0.05\%$ of its volume. Most molecular clouds are gravitationally bound. The densest parts of these clouds, constituted by cores and clumps within filament structures, can be subject to gravitational instability and represent the sites where new star formation occurs (see Stahler & Palla (2005) for a comprehensive review on the process). Since molecular hydrogen can not be easily detected, the main tracers of this ISM phase are emission lines from different molecular species like CO, falling in the mm-wavelength regime.

The Cold Neutral Medium (CNM) primarily made by cold neutral hydrogen (HI) gas is distributed in sheets and filaments occupying $\sim 1 - 4\%$ of the ISM volume with temperatures of $\sim 80 - 100$ K and densities of $\sim 50\ \mathrm{cm}^{-3}$. The main tracers are UV and optical absorption lines seen along bright stars or quasars line of sights. The CNM is approximately in pressure equilibrium with its surroundings.

Warm neutral atomic hydrogen occupies $\sim 30\%$ of the volume of the ISM, and is located mainly in photodissociation regions on the boundaries of HII regions and molecular clouds. It is characterized by temperatures of the order of ~ 8000 K and densities of $\sim 0.5\ \mathrm{cm}^{-3}$, and is traced by the HI 21cm emission line.

Almost the 25% of the ISM volume resides in diffuse gas with temperatures of $\sim 10^4$ K, and densities $\sim 0.1\ \mathrm{cm}^{-3}$. It is mainly photoionized by massive stars and can be traced by low-surface brightness Hα emission. A 10% of the ionized gas can be found instead around newborn O and B stars and forms what are commonly known as HII regions (for a more in-depth treatment see Sec. 1.2.2).

Finally, hot, low-density gas heated by supernovae, with temperatures greater than

10^6 K and very low densities of less than 0.003 cm^{-3} constitute the so called Hot Ionized Medium occupying ~ 50% of the ISM. The vertical scale height of this gas is ~ 3 kpc, so it is sometimes referred to in the literature as the "hot corona" of the galaxy. This hot gas is often buoyant and appears as bubbles and fountains high above the disk. Its primary tracers are absorption lines towards hot stars in the far-UV (e.g., O IV, N V, and C IV) and diffuse soft X-ray emission from gas hotter than 10^6 K.

1.2.2 HII regions

Ionized atomic Hydrogen regions, broadly termed HII Regions, are composed of gas ionized by photons with energies above the Hydrogen ionization threshold of 13.6 eV. One usually refers as "Classical HII Regions" to those objects ionized by hot O or B stars (or clusters of such stars) and associated with regions of recent massive-star formation, while "Planetary Nebulae" are the ejected outer envelopes of AGB stars photoionized by the hot remnant stellar core. Classical HII regions range in size from parsec-scale regions ionized by a few O or B stars (e.g., the Orion Nebula), up to giant HII region complexes ionized by clusters containing hundreds of stars (e.g., 30 Doradus in the LMC). The physics of an HII region is governed by the interplay of three main processes:

- **Photoionization Equilibrium**, the balance between photoionization and recombination. This determines the structure of the nebula and the rough spatial distribution of ionic states of the elements in the ionized zone.
- **Thermal Balance** between heating and cooling. Heating is dominated by photoelectrons ejected from Hydrogen and Helium with thermal energies of a few eV. Cooling is dominated in most HII regions by electron-ion impact excitation of metal ions followed by emission of forbidden lines (i.e. collisionally excited lines, CEL) from low-lying fine structure levels. This emission represents the main cooling channel in the nebula and gives HII regions their characteristic spectra.
- **Hydrodynamics**, including shocks, ionization and photodissociation fronts, and outflows and winds from the embedded stars.

The UV, visible and IR spectra of HII regions are very rich in emission lines, primarily collisionally excited lines of metal ions and recombination lines of Hydrogen and Helium (see e.g. Figure 1.4). HII regions are also observed at radio wavelengths, emitting radio free-free emission from thermalized electrons and radio recombination lines from highly excited states of H, He, and some metals. The strengths of the H and He recombination lines are sensitive to both the total luminosity and the spectrum

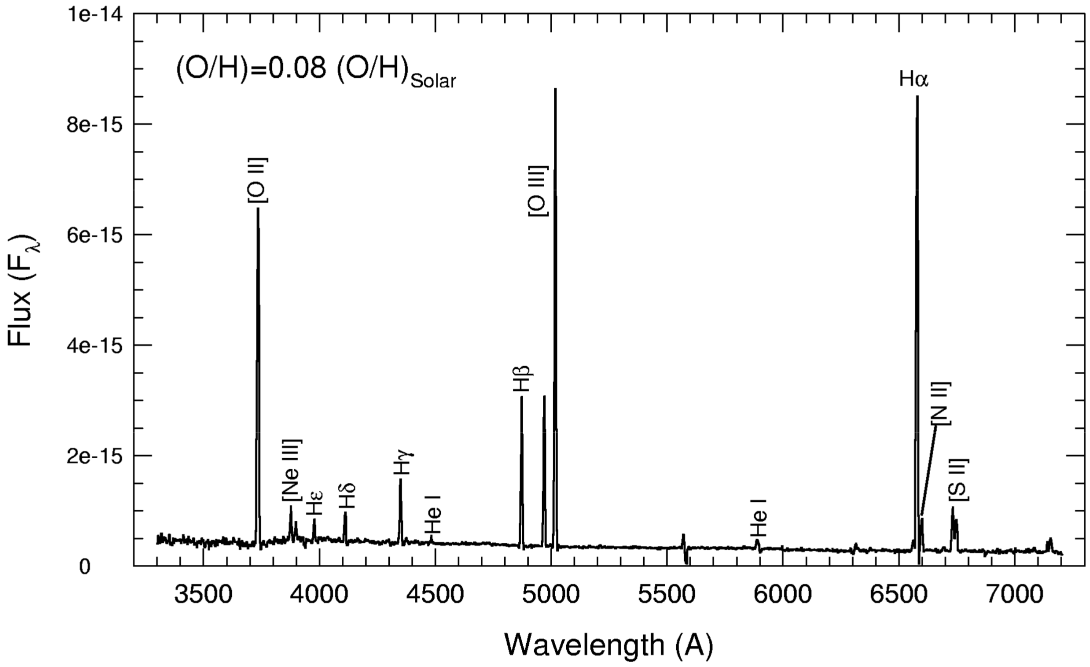

Figure 1.4: Visible spectra of a low metallicity H II region in the galaxy NGC3413. Because of its low metallicity, there is less cooling in the gas, resulting in a hotter nebula (Te ~ 14000 K), which leads to an increase in the excitation of metal lines, like those from [O III].

of the ionizing radiation field, and may be used as diagnostics of the global properties of the nebula. Recombination is the recapture of an electron into one of the excited states of the atom, followed by a cascade of radiative transitions into the ground state. The population of any given excited state is set by both direct recombination into that state and by recombination cascades from all the higher levels. For typical nebular conditions, collisions are unimportant, and the level populations depend on the radiative transition probabilities for each cascade transition. There are two extreme cases of interest in computing the recombination lines of hydrogen: the Case A Recombination assumes that the nebula is optically thin in all of the H I resonance lines arising from the ground state; in the Case B, instead, the nebula is optically thick to UV Lyman resonance line absorption, hence each Lyman photon absorbed is quickly re-emitted at the same wavelength (*resonance scattering*), leading to further ionization. Nebular conditions most often favor Case B over Case A recombination, since the typical optical depth in the Lyman resonance lines is high and, therefore, contributions to the excited level populations by UV resonance absorption out of the ground state cannot be ignored.

In an ideal "ionization bounded" nebula, all ionizing photons with energies above 13.6 eV contribute to hydrogen ionization and none escape the nebula. Since in photoionization equilibrium all photoionizations events within the volume of the nebula are balanced by recombinations, one can use the strengths of the recombination lines to "count" the number of ionizing photons. In the simple assumption of a pure-hydrogen, spherical nebula (i.e. Strömgren sphere), the number of ionizing photons per second Q emitted by the central source can be inferred from, e.g., the Hβ luminosity (hence from the observed integrated Hβ flux, once known the distance). Once Q is known, another important parameter in the context of nebular studies can be derived: the *ionization parameter* U, usually defined as the dimensionless quantity given by[4]

$$U(r) = Q/(4\pi r^2 n_e c) \ , \tag{1.3}$$

where r is the distance between the gas and the source and n_e is the electron density. The ionization parameter is used to quantify the intensity of the ionizing spectrum incident onto the gas and can be thought as the number of ionizing photons per hydrogen atom.

From the analysis of the emission-line spectra of ionized nebulae, many other diagnostics of different physical properties can be defined: some of them will be briefly discussed in the following. For example, the relative level populations of a given ion depend critically on the local thermodynamic properties of the ionized gas, principally density and temperature. These relative level populations are manifest in the intensity ratios of lines emitted by the ion and can be used as powerful diagnostics of the nebular density and temperature in the line-emitting regions. Moreover, the strengths of the metal ion lines relative to Hydrogen are sensitive to the relative ionic and total abundances of these metals in the nebula, as well as to the shape of the ionizing continuum spectrum. These provide a way to measure the gas-phase abundances of particular elements within the nebula.

Nebular diagnostics

Some ionic species, like O^{++} and N^{+}, have a ground-state configuration like the one represented in the left panel of Fig. 1.5. All the levels above the lowest ground state are populated by the excitation due to the collisions between ions and free electrons. The populations of the ^{1}S and ^{1}D states depend critically on the temperature, so the strengths of the emission lines arising from these levels will be temperature sensitive. In particular, the relative strengths of the $^1S \rightarrow {}^1D$ and $^1D \rightarrow {}^3P$ lines will provide a measurement of the nebular temperature, with a slight additional density dependence given by the different critical densities[5] of these levels, which is however usually very

---

[4] in some nebular studies, the ionization parameter is defined as q=Uc, in units of cm s^{-1}, see e.g. Kewley & Dopita 2002.

[5] The critical density is the density where the collisional de-excitation rate equals the radiative de-excitation rate. In a two-level atom, at densities higher than critical the de-excitation of the upper level is dominated by collisions rather than radiative processes

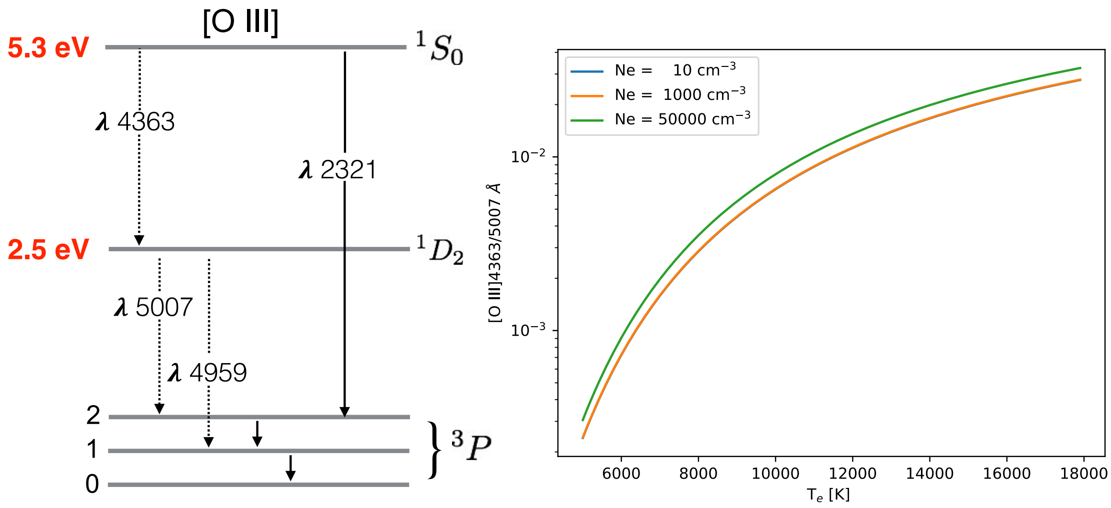

Figure 1.5: *Left Panel*: Ground-state energy level configuration of the O^{++} ion, responsible for the [O III] emission lines. The transitions falling in the optical regime are indicated by dashed lines. *Right Panel*: Temperature dependence of the [O III]$\lambda4363/\lambda5007$ ratio, for different density regimes. This ratio represent a good temperature indicator as it is strongly sensitive to Te over the entire range of typical nebular temperatures, while being almost insensitive to density.

mild (see e.g. the right panel of Fig. 1.5). As an example, the [O III]$\lambda5007$/[O III]$\lambda4363$ is one of the most commonly adopted diagnostic ratios to measure the electron temperature of the ionization zone traced by the O^{++} ion. In this context, we note that the weaker line originating from the highest energy level (e.g. [O III]$\lambda4363$ for oxygen) is often referred to as *auroral*, while the strongest one is referred to as *nebular*. Other temperature indicators involving different ionic species include the [N II]$\lambda6583$/[N II]$\lambda5755$, the [O II]$\lambda3727$/[O II]$\lambda7325$ and the [S III]$\lambda9532$/[S III]$\lambda6312$ ratios. From detailed calculations of 5-level atom structures one can infer numerical formulae to measure the electron temperature from the observed intensity ratios. These expressions strongly depends on the assumed collision strengths of the transitions, which are however usually well tabulated for the typical range of nebular conditions ($T_e \approx 5000 - 20000$ K, $n_e \approx 1 - 10^5$ cm^{-3}). The observational uncertainties are primarily driven by the fact that the auroral lines like [O III]$\lambda4363$ and [N II]$\lambda5755$ are very faint, usually only a few percent the flux of Hβ. Measurement errors in the faintest lines thus drive the error in the final derived temperature more than the typical uncertainties on the atomic data.

The electron density is usually derived from intensity ratios of two lines of the same ion which have similar excitation energy (thus are emitted in wavelength-close doublets), but different critical densities for collisional de-excitation. These emission arise from ground state configurations like those shown in the left panel of Fig. 1.6. These ratios are good diagnostics of electron densities in the density regime between the different critical densities of the two emissions, while saturating in both high- and

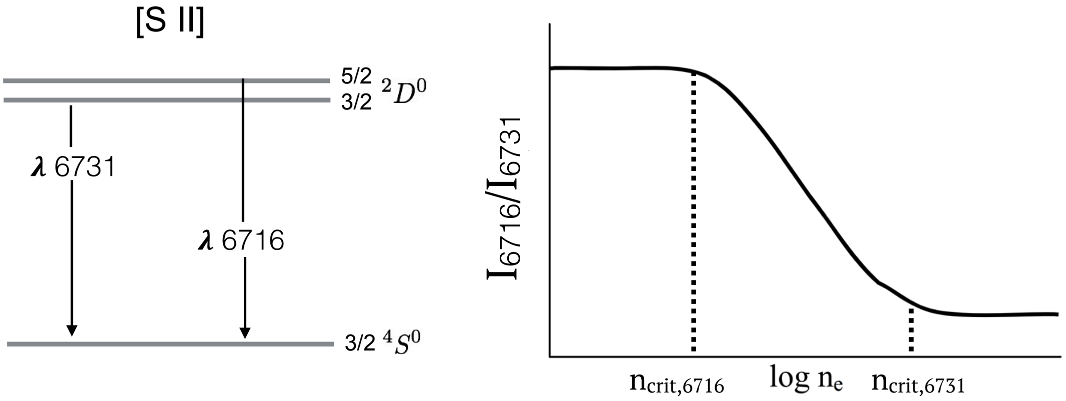

Figure 1.6: *Left Panel*: Ground-state energy level structure of the S^+ ion, responsible for the [S II] emission lines. The two transitions which constitute the density-sensitive doublet are shown. *Right Panel*: Intensity of the [S II]λ6716/λ6731 ratio as a function of density. This ratio acts as a good density indicator within the density regime enclosed between the critical densities of the two different transitions, while saturating in the high- and low- density regime.

low-density regimes (see right panel of Fig. 1.6). The most commonly adopted ratios are those involving the sulfur doublet [S II]λ6717/[S II]λ6731 and the oxygen doublet [O II]λ3726/[O II]λ3729 (when spectrally resolved), which are sensitive to density variations (and almost insensitive to temperature) in the range of densities typically spanned by HII regions (i.e. $n_e \sim 10^2 - 10^4$ cm^{-3}).

1.2.3 The role of dust

Dust is a relevant component of the ISM. It is constituted mostly by grains of graphite and silicate of typical sizes of a few microns. Dust plays a key role in the evolution of galaxies by depleting chemical elements out of the ISM, catalyzing the formation of (even complex) molecules and introducing a number of important effects on the ionization equilibrium and structure of ionized nebulae. When a dust grain absorbs a UV photon, the grain is heated to $T \geq 50$K and then re-radiates the absorbed energy as Far-IR thermal continuum photons that escape from the nebula. In effect, ionizing photons are destroyed by dust grains, substantially modifying the ionizing radiation field, and changing the ionization balance and structure of the nebula. A counterbalancing effect is that the ionizing radiation field, especially in the presence of very hot stars, is sufficient to photoevaporate dust grains. The presence of dust is thus two-edged: dust can alter the ionization and recombination balance in a nebula, and the conditions can be hostile to the survival of the grains themselves. Sorting out these effects is very challenging, since it is very difficult even for detailed photo-ionization models to include dust and predict clear effects that may be tested observationally. Moreover, some elements are strongly depleted from the gas phase and locked into grains, changing the mix of metals in the gas-phase of the nebula. Similarly, photoevaporation of dust grains in a nebula might return elements to the gas-phase, enhancing the abundances. Since metals are the primary coolants in nebulae, how dust depletion or destruction is treated has important implications for the results of model nebula calculations.

From an observational point of view, dust constitutes a source of complications for every study based on optical nebular diagnostics of the ISM, because of its obscuring effects. In this wavelength range in fact, dust both attenuates light (extinction) and also causes a change in the shape of the spectrum, by absorbing at bluer wavelengths more than at redder ones (reddening). At a given wavelength λ, the extinction in magnitudes can be written as

$$\mathrm{A}_\lambda = 2.5\,\log(\mathrm{F}^0_\lambda/\mathrm{F}_\lambda)\ , \tag{1.4}$$

where F^0_λ and F_λ are the intrinsic and observed (thus, attenuated) flux respectively. The parameterization of the wavelength dependence of A_λ is usually expressed in terms of an extinction curve

$$\mathrm{k}_\lambda = \mathrm{A}_\lambda/\mathrm{E(B\text{-}V)}\ , \tag{1.5}$$

where E(B-V) is the color excess quantified by the difference in the B and V magnitudes. Extinction curves can be obtained for the Milky Way (the Cardelli et al. (1989) is among the most widely used), although the situation is much more complicated for extragalactic sources, due to the complex and mainly unknown distribution and geometry of stars and dust (Calzetti et al., 2000). To correct for reddening the observed emission line fluxes, a common procedure consist in comparing the observed ratio of two Balmer lines (generally Hα and Hβ, the so-called *Balmer decrement*) with the one predicted theoretically ($\mathrm{H}\alpha/\mathrm{H}\beta = 2.87$ for case B recombination at 10^4 K) and infer, once assumed a given extinction curve, the E(B-V) from the equation

$$\frac{\mathrm{F}_{\mathrm{H}\alpha}}{\mathrm{F}_{\mathrm{H}\beta}} = \frac{\mathrm{F}^0_{\mathrm{H}\alpha}}{\mathrm{F}^0_{\mathrm{H}\beta}}\ 10^{-0.4\mathrm{E(B\text{-}V)}[\mathrm{k}_{\mathrm{H}\alpha}-\mathrm{k}_{\mathrm{H}\beta}]}\ . \tag{1.6}$$

However, the Balmer decrement is only sensitive to modest extinction levels; when averaged over a wide range of values for example, regions of lower attenuation will dominate the observed flux and this may bias the inferred extinction towards lower values. Thus, despite the relative straightforward approach, it should always be beared in mind that correcting for dust attenuation often represents one of the major sources of uncertainties for extragalactic nebular studies.

1.3 Gas-phase Metallicity: a key diagnostic of galaxy evolution

Galaxy evolution is governed by the complex interplay between many different processes affecting the cycle of baryons in and out of galaxies. As these systems evolve, they assembly more and more stellar mass by means of star formation episodes; during the different phases of stellar evolution, elements heavier than hydrogen and helium are first produced and then dispersed into the ISM by stellar winds and supernova explosions.

The gas-phase metallicity, defined as the relative abundance of all heavy elements with respect to hydrogen in the ISM, represent thus a fossil record of the recent star formation activity of a galaxy. Moreover, being a relative measure to the hydrogen content of the ISM, it is sensitive also to gas flows processes affecting the gas reservoir, like inflows of pristine gas that may dilute it, or outflows that can eject a large fraction of enriched material into the intergalactic medium. Ionized nebulae are our primary probes of the gas-phase abundances in regions of recent star formation, and are the primary tracers of the chemical evolution of the ISM in our and other galaxies.

Since oxygen is the most abundant element, by mass, among the "metals" in the ISM, as well as being responsible for some of the brightest emission lines detected in nebular spectra, its abundance is usually assumed as a proxy of the total metallicity and commonly expressed in units of $12 + \log(\mathrm{O/H})$, where O/H is the relative number of oxygen to hydrogen atoms.

In this Section we will briefly review the most common methods for the determination of chemical abundances from emission line spectra and describe how a deep understanding of the scaling relations involving metallicity can shed light on the star formation and gas flow history of galaxies, helping us to develop a comprehensive picture of galaxy evolution.

1.3.1 Determination of chemical abundances

The accurate determination of gas-phase metallicity truly represents, even nowadays, a challenge for every study aimed at understanding the chemical evolution of galaxies. Many different approaches have been proposed through the years, each of them characterized by its own strengths and weaknesses. Generalizing, these methods can be basically classified into two main categories: direct methods, which measure abundances using the information directly inferred from the emission lines in spectra, and statistical methods, which use a comparative approach based on spectral properties calibrated from families of objects or inferred from prescriptions of detailed photoionization models. In this Section we introduce and discuss these different methodologies in light of their assumptions, strengths and systematics.

The Te method

The T$_\mathrm{e}$ method (which is sometimes referred to as the *direct method*, Menzel et al. 1941; Pagel et al. 1992; Izotov et al. 2006) is based on the assumption that the abundance ratio of two ions can be obtained from the observed intensity ratio of lines emitted by those given ions. In general, assuming a uniform chemical composition and a certain ionization structure of the nebula, one can express the relative abundance of an element compared to hydrogen as:

$$\frac{N(X^i)}{N(H^+)} = \frac{I_\lambda}{I_{H\beta}} \frac{\epsilon_{H\beta}(T_e, n_e)}{\epsilon_\lambda(T_e, n_e)} \text{ icf} \tag{1.7}$$

where I is the intensity of the transition responsible for the emission at λ wavelength, ϵ the volumetric emissivity and T$_\mathrm{e}$, n$_\mathrm{e}$ are the electron temperature and density representative of the emission; icf is the "ionization correction factor". Thus, for example, the relative abundance of the doubled ionized oxygen compared to hydrogen can be inferred from :

$$\frac{O^{++}}{H^+} = \frac{I([\mathrm{O\,III}]\lambda5007)/I(H\beta)}{\epsilon_{[\mathrm{O\,III}]}(T_e, n_e)/\epsilon_{H\beta}(T_e, n_e)} \,. \tag{1.8}$$

Line ratios are measured instead of total line luminosities, primarily because they are distance independent and do not depend on absolute calibration (which is always much harder than relative calibration in spectroscopy). For example, it is common practice at visible wavelengths to measure line strengths relative to Hβ because this line is readily observed and generally unblended with other lines. Since the emissivities of collisionally excited lines (e.g. [O III]λ5007) and hydrogen recombination lines (e.g. Hβ) are characterized by very different temperature dependencies, their relative ratio strongly depend on electron temperature as well. Thus, the application of this method require accurate knowledge and evaluation of both electron temperature and density. In Section 1.2.2 we have already discussed how different emission lines can be involved as diagnostics to measure nebular temperature and density. In practice, density and temperature indicators are commonly used in combination with an iterative approach to remove the residual degeneracy of each given diagnostic on the second parameter (i.e. to remove the density-dependence of Te diagnostics and the temperature dependence of n$_\mathrm{e}$ diagnostics). It is worth noting here that different line diagnostics, involving different ionic species, traces only the physical conditions within the region of the nebula in which they are emitted: [O III] and [N II] emission, for example, probes different temperature zones within the nebula. [O III] is mostly emitted in the high-ionization zone, while [N II] emission originate from the low-ionization zone, which is also traced, for example, by [S II] and [O II]. When only few diagnostics are available, the physical conditions of the other regions can be inferred from theoretical relations predicted by photoionization models or derived empirically (Garnett, 1992; Pilyugin et al., 2006b). However, considerable temperature discrepancies have been reported even when considering ionic species originating from the same zone (Bresolin et al. 2005; Esteban et al. 2009; Pilyugin et al. 2009; Binette et al. 2012; Berg et al. 2015, see also Section 3.3). The origins of these discrepancies are still debated, but temperature and chemical inhomogeneities, as well as shocks, may all possibly contribute.

The total abundance of a given element relative to hydrogen is then given by the sum of the abundances of each individual ionic species. In practice, not all the ions present in a nebula are generally observed. In the case of oxygen abundance in HII regions, it is commonly assumed that $O/H = O^+/H^+ + O^{++}/H^+$, since the abundance of the O^{+++} ion is usually negligible and O^0, which emits the [O I]$\lambda 6300$ line, is tied to neutral hydrogen and not to H^+ and thus is emitted in a different region of the nebula. In many other cases, one should correct for unseen ionized states using appropriate correction factors. Generally one can rely on simple ionization potential considerations, assuming e.g. $N/O=N^+/O^+$ based on the similarity of the ionization potentials of N^+ and O^+, or rely on more accurate predictions from photoionization models.

A number of (sometimes strong) assumptions are at work in these measurements. Since the forbidden lines are optically thin, any measurement is an integral along the line of sight through the nebula. In a reasonably homogeneous nebula, the measured temperature is representative of the mean temperature along the line of sight. In an non-homogeneous nebula characterized by temperature fluctuations however, the integrated line fluxes are emissivity-weighted averages along the line of sight. The interpretation of the temperature so derived in such a case depends critically on the nature of the inhomogeneity. A number of methods have been suggested to estimate the magnitude of the effect, in particular as temperature measurements impact upon nebular abundance determinations (see e.g. Peimbert 1967). The reliability of the T_e method has thus been criticized, especially in the high metallicity regime. In fact, the steep temperature dependence of CELs (especially of the auroral lines used as T_e diagnostics) results in emissivities that are weighted toward higher temperatures and, thus, lower abundances: this is likely to cause a global underestimate of the inferred metallicity (Stasińska, 2002, 2005). Moreover, the contribution of recombination to the intensities of some CELs involved (e.g. [O II]$\lambda 7320, 7330$) in the T_e method can become important at low temperatures (Stasińska, 2005) and, finally, the physical interpretation of electron temperature in this method is bounded to assuming a pure thermodynamic equilibrium with a Maxwell-Boltzmann electron energy distribution, whereas it has been recently suggested that free electrons in ionized nebulae could instead be better represented by a k-distribution (Nicholls et al., 2013). However, this last interpretation lacks of both theoretical and observational confirmations (Ferland et al., 2016).

A different technique is based on exploiting the ratio between hydrogen and oxygen recombination lines (ORLs): these lines show a very weak dependence on electron temperature and density (Esteban et al., 2009, 2014; Peimbert & Peimbert, 2014) and their relative brightness scale almost directly with the ionic abundance, which certifies this approach probably as the most "direct" from a physical point of view. Additionally, its intrinsically mild dependence on electron temperature makes it robust against the typical biases of the T_e method associated with temperature fluctuations. However, typical discrepancies between T_e-based and ORLs-based abundances have been found, with the first ones underestimating the latter by a factor of $0.2-0.3$ dex; the possible origin of these discrepancies is still largely debated (García-Rojas & Esteban, 2007; Stasińska, 2007; Esteban et al., 2009). Moreover, recent spectroscopic studies conducted on individual, supergiant stars in nearby spirals revealed that T_e abundances are in relatively good agreement with the stellar metallicities (once taking into account the depletion onto dust), while metal recombination lines tend to underestimate the stellar metallicities by a significant amount in metal-poor environments (Bresolin et al., 2016). Finally, the direct scaling of Rls intensities with abundance translates into extremely faint lines for metals ($\approx 10^4$ times fainter than Hβ for oxygen). Therefore, ORL abundance measurements require extremely high signal-to-noise, high-resolution spectra and have only been made for He, C, O and Ne in a few dozen bright HII regions in the Milky Way (MW) and the Local Group (Esteban et al., 2004; García-Rojas & Esteban, 2007; Bresolin et al., 2009) but cannot be detected in galaxies more distant than a few kpc (Peimbert et al., 2007).

Strong line methods

The auroral lines involved in the classic T_e method are usually weak (~ 100 times weaker than Hβ for typical nebular conditions) and their emissivity is strongly temperature-dependent: they are thus extremely difficult to detect in high-metallicity galaxies and even more challenging to observe in the high redshift Universe, given the typical sensitivity of the current astronomical instrumentation. Therefore, to be able to measure abundances in faint, distant and metal rich galaxies, different methods have been proposed. In particular, the emission-line ratios between some strong nebular lines are well known to be dependent on the oxygen abundance; this can be motivated by the correlation between metallicity and electron temperature of the gas, or descend from even more indirect correlations between the metallicity and physical quantities like the ionization parameter or the relative abundances of different chemical species (like the nitrogen-to-oxygen ratio, N/O). Thus, it has been proposed that these line ratios could be calibrated against the oxygen abundance and used as metallicity indicators for galaxies in which the application of the T_e method is not possible due to the extreme faintness of auroral lines: these methods are referred to as the statistical or *strong-line* methods.

The oldest method, still among the most popular ones, is based only on hydrogen and oxygen lines. Pagel et al. (1979) introduced the ([O II]λ3727 + [O III]λ4959,5007)/Hβ ratio (later referred to as R_{23}) to estimate the oxygen abundance. This method has been then revised and calibrated many times by several authors (e.g. Skillman 1989), that refined the method also to account for variations in the ionization parameter (e.g McGaugh, 1991). Many other metallicity indicators have been proposed then throughout the years, involving different metal lines: [O III]λ5007/[N II]λ6584 (O3N2) and [N II]λ6584/Hα (N2) (Alloin et al. 1979; Storchi-Bergmann et al. 1994; Pettini & Pagel 2004); ([S III]λ9069+[S II]λ6717,6731)/Hβ (S23) by Vilchez & Esteban (1996); [N II]λ6584/[O II]λ3727 (N2O2, Kewley & Dopita 2002); [Ar III]λ7135/[O III]λ5007 (Ar3O3) by Stasińska (2006); [Ne III]λ3869/[O II]λ3727 (Ne3O2) (Nagao et al., 2006).

Each of these proposed diagnostics carries both advantages and disadvantages, related to the relative strength of the lines involved, their wavelength separation (and hence reddening sensitivity) and dependence on other physical parameters. For example, an important caveat to always bear in mind is that any method based on the ratio of an optical CEL and a recombination line (e.g. R23 or S23) is intrinsically bound to be double-valued. To show that, let us consider the behavior of the [O III]λ5007/Hβ ratio with metallicity, and its temperature dependence :

$$[\mathrm{O\,III}]\lambda5007/\mathrm{H}\beta \propto \mathrm{O/H}\ T_e^{0.5}\mathrm{e}^{-28764/T_e} \ . \tag{1.9}$$

At high metallicities (e.g. O/H$\sim 10^{-3}$), the most efficient cooling channel is represented by the [O III]$\lambda 88\mu$m emission, which lowers the temperature below the excitation threshold of optical CELs. Thus, since Te decreases with increasing O/H, it follows that [O III]λ5007/Hβ decreases with oxygen abundance in this regime. At lower metallicities (O/H$\sim 10^{-4}$), Te is higher, allowing collisional excitation of the [O III]λ5007 line, which becomes the dominant coolant; this represents an intermediate regime where [O III]λ5007/Hβ is almost independent of O/H. At very low metallicities finally, cooling is dominated by recombination and collisional excitation of hydrogen and [O III]λ5007/Hβ scales proportionally with O/H. In such circumstances, external arguments must be found to determine a priori whether the object considered is on the

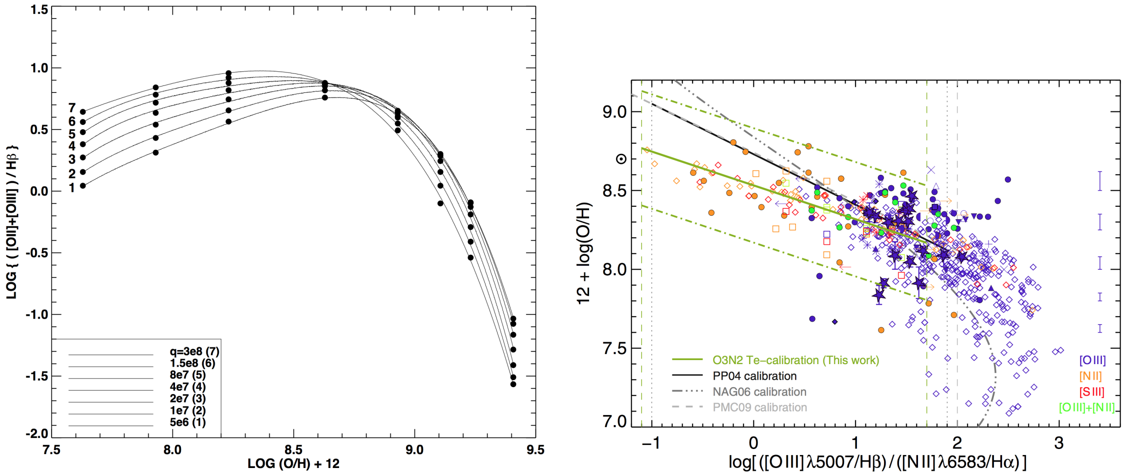

Figure 1.7: Examples of the dependence of some strong-line ratios with oxygen abundance and their relative calibration. In the *left* panel the relation between R_{23} and metallicity is shown as predicted by photoionization models. Its double-valued behavior is clearly visible, as well as its dependence on the ionization parameter, represented by the different solid lines. From Kewley & Dopita (2002). In the *right* panel the O3N2 indicator is plotted as a function of T_e-based metallicity for a collection of HII regions from the literature. A linear fit to the points, which represent the empirical calibration of this diagnostic, is shown in green. From Marino et al. (2013).

"high abundance" or "low abundance" branch, usually exploiting diagnostics involving different lines (e.g. [N II]λ6584).

The use of nitrogen based indicators (e.g. N2 or O3N2) turns out to work well since this ratios show to be correlated with O/H over the almost entire range of observed metallicities in giant HII regions, being N/O observed to increase with increasing O/H at high metallicities. However, the N/O vs O/H relation is known to be affected by a large scatter and its cosmic evolution is still poorly constrained, questioning the validity of these ratios as metallicity indicators in the high redshift Universe (Shapley et al., 2015). Additionally, some strong line ratios like O3O2 ([O III]λ5007/[O II]λ3727) are strongly sensitive to the ionization state of the gas: their dependence on metallicity, therefore, is very indirect and based on the anti-correlation between ionization parameter and oxygen abundance, which is seen to hold fairly well in the local Universe (Nagao et al., 2006) but can sometimes provide misleading results (Cresci et al., 2017).

Calibrations of strong-line methods can be obtained via different approaches: empirically, for samples of objects in which metallicity have been previously derived with the T_e method (e.g. Pettini & Pagel 2004; Pilyugin & Thuan 2005; Pilyugin et al. 2010b, 2012b; Marino et al. 2013; Pilyugin & Grebel 2016), or theoretically, in which the oxygen abundance dependence of different diagnostics follows the predictions of detailed photoionization models (e.g. McGaugh 1991; Zaritsky et al. 1994; Kewley & Dopita 2002; Kobulnicky & Kewley 2004; Tremonti et al. 2004; Dopita et al. 2013, 2016), or be a hybrid combination of the two (Maiolino et al., 2008). An example of two different kinds of calibrations are illustrated in Fig. 1.7. Unfortunately, comparisons among metallicities estimated through different calibrations reveal large discrepancies, even for the same sample of objects, with variations of the order of ~ 0.3 dex and sometimes up to ~ 0.6 dex (Moustakas et al., 2010; Kewley & Ellison, 2008). In fact, theoretical calibrations are known to predict higher metallicities with respect to empirical calibrations based on the T_e method. Despite begin largely discussed in the literature, the origins of these discrepancies are still unclear and we still lack a clear definition of the absolute abundance scale needed to build a coherent picture of galaxy chemical evolution.

A problem with empirically-calibrated strong-line diagnostics is that they sometimes ignore the dependence of the emission line ratios on the ionization state of the gas, for example in the case of diagnostics calibrated against samples of HII regions with direct T_e abundances, which not consider the dispersion and range in ionization parameter of the calibration sample. This issue can be sometimes addressed by the simultaneous use of multiple diagnostics with a recursive technique (McGaugh, 1991; Kobulnicky & Kewley, 2004) or by a marginalization within a fully Bayesian framework (Blanc et al., 2015). Another possible source of discrepancy is the potential underestimation of the chemical abundance by the T_e method in the presence of density and temperature fluctuations and temperature gradients in ionized nebulae (Peimbert, 1967; Stasińska, 2002, 2005). As already discussed in Sec 1.2.2 in fact, HII regions do not have homogeneous density distributions; on the contrary, pockets, filaments, and shells showing enhanced electron temperatures are ubiquitously observed in these objects. In regions where T_e is enhanced, the emissivity of the temperature sensitive auroral lines is disproportionally enhanced over that of the stronger nebular lines. This translates into an overestimation of the average T_e and an underestimation of the abundance when integrating the line ratios over the whole nebula. Additionally, calibrations are sometimes obtained for samples of objects that do not properly cover all the galaxy parameters space; this means, for example, that empirical calibrations obtained from a sample of low excitation HII regions could give unreliable results when applied to global galaxy spectra. The meaning of the measured metallicity as inferred from integrated spectra of galaxies, in this sense, is far from being obvious. Such spectra in fact contain the composite light weighted on HII regions differing in chemical composition and extinction as well as the light from the diffuse ionized interstellar medium, which can bias the determination of the global metallicity (Pilyugin et al., 2012a; Zhang et al., 2016; Sanders et al., 2017). Recently, the application of integral field spectroscopy allowed to study galaxy properties in great detail and to extend the compiled HII regions database with Te-based abundances in order to obtain calibrations based on the direct method (e.g. Marino et al. 2013). However, self-consistent calibrations obtained from integrated galaxy spectra and covering the entire metallicity range are still scarce. In Chapter 3 we present a new approach to obtain a self-consistent calibration of strong line diagnostics, fully anchored to the T_e abundance scale defined by galaxies in the local Universe.

Calibrations based on (grids of) photoionization models, on the other hand, suffer from a series of systematic uncertainties that are not fully understood. In such techniques, a certain number of assumptions are made on a given set of input parameters (the effective temperature of the ionizing radiation, the ionization parameter, the chemical composition, the gas density, the role of dust etc..) which are then varied to predict the intensities of emission lines and compare the inferred line ratios with the observed ones. These models are based on photoionization codes (e.g. CLOUDY, Ferland et al. 2013, or MAPPINGS, Sutherland & Dopita 1993; Dopita et al. 2013) which involve a self-consistent treatment of the transfer of ionizing radiation and of the ionization and thermal balance in each nebular zone. However, a full treatment of all the relevant physical processes involved is never met in practice and, moreover, the available observational constraints are usually not sufficient to fully break the degeneracy between different parameters. Therefore, on one hand different models (characterized by different chemical abundances for example) may be equally good in predicting the observed line ratios; on the other hand instead, the model that best reproduces the observed strong lines may be characterized by a different value of O/H with respect to the one derived using a T_e-based method. For example, the abundances inferred with a Bayesian approach by Tremonti et al. (2004) for a sample of galaxies from the SDSS with measured [O III]λ4363 are significantly larger than those derived with T_e-based methods for the same objects. In addition, these methods typically use libraries of synthetic stellar population models to generate the input ionizing spectra for stellar populations of particular metallicities, ages, and star formation histories; these models are plagued by large uncertainties associated with the effects of stellar rotation, stellar winds, and binarity (Blanc et al., 2015). Furthermore, photoionization models typically assume a single-valued function describing the N/O as a function of log(O/H) and do not take into account the fact that the relation might change systematically depending on the star formation, accretion, and gas ejection history of galaxies. These assumptions regarding the N/O ratio can have significant effects on diagnostics involving nitrogen lines (Yin et al., 2007; Pérez-Montero & Contini, 2009; Pérez-Montero, 2014; Belfiore et al., 2015). Finally, simplified assumptions regarding the ionization-bounded nature of the nebulae and its geometry can also influence the predicted line fluxes. It must be realized, therefore, that such methods can give reliable results only if the predicted model grids are based on assumptions that are sufficiently close to the studied objects in all its relevant aspects (Stasińska, 2002).

As a final consideration, it is always important to bear in mind that strong line methods can be safely used only when applied to the same category of objects that have been used for their calibration; as this prescription is often not easy to follow or sometimes neglected (e.g. by applying locally calibrated diagnostics to high redshift galaxies), one should at least be aware of the potential biases that may be introduced when dealing with these kind of measurements. Moreover, their intrinsic statistical nature may bring them to fail in determining the abundances of individual, peculiar objects.

Nitrogen abundance

Elements like oxygen, carbon and sulphur have a primary nucleosynthetic origin, i.e. their yield[6] is approximately independent from the amount of heavy elements already present in the galaxy. The nucleosynthetic origin on nitrogen, on the other hand, is more complex. It is predicted that in the low-metallicity regime most of the nitrogen has a primary origin and is generated in massive stars (Matteucci, 1986), even though the computation of the nitrogen stellar yields for massive stars is still afflicted from large uncertainties, especially at very low metallicity. At higher metallicity, nitrogen behave like a secondary nucleosynthetic product (i.e. the yield is proportional to the amount of heavy elements already present in the star), since its production becomes dependent on the previous amount of oxygen (and carbon) synthesized in stars via the CNO cycle. Moreover, since nitrogen is primarily produced by intermediate mass stars, it is released into the ISM on different time-scales than oxygen, which is produced by short-lived massive stars; therefore, studying the relative abundance of the two species can provide key and complementary information on gas flow and star formation history of a galaxy to what inferred from the study of the abundances of single species.

The analysis of the N/O ratio from large spectroscopic surveys like SDSS reveal a constant behavior of the N/O ratio ($\log(\mathrm{N/O}) \approx -1.5$) as a function of O/H at low metallicity, and a linear correlation at higher metallicities, a clear signature of the secondary production mechanism of nitrogen in this regime (Edmunds & Pagel, 1978; Vila Costas & Edmunds, 1993; Pérez-Montero & Contini, 2009; Andrews & Martini, 2013; Wu & Zhang, 2013; Vincenzo et al., 2016). The position on the N/O vs O/H diagram can be used to infer information about the star formation history of galaxies, by modeling the evolutionary tracks at fixed star formation efficiency (i.e. the star

---

[6] the stellar *yield* is the amount of mass of a given chemical element produced by a star of a certain mass and metallicity

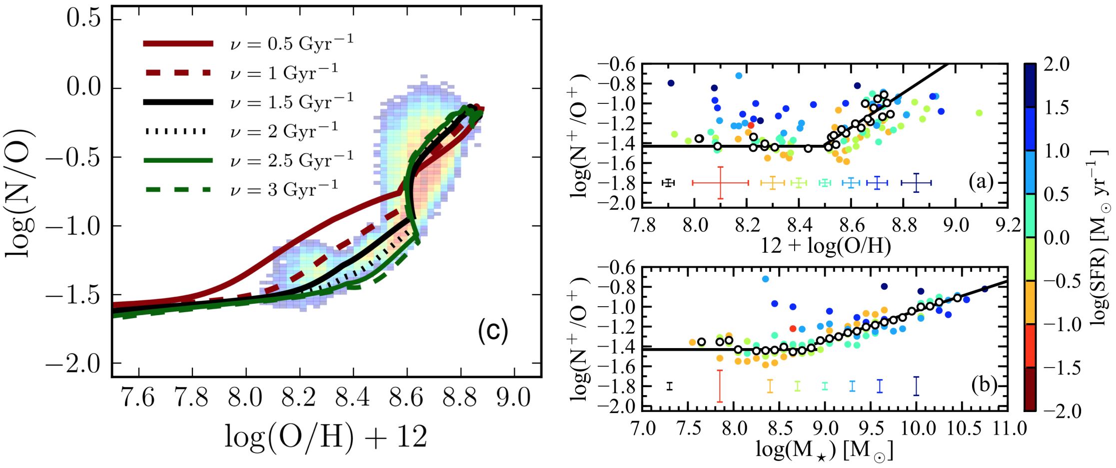

Figure 1.8: *Left Panel*: The N/O vs O/H distribution of local SDSS galaxies is shown enclosed by colored contours. The predictions from model tracks with different star formation efficiencies (ν) are sumperimposed. From Vincenzo et al. 2016. *Right Panel*: N^+/O^+ (which traces N/O) as a function of O/H (upper panel) and stellar mass $M_\star$ (lower panel), as derived from Te measurements on stacked spectra of SDSS galaxies by Andrews & Martini 2013. White points are stacks in bins of stellar mass, while colored points are stacks in bins of equal $M_\star$ for different values of SFR. The relation between N/O and $M_\star$ is tighter and show less secondary dependence on the SFR.

formation rate divided by the gas mass, SFE = SFR/M_g); high values of SFE mean that, at the moment of the beginning of the nitrogen secondary production, the oxygen abundance will be higher than for lower SFEs (Vincenzo et al. (2016), see left panel of Fig. 1.8). The relation between O/H and N/O is also sensitive to metal poor gas inflows: in the case of pristine gas inflow in fact, O/H would decrease but the N/O ratio remains unaffected (Köppen & Hensler, 2005; Belfiore et al., 2015).

To measure the N/O ratio in extragalactic sources, the N2O2 and the N2S2 line ratios are usually adopted. These diagnostics are based on assuming that N^+/O^+ traces N/O, which is physically motivated by the very similar ionization potentials of [N II] and [O II] (and [S II] as well). These diagnostics have been calibrated empirically and theoretically several times (e.g. Pérez-Montero & Contini 2009), and are also often used to infer the oxygen abundance only (i.e. as metallicity indicators, Kewley & Dopita 2002); however, despite being very insensitive to the ionization parameter, they are forced to assume a linear one-to-one relation between the oxygen and the nitrogen abundance, which can be cause of large systematics given the different chemical evolutionary path of the two elements.

Recently, it has been proposed that the relationship between N/O and stellar mass (N/O-$M_\star$) could be even tighter and “more fundamental” than the relation between N/O and O/H (Andrews & Martini 2013; Masters et al. 2016). This is expected, given that the N/O ratio is the result of the integrated processing of material from prior generations of intermediate and massive stars and, as stated before, is relatively independent of variations of gas-phase metallicity caused by inflows of pristine hydrogen gas or outflows of metals. The modest evolution of the N/O-$M_\star$ with redshift can also contribute to the observed offset in line ratios as seen in the BPT diagrams for high-z galaxies (see Sec. 1.1.3); at fixed stellar mass in fact, galaxies would have lower metallicities (given the evolution in the mass-metallicity relation, see next Section) but relatively similar N/O abundances: thus, they would result N/O-enhanced with respect to local galaxies at fixed O/H and [O III]λ5007/Hβ, determining an offset in the [N II]λ5007/Hα ratio (Masters et al., 2016).

1.3.2 Metallicity scaling-relations

As previously stated, gas-phase metallicity is a key quantity sensitive to the processes which regulate the baryon cycle in galaxies. Therefore, we expect that a certain number of *scaling relations* between metallicity and other galaxy properties will show up. Heavy elements are produced by massive stars and are dispersed into the ISM by processes like stellar winds or supernovae events; therefore, the metal content of the ISM is closely linked to the stellar mass of a galaxy. Moreover, since the metallicity of the gas is a relative measure to the hydrogen content, it should depends also on the available gas reservoir, which of course affects the rate at which stars are formed. Finally, how metals are spatially distributed across a galaxy can be used to strongly constrain the radial variation in gas accretion, star formation efficiency and importance of gas flows. In this Section we will introduce some of the most significant and studied scaling relations involving gas-phase metallicity, and discuss how their properties can be related to the physical processes driving the chemical evolution in the Universe.

Mass-metallicity relation

A first proof of the existence of a correlation between stellar mass and metallicity in galaxies (i.e. the mass-metallicity relation, MZR) came from Lequeux et al. (1979), who measured a correlation in a sample of irregular and blue compact galaxies. In the last fifteen years then, many other observational evidences have been reported in the literature. In particular, Tremonti et al. (2004) found a tight correlation (~ 0.1 dex scatter) between mass and O/H spanning over three orders of magnitude in stellar mass in a sample of ~ 50000 star forming galaxies from the SDSS; this relation was then assessed and extended to lower mass regimes (Lee et al., 2006). Observationally, it appears clear how more massive galaxies show to be more metal enriched (Fig 1.9, left panel); this may imply either that more massive galaxies represent more chemically evolved systems and/or that they are more capable to retain metals (thanks to their

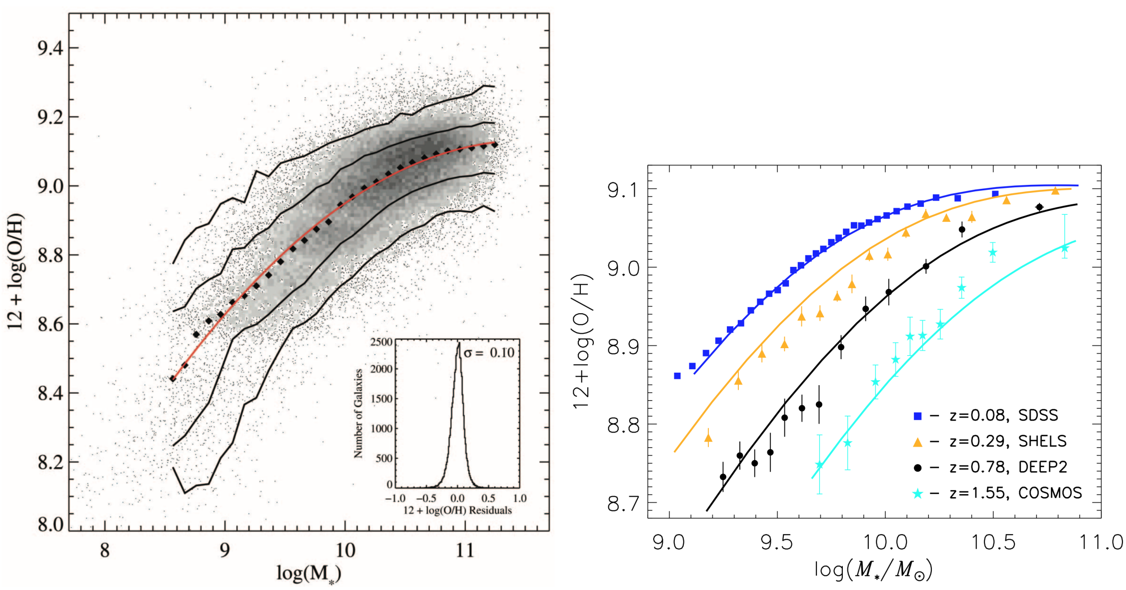

Figure 1.9: *Left Panel*: Mass-metallicity relation (MZR) derived from ~ 50000 SDSS star-forming galaxies. Black diamonds represent the median metallicity in 0.1 dex mass bins. Solid lines enclose the 68% and 95% of the distribution, while the red line is a polynomial fit to the median relation. From Tremonti et al. 2004. *Right Panel*: MZR at various redshifts (up to z~ 1.6), derived from different data samples, as shown in the legend. The MZR evolution is clear, with high-z galaxies, especially low-mass ones, characterized by lower metallicity values with respect to local galaxies, at fixed stellar mass. From Zahid et al. 2014a.

deeper gravitational potential) with respect to low mass systems, which can instead be strongly affected by gas outflows. The MZR in fact can be shaped on one hand by the increase in metallicity due to both star formation activity and metal-poor outflows and on the other hand by the decrease in metallicity given by enriched outflows and inflows of pristine gas which dilute its metal content. Assessing the origin and the intrinsic properties of the MZR (i.e. its slope, scatter, turnover mass, normalization) can thus give key insights to break the degeneracy on the relative contribution that different physical processes play in driving the chemical evolution of galaxies.

The MZR has been observed to hold also at redshifts out to 3 and beyond, despite showing clear signs of evolution (Erb, 2006; Maiolino et al., 2008; Mannucci et al., 2009; Zahid et al., 2011; Yabe et al., 2015; Zahid et al., 2014b). In fact, galaxies at high-z are observed to be less metallic than in the local Universe for a given stellar mass, and this effect appear much more evident for lower mass galaxies (Fig 1.9, right panel). The observed evolution in the main MZR parameters can be explained in terms of the change in the gas content of galaxies at different epochs (Zahid et al., 2014a), thus unveiling the role played by inflows and outflows in its regulation at different times and for different mass regimes. The fact that, at a given epoch, more massive galaxies tend to be closer to their local counterparts in terms of their position on the MZR may be indicative of a *downsizing* scenario of chemical evolution.

Fundamental metallicity relation

The scatter in the MZR has been observed to correlate with different galaxy properties. Ellison et al. (2008) first showed an anti-correlation between metallicity and specific star formation rate for galaxies at a fixed stellar mass. Mannucci et al. (2010) clearly observed a secondary dependence of the MZR on the SFR in a large sample of SDSS galaxies, with low star forming galaxies showing higher metallicities at fixed stellar mass, and first proposed the existence of a tight (i.e. ~ 0.05 dex dispersion) surface in 3D space defined by mass, metallicity and SFR (i.e. the Fundamental Metallicity Relation, FMR) where galaxies lie and *surf* across the epochs driven by the effect of inflows and outflows that regulates their gas content and thus their current level of star formation activity (Fig. 1.10). In this framework, therefore, the MZR arises from a projection of the FMR on the $M_\star$-log(O/H) plane, and the observed cosmic evolution of the MZR follows from sampling different regions of the FMR due to the increase in the average SFR density with redshift. Mannucci et al. (2010) also introduced a 2D-projection of the FMR that minimises the scatter of the relation between O/H and a new variable defined as a linear combination of stellar mass and SFR:

$$\mu_\alpha = log(M_\star) - \alpha log(SFR) \; ; \tag{1.10}$$

they found the value of minimum scatter for α to be equal to 0.32, although this can be subject to variations according for example to the different calibrations used for metallicity determination (e.g. Andrews & Martini 2013, also see the new relations presented in Sec. 3.7) .

The small amount of scatter around the FMR supports the scenario in which the chemical enrichment is regulated by smooth, secular evolutionary processes which set an equilibrium between the involved physical quantities. Indeed, the existence of the FMR can be explained assuming that star-forming galaxies do most of their growing in a quiescent mode where the global SFR, Z, and gas fraction constantly adjust on a relatively short timescale to reflect the influence of inflows. The advent of external gas does not change $M_\star$, but it decreases the mean metallicity of the star-forming gas while simultaneously triggering new star formation episodes. As time goes on, star formation consumes gas and increases its metallicity, until new metal-poor gas arrives and the cycle starts over. If a sample of galaxies with similar stellar masses are observed at different phases of this cycle, triggered by a gas accretion event, they will show a dispersion in metallicity which anti correlates with the instantaneous SFR: this is, indeed, the observational signature of the FMR. The existence of the FMR has been thoroughly tested so far by many studies, with different observational approaches (Andrews & Martini, 2013) and within different frameworks (Salim et al., 2014), despite

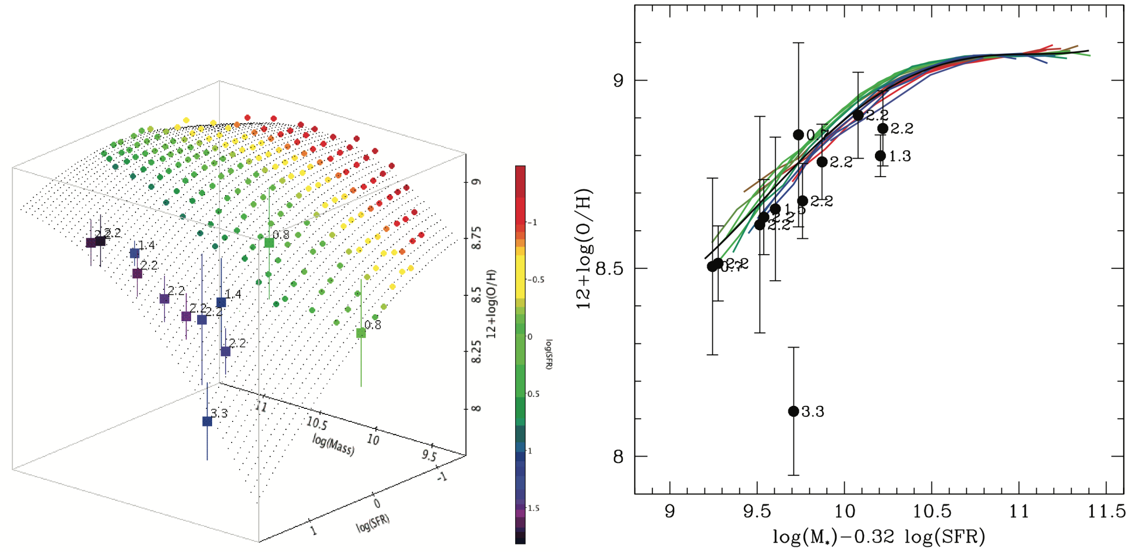

Figure 1.10: *Left Panel*: The 3D space defined by stellar mass, star formation rate and metallicity. Circles without error bars are the median values of metallicity of local SDSS galaxies in bin of $M_\star$ and SFR, colour-coded according to their SFR. These galaxies define a tight surface in the 3D space, the FMR, with dispersion of single galaxies of ~ 0.05 dex. The black dots show a second-order fit to these SDSS data, extrapolated towards higher SFR. Square dots with error bars are the median values of some high-redshift galaxies. *Right Panel*: Metallicity as a function of μ0.32, the 2D projection which minimizes the residual scatter around the FMR. Local SDSS galaxies are color-coded with SFR as in the *left* panel. The black line shows the polynomial best fit. Black dots are high-redshift galaxies, labelled with redshifts. These galaxies appear to follow the same relation defined in the local Universe, with the exception of those at z~ 3.3. From Mannucci et al. 2010.

it seem to disappear on local scales, as seen by recent studies based on integral field spectroscopy (Sánchez et al. 2013; Barrera-Ballesteros et al. 2016). However, an $M_\star$-SFR-metallicity relation can be predicted and nicely reproduced by different theoretical frameworks and models, both based on equilibrium (Davé et al., 2011b; Lilly et al., 2013) and non-equilibrium (Dayal et al., 2013; Hunt et al., 2016) treatments, as well as zoom-in cosmological simulations (De Rossi et al., 2015). In Lilly et al. (2013), for example, the assumption that the galaxy's gas reservoir does not grow is relaxed, allowing the gas fraction to fluctuate; this naturally give rise to the observed correlation between $M_\star$, SFR and log(O/H). If the star formation timescale is long enough in fact, the ISM does not recover quickly form perturbations and can be out of equilibrium for some time: in this case, a high sSFR is associated with low metallicity, as observed. With a slightly different and purely analytical approach, Dayal et al. (2013) presented a model, that can be fit on the observed FMR, in which the evolution of the stellar, gas, and metal reservoirs depends only on the unknown gas accretion and outflow rates. They assume that outflow and infall rates depend only on stellar mass, that the metal yield is constant, and that inflows are pristine, with no assumptions on gas processing or enrichment equilibrium.

Interestingly, both models predicts no cosmic evolution of the FMR, as initially suggested by Mannucci et al. (2010) up to z~ 3; observational evidences in favor of the redshift invariance of the FMR are, however, still tentative and its possible cosmic evolution is subject of hot debate (Troncoso et al., 2014; Cullen et al., 2014; Sanders et al., 2015a; Wuyts et al., 2016).

As previously stated, both SFR and metallicity are dependent on the gas content of galaxies; thus, the anti-correlation between metallicity and SFR is likely the result of variations in the gas content. It is no surprising then, that clues for an even more fundamental relation between stellar mass, metallicity and gas content (both atomic and molecular) have been found (Bothwell et al. 2013, 2016). However, the intrinsic challenges in the observations of atomic and molecular gas at high redshifts prevented so far to test this scenario outside the local Universe.

Metallicity gradients

In addition to the total metal content of galaxies, the spatial distribution of heavy elements within galaxies further constrains their baryonic and chemical assembly history, in particular the effects of gas flows and dynamical evolution: seeking how metallicity gradients evolve with time is thus another important piece to solve the puzzle of galaxy evolution.

In the local Universe, abundance measurements of individual HII regions generally find that galaxies are characterized by negative gradients, with their inner regions more enriched than the outer disk regions (e.g Zaritsky et al., 1994; van Zee et al., 1998; Sánchez et al., 2014). This is generally interpreted as indicative of the so-called *inside-out* scenario of galaxy formation, in which compact cores are formed at high redshift through highly dissipative processes, with a disk that grows later around them. Recent theoretical frameworks differently predict how it could occur in terms of radial variation of star forming efficiency, gas fraction and local enrichment equilibrium regulated by inflows and outflows, whose relative contribution may remain degenerate (Fu et al. 2013; Carton et al. 2015; Ho et al. 2015). Gradients have been found to typically flatten at large radii (Bresolin et al., 2009; Yoachim et al., 2010; Rosales-Ortega et al., 2011; Marino et al., 2012; Bresolin et al., 2012), possibly due to secular dynamical evolution or recycling of metal-enriched gas which was previously ejected in outflows (the so-called "galactic fountain" effect, Werk et al. 2011). Mergers have been found to exhibit flat gradients, likely due to interaction-induced inflow of metal-poor gas in the center and metal mixing (Rupke et al., 2010a; Kewley et al., 2010). Studies from integral field spectroscopy highlighted that disk galaxies in the local Universe seem to present a common or characteristic scale-normalized gradient in the oxygen abundance up to ~ 2 disk effective radii, while flattening at larger distances and with no clear dependence on other galaxy properties, suggesting a common chemical evolutionary path (Sánchez et al., 2014).

On the other side, the status at higher redshifts is far from being clear, despite the growing number of observational efforts during the last years, that nevertheless produced a variety of different results and, hence, different predictions about the evolution of metallicity gradients. Studies conducted on data reaching ≤ 1 kpc resolution with adaptive optics (and down to ~ 100 pc in the case of lensed galaxies) have reported a few example of negative gradients with steeper slopes than local descendants, suggesting that, for a given population of galaxies at least, gradients flatten as they grow with time (Jones et al., 2010b, 2013; Swinbank et al., 2012), as predicted by the standard inside-out growth picture. However, larger surveys with seeing-limited resolution of ~ 5 kpc have reported mostly flat gradients (e.g. KMOS^{3D}, Wuyts et al. 2016), as well as a significant fraction of positive slopes (Cresci et al., 2010; Queyrel et al., 2012; Troncoso et al., 2014). The latter have been interpreted as evidence for cold flows of pristine gas which dilute the metal content in the central regions of these galaxies, but these results are in contrast with some of the high-resolution measurements. The discrepancy in the observed metallicity gradients at high redshift must be addressed in order to reliably understand the role of gas flows and metal transport and mixing in galaxy evolution. High spatial resolution is clearly an advantage: Yuan et al. (2013) demonstrate how degraded resolution can dramatically bias gradient measurements. At high redshift and for low mass galaxies in particular, sub-kpc resolution would be desirable to properly sample the metallicity distribution within the effective radius. Adaptive optics and gravitational lensing provide a great aid in overcoming the limitations in spatial resolution achievable with current instrumentation (Jones et al., 2013; Leethochawalit et al., 2016), and great effort can come as well from space based campaigns with HST (Jones et al., 2015b; Wang et al., 2017). However, the number of sub-kpc reliably measured metallicity gradients in the high redshift Universe is still limited and, moreover, even when accounting for beam smearing effects due to poor resolution in seeing-limited studies, the recovered number of intrinsically steep gradients remain scarce.

From a theoretical point of view, the cosmic evolution of abundance gradients can be predicted from classical analytical models of the chemical evolution of the Milky Way disk (Chiappini et al., 2001; Mollá & Díaz, 2005), or from cosmological hydrodynamical simulations (Rahimi et al., 2011; Pilkington et al., 2012; Gibson et al., 2013a,b). Pilkington et al. (2012) find little agreement in an extensive comparison of different simulations and chemical evolution models, which they associate to the varying treatment of star formation and feedback in the simulations. The impact of the assumed feedback scenario is examined, for example, by Gibson et al. (2013a). In this study, "normal" feedback (involving $10-40\%$ of energy from supernovae to heat the surrounding ISM) predicts steep gradients of -0.3 dex/kpc at z$\sim$ 2, which then flatten over time, while "enhanced" feedback (including radiation pressure from massive stars) can better redistribute metal-enriched gas over large spatial scales and produces relatively flat gradients at all times. These studies highlight how robust measurements of abundance gradients at high redshift can help to discriminate among different scenarios of mass assembly and chemical enrichment during galaxy formation and evolution. In Chapter 4 and Chapter 5 we address this topic by presenting new observations of spatially resolved chemical abundances in high-redshift galaxies.

1.4 Thesis aims and structure

Within the context outlined so far, it appears clear that the role played by gas-phase metallicity represents one of the key elements to consider for those willing to get a comprehensive understanding of the mechanisms driving galaxy evolution. The work presented in this thesis aims at addressing a few aspects related to chemical abundances in local and high-redshift galaxies, by means of different observational techniques, which are briefly described in Chapter 2.

In Chapter 3, we focus on how gas-phase metallicity is measured from galaxy spectra. To address the long-standing issue related to the systematic uncertainty on the absolute abundance scale, we here propose a novel method to obtain a robust and self-consistent calibration of the most common metallicity diagnostics based on strong-line ratios. Te-based metallicity measurements are obtained by stacking the spectra of star-forming galaxies from the SDSS according to their observed line ratios. The goal of the study is to obtain a new set of calibrations uniformly anchored to the T_e abundance scale over the entire range of metallicities spanned by local galaxies. The new set can then be used in a variety of different cases, starting from defining a new MZR and FMR in the local Universe, while moving to high-redshift studies as pursued in later chapters. Chapter 4 and Chapter 5, in fact, are dedicated to the investigation of the chemical properties in different samples of high-redshift (i.e. 1<z<2.5) galaxies.

Chapter 4 is based upon the observations recently conducted in the framework of the ESO Large Programme KLEVER. Combining integral field spectroscopy in the near-infrared from KMOS with the increased sensitivity and resolution provided by gravitational lensing, we are able to investigate in detail the physical properties of the ionized gas in our sample, taking also advantage from the broad wavelength coverage given by the multi-band approach of the program, which allows to cover the entire set of rest-frame optical emission lines. Spatially resolved metallicity maps are derived to shed light on the cosmic evolution of abundance gradients and on the role that star formation and gas flows plays in shaping the distribution of metals at different spatial scales.

Spatial resolution is of course key for every study aimed at obtaining accurate determination of physical properties in high-redshift sources. However, seeing limited observations are often not enough to properly infer the intrinsic morphology, kinematics and metallicity distribution on few-kpc scales: in this regard, a strong aid comes from adaptive optics techniques. In Chapter5, we present the very first observations obtained from the near-infrared spectrograph LUCI assisted by ARGOS, the new ground-layer adaptive optics facility for the LBT. Strongly-lensed galaxies at z $\sim$ 2 with arc-like shapes are observed with narrow slits to infer kinematics and abundances from detected emission lines.

Finally, the conclusions arising from this work, as well as some prospects of future research, are presented in Chapter6.

The third Chapter of this dissertation is a published work which have been accepted after a standard scientific peer review process. Chapters4 and 5 represent the current versions of forthcoming papers that are about to be submitted shortly at the time of writing. Therefore, each chapter is self-consistent and can be read individually. Those reading this dissertation in its entirety are free to skip the introductory section of each subsequent chapter, as these sections may be redundant.

2 Instrumentation and Data

The work presented in this dissertation is mostly based on spectroscopic data coming from a variety of different facilities and instrumentation, from single-fiber imaging and spectroscopic surveys like the SDSS to new generation multi-object and integral field spectrographs mounted on large ground-based telescopes like KMOS on the VLT and LUCI/ARGOS on the LBT. Therefore, in the following sections, we give a brief overview on the instrumentation which provided the data analyzed in the subsequent chapters.

2.1 The Sloan Digital Sky Survey

The Sloan Digital Sky Survey (SDSS, York et al. (2000)) represents one of the most ambitious, influential and successful surveys in the history of astronomy. Over more than fifteen years of operations, it obtained images and spectra covering more than 35% of the sky, revolutionizing our understanding of the Universe by addressing a variety of different scientific fields, from the study of peculiar stellar objects to the star formation history of galaxies and their large scale cosmological distribution (Fig. 2.1). The reduced and calibrated data is publicly released in a series of annual data releases and made accessible through efficient databases, with both spectra and images that can be downloaded by means of a very simple and user-friendly interface[1].

The SDSS uses a dedicated 2.5-m f/5 modified Ritchey-Chrétien altitude-azimuth telescope located at Apache Point Observatory, in south east New Mexico. The 120-megapixel camera imaged 1.5 square degrees of sky at a time, about eight times the area of the full moon. A pair of spectrographs fed by optical fibers can obtain spectra of more than 600 galaxies and quasars in a single observation. For imaging, the SDSS telescope used the drift scanning technique, which tracks the telescope along a great circle on the sky and continuously records small strips of the sky. The telescope's

---

[1] accessible from the sdss website, `http://www.sdss.org/`

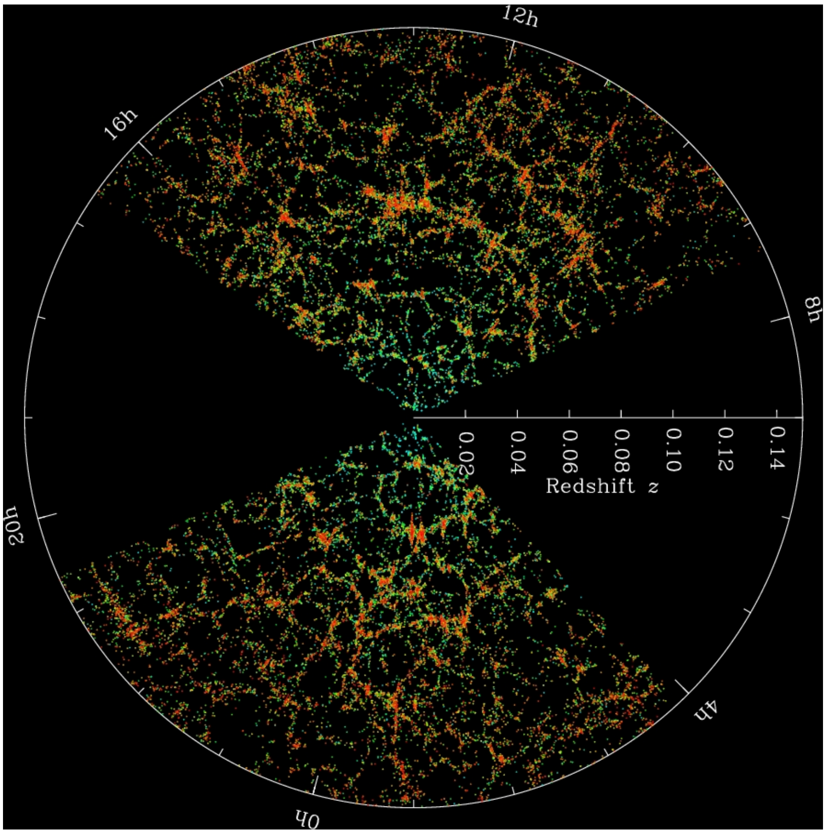

Figure 2.1: Slices through the SDSS 3-dimensional map of the distribution of galaxies. Earth is at the center, and each point represents a galaxy. Galaxies are colored according to the ages of their stars, with the redder showing galaxies that are made of older stars. The outer circle is at a distance of two billion light years. The region between the wedges was not mapped by the SDSS because dust in our own Galaxy obscures the view of the distant universe in these directions. Both slices contain all galaxies within -1.25 and 1.25 degrees declination. Image courtesy of M. Blanton and the Sloan Digital Sky Survey.

imaging camera is made up of thirty CCD chips each with a resolution of 2048x2048 pixels. The chips are arranged in five rows of six chips. Each row has a different optical filter with average wavelengths of 355.1, 468.6, 616.5, 748.1 and 893.1 nm, with 95% completeness in typical seeing to magnitudes of 22.0, 22.2, 22.2, 21.3, and 20.5, for u, g, r, i, z, respectively. The filters are placed on the camera in the order r,i,u,z,g and the camera is cooled to 190 K by liquid nitrogen to reduce the noise contribution. The spectrograph operates by feeding an individual optical fibre of 3" diameter for each target through a hole drilled in an aluminum plate. Each hole is positioned specifically for a selected target, so every field in which spectra are to be acquired requires a unique plate. The simultaneous use of two double spectrographs allowed to reach the desired spectral coverage of 3900-9100 Å, while maintaining approximately a resolving power of R=2000. The original spectrograph was capable of recording 640 spectra simultaneously, while the updated spectrograph can record 1000 spectra at once. In spectroscopic mode, the telescope tracks the sky in the standard way, keeping the objects focused on their corresponding fibre tips.

In its first five years of operations, the SDSS carried out deep, optical multi-band imaging (based on a photometric system of five filters, namely u,g,r,i and z) over 8000 square degrees and measured spectra of more than 700,000 celestial objects. With an ever-growing collaboration, SDSS-II (2005-2008) completed the original survey goals, providing 230 million celestial objects detected in 8,400 square degrees of imaging and spectra of 930,000 galaxies, 120,000 quasars, and 225,000 stars.

SDSS-II carried out two additional surveys: the Sloan Supernova Survey, which discovered and monitored hundreds of supernovae to measure the expansion history of the universe, and the Sloan Extension for Galactic Understanding and Exploration (SEGUE), which extended SDSS imaging towards the plane of the Galaxy and mapped the motions and composition of more than a quarter million Milky Way stars. On the final public data release from SDSS-II, the Data Release 7 (DR7, Abazajian et al. 2009), is based the work presented in Chapter 3.

The SDSS project continued with the Third Sloan Digital Sky Survey (SDSS-III), a program of new surveys using the SDSS facilities. SDSS-III operated from 2008 to 2014 and undertook a major upgrade of the SDSS spectrographs and added two powerful new instruments to execute an set of four surveys, mapping the clustering of galaxies and intergalactic gas in the distant universe (BOSS), the dynamics and chemical evolution of the Milky Way (SEGUE-2 and APOGEE), and the population of extra-solar giant planets (MARVELS).

The latest generation of the SDSS (SDSS-IV, 2014-2020) is extending precision cosmological measurements to a critical early phase of cosmic history (eBOSS), expanding its revolutionary infrared spectroscopic survey of the Galaxy in the northern and southern hemispheres (APOGEE-2), and for the first time using the Sloan spectrographs to make spatially resolved maps of individual galaxies (MaNGA). In particular, MANGA (Mapping Nearby Galaxies at Apache Point Observatory, Bundy et al. 2015) makes use of 17 simultaneous integral field units (IFUs), each composed of tightly-packed arrays of optical fibers, to overcome the classical drawback of single-fiber surveys which gather light only from the central region of galaxies, introducing considerable aperture effects that must be always taken into account. Large IFU-based spectroscopic surveys represents the natural evolution of the original SDSS "concept" and, in this respect, MANGA is currently providing the most deep and statistically representative view of the spatially resolved properties of galaxies in the local Universe.

2.2 KMOS on the VLT

The K-band Multi Object Spectrograph (KMOS) is a second-generation instrument installed at the Naysmith focus of the 8.2-m Unit Telescope 1 (UT1) of the Very Large Telescope (VLT, Cerro Paranal, Chile), designed to observe at the near-infrared wavelengths between 0.8 - 2.5 μm. The instrument can operate in five different spectral bands, namely IZ, YJ, H, K and H+K, with spectral resolving power around 3400, 3600, 4000, 4200 and 2000 respectively. The key feature of KMOS is its high multiplexing capability to perform Integral Field Spectroscopy (IFS) in the near-infrared bands for 24 targets simultaneously.

The instrument design employs 24 configurable arms that position pickoff mirrors at user-specified locations in the Nasmyth focal plane. The sub-fields thus selected are then fed to 24 image slicer integral-field units that partition each sub-field into 14 identical slices, with 14 spatial pixels along each slice. Light from the IFUs is then dispersed by three cryogenic grating spectrometers which generate 14x14 spectra with ~ 1000 Nyquist-sampled spectral resolution elements for each of the 24 independent sub-fields.

The patrol field of the pickoffs is 7.2 arcmin in diameter, while each individual IFU has a square field of view of 2.8 x 2.8 arcsec, with a sampling of 0.2 arcsec per pixel. KMOS is designed so that 8 IFU arms are fed into a single spectrograph and have their light dispersed onto a single detector. Thus, in total there are 3 spectrographs and 3 detectors. Each section is thus identical with all the others, modulo optical alignment and manufacturing tolerances.

The use of focal-plane pick-off arms allows considerable flexibility in selecting targets and in particular the important capacity to deal with strongly clustered or close-paired sources. In addition to observing multiple individual sources, KMOS has the capability for integral field mapping of contiguous areas in an 8-point or 16-point dither pattern.

2.2.1 From raw data to 3D datacubes

The data from each KMOS IFU are recorded by three 2k x 2k HAWAII 2RG detectors, with 8 IFUs assigned to each detector. Each of the IFUs operates on the bases of the “image slicer” technique: the field of each IFU is sliced into 14 slitlets which are rearranged along a pseudo-longslit and then dispersed. The raw data for each IFU therefore consists of 14 sets of standard 2-dimensional slit spectra, which is arranged next to each other on the detector, separated by a few blank pixels. The same pattern is repeated 8 times for each of the 3 detectors. Figure 2.2 shows an example of how KMOS raw data appears.

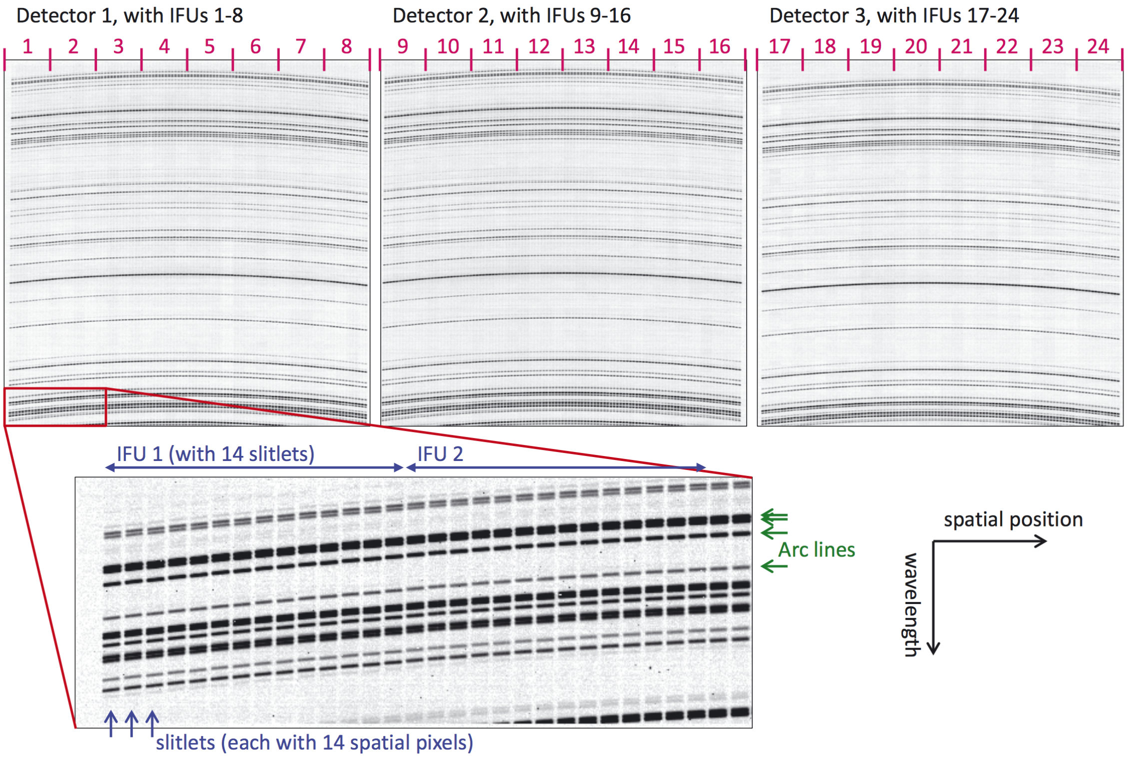

Figure 2.2: Images of H-band arc lines illustrating how the data are arranged on the three detectors. The dispersion axis is vertical, with longer wavelengths at the top and shorter wavelengths at the bottom. The horizontal axis denotes spatial position. The curved black lines across each detector are the arc lines. Closer inspection shows that these are split into slitlets of 14 pixels, with 14 slitlets making up each IFU, and 8 IFUs across each detector. From Davies et al. 2013.

In KMOS, reconstruction of a 3D datacube from raw 2D data is performed within a single procedure. Being able to conceptualise it requires that the calibrations are viewed in a particular way: in the “detector space” there can be no concept of a wavelength or spatial axis. These concepts apply only to processed data, while the detector is nothing more than the medium on which raw data values are recorded. Traditionally, calibrations are considered to be the mathematical functions which allow one to correct the curvature in the recorded data; instead, they should be considered as look-up tables allowing to assign each measured value on the detector to a spatial/spectral location in the reconstructed cube. The recorded data on the detector can then be considered as a set of values at irregularly spaced sampling positions in the final cube. The aim is thus to reduce the raw data and the calibrations to a list of sample values with their associated locations in the cube, which can then be interpolated to generate the final science product. There are different schemes available for interpolating points in 3-D space, since no single one is optimal for every situation and each has its advantages and disadvantages. It is important to realize that all the methods are weighted averages of neighboring points, and so are limited in their performance by the sampling of the data.

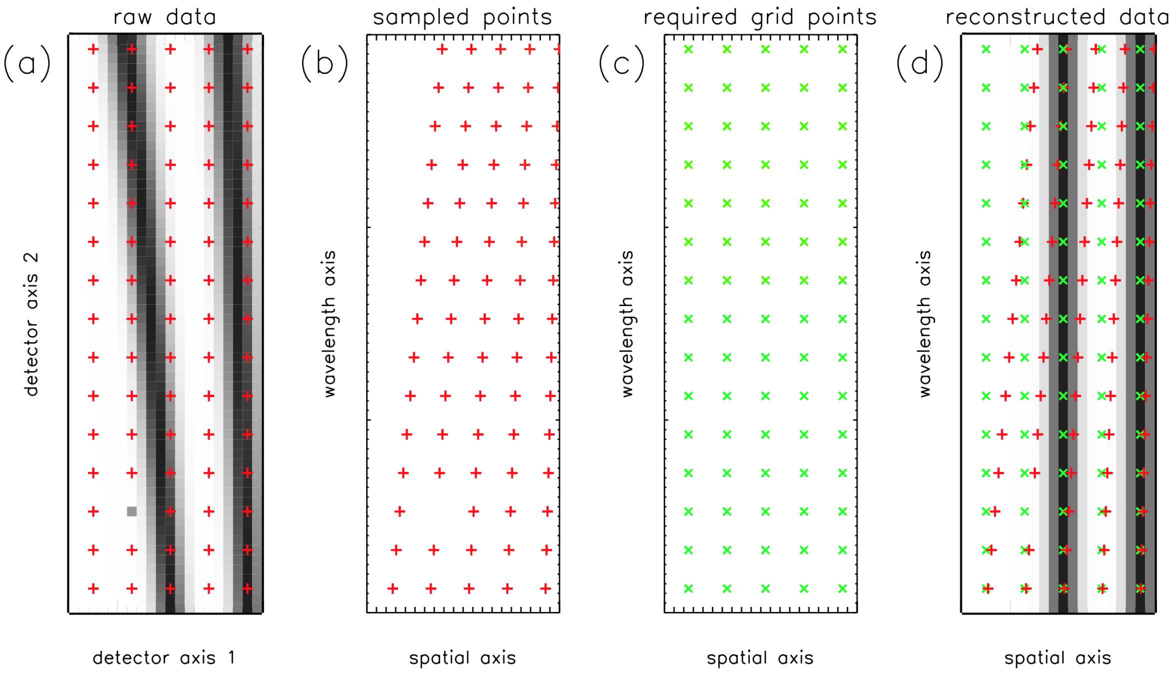

Figure 2.3: Interpolation scheme illustrated in 2-dimensions. a) Observed data are sampled regularly in the reference frame of the detector (red points). b) This sampling is irregular in the reference frame of the reconstructed cube. The calibration look-up tables directly provide the mapping from a) to b). c) One can freely specify the required gridding (i.e. spatial/spectral pixel scale) for the reconstructed data (green points). d) Each required grid point (green) is interpolated from sampled points (red) which lie in its local neighbourhood. Different algorithms can be used for the interpolation. From Davies et al. 2013.

This approach brings several advantages, including the freedom to choose any arbitrary spectral and spatial sampling of the reconstructed cube and the possibility to account and correct for spatial and spectral flexures (mainly introduced by the instrument rotation) directly within the process by appropriately modifying the look-up tables before reconstructing the data. Figure 2.3 provides a simple illustration of the concept behind the 3D datacube reconstruction in KMOS. The entire procedure is described in more detail in Davies et al. (2013), as well as in the KMOS pipeline manual[2].

2.3 LUCI and ARGOS on the LBT

With its single alt-azimuth mount supporting two 8.4 m diameter primary mirrors, the Large Binocular Telescope (LBT), situated on Mount Graham, Arizona (USA), is the largest ground-based telescope for optical/infrared observations. The telescope is equipped with two Adaptive Secondary Mirrors (ASM, one for each side), which are deformed at kHz frequencies by 672 voice coil actuators; this provide the possibility

---

[2] available for download at `https://www.eso.org/sci/facilities/paranal/instruments/kmos/doc.html`

to exploit adaptive optics correction at any focal station, decreasing at the same time the required number of optics to place before the different instruments. Both LBT "eyes" host instruments at the prime focus (the two wide-field cameras LBC), at the direct Gregorian focus under the primary mirrors (the two imager and spectrographs in the visible MODS) and at bent Gregorian focus (the couple of near infrared imager and spectrographs LUCI and the high-resolution echelle spectrograph PEPSI), which is accessible via a flat tertiary mirror and where the instrumentation can benefit from the adaptive optics correction provided by the ASM. The intrinsic binocular nature allows LBT to be used also as a Fizeau-interferometric facility (with the near-infrared coronograph LBTI used in nulling interferometry and the near-infrared interferometer LINC-NIRVANA), with a potential equivalent 22.8 m baseline.

In the following, we briefly give an overview on the instrument LUCI and on the new adaptive-optics system ARGOS, whose combined efforts provided the data analyzed and presented in Chapter 6.

2.3.1 The near-infrared imager and multi-object spectrograph LUCI

LUCI is a spectrograph and imager for the LBT, operating in the near-infrared wavelength range from 0.85 μm to 2.5 μm. A pair of nearly identical instruments (i.e. LUCI 1 and LUCI 2) are available at the telescope and mounted on the bent Gregorian foci of the SX and DX mirror respectively. The instrument provides different observing modes, from imaging to long-slit and multi-object spectroscopy (MOS), over a 4x4 arcmin field of view (FOV), at different resolutions and spatial/spectral configurations according to the choice of the grating and the camera. In particular, the instrument is provided with a set of broad (J, H, K, H + K) and narrow filters (e.g. Brγ, FeII 1.64 μm, H_2 2.12 μm) and offer three resolution configurations with pixel scales of 0.25" (N1.8 camera), 0.12" (N3.75 camera) for seeing limited, and 0.015" (N30 camera) for diffraction limited operations. Depending on the grating (and the camera), the spectral resolution may vary from ~ 2000 to ~ 40000. The MOS mode can also benefit from the large multiplexing capabilities of the instrument, allowing to allocate up to 20 slits, or even more, in one single pointing. The main observing modes for LUCI are summarized in Table 2.1.

Both LUCIs can now benefit from the correction provided by the Adaptive Optics (AO) system of the telescope. The First Light AO (FLAO, Esposito et al. 2010) system uses the visible light from an astronomical object close to the LUCI science target to measure the wavefront distortions introduced by the atmosphere, thanks to

	Camera		
	N1.8	N3.75	N30
Imaging			
Scale (arcsec/pixel)	0.25	0.12	0.015
FOV (arcmin)	4 x 4	4 x 4	0.5 x 0.5
Spectroscopy			
Scale (arcsec/pixel)	0.25	0.12	0.015
Resolution (2 pixels)	1900÷8500	3800÷17000	10000÷40000
Modes	LSS & MOS	LSS & MOS	LSS

Table 2.1: LUCI imaging and spectroscopic observing modes. LSS stands for Long-Slit Spectroscopy and MOS for Multi-Object Spectroscopy.

a Pyramid wavefront sensor. The system achieved a maximum Strehl Ratio[3] of 80% in H band (1.6μm) observing a bright (R=6.5) star with a infrared test camera during its commissioning (Esposito et al., 2011). When operating in *diffraction limited* mode, the use of the dedicated N30 camera reduce the LUCI's FOV to 30 x 30 arcsec, with a sampling of 0.015"/pxl.

As any AO system, FLAO needs to find a bright star close to the science target to perform the wavefront sensing. The limiting magnitude on this guide star (GS) and its availability within the observed FOV set the main limitations on the performance of an AO system: in fact, looking for a fainter GS increases the noise contribution to the wavefront measurement, whereas searching for natural guide stars (NGS) at larger distances from the science target may introduce strong angular anisoplanatism effects. Requiring a bright and reasonably close NGS strongly reduce the sky coverage available to conduct astronomical observations. A possible solution to overcome this problem is to artificially generate a bright GS close to the science object: this can be achieved by projecting a laser beam into the atmosphere. These Laser Guide Stars (LGS) are of two types, Sodium and Rayleigh LGS, whose generations is based on different physical processes. Sodium LGS exploit the absorption and subsequent re-emission of laser light tuned at 589.6 nm from Sodium atoms in the Earth's mesosphere to generate artificial sources at an altitude of ~ 100 km. Rayleigh LSG instead, are based on the elastic scattering provided by atmospheric particles that diffuse photons from a pulsed laser beam; the beam is usually focused at 10 ÷ 20 km altitude in the atmosphere, where the particle density is still sufficiently high. Both types of LGS have their own advantages and disadvantages, the choice on which to prefer usually depending on each specific AO application. The ground layer adaptive optics facility for LUCI, ARGOS, is indeed

---

[3] defined as the ratio of the observed peak intensity generated by a point-like object on the image plane compared to the theoretical maximum peak intensity of an imaging system working at the diffraction limit.

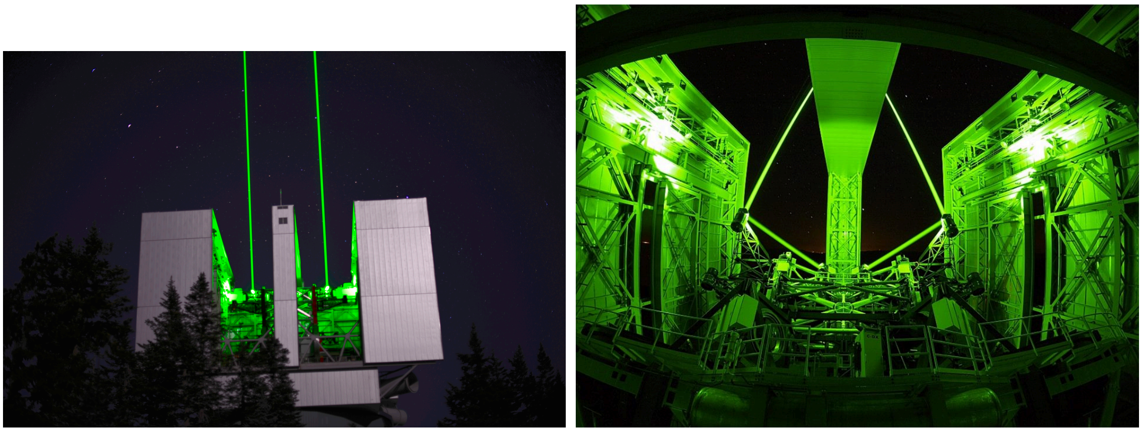

Figure 2.4: *Left Panel*: The green lasers of ARGOS in operation at LBT. *Right Panel*: Inside view of the LBT dome. The laser system generates the two beams, then a launch beam expander and 2 large fold flat mirrors situated above the adaptive secondary mirrors direct them on sky, focusing at 12km.

based on the latter approach.

2.3.2 The ARGOS system on the LBT

ARGOS (Advanced Rayleigh Guided Ground Layer Adaptive Optics System) is the laser-guide star ground layer adaptive optics (GLAO) system for LUCI 1 and LUCI 2 on the LBT (Fig. 2.4). It is aimed at improving the resolution and sensitivity for both imaging and multi-object spectroscopy over the entire field of view of the instrument, ensuring at the same time an almost full sky coverage. The primary goal of ARGOS is to provide a gain of a factor 2-3 in Full Width Half Maximum (FWHM) from the J to the K band over the full $4'$ x $4'$ LUCI's field of view. This could, in principle, lead to a corresponding decrease of the observing time by a factor 4-9 to reach a given signal-to-noise in background limited regime, and to a better coupling efficiency of the PSF into the slits. Moreover, the "seeing enhancement" provided by ARGOS could transforms good nights into excellent seeing conditions, with demanding observing programmes that could therefore be carried out most of the nights.

Many scientific cases could largely benefit from the unique combination of LUCI's high multiplexing, wide FOV and AO correction provided by ARGOS. In particular, multi-object spectroscopy would benefit enormously from such a capability, especially for extragalactic studies. Studying the morphologies, kinematics, star formation rates, and metallicities of high redshift galaxies provide crucial insights into galaxy formation and evolution, but require deep, spatially resolved spectroscopy of faint sources with sizes of 0.1-1". On 8-10 m class telescopes, seeing limited conditions do not provide the necessary spatial resolution, while at the diffraction limit signal-to-noise is a major constraint due to the faint surface brightness of the spatially extended regions. For a comprehensive review of the scientific applications of ground layer (and others) adaptive optics techniques, see Davies & Kasper (2012). In the following, we briefly describe the concept behind ground-layer AO, and give an overview of the ARGOS system.

Ground Layer Adaptive Optics

In GLAO systems only the atmospheric turbulence close to the ground is corrected, combining the wavefronts from several, well separated, reference sources placed at the edge of the FOV, whose light rays passes through the same low layer of turbulence regardless of their angular offset from the field center. In principle, to fully compensate for the atmospheric turbulence in 3 dimensions, it should be necessary to introduce many deformable mirrors (DM) in the optical path (which is at the base of the so called multi-conjugate adaptive optics systems, MCAO). However, GLAO systems are characterized by the presence of only one DM, which is typically conjugated to an altitude of several hundreds meters above the ground, where most of the turbulence lays. In this way the lower layers, where light patterns of the different GS overlap, are enhanced while the higher layers, where the light patterns are uncorrelated, contribute with a residual error to the GLAO correction. This can provide enhanced resolution over a wide field even though not allowing to reach the diffraction limit of the telescope. A simple scheme illustrating the principle of a GLAO system is shown in Fig. 2.5.

System Overview

ARGOS performs ground-layer adaptive optics by means of multi-laser guide stars. More in detail, the system consists of six Rayleigh lasers (generating three laser guide stars for each LBT eye) and one wavefront sensor unit per primary mirror; each unit is equipped with three *Shack-Hartmann* WFS, which are imaged on one detector. The 532 nm laser beams are expanded, first by the laser system and then by the launch optics, and launched on-axis above the secondary mirror by two large flat mirrors, which focus them at an altitude of 12 km. As the beams propagate through the atmosphere, photons are scattered back by air molecules. After ~ 80 μs, the light from 12 km distance returns back to the telescope. This backscattered light is then directed, by a dichroic positioned in front of LUCI, towards the *Shack-Hartmann* wavefront sensor units, characterized by 15 x 15 subapertures, which allows ARGOS to correct for approximately 150 turbulence modes. Nevertheless, since laser beacons propagate back and forth through the atmosphere layers, they are not sensitive to the global wavefront tip-tilt, which thus still require a dedicated natural guide star for its determination and correction; however, the limiting magnitude requirements for the ARGOS-NGS can be relaxed down to R ~ 16. The tip/tilt sensing is performed by a set of Avalanche Photo

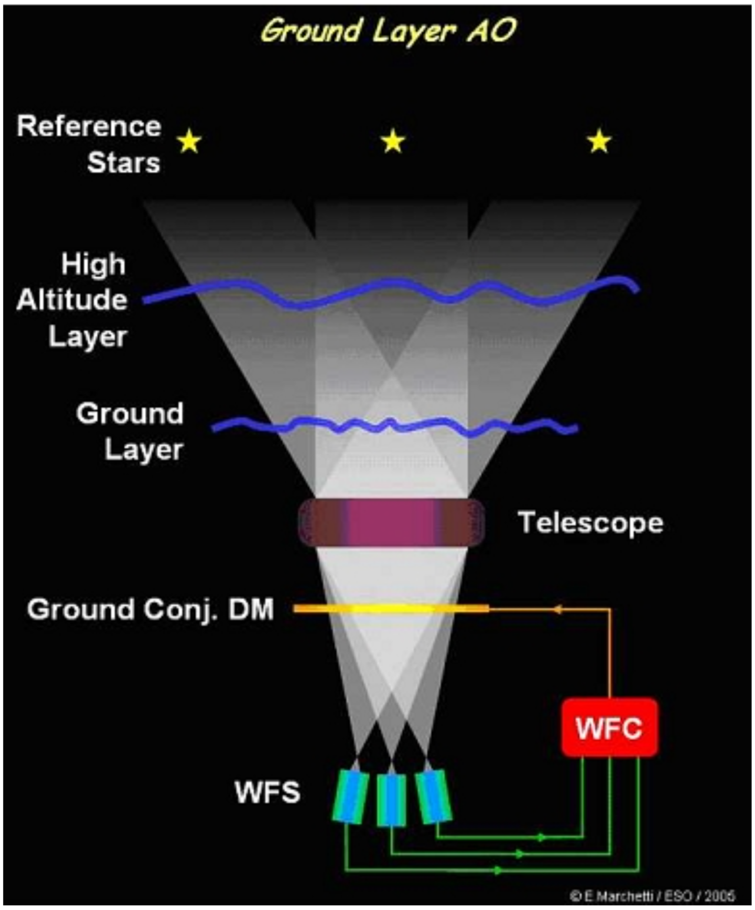

Figure 2.5: Scheme of the working principle of GLAO systems. Light rays from all objects in the field, regardless of their angular offset from the centre, pass through the same low layer of turbulence because it lies directly in front of the telescope mirror. Several GS placed at the edge of the science FOV are used to probe the ground layer atmospheric structure by means of several WFS measurements, which are combined to compensate the turbulence thanks to a single DM optically conjugated close to the telescope aperture. Image courtesy of E. Marchetti (ESO).

Diode (APD) units, exploiting the NGS wavefront sensor board of the FLAO system; for this reason, the tip/tilt NGS must be located within the ~ 2 x 3 arcmin field that can be reached by the FLAO stage, which is however not symmetric with respect to the center of field of view of LUCI. The Pyramid WFS of the FLAO system is used instead for truth-sensing correction, which account for the uncommon portion of the light paths between the Rayleigh WFS and the instrument, that can thus be affected by differential variations induced by the mechanical flexures of the telescope. The sampled turbulence images (from LGS, NGS tip-tilt and truth sensing) are then treated by the ARGOS slope computer, whose computation is used by the 672 actuators of the adaptive secondary mirror of the telescope to compensate for the ground-layer turbulence. The system is calibrated thanks to a calibration unit attached to a deployable arm that can be placed just below the ASM. An overview of the system configuration is sketched in Fig. 2.6.

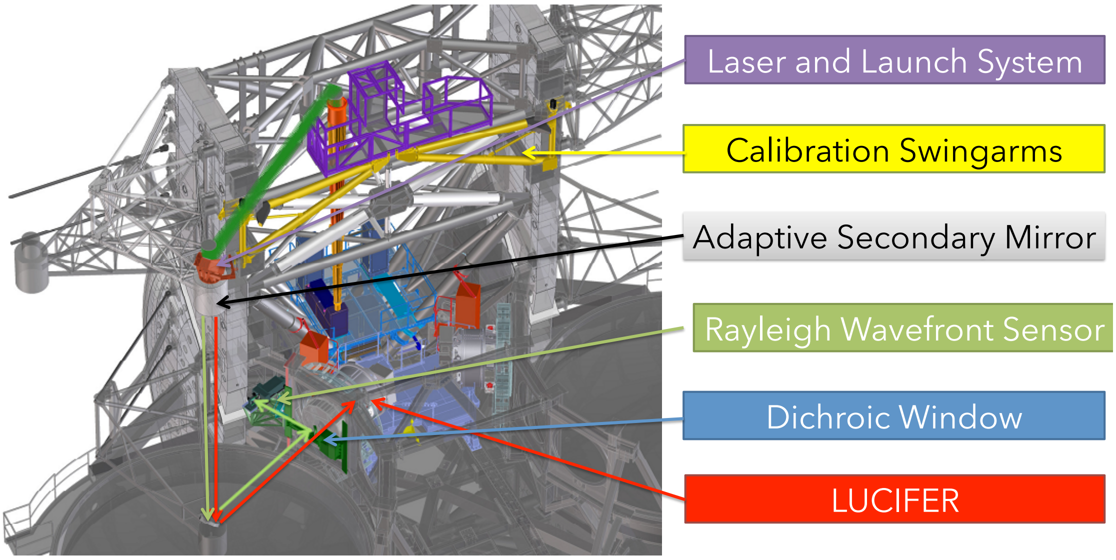

Figure 2.6: 3D CAD model showing the location of the components of ARGOS (in color) on the LBT structure (in grey). The main sub-systems are labeled on the side. The light rays paths are indicated by colored arrows from the ASM to the WFS (green) and to LUCI (red). Modified image from M. Deysenroth and H. Gemperlein.

ARGOS performances

During the commissioning phase of ARGOS we had the opportunity to perform some analysis on the first on-sky images, focusing in particular on Point Spread Function (PSF) modeling and characterization; the precise evaluation of the shape and of the uniformity of the PSF is indeed crucial to maximize the scientific return of the system. We made use of some of the most common tools for PSF extraction and photometry like DAOPHOT (Stetson, 1987), as well as dedicated python-based packages like Astropy, to directly extract and model the PSF from selected sources on the image. After performing the PSF fitting and photometry both on open loop (OL) and closed loop (CL)[4] images of the globular cluster NGC2419 (Fig 2.7), we found that the GLAO correction provided by ARGOS allowed us to reach a resolution down to 0.25 – 0.3" in the K band (for a DIMM-measured seeing of ~ 0.8" – 1"). Moreover, investigating the radial trend of the FWHM derived from PSF fitting, as a function of the distance from the reference tip/tilt star in the center of the field, allowed us to test the spatial uniformity of the correction. Right panel of Figure 2.7 show that ARGOS is able to provide an enhancement of a factor 1.5-2 in FWHM from OL to CL observations both in J and H band; PSF uniformity also appear to be good despite some very little evidence of anisoplanatism still visible. Equally meaningful in terms of the gain in energy distribution of the PSF provided by the AO correction is the evaluation of the

---

[4] If the wavefront error is measured before it has been corrected, then operation is said to be in open loop. If the wavefront error is measured after it has been corrected, the adaptive optics system is said to be operating in closed loop. In the latter case, the system operates on small residual errors.

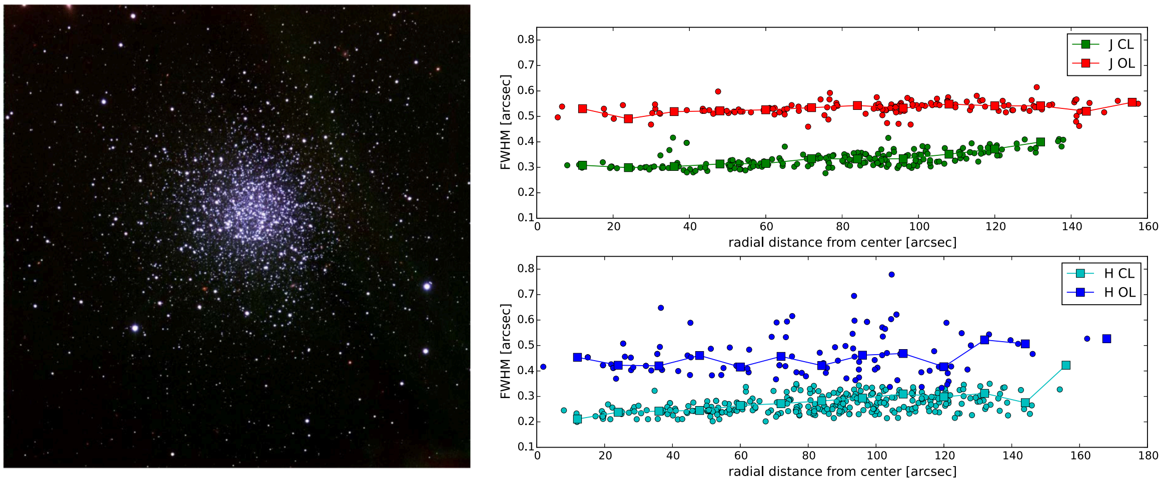

Figure 2.7: *Left Panel*: Composite image of the globular cluster NGC2419, combining 3-5 min exposures in J,H and K band with LUCI 1 during the commissioning run of December 2016. The average spatial resolution obtained is ~ 0.25" in the K band. Image courtesy of Sebastian Rabien (MPE). *Rigth Panel*: FWHM of detected sources as a function of radial distances from the tip-tilt star in the center of the field demonstrate an enhancement of a factor 1.5-2 over the entire range between close loop (CL) and open loop (OL) operations, although some small anisoplanatism is still visible. The filled squares are median values evaluated in radial distance bin of 12" (100 pixels).

Encircled Energy (EE). From the analysis of commissioning data we could demonstrate that the radius of 50% EE (i.e. the radius of the PSF at which 50% of the energy is enclosed) remains fairly constant as a function of the distance from the center; moreover, almost the entirety of data points lie below the 0.25 arcsec threshold, namely the width of the 2-pixel slit for LUCI-MOS configuration. A more in-depth analysis of the ARGOS performances will be presented soon by Rabien et al. (in prep).

3

A new calibration of strong-line metallicity indicators in star forming galaxies

This Chapter reproduces the paper: *New fully empirical calibrations of strong-line metallicity indicators in star-forming galaxies*, M. Curti, G. Cresci, F. Mannucci, A. Marconi, R. Maiolino and S. Esposito, 2017, MNRAS, 465, 1384.
The work was conducted in collaborations with listed co-authors, but I led and performed all the steps of the analysis, including the stacking of the spectra, the continuum subtraction and emission line fitting procedure, the measurement of the electron temperatures and ionic abundances and the scientific interpretation of the results.
The last Section of the Chapter (Appendix 3.7) represents preliminary results from ongoing work at the time of writing, that will constitute the base of a forthcoming paper (Curti et al, in prep).

3.1 Introduction

The accurate determination of gas phase metallicity represents a challenging topic for studies that aim at understanding the chemical evolution of galaxies. The metal content of a galaxy is regulated by complex interactions between physical processes occurring on different spatial and time scales: heavy elements produced by stellar activity contribute to the enrichment of the interstellar medium (ISM), while cosmological infall of pristine gas from the intergalactic medium (IGM) and outflows due to Active Galactic Nuclei (AGNs) and supernovae could dilute the ISM and at the same time trigger new star formation episodes (Davé et al., 2011b). These processes directly impact the global baryon cycle and thus affect other physical quantities strictly related to the history of chemical enrichment in galaxies like stellar mass ($M_\star$) and star formation rate (SFR); therefore, relationships between these parameters and gas-phase metallicity are expected. Indeed in the last decades strong observational evidences of a correlation between $M_\star$ and gas-phase metallicity (the so called mass-metallicity relation, M-Z) have been reported by several studies, both in the local Universe (e.g. Tremonti et al. 2004; Lee et al. 2006; Liang et al. 2007) and at higher redshift, where signatures of a cosmic evolution have been found (e.g Erb et al. 2006; Maiolino et al. 2008; Mannucci et al. 2009; Zahid et al. 2012; Cresci et al. 2012; Troncoso et al. 2014). Furthermore, Mannucci et al. (2010) showed that the intrinsic scatter in the M-Z could be reduced when SFR is taken into account, introducing the concept of a Fundamental Metallicity Relation (FMR) that reduces the M-Z to a two-dimensional projection of a three dimensional surface. The FMR appear to be *more fundamental* in the sense that it does not seem to present clear signs of evolution up to $z \sim 2.5$. Even though the physical origin of these relations is still debated, the knowledge of the main properties of the M-Z and the exact form of its dependence upon the SFR is important to investigate the processes regulating star formation and to assess the role of outflows in ejecting metals out of the galaxy (Davé et al., 2011b; Lilly et al., 2013; Dayal et al., 2013); this could provide crucial observational constraints for models aimed at reproducing the chemical evolution of galaxies across cosmic time.

Investigating the properties of these relationships and their redshift evolution requires precise and robust metallicity estimates. Since the scatter in the FMR is of the order of 0.05 dex (Mannucci et al., 2010), such a level of precision in metallicity determination would be desirable. There are several ways to measure abundances in galaxies, but unfortunately none of them is considered reliable or applicable over the whole metallicity range covered by large galaxy samples. The most commonly used method relies on the determination of the electron temperature of the nebulae responsible for emission lines in galaxies: in fact, electron temperature is known to be strongly correlated with metallicity, such that higher metallicities are associated to lower T_e, because forbidden emission lines from metals are the primary coolants in HII regions. Electron temperatures can be inferred by exploiting the temperature sensitive auroral to nebular line ratios of particular ions (e.g. [OIII] $\lambda 4363/5007$ is one of the most widely used); in fact, the atomic structure of these ions is such that auroral and nebular lines originate from excited states that are well spaced in energy and thus their relative level populations depend heavily on electron temperature. This so called T_e method is widely accepted as the preferred one to estimate abundances since it is a direct probe of the processes that regulate the physics of ionized nebulae. Unfortunately, auroral lines are weak in most of individual galaxy spectra, especially for metal rich objects, which typically prevents the T_e from being used method to determine abundances of metal enriched galaxies. A different technique is based instead on exploiting the ratio between oxygen and hydrogen recombination lines (RLs): since these lines show a very weak dependence on electron temperature and density (Esteban et al. 2009, 2014; Peimbert et al. 2014) this is probably the most reliable method beacuse is unaffected by the typical biases of the T_e method associated with temperature fluctuations. Typical discrepancies between T_e and RLs based abundances are found to be of the order of 0.2-0.3 dex, with the first ones underestimating the latter (García-Rojas & Esteban 2007; Esteban et al. 2009). Recently, Bresolin et al. (2016) showed that metal RLs yield nebular abundances in excellent agreement with stellar abundances for high metallicity systems, while in more metal-poor environments they tend to underestimate the stellar metallicities by a significant amount. However, RLs are extremely faint (even hundred times fainter than oxygen auroral lines) and cannot be detected in galaxies more distant than a few kpc (Peimbert et al., 2007). For this reason, different methods have been developed to measure abundances in faint, distant and high metallicity galaxies. In particular, it is known that some line ratios between strong collisionally excited lines (CELs) and Balmer lines show a dependence on metallicity, which can be either directly motivated or indirectly related to other physical quantities (e.g. the ionization parameter). Thus, it has been proposed that these line ratios could be calibrated against the oxygen abundance and used as metallicity indicators for galaxies in which the application of the T_e method is not possible due to the extreme faintness of auroral lines (Pagel et al., 1979; Alloin et al., 1979): these are referred to as the strong-line-methods. Calibrations can be obtained either empirically, for samples in which metallicity have been previously derived with the T_e method (e.g. Pettini & Pagel 2004; Pilyugin & Thuan 2005; Pilyugin et al. 2010b, 2012b; Marino et al. 2013; Pilyugin & Grebel 2016), or theoretically, in which oxygen abundance have been inferred via photoionization models (e.g. McGaugh 1991; Zaritsky et al. 1994; Kewley & Dopita 2002; Kobulnicky & Kewley 2004; Tremonti et al. 2004; Dopita et al. 2013, 2016), or be a combination of the two. Unfortunately, comparisons among metallicities estimated through different calibrations reveal large discrepancies, even for the same sample of objects, with variations up to ~ 0.6 dex (Moustakas et al., 2010; Kewley & Ellison, 2008). In fact, theoretical calibrations are known to produce higher metallicity estimates with respect to empirical calibrations based on the T_e method. The origin of these discrepancies is still unclear, but they could be attributed on one hand to oversimplified assumptions made in most of the photoionization models, e.g. about the geometry of the nebulae and the age of the ionizing source (Moustakas et al., 2010) and on the other hand to temperature gradients and fluctuations that may cause an overestimate of the electron temperature and a consequent underestimate of the true metallicity with the T_e method (Peimbert, 1967; Stasińska, 2002, 2005). Great care is therefore needed when using composite calibrations built with different methods over different metallicity ranges, due to the large uncertainties introduced on the absolute metallicity scale. Empirical calibrations are generally preferable because they are based on the T_e method abundance scale, which is directly inferred from observed quantities. Moreover, on the abundance scale based on photoionization models the Milky Way, where abundances can be precisely measured, would represent a very peculiar galaxy, falling well below the M-Z defined by similar star forming galaxies. The discrepancy is reduced by more empirical metallicity calibrations that provide lower abundances. At the same time, one of their main limitations is that they are often calibrated for samples of objects that do not properly cover all the galaxy parameters space; this means, for example, that empirical calibrations obtained from a sample of low excitation HII regions could give unreliable results when applied to global galaxy spectra. Recently, the application of integral field spectroscopy allowed to study galaxy properties in great detail and to extend the HII regions database for compiling abundances in order to obtain calibrations based on the T_e method (e.g. Marino et al. 2013 for the CALIFA survey). However, self-consistent calibrations obtained from integrated galaxy spectra and covering the entire metallicity range are still scarce.

In this work we derive a set of new empirical calibrations for some of the most common strong line metallicity indicators, thanks to a uniform application of the T_e method over the full metallicity range covered by SDSS galaxies. We combined a sample of low metallicity galaxies with [OIII] λ4363 detection from the SDSS together with stacked spectra of more than 110 000 galaxies in bins of log[OII]/Hβ - log[OIII]/Hβ that allowed us to detect and measure the flux of the crucial auroral lines needed for the application of the T_e method also at high metallicity. Other studies demonstrated the potentiality and reliability of the stacking technique (Liang et al., 2007; Andrews & Martini, 2013; Brown et al., 2016); compared to these works, our approach differs in the sense that we do not rely on any assumption regarding the nature and the form of the relationships between metallicity, mass and SFR, but only on the hypothesis that oxygen abundance can be determined from a combination of [OII] and [OIII] emission line ratios.

The paper is organized as follows: in Section 3.2 we describe the sample selection and the procedure used to stack the spectra, subtract the stellar continuum and fit the emission lines of interest. Section 3.3 describes the method we used to derive electron temperatures and chemical abundances. We then discuss the relations between different temperature diagnostics and between temperatures of different ionization zones. In Section 3.4 we report some tests we performed to verify the consistency of our hypothesis and stacking procedure. In Section 3.5 we present our new empirical calibrations for some of the most common strong-line abundances diagnostics and we compare them with previous ones from literature. We then apply them to the original SDSS sample as a test of their self consistency. Section 3.6 summarize our main results.

Publicly available tools to apply these new calibrations can be found on the webpage `http://www.arcetri.astro.it/metallicity/`.

3.2 Method

3.2.1 Sample Selection

Our galaxy sample come from the SDSS Data Release 7 (DR7; Abazajian et al. 2009), a survey including ~ 930000 galaxies in an area of 8423 square degrees. Emission line data has been taken from the MPA/JHU[1] catalog, in which also stellar masses (Kauffmann et al., 2003a), SFRs (Brinchmann et al., 2004; Salim et al., 2007) and metallicities (Tremonti et al., 2004) are measured. We chose only galaxies with redshifts in the range $0.027 < z < 0.25$, to ensure the presence of the [OII] $\lambda3727$ emission line and of the [OII] $\lambda\lambda7320,7330$ doublet within the useful spectral range of the SDSS spectrograph (3800-9200 Å). We selected only galaxies classified in the MPA/JHU as star forming, discarding galaxies dominated by AGN contribution according to criteria for BPT-diagram classification illustrated in Kauffmann et al. (2003b), in order to avoid any effect on the emission line ratios that could cause spurious metallicity measurements. We also used a SNR threshold of 5 on the Hα, Hβ, [OIII] $\lambda5007$ and [OII] $\lambda3727$ emission line fluxes. After applying these selection criteria the total number of galaxies in our sample was reduced to 118478, with a median redshift of $z = 0.072$. At this redshift, the $3''$ diameter of the SDSS spectroscopic fiber corresponds to ~ 3 kpc.

3.2.2 Stacking procedure

Our primary goal is to perform accurate measurements of galaxy metallicity in order to obtain more consistent calibrations for the main strong-line indicators, thanks to a uniform application of the T_e method. Unfortunately, in distant galaxies the [OIII] $\lambda4363$ and [OII] $\lambda\lambda7320,7330$ auroral lines are too weak to be detected in the individual spectra at metallicities higher than $12 + \log(O/H) \gtrsim 8.3$. Thus, we decided to stack spectra for galaxies that are expected to have similar metallicities.

Galaxies are stacked according to their values of reddening corrected [OII]$\lambda3727$/Hβ and [OIII]$\lambda5007$/Hβ flux ratios. This is based on the assumption that the so called strong-line methods can be used to discriminate the metallicities of star forming galaxies

---

[1] `http://www.mpa-garching.mpg.de/SDSS/DR7/`

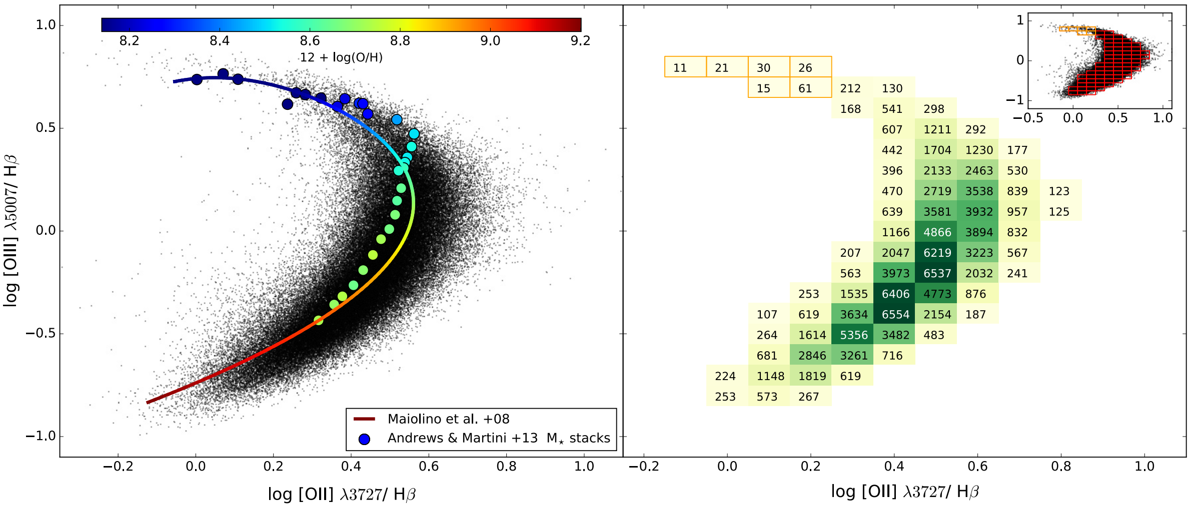

Figure 3.1: *Left Panel*: The distribution of our galaxy sample in the log [OII] λ3727/Hβ - log [OIII] λ5007/Hβ diagram. The curve represents the combined calibrations for the [OII]/Hβ and [OIII]/Hβ metallicity indicators from Maiolino et al. (2008), color coded by the metallicity inferred from the combination of the two indicators. The Andrews & Martini (2013) stacks in bins of stellar mass are shown as circle points and color coded for their direct metallicity measurement. *Right Panel*: Stacking grid for our sample of SDSS galaxies in the log [OII] λ3727/Hβ - log [OIII] λ5007/Hβ diagram. Each square represents a 0.1 x 0.1 dex^2 bin, color-coded by the number of galaxies included in it, which is also written for each bin. Orange boxes represent stacks of low metallicity galaxies for which we relaxed the 100-object threshold in the definition of our grid. In the upper right box of the panel our stacking grid is shown superimposed on the distribution of galaxies in the diagram.

when multiple line ratios are simultaneously considered. We stress that we are not assuming that a particular combination of these line ratios, such as R_{23}, is related to metallicity, but only that galaxies with simultaneously the same values of both [OIII]λ5007/Hβ and [OII]λ5007/Hβ have approximately the same oxygen abundance. In fact, these are the two line ratios directly proportional to the main ionization states of oxygen and are thus individually used as metallicity diagnostics (Nagao et al., 2006; Maiolino et al., 2008). Moreover, their ratio [OIII]/[OII] is sensitive to the ionization parameter and it is also used as an indicator of oxygen abundance, especially in metal enriched galaxies, due to the physical link between ionization and gas-phase metallicity (e.g. Nagao et al. 2006; Masters et al. 2016). This means that the location of a galaxy on the [OII]λ3727/Hβ-[OIII]λ5007/Hβ diagram is primarily driven by the metal content and the ionization properties of galaxies. Since the scatter in a given line ratio at fixed metallicity is often regarded as driven by variations in the ionization parameter (e.g. Kewley & Dopita 2002, López-Sánchez et al. 2012, Blanc et al. 2015) our binning choice takes into account this possible source of scatter.

The left panel of Figure 1 shows the distribution of our selected SDSS galaxies in the log [OII]λ3727/Hβ - log [OIII]λ5007/Hβ diagnostic diagram. We overplot the semi-empirical calibration of Maiolino et al. (2008) for the [OII]$\lambda5007/\mathrm{H}\beta$ and [OIII]$\lambda5007/\mathrm{H}\beta$ indicators in order to better visualize how the position on the 2d-diagram given by the combination of these line ratios represent a metallicity sequence. The curve, color coded for the metallicity inferred from the combination of the two indicators, follows quite tightly the distribution of galaxies on the map, showing how metallicity increases from the upper left region of the diagram to the bottom left one. To further illustrate how metallicity varies along this diagram we can also use the metallicity obtained with the $\mathrm{T_e}$ method from composite spectra in bins of stellar mass by Andrews & Martini (2013), whose stacks are shown as circled points in the left panel of the figure. Also in this case we can recognize a pattern in which their mass stacks, each point being representative of the line ratios measured from the associated composite spectra, increase monotonically in metallicity following the galaxy sequence on the diagram. Thus, both methods reveal a clean variation of oxygen abundance with location on the diagram, though being based on different and independent approaches; this strengthens the idea of using the combination of [OII]/Hβ and [OIII]/Hβ as a metallicity indicator. We note that differences among metallicity values predicted by the Maiolino et al. (2008) calibrations and the Andrews & Martini (2013) stacks (with the first ones predicting higher abundances than the latter) is only due to the different abundance scale upon which the two methods are defined, being the Maiolino et al. (2008) indicators calibrated with photoionization models at high metallicities and the Andrews & Martini (2013) stacks based on $\mathrm{T_e}$ method metallicities.

In Sec. 3.4 we test our assumptions by comparing $\mathrm{T_e}$ metallicities inferred from single galaxy spectra belonging to the same bin; this allows also to evaluate the main issues related to the stacking technique (see also the discussion in Sec. 3.3.2). We refer to these sections for an exhaustive discussion on this topic.

We thus created stacked spectra in bins of 0.1 dex of log [OII]/Hβ and log [OIII]/Hβ. The choice of the 0.1 dex width in the binning grid represents a good compromise between keeping an high enough number of galaxy in each bin to ensure auroral line detection and at the same time avoid wider bins in which we could have mixed object with too different properties. We performed some tests in stacking spectra and computing oxygen abundance with different bin sizes, finding no relevant differences.

We adopted the emission line values provided by the MPA/JHU catalog to create the set of galaxy stacks. All line fluxes have been corrected for Galactic reddening, adopting the extinction law from Cardelli et al. (1989) and assuming an intrinsic ratio for the Balmer lines $\mathrm{H}\alpha/\mathrm{H}\beta = 2.86$ (as set by case B recombination theory for typical nebular temperatures of $T_e = 10\,000\,\mathrm{K}$ and densities of $n_e \approx 100\,\mathrm{cm}^{-3}$).

In the right panel of Figure **??** the binning grid for our galaxy sample in the space

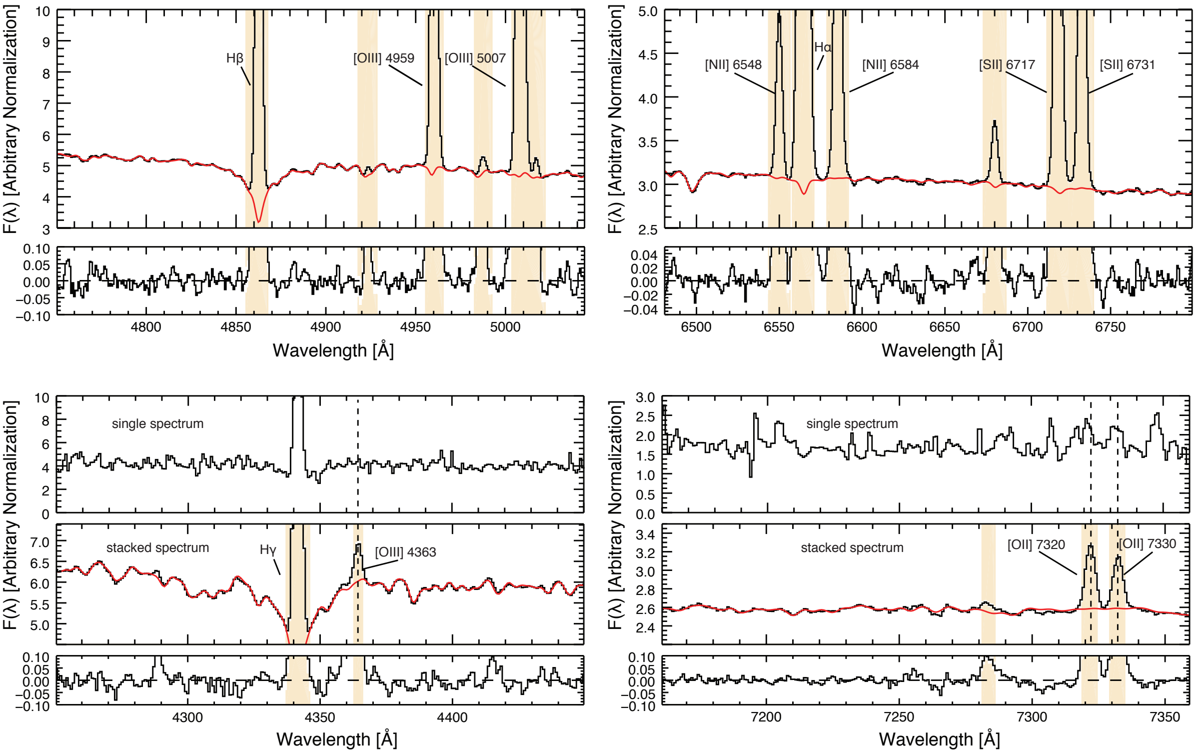

Figure 3.2: Fit and subtracted spectra for wavelength ranges relative to Hβ and [OIII] nebular lines (upper left panels), Hα, [NII] and [SII] nebular lines (upper right panels), [OIII] λ4363 auroral line (lower left panels) and [OII] λ7320, 7330 auroral lines (lower right panels) respectively, for the 0.5; 0.5 stack. For strong nebular lines, the upper panel shows the stacked spectrum (black) and the stellar continuum best-fit component (red), while the bottom panel shows the residual spectrum after the stellar continuum subtraction. For auroral lines boxes, a single galaxy spectrum is shown in the upper panel for comparison, while the stacked spectrum is shown in the middle one. The yellow shaded regions mark the spectral interval masked out during the stellar continuum fitting procedure.

defined by log([OII] λ3727/Hβ) and log([OIII] λ5007/Hβ) is shown, color coded by the number of objects in each bin. In the up-right corner of the figure we show the distribution of the galaxy sample in the diagnostic diagram, with our binning grid superimposed. In the construction of our binning grid we required a minimum of 100 sources per bin: this was a conservative choice in order to average enough galaxy spectra to ensure the required SNR (i.e. at least 3) on auroral lines detection after the stacking procedure. Since we imposed a threshold of 100 sources per bin, the upper-left corner of the diagram, occupied by the galaxies of lower metallicity in the sample, is not well covered by our stacking grid. For this reason, we extended our grid to include also low-metallicity galaxies by reducing the threshold to 10 sources in that area of the diagram, enough to detect auroral lines in stacked spectra with a SNR higher than 3 in this metallicity regime. This extension of the grid is marked with orange borders in the figure. This allows our grid to entirely cover the region occupied by SDSS galaxies, probing the largest possible combination of physical parameters in the sample.

Throughout this paper we will refer to a particular stack by indicating the center of the corresponding bin in both the line ratios considered (e.g. 0.5; 0.2 corresponds to the bin centered in log[O II] λ3727/Hβ = 0.5 and log[O III] λ5007/Hβ = 0.2).

Before creating the composite spectrum from galaxies belonging to the same bin, each individual spectrum has been corrected for reddening with a Cardelli et al. (1989) extinction law and normalized to the extinction corrected Hβ. We have verified that the final results do not depend on the choice of the extinction law, by alternatively using the Calzetti et al. (1994) extinction law in a few random bins. Then, each spectrum has been re-mapped onto a linear grid (3000-9200 Å), with wavelength steps of $\Delta\lambda$ = 0.8 Å, and shifted at the same time to the rest frame to compensate for the intrinsic redshift of the sources. This procedure may cause a redistribution of the flux contained in a single input channel to more than one output channel; in order to take into account this effect, the incoming flux is weighted on the overlap area between the input and output channels. Finally, to create the stacked spectra we took the mean pixel by pixel between the 25th and the 75th percentile of the flux distribution in each wavelength bin; in this way we could avoid biases introduced by the flux distribution asymmetry clearly visible in every flux channel as a right-end tail.

3.2.3 Stellar continuum subtraction

Stacking the spectra improve significantly the SNR of the auroral lines, but we must also fit and subtract the stellar continuum to accurately measure their fluxes. To perform the stellar continuum fit and subtraction on our stacked spectra we have created a synthetic spectrum using the MIUSCAT library of spectral templates (Vazdekis et al., 2012; Ricciardelli et al., 2012), an extension of the previous MILES library (Falcón-Barroso et al., 2011; Cenarro et al., 2001; Vazdekis et al., 2010; Sánchez-Blázquez et al., 2006) in which both Indo-U.S. and CaT libraries have been added to fill the gaps in wavelength coverage. The new MIUSCAT library covers a wavelength range of 3525-9469 Å, although the useful spectral window for this work is entirely covered by MILES templates, whose resolution is 2.51 Å(FWHM). Stellar templates have been retrieved from the MILES website[2] for a wide range of ages and metallicities, assuming an unimodal initial mass function with a 1.3 slope (i.e. a Salpeter IMF). The stellar continuum subtraction in the [S II] λ4069 spectral window (close to Hδ) has been performed using a different kind of stellar templates, the PÉGASE HR[3](Le Borgne et al., 2004), a library which covers a wavelength range of 4000-6800 Å with a spectral resolution of R = 10000 at λ = 5500 Å; this allowed a better stellar continuum fit in

---

[2] `http://miles.iac.es`

[3] `http://www2.iap.fr/pegase/`

Line (1)	Fit Range [Å] (2)	Mask Range [Å] (3)
[OII] $\lambda3727$	3650-3830	3723.36-3733.60
[NeIII]$\lambda3870$	3850-4150	3866.29-3874.03
[SII]$\lambda4069$	4000-4150	4068.39-4071.11
Hδ $\lambda4102$	3850-4150	4098.79-4107.00
Hγ $\lambda4340$	4250-4450	4337.34-4346.03
[OIII] $\lambda4363$	4250-4450	4362.98-4365.89
Hβ $\lambda4861$	4750-5050	4857.82-4867.55
[OIII] $\lambda4960$	4750-5050	4955.33-4965.26
[OIII] $\lambda5007$	4750-5050	5003.23-5013.25
[NII] $\lambda5756$	5650-5850	5754.32-5758.16
[NII] $\lambda6549$	6480-6800	6543.30-6556.40
Hα $\lambda6563$	6480-6800	6558.05-6571.17
[NII] $\lambda6584$	6480-6800	6578.69-6591.87
[SII] $\lambda6717$	6480-6800	6711.57-6725.01
[SII] $\lambda6731$	6480-6800	6725.94-6739.40
[OII] $\lambda7320$	7160-7360	7318.50-7323.28
[OII] $\lambda7330$	7160-7360	7329.24-7334.12

Table 3.1: (1) Emission lines. (2) Wavelength range of stellar continuum fit. (3) Spectral range that was masked out.

the proximity of the [SII] $\lambda4069$ auroral line. To further improve emission line fluxes measurements, stellar continuum fits and subtractions have been performed selecting subregions of the spectrum centred on the lines of interest, each subregion being large a few hundred angstrom. During the procedure the location of the emission lines have been masked out in order to prevent the fit to be affected by non stellar features. We performed the fit exploiting the IDL version of the penalized pixel-fitting (pPXF) procedure by Cappellari & Emsellem (2004). In Table 3.1 are reported, for each emission lines whose flux have been measured in this work, the spectral window of the stellar continuum fit and the wavelength range that has been masked out.

Figure 3.2 shows examples of the results of the stacking procedure and stellar continuum subtraction for the $0.5; 0.5$ bin, in particular in spectral windows including Hβ, [OIII] , Hα, [NII] and [SII] nebular lines and [OIII] $\lambda4363$, [OII] $\lambda7320,7330$ auroral lines respectively. For latter emission lines, a single galaxy spectrum from the same stack is shown for comparison, to underline the dramatic increase in SNR that allow to reveal the otherwise invisible auroral lines. The orange regions mark the spectral range masked out from the stellar fitting around nebular lines. In each plot, the lower panel shows the residual spectrum of the fit.

3.2.4 Line Flux Measurement and Iron contamination of [O III] λ4363 auroral line at high metallicity

We fit emission lines with a single Gaussian profile, fixing velocities and widths of the weak auroral lines by linking them to the strongest line of the same spectral region. For doublets, we fixed the velocity width of the weaker lines to the stronger ones ([O II] λ3727 to [O II] λ3729, [O III] λ4960 to [O III] λ5007, [N II] λ6548 to [N II] λ6583, [S II] λ6731 to [S II] λ6717 and [O II] λ7330 to [O II] λ7320).

During the fitting procedure an emission feature close to 4360 Å has been detected and became blended with the [O III] λ4363 auroral line, especially in the high metallicity stacks. A similar contamination was previously found also by Andrews & Martini (2013) in their composite spectra. The nature of this feature is unknown, but it may reasonably be associated to emission lines from [Fe II] λ4360. In fact, many others features from the same ion are clearly observable both in the same (e.g. [Fe II] λ4288) and in different spectral windows; this particular emission have been reported also in studies on the Orion nebula (see e.g. Table 2 of Esteban et al. (2004)). Moreover, the strength of of the line increases with increasing metallicity, as well as the other [Fe II] lines in the spectra. In Figure 3.3 we show three stacked spectra corresponding to different metallicities, namely $0.4; 0.6$, $0.5; 0.0$ and $0.2; -0.6$, after performing the stellar continuum subtraction in the spectral window that contains the [O III] λ4363 line. The metallicity of each stack (see Sect. 3.5) is reported on every panel. The figure clearly shows how [O III] λ4363 becomes more contaminated as the metallicity increases, with the [Fe II] emission being just a few percent of the flux of the oxygen one in the upper panel and then completely blending with it in the other two. The [Fe II] emission line at 4288 Å is also clearly visible in all the composite spectra, with increasing strength for increasing metallicity, as expected.

Therefore we simultaneously fit the λ4360 feature and [O III] λ4363, linking both velocity widths and central wavelengths to Hγ. The different components of the fit are shown in blue in Figure 3.3, with the red line representing the total fit. Similarly to Andrews & Martini (2013), we consider the fit not sufficiently robust when the λ4360 emission flux resulted ≥ 0.5 times the flux measured for [O III] λ4363. The use of contaminated [O III] λ4363 line would result in totally non-physical temperatures, which result overestimated by a factor of ten. According to this criteria, 42 out of 69 bins have been flagged for undetected [O III] λ4363. We note that many previous detection of the [O III] λ4363 may be possibly contaminated by this feature, resulting in unreliable measurements for this crucial auroral line; therefore we recommend great care in using [O III] λ4363, when detected, to measure electron temperature from high

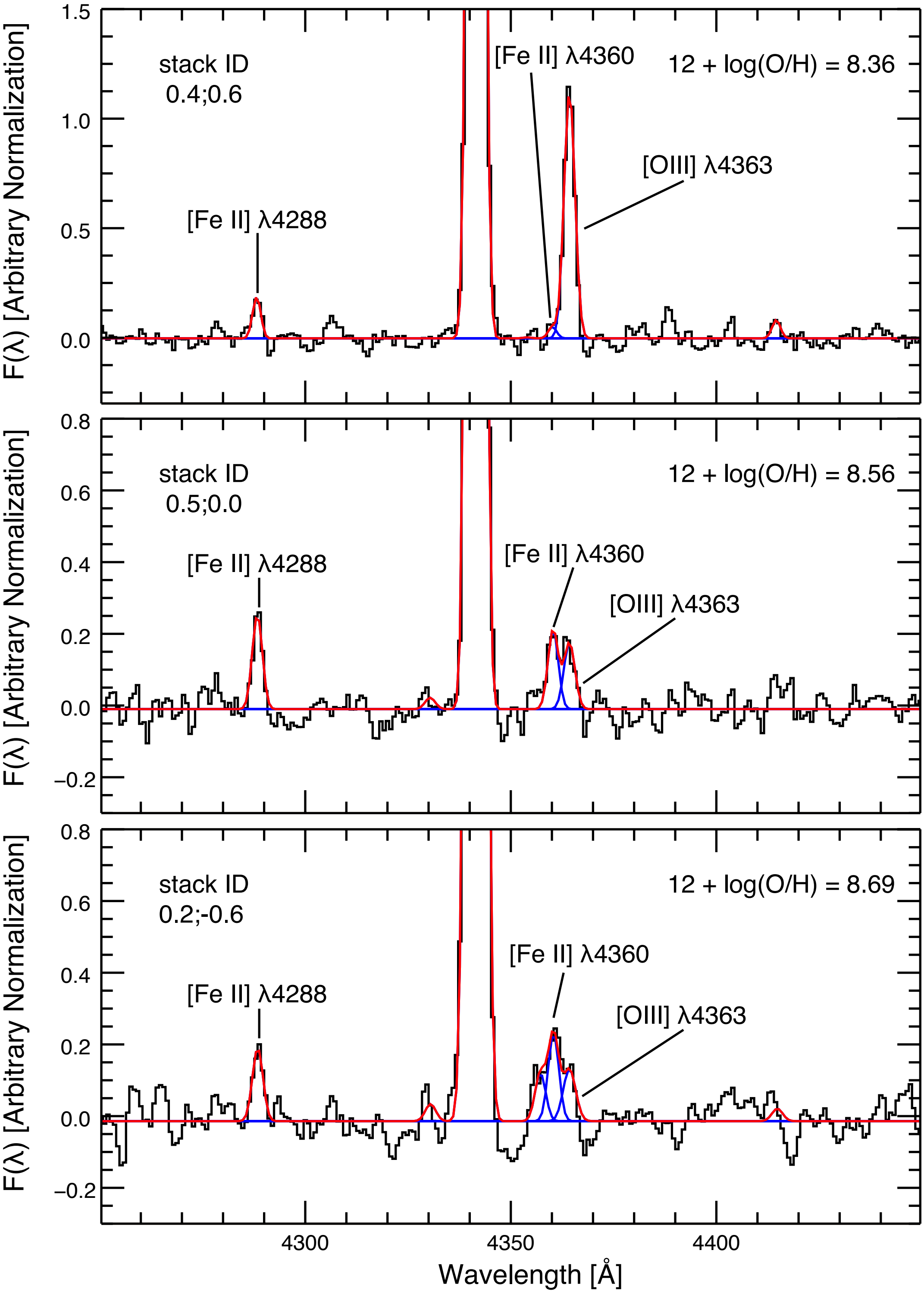

Figure 3.3: *Left*: Composite spectra for the 0.4; 0.6 (upper panel), 0.5; 0.0 (middle panel) and 0.2; −0.6 (lower panel) stack, in the wavelength range relative to [OIII] λ4363, after the stellar continuum subtraction. The different components of the fit are reported in blue while the red curve represents the total fit. The metallicity of each stack is reported in the right-upper part of the corresponding panel. The contamination of the [OIII] λ4363 line becomes more relevant with increasing metallicity (in the last case we can fit up to three components), as well as the intensity of the [Fe II] emission line at 4288 Å.

metallicity (12+log(O/H)$\geq$ 8.3) galaxy spectra. In the next section we will discuss how to derive the electron temperature for the high ionization zone for those stacks where the [OIII] λ4363 was not considered sufficiently robust.

Despite the large number of galaxies in each bin and the great care in the fitting procedure, in some of our stacks we were unable to measure both [OII] and [OIII] auroral line fluxes with sufficient precision. These are the stacked spectra corresponding to the 0.0;−0.8, 0.1;−0.4, 0.1;−0.7, 0.1;−0.8, 0.8;0.2 and 0.6;−0.3 bins and we decided to exclude this stacks from all the forthcoming analysis.

3.3 Electron Temperatures and Ionic Abundances Determination

3.3.1 Electron Temperatures

In principle, to measure electron temperatures and densities of different zones, the complete ionization structure of a HII region is needed. This is actually not possible and simpler approximations are always used. Usually a two-zone (of low and high ionization) or even a three-zone (of low, intermediate and high ionization) structure is adopted to model the HII regions responsible for emission lines in galaxies. In this work we consider a two-zone HII region: in this scenario, the high ionization zone is traced by the O^{++} ion, while the low ionization zone could be traced by different ionic species, e.g. O^+, N^+ and S^+. Thus, given the SDSS spectral coverage, in our case we have three different diagnostics for the temperature of the low ionization zone (which we will refer to as t_2 from now on), namely [OII] λ3727,3729/[OII] λ7320,7330, [NII] λ6584/[NII] λ5755 and [SII] λ6717,6731/[SII] λ4969, but only one for the temperature of the high ionization zone (t_3), namely [OIII] λ5007/[OIII] λ4363. Other collisionally excited lines probing the temperature of the intermediate and high ionization region are either too weak and thus undetectable even in galaxy stacks (e.g. [Ar III] λ5192) or fall outside the spectral range of the SDSS spectrograph (e.g. [S III] λ9069, [Ne III] λ3342) and we could not use them.

We computed electron temperatures exploiting PyNeb (Luridiana et al., 2012, 2015), the Python-based version of the *stsdas nebular* routines in IRAF, using the new atomic dataset presented in Palay et al. (2012). This routines, which are based on the solution of a five level atomic structure following De Robertis et al. (1987), determine the electron temperature of a given ionized state from the nebular to auroral flux ratio assuming a value for electron density. The electron density n_e can be measured from the density sensitive [SII] $\lambda\lambda$6717,6731 or [OII] $\lambda\lambda$3727,3729 doublets. In the ma-

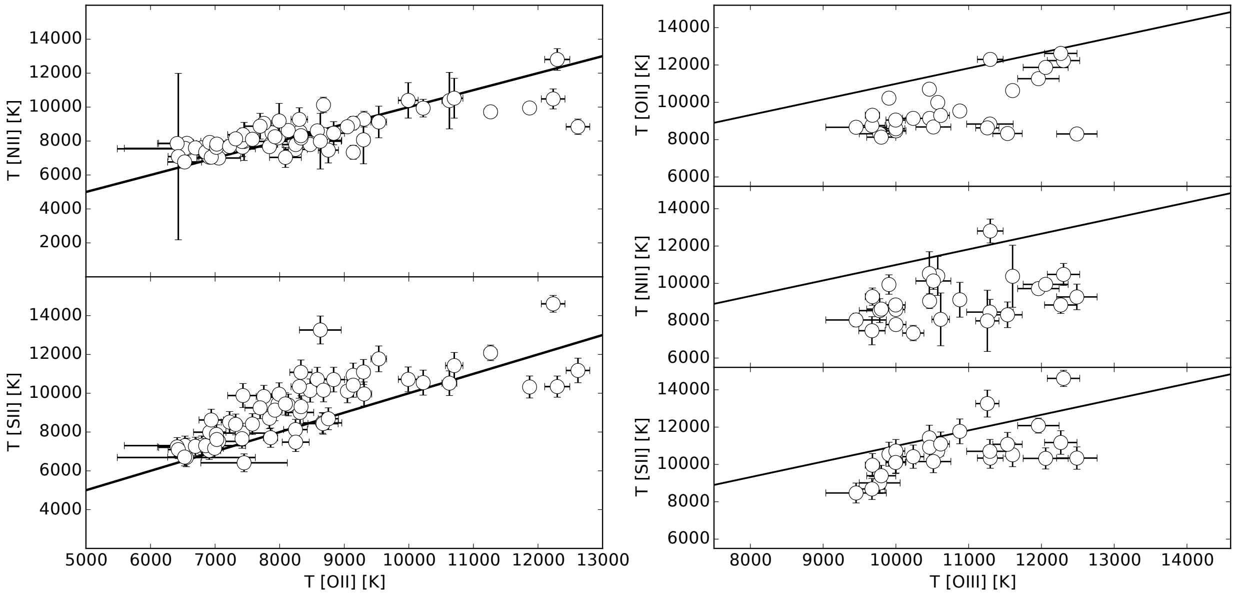

Figure 3.4: *Left Panels*: Electron temperatures derived from the [NII] and [SII] line ratios as a function of the electron temperature derived from [OII] ; the equality line is shown in black. While the [NII] temperatures are consistent with the [OII] ones, the [SII] provides temperatures systematically higher. *Right Panels*: Electron temperatures of the low ionization zone derived with all three different diagnostics as a function of the electron temperature of the high ionization zone derived from [OIII] line ratio. The black line represents the t_2-t_3 relation from equation 3.1, which does not provide a good representation of the data.

jority of our stacks we fall in the low density regime ($n_e < 100\,cm^{-3}$), for we measure for example a [SII] ratio close to the theoretical limit of 1.41; in this cases the dependence of our temperature diagnostics upon density is small. We note that using older atomic datasets (e.g. Aggarwal & Keenan 1999), instead on the new ones by Palay et al. (2012), would result in similar t_2 but t_3 systematically higher on average by 400 K. This is consistent with expectations given the updated effective collision strengths for [OIII] lines, as pointed out e.g. in Nicholls et al. (2013) where a discrepancy of $\sim$ 500 K is expected at T[OIII] $\sim 10^4$ K (see e.g. Section 7 and Figure 2 and 12 of their paper for further details). We also note that the collision strengths presented in Palay et al. (2012) for the [OIII] optical transitions are tabulated for a wide range of temperatures typical of nebular environments (from 100 K to 30000 K), which include all the temperatures we expect to find given the metallicity range spanned by the SDSS galaxies. Temperatures uncertainties were computed with Monte Carlo simulations. We generated 1000 realizations of the flux ratios, following a normal distribution with σ equal to the errors associated to the flux measurement by the fitting procedure and propagated analytically, and for each of them a temperature value was calculated. Then, we took the standard deviation of the resulting distribution as the error to associate to our temperature measure.

The left panels of Figure 3.4 show the relations between the temperatures of the low ionization zone of our stacks inferred through different diagnostics, i.e. T_e[NII] (upper panel) and T_e[SII] (lower panel) as a function of T_e[OII] ; the black line represents the line of equality. In the upper panel, we can see how the electron temperatures derived from nitrogen line ratios are consistent with T_e[OII] , although with a large scatter, while in the lower panel we show that T_e[SII] is larger than T_e[OII] for almost all of our points, thus overpredicting t_2 with respect to that derived through oxygen lines. Evidences of similar temperatures discrepancies have been reported by several works in the literature aimed at studying the physical properties of single HII regions (see e.g. Kennicutt et al. 2003; Bresolin et al. 2005; Esteban et al. 2009; Pilyugin et al. 2009; Binette et al. 2012; Berg et al. 2015). Interestingly, when T_e[SII] and T_e[OII] are considered in these papers, average offsets are usually found in the direction of larger T_e[OII] , differently from what we found for our stacks. The most likely explanation resides in the different atomic dataset for energy levels and collision strengths used among these works and ours. In fact, when computing T_e[SII] for our stacks exploiting different datasets, we find variations up to thousands kelvins even at fixed diagnostic ratio. Temperature fluctuations and inhomogeneities as well as shocks propagating within the photoionized gas have been proposed as the main sources of discrepancies between T_e inferred through different ionic tracers. Moreover, we are here considering the simple case of Maxwell-Boltzmann distributed electrons, while recent studies suggested that k-distributions could better represent the behavior of free electrons inside single HII regions (Nicholls et al., 2012, 2013; Dopita et al., 2013). In particular, when considering only Maxwell-Boltzmann distributions, the electron temperature inferred using the most common diagnostics could be overestimated and this effect is more relevant for ions in which the excitation temperature of the upper level involved in the transitions results different from the kinetic temperature of the distribution (Nicholls et al., 2012): the effect of k-distributed electrons could therefore affect different temperature diagnostics in different ways and thus explain the observed discrepancies in T_e estimates. For an in-depth discussion on how k-distributed electrons could affect the main metallicity diagnostics in HII regions, see Dopita et al. (2013). However, it is not clear to what extent these processes can affect the determination of electron temperature when considering global galaxy spectra and, in particular, a stacking of many galaxies, as we do in this work.

3.3.2 The t_2-t_3 relation

In the right panels of Figure 3.4 the relations between the temperatures of the low and high ionization zones are shown for those stacks in which we have been able determine

T_e[OIII] directly from the spectra. Many works in literature report the existence of a relation between the temperatures of the different ionization zones. The linear form of this relation, called t_2-t_3 relation , have been proposed for the first time by Campbell et al. (1986) and then revised in several studies (Garnett, 1992; Izotov et al., 2006; Pilyugin et al., 2006b; Pilyugin, 2007; Pilyugin et al., 2009, 2010a). This relation is of great interest in the context of nebular studies since it is generally used to compute the electron temperature for unseen ionization states. In this work we will consider the linear relation suggested by Pilyugin et al. (2009) for temperatures derived through oxygen lines in their sample of HII regions, given by the equation

$$t_2 = 0.264 + 0.835\ t_3\ , \tag{3.1}$$

where both temperatures are in units of 10^4K. The t_2-t_3 relation of equation 3.1 is shown for comparison in each plot as a black line. We can see that the great majority of our stacks falls below the t_2-t_3 relation independently of the type of ion tracer, although with different median offsets from the relation corresponding to different tracers. In any case, it is clear that this t_2-t_3 relation underestimates the temperature of the high ionization zone (or overestimates the temperature of the low ionization zone) for our composite spectra. A very similar result was found by Andrews & Martini (2013) for their stacked spectra in bins of stellar mass, even though they used a different, but quite similar, form for the t_2-t_3 relation. The median offsets from the t_2-t_3 relation for our stacks are -2642 K, -2712 K and -1055 K for T_e[OII] , T_e[NII] and T_e[SII] respectively.

The offset between the electron temperatures of the stacks and the t_2-t_3 relation is in agreement with the trend found by Andrews & Martini (2013) for galaxy stacks but also by Pilyugin et al. (2010a) for individual galaxies, suggesting that this effect is not a product of the stacking procedure but rather reflects the intrinsic properties of global galaxy spectra. The most likely explanation indeed is that galaxy spectra are the result of several contributions from HII regions that could present very different physical properties, both in terms of chemical composition and hardness of their ionizing sources: this may affect the auroral line fluxes in the sense that they are weighted differently in HII regions of different temperatures. Since the auroral line flux does not scale linearly with metallicity, the effect of a luminosity-weighted average towards warmer HII regions on their total flux can be substantial and difficult to account for, in a way similar to temperature fluctuations for single HII regions described by Peimbert (1967); therefore one can obtain results that do not agree with the observed t_2-t_3 relation for single HII regions (Kobulnicky et al., 1999; Kennicutt et al., 2003). For example, Pilyugin et al. (2010a) showed that the t_2-t_3 relation offset can be substantially reproduced considering composite spectra obtained mixing contributions from few HII regions of

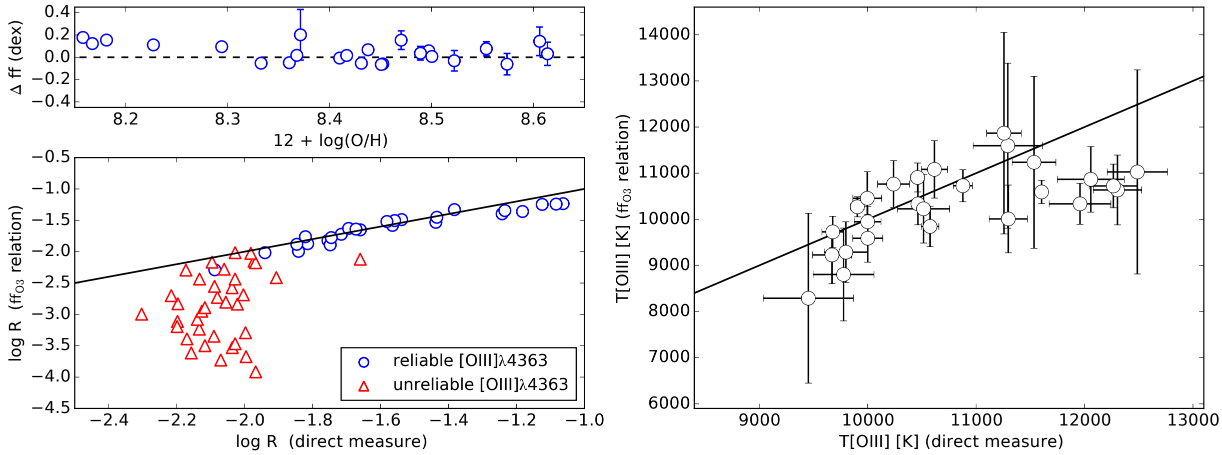

Figure 3.5: *Left Panel*: Log R (i.e. log [OIII] λ4363/Hβ) directly measured from the stacked spectra as a function of the same quantity obtained through the ff relation. Blue circles represent stacks whose [OIII] λ4363 detection was considered robust according to the criteria described in the text, while red triangles are stacks whose [OIII] λ4363 detection was considered unreliable. The black line represent the ff$_{O3}$ relation of equation 3.2. In the upper box the offset of log(R) from the ff$_{O3}$ relation for the stacks with reliable [OIII] λ4363 measurements is plotted as a function of the metallicity of the stacks.
Right Panel: T$_e$[OIII] derived from the ff$_{O3}$ relation as a function of direct measure T$_e$[OIII] for the stacks with detected [OIII] λ4363; black line represents equality.

very different temperatures. Moreover, the variation of the relative contribution of each HII region for different ionic species, together with the contribution from diffuse ionized gas (Moustakas & Kennicutt, 2006), can explain the different distributions in the t2-t3 plane for different temperature diagnostics as well as the offset between different estimations of the temperature of the low ionization zone. Despite these difficulties, the t_2-t_3 relation has been widely used in literature to compute electron temperatures of unseen ionization states.

3.3.3 The ff relations

Another possibility to solve the problem of determining the temperature of the high ionization zone for stacks with unmeasured [OIII] λ4363 is to rely on the relationship between the strong emission lines and the auroral line itself. As pointed out by Pilyugin (2005), a relation between auroral and nebular oxygen line fluxes has been demonstrated for HII regions of metallicity higher than 12 + log(O/H) ~ 8.25. This so called "ff relation" allow to estimate the auroral line flux from the measured nebular line fluxes when the first is not available. In this work we employed the following ff relation (which we will refer to from now on as the ff$_{O3}$ relation) obtained by Pilyugin et al. (2006a) to infer the [OIII] λ4363 flux for stacks where the flux of this line was not properly measured :

$$\log \mathrm{R} = -4.151 - 3.118 \log \mathrm{P} + 2.958 \log \mathrm{R}_3 - 0.680 (\log \mathrm{P})^2 \tag{3.2}$$

where R = $I_{[\mathrm{O\,III}]\,\lambda4363}/I_{\mathrm{H}\beta}$, $\mathrm{R}_3 = I_{[\mathrm{O\,III}]\,\lambda4949,5007}/I_{\mathrm{H}\beta}$ and P(i.e. the excitation parameter) = $\mathrm{R}_3/(\mathrm{R}_3 + \mathrm{R}_2)$, with $\mathrm{R}_2 = I_{[\mathrm{O\,II}]\,\lambda3727,3729}/I_{\mathrm{H}\beta}$.

Inspection of the left panel of Figure 3.5, where log(R) obtained through the $\mathrm{ff}_{\mathrm{O3}}$ relation is plotted against its direct measure from the spectra, reveals that our stacks which satisfy the criteria for good [OIII] λ4363 detection (blue circle points) are in good agreement with equation 3.2, represented by the black line. We also plot as red triangles the points representing the composite spectra whose [OIII] λ4363 detection was flagged as unreliable due to [Fe II] contamination. Almost all of these points does not follow the $\mathrm{ff}_{\mathrm{O3}}$ relation, falling well below the black line of Figure 3.5. This was expected and corroborates the fact that the [OIII] λ4363 flux measurements in those stacks can not be considered reliable. In the upper box of the same figure the deviations of log(R) from the $\mathrm{ff}_{\mathrm{O3}}$ relation (defined as $\Delta\mathrm{ff} = \log(\mathrm{R})_{\mathrm{direct}} - \log(\mathrm{R})_{\mathrm{ff\ relation}}$) for the stacks with good [OIII] λ4363 detection are plotted as a function of metallicity derived with the $\mathrm{T_e}$ method; the points scatter around zero with a $\sigma = 0.09$ dex, showing no trends with metallicity. The error bars in the upper box of Figure 3.5 represent the uncertainties on Δff, derived propagating the errors on the line flux measurements through the equation 3.2; with the exception of a few points, this source of uncertainty (0.05 dex on average) can not account for the total dispersion shown, being the larger part due to the intrinsic dispersion of the $\mathrm{ff}_{\mathrm{O3}}$ relation itself.

In the right panel of Figure 3.5 we compare $\mathrm{T_e}$[OIII] derived through the $\mathrm{ff}_{\mathrm{O3}}$ relation with the one directly measured from the spectra, for stacks with good detection of [OIII] λ4363; black line represents equality in this plot. Temperatures predicted by the $\mathrm{ff}_{\mathrm{O3}}$ relation are in good agreement with direct measurements within the uncertainties, and there is no evident and systematic trend unlike what happens with the t_2-t_3 relation (see, for comparison, the upper right panel of Figure 3.4). From the above considerations and since all of our stacks, given the construction of our stacking grid, have a well defined value for R_2 and R_3 (and thus P), we decided to use the equation 3.2 instead of the t_2-t_3 relation to determine the flux of [OIII] λ4363, and consequently the t_3, for stacks with no reliable detection of this auroral line. This allow to minimize the systematic offset introduced on abundances determination (see also Section 3.3.5).

3.3.4 Defining an ff relation for [OII] auroral lines

Following the same idea of Pilyugin (2005), we can exploit the direct measurements of [OII] λ7320,7330 in our stacks to define an analogous ff relation for the [OII] auroral

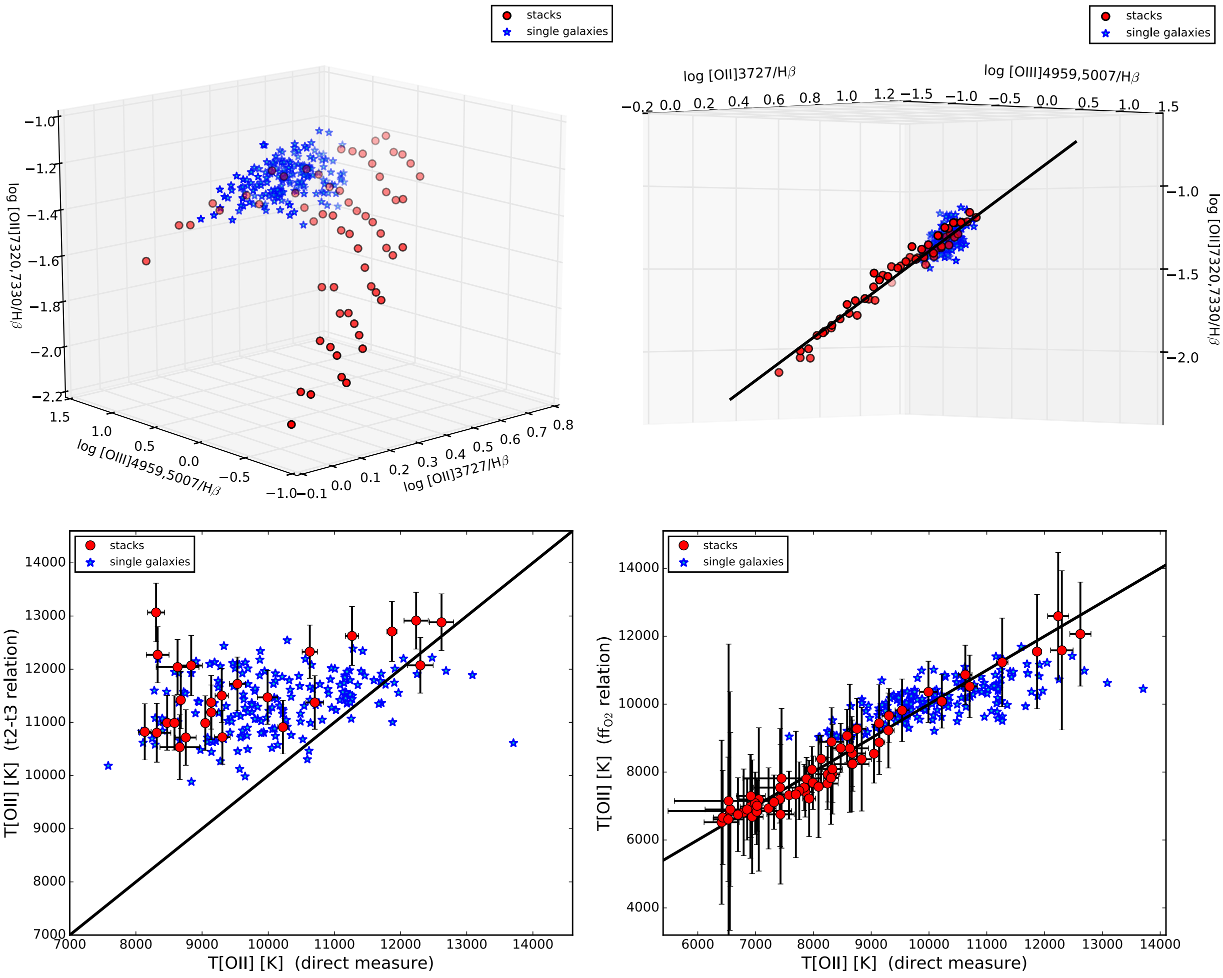

Figure 3.6: *Upper Panels* : Log [OII] λ7320,7330/Hβ as a function of log [OII] λ3727/Hβ and log [OIII] λ5007/Hβ for the sample of our stacks (red circles) and the Pilyugin et al. (2010a) galaxies (blue stars). All the points lie on a tight surface and in the right panel we show the 2-D projection that minimizes the scatter and predicts the flux of the oxygen auroral doublet from a combination of the two strong line ratios; the black line represents the linear fit which defines our new ff relation. *Bottom Panels* : T$_e$[OII] inferred through the t_2-t_3 relation (left panel) and through the ff$_{O3}$ relation (right panel) as a function of the direct measure T$_e$[OII] . Symbols are the same as in the upper panels. The equality line is shown in black in both panels.

doublet, which we will refer to as the ff_{O2} relation. Pilyugin et al. (2009) manage to obtain a similar relation for their sample of single HII regions in the low-R_3 range (i.e. $\log R_3 < 0.5$). In particular, here we search for a combination of [OII]/Hβ and [OIII]/Hβ (which define our stacking grid) that predicts the flux of the [OII] λ7320,7330 auroral doublet. Inspection of the upper panels of Figure 3.6 reveals that since our stacks appear to lie on a surface in the 3-D space defined by log[OII] λ3727/Hβ - log[OIII] λ5007/Hβ - log[OII] λ7320,7330/Hβ, we can search for the projection that minimizes the scatter in our sample and gives the combination of the first two indices that predicts the value of the latter; such a combination could be easily formalized with a linear fit, which we show as a black line in the upper right panel of the same figure. In order to better constrain the definition of our new ff_{O2} relation, we included the sample of low metallicity SDSS DR6 galaxies from Pilyugin et al. (2010a) with detected [OII] λ7320,7330; these objects lie in the upper left zone of our original diagram, which is characterized by high excitation galaxies. Even though these objects are characterized by a larger scatter than the stacks, they do not show any extreme offset from the surface defined by the stacks in the 3-D space.

The functional form of our linear fit is the following :

$$\log R_{[\text{OII}]} = -1.913 + 0.806 \log R_2 + 0.374 \log R_3 \tag{3.3}$$

where $R_{[\text{OII}]} = I_{[\text{OII}]\,\lambda 7320,7330}/I_{\text{H}\beta}$; the results of the fit is shown in the upper right panel of Figure 3.6 as the black line. The dispersion around the ff_{O2} relation is 0.04 dex for the stacks and 0.06 dex for individual galaxies.

We can test the consistency of our new ff_{O2} relation by comparing the electron temperatures predicted and those directly measured from the spectra. The bottom right panel of Figure 3.6 shows that our ff_{O2} relation predicts T_e[OII] with good precision both for the stacks (red circles) and the single galaxies (blue points), even though single galaxies show a larger scatter from the equality line (in black) as the result of their intrinsic dispersion in the plane which define the ff_{O2} relation, with a few points whose temperature predictions deviate more than 1000 K from those observed. In addition, we can also compare the temperature prediction of the ff_{O2} relation with that from the t_2-t_3 relation of equation 3.1 (applied only to stacks with direct measurement of T_e[OIII]), for which the comparison with the direct T_e[OII] is shown in the bottom left panel of Figure 3.6. Our new ff_{O2} relation clearly reproduces the observed T_e[OII] better than the t_2-t_3 relation both for our stacks and the Pilyugin et al. (2010a) galaxies, as expected given the considerations made in the previous section about how the t_2-t_3 relation underestimates the temperature of the low ionization zone when measured from global galaxy spectra. For these reasons, in this work we decided to use the new ff_{O2} relation defined by equation 3.3, instead of the t_2-t_3 relation , to infer the temperature of the low ionization zone in single, low metallicity galaxies where a direct measurement of T$_e$[OII] was not available (see Sect. 3.5).

Summarizing, temperatures are derived as follows: when both [OIII] λ4363 and [OII] λ7320 are detected, t_2 and t_3 are computed directly from the diagnostic ratios involving these auroral lines; when one of the two lines is missing, we use the relative ff relation to infer the flux of that line, compute the diagnostic ratio and derive T$_e$. We do not rely in this work on any relation, either empirically derived or based on photoionization models calculations, which links the temperatures of the different ionization zones.

3.3.5 Ionic Abundances

We have calculated the ionic abundances of O$^+$ and O^{++} for our stacks with the Pyneb version of the IRAF *nebular.ionic* routine, which determines the abundance of a ionic species given the electron temperature, electron density and the flux ratio of the relative strong emission line with respect to Hβ. We then assume that the total oxygen abundance is the sum of the two species considered,

$$\frac{\mathrm{O}}{\mathrm{H}} = \frac{\mathrm{O}^+}{\mathrm{H}^+} + \frac{\mathrm{O}^{++}}{\mathrm{H}^+} \, , \tag{3.4}$$

neglecting the contribution from O^{3+}, that can be found in highly ionized gas but it is typically minimal (Andrews & Martini, 2013). In calculating the O$^+$ abundance we used the electron temperature derived from the [OII] diagnostic ratios, while to derive the O^{++} abundance we used the electron temperature derived from the [OIII] diagnostic ratios. For stacks with undetected [OIII] λ4363 we used the ff$_{\mathrm{O3}}$ relation of equation 3.2 to infer T$_e$[OIII] and compute the O^{++} abundance of unseen ionization states. The systematic offset introduced in abundance determination is small, as we can see by comparing the total oxygen abundance inferred both from T$_e$[OIII] and from the ff$_{\mathrm{O3}}$ relation in stacks with [OIII] λ4363 detection. The mean offset in metallicity is 0.028 dex, smaller than the typical abundance uncertainty. For comparison, the t_2-t_3 relation introduces an average metallicity overestimation of 0.19 dex, as a direct consequence of the underestimation of the T$_e$[OIII]. However, since the relative contribution of the O$^+$ state is dominant in almost all the stacks, especially in the high metallicity region, the inferred O^{++} represent only a small contribution to the total oxygen abundance. This is shown in Figure 3.7, where the single ionic abundances for the O^{++} and O$^+$ species and their ratio are plotted as a function of the total oxygen abundance: a large part of our stacks above 12 + log(O/H) = 8.5 presents an O^{++} contribution to total oxygen abundance that does not exceed the $10-20\%$. The upper and middle panels of Figure 3.7 show how the O$^+$ abundance is seen increasing monotonically in our stacks with the total metallicity, while the O^{++} seems to remain constant or slightly decrease, being in any case affected by a large scatter. A very similar trend was found also by Andrews & Martini (2013) (see Figure 5 of their paper). We note that in almost all the stacks with significant contribution of the O^{++} abundance (i.e. $\geq 50\%$) we were able to measure T_e[OIII] directly. Uncertainties on ionic abundances were evaluated following the same Monte Carlo simulations used to compute errors on electron temperatures.

3.4 Tests on the method

In this work we stacked spectra of several hundreds of galaxies per bin in order to enhance the signal-to-noise ratio and detect the auroral lines needed for the application of the T_e method. Of course, physical properties like electron temperatures and metallicities inferred from stacked spectra are meaningful only if they are a good representation of the average properties of objects that went into the stack. In particular, the risk is that few objects could dominate the contribution on auroral line fluxes, thus biasing the estimate of electron temperature, and consequently of metallicity, from stacked spectra. This work is also based on the assumption that galaxies with similar values for both [OII] $\lambda 3727/H\beta$ and [OIII] $\lambda 5007/H\beta$ have similar metallicities.

In order to test our hypothesis and the stacking procedure, we took the sample of galaxies from Pilyugin et al. (2010a) with detected [OIII] $\lambda 4363$ and [OII] $\lambda 7320,7330$, and stacked these spectra in bins of [OII] $/H\beta$ and [OIII] $/H\beta$ according to our pipeline. For this analysis we considered only those bins with at least 15 objects, which namely are $0.4; 0.6$, $0.4; 0.7$, $0.5; 0.5$ and $0.5; 0.6$, as reported at the top of Figure 3.8. Furthermore, we searched for those galaxies in our original sample (described in Section 2), with detection of [OIII] $\lambda 4363$ in the MPA/JHU catalog, falling into the same bins. In particular, we selected only galaxies with [OIII] $\lambda 4363$ detected at $\geq 10\sigma$.

Temperatures and metallicities were computed for each single galaxy in both samples. The sample of Pilyugin et al. (2010a) galaxies has both the oxygen auroral lines detected, thus we were able to directly infer the temperatures and abundances of both oxygen ionic species. Since only the [OIII] $\lambda 4363$ auroral line is instead available for objects selected from the MPA/JHU catalog, we used the ff_{O2} relation of equation 3.3 to determine the flux of the [OII] $\lambda 7320,7330$ auroral doublet and compute T_e[OII] and the O^+ abundance. Then, we generated, for each bin, separate composite spectra for both samples and we measured T_e and metallicities with the T_e method from the stacked spectra.

Figure 3.8 shows the histograms of metallicity distribution of individual galaxies in each bin for the Pilyugin et al. (2010a) sample (from now on: the blue sample) and the sample selected from the MPA/JHU catalog (from now on: the red sample).

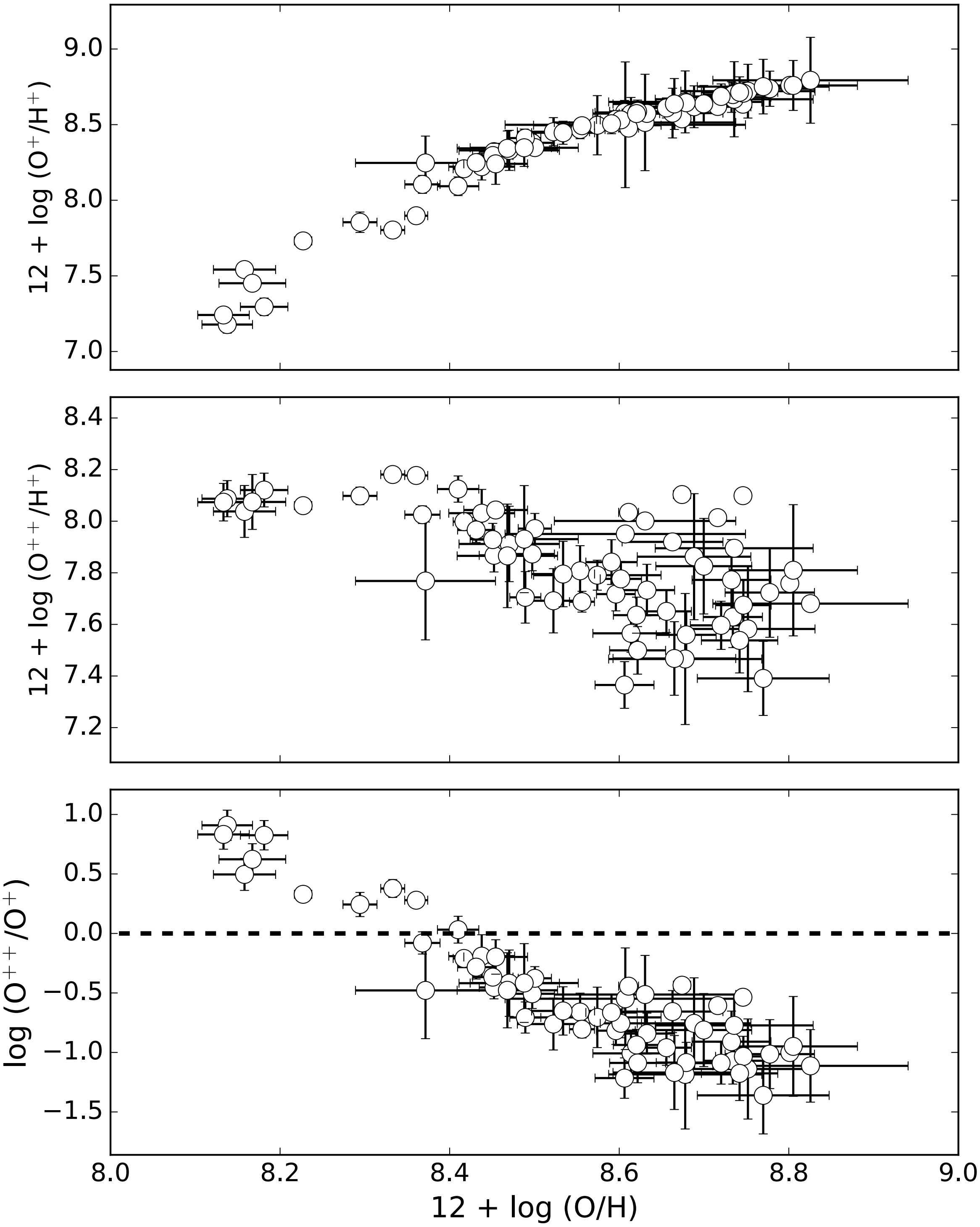

Figure 3.7: The O$^+$ abundance (upper panel), the O^{++} abundance (middle panel) and the relative ionic abundance of the two species (bottom panel) are shown as a function of the total oxygen abundance.

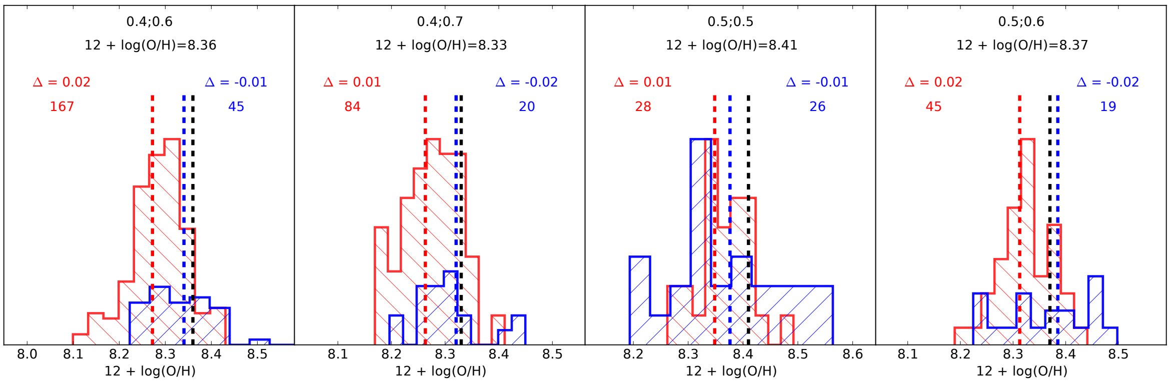

Figure 3.8: Histograms of T_e method metallicities for the subsample of galaxies selected from Pilyugin et al. (2010a) with detected [OIII] λ4363 and [OII] λ7320, 7330 auroral lines (blue sample) and for galaxies with [OIII] λ4363 detected at $> 10\sigma$ from the MPA/JHU catalog (red sample) for the 0.4; 0.6, 0.4; 0.7, 0.5; 0.5 and 0.5; 0.6 bin. The dashed lines indicate the metallicity inferred from the composite spectra obtained stacking the relative sample of galaxies. In every panel are also reported, for both subsamples, the difference between the average metallicity of the distribution and the value inferred from the associated stacked spectrum (Δ) and the number of objects per stack. The metallicity of the global stack, i.e. the stack obtained from the full sample of galaxies that fall in that bin, is written in the upper part of each panel and indicated by the dashed black line.

We note the quite small range of metallicities spanned by single galaxies in each bin, with typical dispersions of 0.1 dex, consistently with the width of our binning grid. Even though we can not perform the same test for higher metallicity stacks due to the lackness of auroral line detection in single galaxies, this corroborates the assumption that galaxies belonging to a given bin of fixed [OIII] $\lambda 5007/\mathrm{H}\beta$ and [OII] $\lambda 3727/\mathrm{H}\beta$ have similar metallicities and that we are thus stacking objects with similar properties in terms of oxygen abundance. The dashed lines in Figure 3.8 indicate instead the metallicity inferred from the associated stacked spectrum for both samples. The difference between the average metallicity of single galaxies in a given bin and the one inferred from the stacked spectrum is reported as Δ; the number of objects per bin is also written. We note that abundances estimated from stacks are well matched to the average of the metallicity distributions in every bin, with offsets being at most 0.02 dex for both samples. However, both the red and the blue sample could not be fully representative of the galaxy population inside each bin, which consist also of a large number of galaxies with no detection of auroral lines. Therefore, we compare the metallicity inferred from the stacked spectra of both sub-samples with the one derived from the global composite spectrum, i.e. the spectrum obtained stacking all the galaxies included in that bin according to the procedure described in Section 3.2. These values are reported at the top of each box of Figure 3.8 and indicated by the black dashed lines. We find good agreement between the global stack metallicity and the one inferred from the stacked spectra of the two different sub-samples, with typical offsets on average of 0.04 dex, even though we note a systematic metallicity underestimation when considering the two sub-samples with respect to the global one. This is probably due to the fact that, when creating the stacked spectra for the different sub samples, we are averaging upon the most metal poor galaxies in the bin, which in fact have the auroral lines detected. This could bias the sub-sample stacks toward lower metallicities, but this effect is smaller both than our bin size and than the average uncertainty associated to abundances measurements in our stacks. We therefore conclude that different sub-sampling criteria inside the same bin does not dramatically affect the metallicity estimation from composite spectra and therefore that stacked spectra are effectively representative of the average properties, in terms of oxygen abundance, of the objects from which they are generated.

3.5 Calibrations of strong-line metallicity indicators

In order to extend the metallicity range covered by our calibrations, we add to our stacks a sample of single galaxies with robust detection of [OIII] λ4363. We selected galaxies from our original SDSS DR 7 sample with [OIII] λ4363 detection at $> 10\sigma$, and we re-computed the oxygen abundance for these galaxies according to the procedure described in the previous Section. In particular, we derive T_e[OIII] directly exploiting the [OIII] λ4363 value reported on the MPA/JHU catalog and used the ff_{O2} relation of equation 3.3 to infer T_e[OII] and the O^+ ionic abundance. Even though a part of these galaxies, although not all of them, are already included into our stacking grid, we are able in this way to directly account for some of the most metal poor galaxies of our sample, without averaging them into the stacking bins; thus, we can better constrain the low metallicity region of our calibrations.

In Figure 3.9 we plot the relations between some of the most widely used strong-line metallicity indicators and gas-phase oxygen abundance for our full sample. In particular, we re-calibrate R_2([OII] λ3727/Hβ), R_3([OIII] λ5007/Hβ), R_{23}(([OII] λ3727+[OIII] λ4959,5007)/Hβ), O_{32} ([OIII] λ5007/[OII] λ3727), N_2([NII] λ6584/Hα) and O_3N_2 (([OIII] λ5007/Hβ)/([NII] λ6584/Hα)). Green small stars represent single galaxies, while circles represent our stacked spectra, color coded by the number of objects that went into each stack. To derive our new calibrations, we performed a polynomial fitting whose general functional form is

$$\log \mathrm{R} = \sum_{N} c_n x^n \tag{3.5}$$

where R is a given diagnostic and x is the oxygen abundance normalized to the solar value ($12 + \log(\mathrm{O/H})_\odot = 8.69$, Allende Prieto et al. 2001). Since the indicators based on the ratio between oxygen forbidden lines over hydrogen recombination lines exhibit the well-known double branch behavior, a high order polynomial fitting is required. Assuming that the uncertainty on the auroral line flux, which represents the main contribution to the error in the T_e abundances determination in our stacks, decreases as the square root of the number of galaxies, in our fitting procedure we assigned a weight equal to this value to each point representing a stack; points associated to single galaxies have been weighted as they were stacks of only one object. In this way we also avoid our fit to be dominated by the low metallicity single galaxies which are far more numerous than the stacks. In Figure 3.9 our new calibrations are shown with the blue curve and in Table 3.2 the best fit coefficients and the RMS of the residuals of the fit are reported for each of them.

We then applied each calibration to our total sample of single galaxies and stacks and computed the differences between T_e method metallicity and metallicity predicted by the calibration, in order to give an estimate of the dispersion along the log(O/H) direction, which is reported as σ in Table 3.2. For double branched diagnostics (i.e. R_3, R_2 and R_{23}) this estimate is provided only considering the metallicity range where they show monotonic dependence on log(O/H), which is reported in the *Range* column of Table 3.2. This column represents indeed the range of applicability for a given diagnostics when used as single metallicity indicator. We note that σ should not be directly interpreted as the uncertainty to associate to metallicity determination with our calibrations, since uncertainties in emission line ratios could introduce comparable errors.

Since our calibrations are build from a non homogeneous combination of single galaxies and stacks, dispersion in our diagrams is due to different contributions. In the range covered by single SDSS galaxies, it is the consequence of the intrinsic spread in a given strong line ratio at fixed metallicity and of the uncertainty on the auroral line fluxes measurement. For the high metallicity region covered by our stacks, since we are averaging on a large number of objects, the scatter due to the intrinsic dispersion should be in principle reduced. However, we must consider the effects associated with the particular choice of our stacking grid. Every stack has, by definition, a defined value of [OII]/Hβ and [OIII] /Hβ; therefore, in the R_2 and R_3 calibration diagrams the residual dispersion reflects the segregation in a given diagnostic when the other is fixed. This means that for any given value of one line ratio, different metallicities can be found varying the other one. This is particularly clear in the R_2 calibration, where different sequences for different [OIII]/Hβ values appears at metallicities above 8.2. Therefore, this diagnostic shows a clear dependence on oxygen abundance only in the low metallicity regime, revealing how most of SDSS galaxies are falling in the transition

Diagnostic	c_0	c_1	c_2	c_3	c_4	RMS	σ	Range
R_2	0.418	-0.961	-3.505	-1.949		0.11	0.26	$7.6 < 12+\log(O/H) < 8.3$
R_3	-0.277	-3.549	-3.593	-0.981		0.09	0.07	$8.3 < 12+\log(O/H) < 8.85$
O_{32}	-0.691	-2.944	-1.308			0.15	0.14	$7.6 < 12+\log(O/H) < 8.85$
R_{23}	0.527	-1.569	-1.652	-0.421		0.06	0.12	$8.4 < 12+\log(O/H) < 8.85$
N_2	-0.489	1.513	-2.554	-5.293	-2.867	0.16	0.10	$7.6 < 12+\log(O/H) < 8.85$
O_3N_2	0.281	-4.765	-2.268			0.21	0.09	$7.6 < 12+\log(O/H) < 8.85$

Table 3.2: Best fit coefficients and RMS of the residuals for calibrations of metallicity diagnostics given by equation 3.5. The σ parameter is an estimate of the dispersion along the log(O/H) direction in the interval of applicability given in the *Range* column.

zone between the two branches of this indicator. Thus, for the majority of our stacks the metallicity dependence is driven by [OIII]/Hβ, and indeed for this diagnostic the segregation in sequences of [OII]/Hβ is much less prominent.

For other indicators, the dispersion mainly reflects the scatter for a given diagnostic line ratio inside each [OII]/Hβ-[OIII]/Hβ bin. For each diagnostic the distribution of the corresponding line ratio inside our bins is generally strongly peaked, even though we are affected by different dispersions when considering different positions on our stacking grid. This means that a given line ratio, as measured from the stacked spectra, can be respectively more or less representative of the distribution of galaxies inside a given bin for different positions on the diagram. However, for every diagnostic ratio here considered, the typical dispersion of its distribution inside a given bin is of the order of 0.1 dex (or less), thus being consistent with the choice of our bin size.

In Figure 3.9 we compare our new calibrations with those from Maiolino et al. (2008). They obtained semi empirical calibrations combining direct abundance determination for galaxies from the Nagao et al. (2006) sample with metallicity estimation from theoretical models by Kewley & Dopita (2002). The two calibrations agree well, as expected, for most of the indicators at low metallicities, the main discrepancies arising in the high metallicity regime where T_e method metallicities of our stacks result lower than those predicted by photoionization models. This introduce a clear deviation in the slope in all our calibrations, that change significantly their steepness after $12 + \log(O/H) \sim 8.2$. In fact, we note that the highest metallicities inferred from our composite spectra are only slightly higher (~ 0.1 dex) than the solar value.

For the O_3N_2 and N_2 indicators we can compare our calibrations also with empirical ones from Pettini & Pagel (2004) and Marino et al. (2013), who used single HII regions and not integrated galaxy spectra to calibrate these line ratios against metallicity. Our calibrations have comparable slopes to those of Marino et al. (2013), but they present a systematic offset towards higher metallicities. This is probably due to the fact that calibrations entirely based on HII regions like Marino et al. (2013) are biased

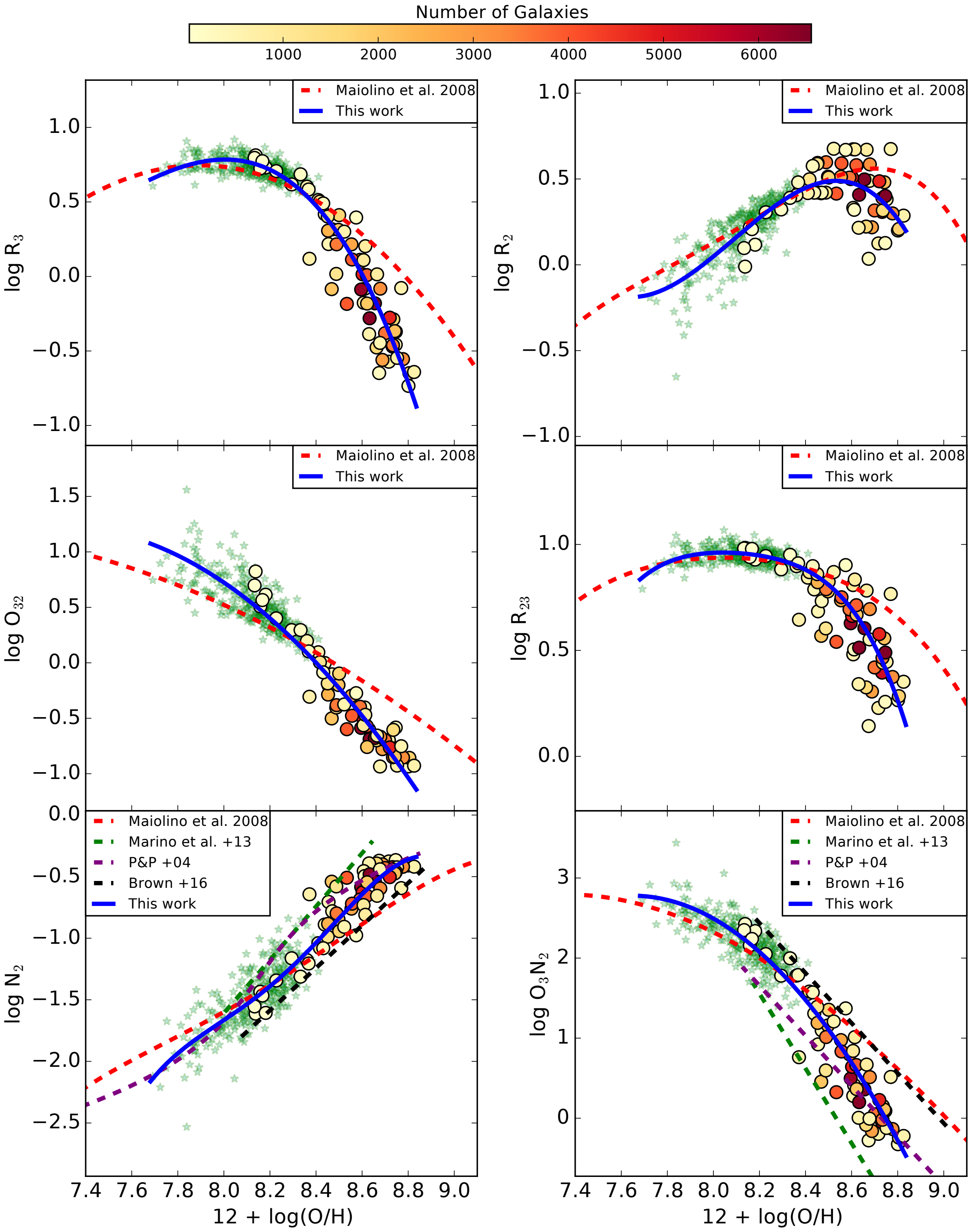

Figure 3.9: Strong Line diagnostics as a function of oxygen abundance for our full sample: small green stars represent the sample of single SDSS galaxies with [OIII] λ4363 detected at S/N > 10, while circles are the stacks color coded by the number of galaxies in each bin. Our best fit polynomial functions are shown as solid blue curves, while the dashed red line represents the Maiolino et al. (2008) semi-empirical calibrations. In the N_2 and O_3N_2 diagrams also the Pettini & Pagel (2004)(dashed purple curve), Marino et al. (2013)(dashed green curve) and Brown et al. (2016) for Δ(SSFR)=0 (dashed black curve) calibrations are shown. A publicly available routine to apply these calibrations can be found at `http://www.arcetri.astro.it/metallicity/`.

towards high excitation conditions and low metallicities. Our N_2 calibration is in good agreement with Pettini & Pagel (2004) at low metallicities but diverge, in the direction of predicting higher abundances, in the middle region. At metallicities close to solar this diagnostic begin to saturate, as expected from the fact that nitrogen becomes the dominant coolant of the ISM: the two calibrations then become comparable again. The O_3N_2 calibration instead presents a different slope than the Pettini & Pagel (2004) since the slope of their calibration is determined by the use of photoionization models at high metallicities due to the lack in their sample of HII regions with direct abundances in that region of the diagram. We note that our calibrations are better constrained to be used for integrated galaxy spectra, since single HII regions upon which most of the empirical calibrations are based on do not properly and fully cover the parameter space where many galaxies lie.

In Figure 3.9 we also compare our calibrations for the N_2 and O_3N_2 indicators with those derived by Brown et al. (2016), who derived oxygen abundances with the T_e method from stacked spectra in bins of stellar mass and Δ(SSFR), i.e. the deviation of the specific star formation rate from the star forming main sequence (SFMS) (Noeske et al., 2007). Since they include Δ(SSFR) as a second parameter in their calibrations, we decide to plot here (in black) only the curves representative of SFMS galaxies, i.e those obtained assuming Δ(SSFR)=0. In fact, our galaxy sample is distributed around their SFMS representation (see equation 6 of Brown et al. 2016), with a small median offset of 0.009 dex. Their calibrations show an offset of ~ 0.1 dex towards higher metallicities for both indicators with respect to ours. We note that our calibrations are more consistent with Brown et al. (2016) calibrations when considering their curves for Δ(SSFR)$= -0.75$.

In order to test the self-consistency of our calibrations, we applied them individually to our original sample of SDSS galaxies. Diagnostics behaving monotonically (i.e. N_2,O_3N_2 and O_{32}) can be compared over the full metallicity range spanned by our sample, to which we can straightly apply the calibration, while for those double valued we restricted our analysis to the interval given in the *Range* column of Table 3.2. Given that our R_2 calibration mostly cover the transition zone for such indicator in our SDSS galaxy sample (i.e. for $12 + \log(O/H) > 8.2$), we decide not to include it in this analysis. In each panel of Figure 3.10 and 3.11 we show the histograms of the differences in metallicity estimation between a given diagnostic and all the others. Every strong-line indicator is identified by a different colour, and in each panel the name of the reference indicator is written in the upper region. The $\Delta\log(O/H)$ is then evaluated as the difference between the metallicity probed by the reference indicator and the metallicities estimated with the other four; in each panel the average offset of

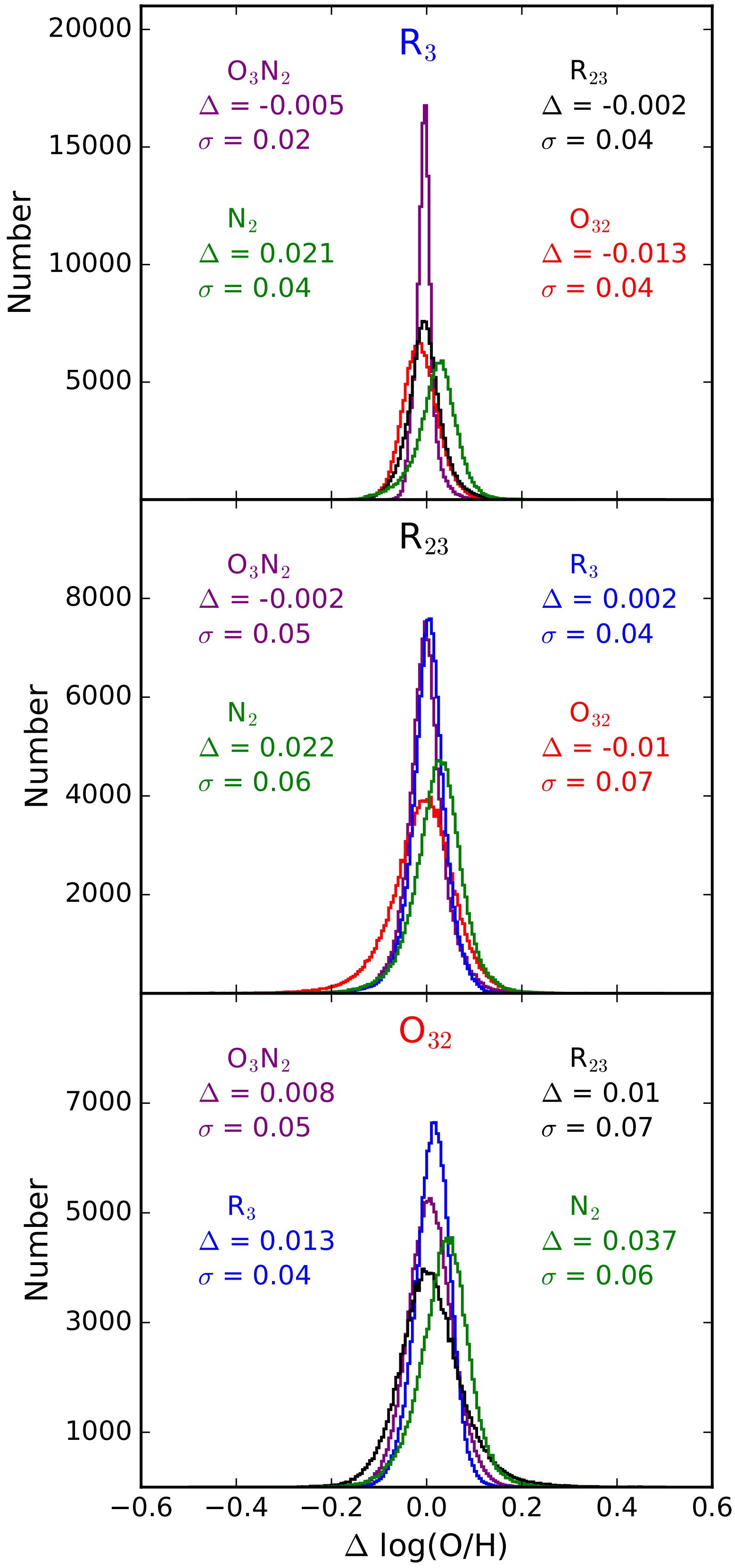

Figure 3.10: *Upper Panel* : Histograms of the difference between metallicities of the SDSS galaxies derived with the R_3 calibration and through the other diagnostics. Each diagnostic is identified by a different color: blue for R_3, red for O_{32}, black for R_{23}, purple for O_3N_2 and green for N_2. The average offset and sigma of the Δ(O/H) distributions is written for every diagnostic with the associated color. *Middle Panel* : Same as Upper Panel, with R_{23} as reference diagnostic. *Bottom Panel* : Same as Upper Panel, with O_{32} as reference diagnostic.

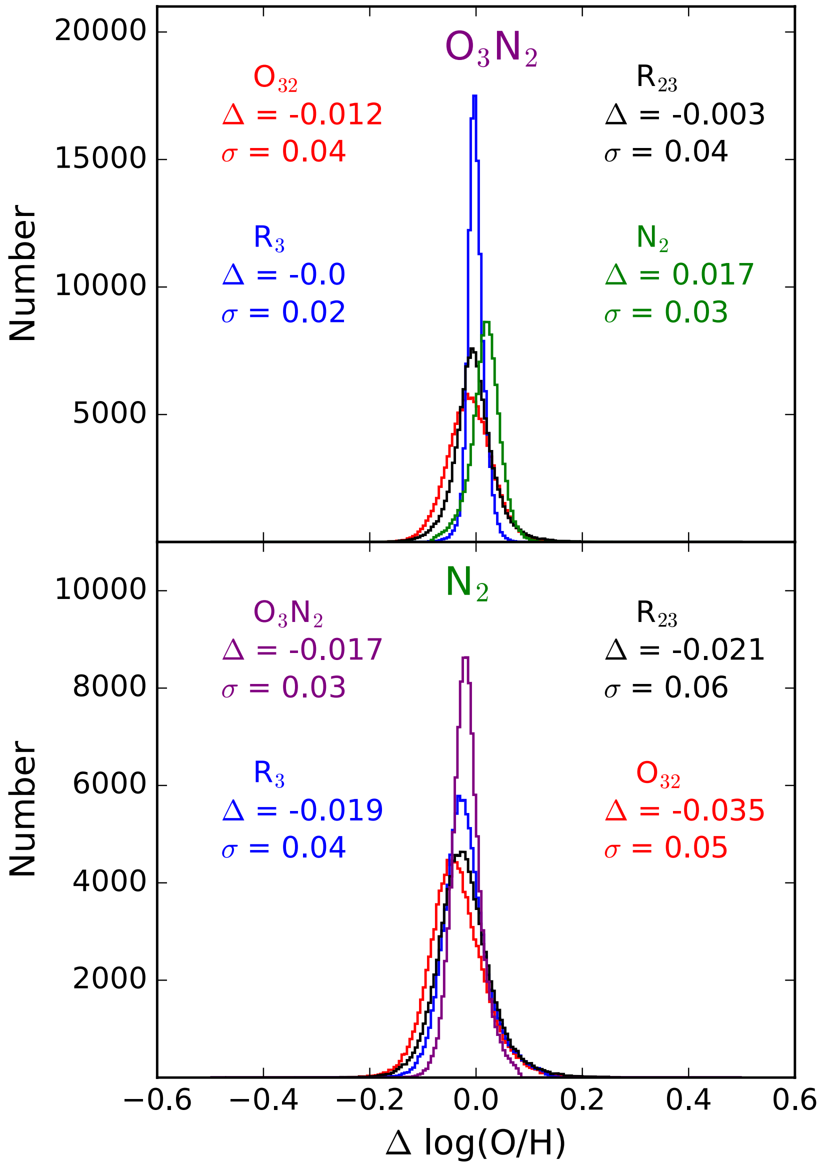

Figure 3.11: *Upper Panel* : Same as Upper Panel of Figure 3.10, with O_3N_2 as reference diagnostic. *Bottom Panel* : Same as Upper Panel of Figure 3.10, with N_2 as reference diagnostic.

the Δlog(O/H) distribution and the associated σ are reported.

Inspection of the different panels of Figures 3.10 and 3.11 reveals that metallicities probed by different indicators are in good agreement among each other, with average offsets below 0.04 dex and typical dispersions below 0.1 dex. The little systematic metallicity overestimate reported for the O_{32} indicator and underestimate for the N_2 indicator with respect to the others can be accounted for as a product of the fitting procedure. In this sense, the use of higher order polynomials allow to straighten the consistency of all our calibrations, since it minimizes the mutual disagreement between metallicity determined with different indicators. Thus, Figures 3.10 and 3.11 show that consistent metallicities are obtained in individual galaxies when using different calibrations, allowing to compare for example abundances obtained from diagnostics located in different spectral regions.

From the above considerations, we can say that our calibrations represent a self consistent set totally based on the T_e metallicity scale. This is important since at the present time there is not an established absolute abundance scale for galaxies. Most of the calibrations found in literature either rely on the assumptions of photoionization models or are based on individual HII regions metallicities. In the first case the metallicity scale defined by models is inconsistent with the T_e scale. In the second case the emission lines properties of HII regions differs from those of integrated galaxy spectra and higher excitation conditions affect T_e abundances estimation towards lower values. Until the number of high metallicity galaxy with detected auroral lines will increase, allowing to build fully T_e method calibrations based on samples of individual objects, our stacking technique represents a valuable approach to define T_e based calibrations. However, it should be stressed that metallicity estimates obtained from these calibrations are always affected by the particular choice of the stacking procedure. For example, the Brown et al. (2016) calibrations from stacked spectra in bins of stellar mass and Δ(SSFR) rely on a particular parametrization of the local star forming main sequence and their metallicity predictions could differ from ours despite the fact that abundances are evaluated with the T_e method in both cases.

In this work we chose to re-calibrate the strong-line diagnostics relying only on the values assumed by galaxies on particular emission line ratios, thus assuming only the validity of the strong-line-methods to infer metallicity from spectra of star forming galaxies. In this way our calibrations could be in principle applied to a great variety of cases, in particular to large IFU galaxy surveys that allow spatially resolved abundance studies (e.g CALIFA, Sánchez et al. 2012, MaNGA, Bundy et al. 2015 or SAMI, Croom et al. 2012). In such cases for example, the use of our calibrations allows to relax the assumption that scaling relations well assessed on global scales (e.g. the M-Z and the M-Z-SFR relations) still hold on smaller, local ones.

3.6 Summary

We provided new and totally empirical calibrations for some of the most widely used strong-line diagnostics for the determination of oxygen abundance in star forming galaxies. These relations have been derived combining a sample of single low metallicity galaxies together with the stacking of more than 110 000 galaxies of the SDSS in bins of 0.1 dex in the log [OII] $\lambda3737/\mathrm{H}\beta$ - log [OIII] $\lambda5007/\mathrm{H}\beta$ diagram, just assuming that galaxies with such similar strong line ratios also show similar metallicity (i.e. assuming the validity of the so called Strong Line Method). The increase in signal-to-noise ratio provided by the stacking procedure allowed us to detect and measure both the [OIII] λ4363 and [OII] λ7320, 7330 auroral lines necessary to compute electron temperatures of the different ionization zones and apply the T_e method for measuring metallicity on the full range of metal abundances spanned by galaxies in the SDSS survey. Here are summarized our main results :

- We found evidence for [Fe II] contamination of the [OIII] λ4363 auroral line in high metallicity stacks (Figure 3.3) . This is one of the crucial lines for the application of the T_e method for abundances estimation, thus we recommend care in using this line as electron temperature diagnostic when detected in high metallicity (12 + log(O/H) $\gtrsim$ 8.3) galaxy spectra.

- We analysed the relations between electron temperatures of different ionization zones, finding that our stacks do not follow the established t_2-t_3 relation for HII regions (Figure 3.4) . They show instead better agreement with a relation that correlates auroral and nebular line fluxes ($\mathrm{ff}_{\mathrm{O3}}$ relation). Exploiting the direct detection of the [OII] λ7320, 7330 auroral doublet in all of our composite spectra, we provided a new relation (the $\mathrm{ff}_{\mathrm{O2}}$ relation) for the determination of the flux of this auroral line (Figure 3.6).

- We then analysed the relations between some of the most common strong line diagnostics and oxygen abundance in order to obtain a reliable calibration (Figure 3.9). Our global sample allowed us to construct a set of calibrations, spanning more than 1 dex in metallicity, which are based on the uniform application of the T_e method for oxygen abundances estimation on global galaxy spectra. All our calibrations are therefore defined, over their whole range, on a consistent absolute T_e metallicity scale for local star forming galaxies. The scatter around the best fitting calibration varies between 0.05 and 0.15 for different indicators.

- Comparing our new calibrations with different ones from literature reveals how our calibrations deviate significantly both from empirical ones based on HII regions and from theoretical ones based on photoionization models, especially at high metallicities. In fact, we find that our most metal rich stacks have oxygen abundance significantly lower than those predicted by models, and at most 0.14 dex higher than the solar one (i.e. $\sim 1.4\ Z_{\odot}$). On the other hand, classical empirical calibrations obtained from HII regions samples generally show lower metallicities for fixed line ratios, probably due to the fact that the single HII regions used for those calibrations are somehow biased towards high excitation conditions in order to ensure auroral line detection at high metallicity.

- We applied our calibrations to the original sample of SDSS galaxies. Metallicity estimates from different calibrations result in good agreement between each other, with typical average offsets lower than 0.04 dex and dispersions of the order of 0.05 dex. We do not find any systematic effect of metallicity overestimate or underestimate between the different diagnostics. Thus, our calibrations represent a self consistent set that could be used in a variety of different cases depending on the availability of emission lines.

3.7 Appendix: The mass-metallicity-star formation rate relation in the local Universe

As a first application of the new set of calibrations of metallicity diagnostics, we can derive a new mass-metallicity relation and investigate its possible secondary dependences on star formation rate in the local Universe, for the original SDSS sample presented in Sec. 3.2. This section will be expanded to be part of a future paper (Curti et al., in prep.)

We required galaxies to be classified as star forming, and that they belong to the redshift interval z $\in$ [0.027,0.27], to ensure the presence of the [O II]λ3727 emission line. We apply a SNR threshold of 3 on Hβ, [O II]λ3726,3729, [O III]λ5007 and [N II]λ6584, and of 15 to Hα. We also discarded all galaxies with inferred E(B-V) (from Balmer decrement) higher than 0.7. This reduce the total analyzed sample to 153,411 galaxies.

To compute the metallicity, we use a combination of three independent indicators among those presented in Fig. 3.9, involving both oxygen and nitrogen emission lines, namely R23, O32 and N2; using a slightly different combination like R3, R2 and N2 does not produce appreciable statistical differences (however, a more in-depth analysis on the systematics introduced in the metallicity determination by the use of different set of diagnostics will be discussed in Curti et al., in prep.).

An MCMC is run to sample the log(O/H) distribution, at each step minimizing the chi-square defined simultaneously by the 3 diagnostics as :

$$\chi^2 = \sum_i \frac{(F_{\mathrm{obs}_i} - R_i)^2}{\sigma^2_{\mathrm{obs}} + \sigma^2_{R_i}} \ , \tag{3.6}$$

where $\mathrm{F}_{\mathrm{obs}_i}$ are the observed line ratio while R_i are the value predicted by the calibration for a given metallicity. Both the uncertainty on the observed line ratio σ_{obs} and the intrinsic dispersion of calibration σ_{R_i} are taken into account in the procedure. All line ratios have been preliminary corrected for reddening (via Balmer decrement and assuming a Calzetti et al. 2000 law), so extinction is not a free parameter in the procedure. Once computed the log(O/H) posterior distribution, its median value is then assumed as the inferred metallicity and the 1σ confidence intervals define the associated uncertainties.

We then sort the sample in 0.1 dex stellar mass bins and compute the median and standard deviation of the metallicity distribution in each bin; we limit the analysis only to those bins including at least 100 galaxies.

This median mass-metallicity relation is parametrized with the functional form proposed by Zahid et al. (2014a) :

$$12 + \log(\mathrm{O/H}) = \mathrm{Z}_0 + \log\left(1 - \exp\left(\frac{M_\star}{M_0}\right)^\gamma\right) . \tag{3.7}$$

In this model, Z_0 is the metallicity at which the relation saturates: it quantifies the asymptotic upper metallicity limit (see also Moustakas et al. 2011); M_0, instead, is the characteristic turnover mass above which the metallicity asymptotically approaches the upper metallicity limit, Z_0. At stellar masses $\mathrm{M}_\star < \mathrm{M}_0$, the MZR reduces to a power law with an index γ. We fit our median MZR relation with the above functional form using the python-based LMFIT package (Newville et al., 2014); the data are inverse variance weighted and the errors are propagated through to the fit parameters. The best-fit parameters with associated errors are given in Table 3.3. Upper panel of Figure 3.12 shows the density histrogram of the SDSS sample in the stellar mass vs metallicity diagram, color coded by the galaxy number density in each region. White points are the median metallicities in stellar mass bins, while the red curve represents the best-fit MZR according to the functional form of equation 3.7. The solar abundance (8.69, Allende Prieto et al. 2001) is marked in orange.

Our median MZR asymptotes at 12+log(O/H) = 8.77 (i.e. 1.2 times the solar abundance) and has a turnover mass at 9.212, consistent with previous estimates by Zahid et al. (2014a); however, our MZR is characterized by a weaker slope of the low-mass region with respect to previous findings in the literature (e.g. Andrews & Martini 2013; Zahid et al. 2014a). In fact, the overall agreement with the Andrews & Martini (2013) MZR (derived from T_e metallicity measurements from stacked spectra in bins of stellar mass) is quite remarkable for $\log(\mathrm{M}_\star) \gtrsim 9$, while the two relations deviate at lower masses. Our median MZR presents considerable differences in slope and normalization, as expected, from the MZRs derived with theoretical strong-line calibrations.

In order to assess the presence of secondary dependence on star formation rate, we sorted the sample in 0.1 dex bins of stellar mass and 0.25 dex in SFR and sSFR, and computed the median metallicity in each bin; in this case, we limit the analysis only to those bins including at least 30 galaxies. Figure 3.13 shows the various mass-

Z_0	$\log(M_0)$ [$M_\odot$]	γ
8.769 ± 0.003	9.212 ± 0.007	0.367 ± 0.008

Table 3.3: Best-fit parameters for the MZR derived with the new set of calibrations on the SDSS galaxy sample.

metallicity relations, color coded for each value of SFR and sSFR. The fit to the median MZR is reported in black, while grey contours encompass the 1σ dispersion from the median MZR in each mass bin. A clear segregation is visible both in SFR and sSFR, with highly star forming galaxies characterized by lower metallicities with respect to low star forming galaxies at fixed stellar mass. Interestingly, at low masses the slope of the different MZRs is not constant and shows a dependence on SFR: this may have implications in the definition of the projection of minimum scatter of the FMR (see Sec. 1.3.2), which may be SFR-dependent. The tightness of the observed secondary dependence also strongly decrease in the high mass regime (i.e. above $\log(M_\star) \gtrsim 10$), where all the different MZRs flatten; a mild intersection between the different curves is also visibile, which could suggest an inversion in the nature of the metallicity-SFR dependence, or descend from low-SFR mass-metallicity relations characterized by lower turnover masses. However, we know that the strength of this effect could also be strongly dependent both on sample selection effects and on the choice of the metallicity diagnostic.

All the material presented in this last section represents the very preliminary outcome of a work still in progress at the time of writing; a more comprehensive discussion about the issues briefly discussed above will be provided in a forthcoming paper (Curti et al. in prep).

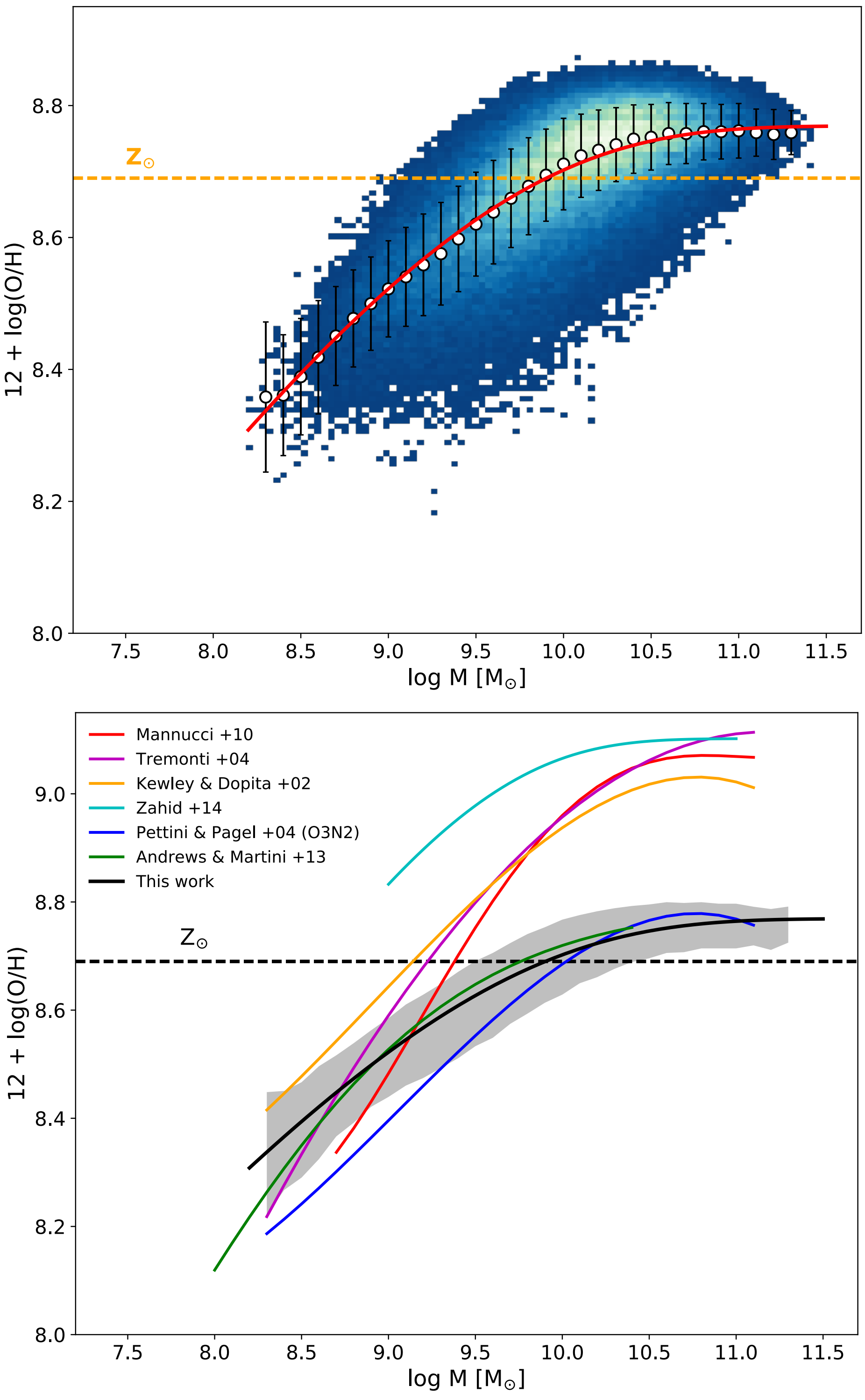

Figure 3.12: *Upper Panel*: Mass-metallcity relation for the SDSS sample, as derived with our new set of calibrations. The density histrogram of the SDSS sample in the stellar mass vs metallicity diagram is shown, color coded by the galaxy number density in each region. White points are the median metallicities in stellar mass bins, while the red curve represents the best-fit MZR according to the functional form of equation 3.7. The solar abundance value is marked in orange. *Bottom Panel*: Comparison between the mass-metallicity relation derived in this work (in black) and different predictions of the MZR from the literature, obtained with a variety of method and calibrations, both based on photoionization models (Kewley & Dopita (2002); Tremonti et al. (2004); Mannucci et al. (2010); Zahid et al. (2014b)) and anchored to the T_e abundance scale (Pettini & Pagel (2004); Andrews & Martini (2013)). Grey contours encompass the 1σ dispersion from our median MZR in each mass bin.

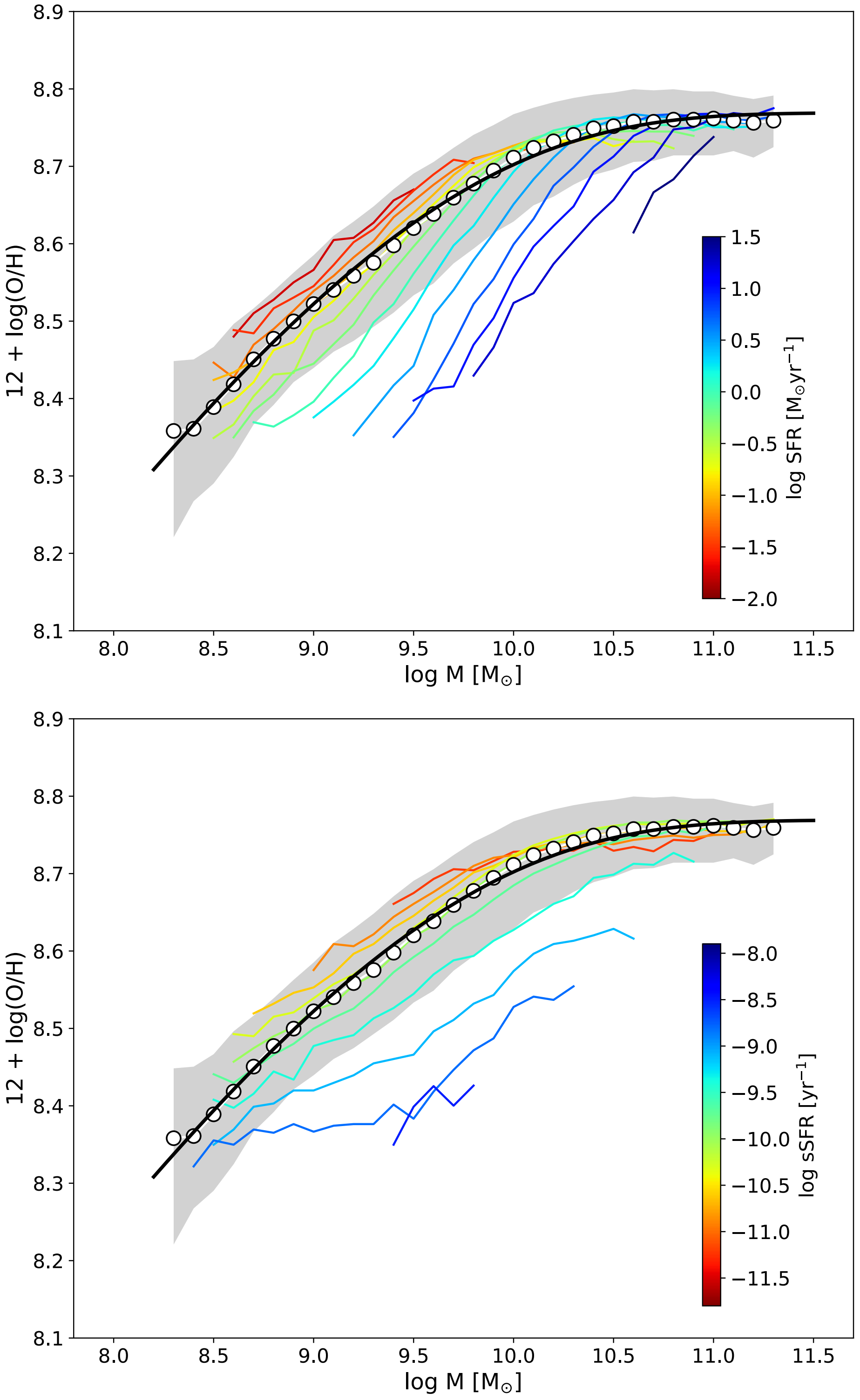

Figure 3.13: Mass-metallicity relations for different values of star formation rate (*upper panel*) and specific star formation rate (*bottom panel*). The secondary dependence of the MZR on SFR is clearly visible in the low mass regime, while disappearing for low-SFR (low-sSFR) galaxies after the turnover mass.

4 Metallicity gradients in high redshift galaxies from near-infrared integral field spectroscopy

This Chapter mainly reproduces the draft of a paper intended to be submitted to MNRAS as: Curti, M., Williams, R. J., Maiolino, R., Cresci, G., Mannucci, F., Marconi, A. et al. *The KLEVER Survey: Spatially resolved metallicity maps and gradients in a sample of 1.2<z<2.5 lensed galaxies* (2017, in prep). I was in charge of KMOS data reduction, emission line fitting and de-lensing procedure for the RXJ2248 cluster. Then, I performed the scientific analysis of the metallicity maps and gradients for the entire sample.
In a companion paper of the KLEVER collaboration (Williams, R. J., Maiolino, R., Curti, M. et al. *The KLEVER Survey: Exploiting lensed galaxies to investigate the gas excitation mechanisms in high-z galaxies*, 2017, in prep.), we investigated the main drivers of the observed offset of high-z galaxies in the classical BPT diagrams: I analyzed the BPT diagrams for nearly half of the sample (i.e. for galaxies belonging to RXJ2248) and contributed to the general scientific interpretation of the results, which are briefly summarized in Appendix 4.6; the spatially resolved BPT diagrams for the entire analyzed sample are also reported in the same Section.

4.1 Introduction

During the epoch characterized by the peak of the cosmic star formation history (i.e. $1.5 < z < 3$, which is often referred to as the *cosmic noon*) galaxies were experiencing dramatic transformations affecting their morphology and dynamics. The enhanced star formation activity, regulated by the interplay between cosmic gas accretion, merger events and gas outflows due to stellar and AGN winds, was responsible for the the bulk of the cosmic evolution of galaxies (Davé et al., 2011a). All these processes also left a clear imprint on the content of heavy elements (i.e. metals) in the interstellar medium (ISM) and their spatial distribution across a galaxy (Davé et al., 2011b). Measuring gas-phase metallicity (which we refer henceforth only as metallicity) at those epochs therefore provides unique insights on the history of the baryonic cycling and its influence on the evolution of galaxies.

The existence of scaling relations between metallicity and intrinsic galaxy properties, like stellar mass (i.e. the mass-metallicty relation, MZR, Tremonti et al. 2004, Andrews & Martini 2013 and many others) have been assessed through the years on global scales thanks to the advent of large astronomical databases such as the Sloan Digital Sky Survey (SDSS). These relationships have been further investigated also at higher redshifts to seek for clues of a possible cosmic evolution and set tighter constraints on galaxy evolution models. Several evidences of an overall decrease in metallicity at fixed stellar mass have been found from deep observational campaigns conducted in the near-infrared both from space and ground-based facilities (e.g. Erb 2006, Maiolino et al. 2008, Mannucci et al. 2009,Zahid et al. 2011, Cullen et al. 2014, Steidel et al. 2014,Sanders et al. 2015b, Guo et al. 2016).

Moreover, evidences of more tight link between stellar mass, metallicity and star formation rate (the Fundamental Metallicity Relation, FMR) have been suggested first by Mannucci et al. (2010) and then revised by different authors (e.g.Cresci et al. 2012; Salim et al. 2014; Zahid et al. 2014a). This tight relation has been interpreted as a consequence of a long lasting equilibrium between gas accretion, mass growth, metal production and outflows of enriched material. Galaxies are thus found to lie on a surface in the 3D space defined by these three quantities, and the observed MZR just follows from a 2D-projection of this distribution on the $M_\star$ vs log(O/H) plane. Despite numerous confirmations (e.g., Richard et al. 2011; Belli et al. 2013; Salim et al. 2014), and a variety of theoretical frameworks explaining the existence of such relations (e.g. Lilly et al. 2013, Dayal et al. 2013, Hunt et al. 2016, Davé et al. 2017), its possible cosmic evolution is currently debated (Wuyts et al. 2014, Sanders et al. 2015b).

With the increased availability of multi-object spectroscopic and integral field instrumentation, both from space and ground based facilities, many studies have also turned to investigating the spatial distribution of metals inside galaxies, assessing the presence of radial variations in the chemical enrichment level. Tracing the evolution of these metallicity gradients across the cosmic epochs is a crucial benchmark for theoretical models aimed at describing the relative contribution that star formation, gas flows and feedback processes play in driving galaxy evolution. Although relatively well characterized in the local Universe, their properties still remain so far very poorly constrained at higher redshifts. Locally the large majority of spiral galaxies exhibit negative metallicity gradients, with inner regions more chemically enriched with respect to the outskirts of galactic discs; this follows observationally from the spectroscopic analysis of HII regions (Zaritsky et al., 1994; Kewley et al., 2010; Bresolin, 2011), as well as from IFUs observations (Sánchez et al., 2014; Ho et al., 2015; Belfiore et al., 2017) and from abundance measurements in individual young stars in very nearby galaxies (Kudritzki et al., 2015; Gazak et al., 2015; Bresolin et al., 2016). This is generally interpreted as indicative of the so called inside-out growth scenario of galaxy formation. Indications of flattening gradients beyond a certain radius may indicate the presence of radial mixing processes or (re)accretion of metal-enriched gas in the outer regions (Bresolin et al., 2012). Merger events could also play an important role in flattening metallicity gradients (Kewley et al., 2010; Rupke et al., 2010b,a).

The situation is, on the contrary, much less defined at high-z, where diverse and sometimes contradictory results have been reported in the literature so far (e.g. Swinbank et al. 2012; Queyrel et al. 2012; Stott et al. 2014; Jones et al. 2013; Wuyts et al. 2016; Leethochawalit et al. 2016). This could be mainly ascribed to the intrinsic challenges in obtaining reliable measurements of metallicity gradients at high-z, due to the lack of angular resolution (Yuan et al., 2013) and to uncertainties affecting metallicity diagnostics (especially at high redshifts). If the latter problem is still now a source of large systematics, the former could be addressed and partly mitigated thanks to modern observational techniques exploiting new adaptive optics systems, the magnification provided by the gravitational lensing effect, or even a combination of the two. Several metallicity gradients measurements are now becoming available also thanks to multi-IFU instrumentation like KMOS, with surveys targeting hundreds of galaxies in different redshift ranges (e.g. Stott et al. 2014; Wuyts et al. 2016). However, a typical seeing of about 0.6", which roughly correspond to ~ 5kpc at z ~ 2, does not allow us to properly resolve the inner structure of high-redshift galaxies, especially for low mass ones. As previously stated, adaptive optics assisted observations could greatly enhance the spatial resolution down to ~ 1kpc (Swinbank et al., 2012), which can be further improved targeting gravitationally lensed sources (Jones et al., 2010a,b, 2013; Leethochawalit et al., 2016). Space-based grism spectroscopy from HST has also been recently used to infer sub-kpc resolution metallicity maps and gradients (Jones et al., 2015b; Wang et al., 2017), which are however affected by poor spectral resolution. Despite these efforts, high angular resolution measurements of metallicity gradients are still scarce in terms of statistical significance. Moreover, the large majority of the studies conducted so far relies only on a limited number of emission line detections, with metallicity estimates that could therefore suffer from potential biases due to the different physical properties of high redshift galaxies with respect to the local samples used to calibrate the abundance diagnostics.

In this Chapter we investigate metallicity gradients in a sample of gravitationally lensed galaxies at $1.2 < z < 2.5$ by exploiting some of the first data from the KLEVER survey, an ESO Large Programme which take advantage of the high multiplexing and IFU capabilities of KMOS, combined with multi-band observations. The KLEVER observational strategy allow us to keep a good compromise between spatial resolution (boosted by the lensing effect) and statistical strength of the sample, with the addition of an unprecedented diagnostic power given by the simultaneous detection of multiple emission line ratios. Here we present the results from the analysis of the first observations carried out in the program. We derive spatially resolved metallicity maps using different diagnostics, assess the presence of metallicity gradients and their correlation with other galaxy properties. We also discuss our findings in light of some of the last predictions from chemical evolution models and simulations.

4.2 Observations and Data reduction

4.2.1 Sample and observing strategy

KLEVER (Kmos LEnsed galaxies Velocity and Emission line Review) is an ESO Large Program conducted with the multi-object near-IR integral field spectrograph KMOS on the VLT (Sharples et al., 2013), aimed at investigating spatially resolved kinematics, dynamics and properties of the ionised gas in a sample of ∼ 100 galaxies at $1.2 < z < 2.5$. The survey is designed to provide a full near-IR wavelength coverage of the sample by observing each target in 3 different bands (namely YJ, H and K), thus allowing us to detect and map the entire set of optical rest-frame nebular lines, which constitutes a unique and powerful diagnostic tool to characterize the physical conditions of galaxies at these cosmic epochs. Targets have been selected to fall in specific redshift ranges in order to have either Hβ+[O III] in the J band, Hα+[N II]+[S II] in the H band and [S III] in the K band or [O II] in the J band, Hβ+[O III] in the H band and Hα+[N II]+[S II] in the K band, as well as to avoid, as much as possible, OH sky line contamination. The survey targets both gravitationally lensed galaxies within well studied cluster fields from the CLASH (Postman et al., 2012) and FRONTIER FIELDS (Lotz et al., 2017) programs, as well as unlensed galaxies in the southern CANDELS fields UDS, COSMOS and GOODS-S.

This work includes KMOS observations of 29 lensed sources from the first available pointings in KLEVER, targeting the clusters RXJ2248 and MS2137-2353 (Fig. 4.1);

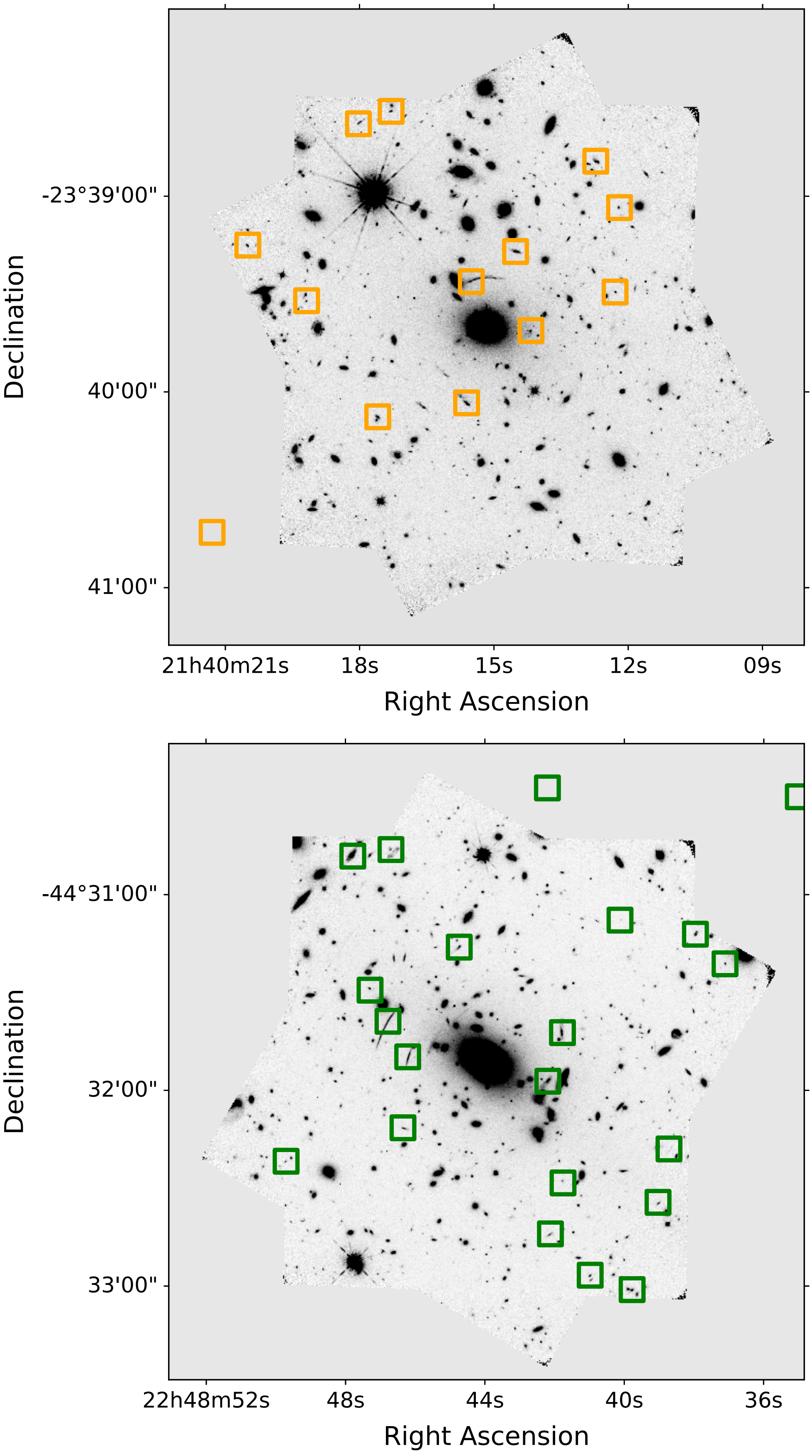

Figure 4.1: *HST* images in the broad band F160W filter of the MS2137 (*upper panel*) and RXJ2248 (*bottom panel*) clusters. The colored squares superimposed mark the position of deployed KMOS IFUs targeting the high redshift sources analysed in this work.

Galaxy	R.A.	Dec.	z(Hα)	OB. Date	*J*-Band	*H*-Band	*K*-Band
SINFONI							
Horseshoe *(Western arc)*	11:48:32.7	19:30:03.5	2.383	Jan13-May14	-	[O III]+Hβ	Hα+[N II]+[S II]
Horseshoe *(South+western arc)*	11:48:32.7	19:30:03.5	2.383	Apr-Jun09	-	-	Hα+[N II]+[S II]
MACS0451	04:51:57.3	00:06:19.7	2.014	Oct-Nov12	[O II]	-	Hα+[N II]+[S II]
MACS0451	04:51:57.3	00:06:19.7	2.014	Oct11-Nov11	-	[O III]+Hβ	-
SGAS	11:11:24.2	14:09:02.7	2.138	Feb13-Mar14	-	[O III]+Hβ	Hα+[N II]+[S II]
A68/HLS115	00:37:09.2	09:09:04.5	1.560	Oct13	[O III]+Hβ	Hα+[N II]+[S II]	-
CSWA64	02:32:49.8	-03:23:26.6	2.530	Nov14-Jan15	[O II]	[O III]+Hβ	Hα+[N II]+[S II]
KMOS							
SP1	21:40:18.0	-23:38:37.8	1.393	May-Sep15	[O III]+Hβ	Hα+[N II]+[S II]	-
SP2	21:40:12.7	-23:38:49.3	2.242	May-Sep15	[O II]	[O III]+Hβ	Hα+[N II]+[S II]
SP3	21:40:14.5	-23:39:17.0	1.264	May-Sep15	[O III]+Hβ	Hα+[N II]+[S II]	[S III]
SP5	21:40:12.3	-23:39:29.4	2.014	May-Sep15	[O II]	[O III]+Hβ	Hα+[N II]+[S II]
SP6	21:40:19.2	-23:39:32.1	2.488	May-Sep15	[O II]	[O III]+Hβ	Hα+[N II]+[S II]
SP7	21:40:17.6	-23:40:07.7	1.652	May-Sep15	[O III]+Hβ	Hα+[N II]+[S II]	-
SP13	21:40:15.5	-23:39:26.3	1.495	May-Sep15	[O III]+Hβ	Hα+[N II]+[S II]	-
SP14	21:40:14.2	-23:39:41.2	1.495	May-Sep15	[O III]+Hβ	Hα+[N II]+[S II]	-
SP15	21:40:15.6	-23:40:03.4	1.496	May-Sep15	[O III]+Hβ	Hα+[N II]+[S II]	-
PH2594	21:40:17.3	-23:38:34.0	1.348	May-Sep15	[O III]+Hβ	Hα+[N II]+[S II]	-
PH3729	21:40:12.2	-23:39:03.5	1.429	May-Sep15	[O III]+Hβ	Hα+[N II]+[S II]	-
PH3912	21:40:20.5	-23:39:15.1	1.327	May-Sep15	[O III]+Hβ	Hα+[N II]+[S II]	-
PH6532	21:40:21.3	-23:40:43.1	2.071	May-Sep15	-	[O III]+Hβ	Hα+[N II]+[S II]
PH8073	21:40:10.6	-23:41:37.7	1.238	May-Sep15	[O III]+Hβ	Hα+[N II]+[S II]	[S III]
GLASS_00093-99-99	22:48:46.701	-44:30:46.27	1.4321	May-Sep16	[O III]+Hβ	Hα+[N II]+[S II]	-
R2248_LRb_p1_M3_Q4_58__2	22:48:42.213	-44:30:27.38	1.4204	May-Sep16	[O III]+Hβ	Hα+[N II]+[S II]	-
MUSE_SW_462-99-99	22:48:41.781	-44:31:42.39	1.4290	May-Sep16	[O III]+Hβ	Hα+[N II]+[S II]	[S III]
GLASS_00333-99-99	22:48:40.130	-44:31:07.90	1.4288	May-Sep16	[O III]+Hβ	Hα+[N II]+[S II]	-
R2248_LRb_p3_M4_Q3_93__1	22:48:37.966	-44:31:12.21	1.4853	May-Sep16	[O III]+Hβ	Hα+[N II]+[S II]	[S III]
R2248_MR_p1_M1_Q4_10__1	22:48:35.016	-44:30:30.07	1.4315	May-Sep16	[O III]+Hβ	Hα+[N II]+[S II]	-
R2248_LRb_p3_M4_Q3_94__1	22:48:37.116	-44:31:21.29	2.0669	May-Sep16	[O II]	[O III]+Hβ	Hα+[S II]
GLASS_01845-99-99	22:48:40.984	-44:32:56.75	2.3024	May-Sep16	[O II]	[O III]+Hβ	Hα
MUSE_SW_45-99-99	22:48:42.125	-44:32:44.08	1.2696	May-Sep16	[O III]+Hβ	Hα+[N II]+[S II]	[S III]
MUSE_SW_461-99-99	22:48:42.199	-44:31:57.29	1.4289	May-Sep16	[O III]+Hβ	Hα+[N II]+[S II]	[S III]
MUSE_NE_111-99-99	22:48:46.358	-44:32:11.56	1.3978	May-Sep16	[O III]+Hβ	Hα+[N II]+[S II]	[S III]
GLASS_00800-99-99	22:48:46.787	-44:31:38.91	1.2284	May-Sep16	[O III]+Hβ	Hα+[N II]+[S II]	-
MUSE_NE_23-99-99	22:48:44.742	-44:31:16.18	1.2279	May-Sep16	[O III]+Hβ	Hα+[N II]+[S II]	[S III]
R2248_MR_p1_M1_Q4_59__1	22:48:47.796	-44:30:48.28	1.4271	May-Sep16	-	Hα+[N II]+[S II]	-

Table 4.1: The full sample of galaxies analysed in this work. The systemic redshift reported is derived from the Hα detection in the integrated spectra. The main emission lines detected in our sources from the integrated spectra are reported for each observed band; a '-' denotes that either no observations were available in that band or observations in that band were available, but we did not detect any emission line.

spectroscopic redshifts used for the target selection were previously obtained with the VIMOS spectrograph at the VLT, as part of the CLASH-VLT survey (Rosati et al., 2014). Each lensed galaxy belonging to RXJ2248 have been observed for a total exposure time on source of 11 hours (3h in the YJ band, 3h in H and 5h in K respectively), while galaxies from MS2137-2353 have been observed in total for 13.1 hours (4.2 in YJ, 4.5 in H and 4.4 in K band respectively) . In KMOS observations, we adopted a ABA nodding (with dithering) strategy for sky sampling and subtraction. From the KMOS observations of the two clusters, as mentioned above, we obtained an almost full near-IR coverage in J,H and K band, spanning respectively the 1.025 – 1.344 μm, 1.456 – 1.846 μm and 1.34 – 2.46 μm wavelength windows. The average seeing of the observations (as inferred from reference stars placed in three KMOS IFUs) ranged between 0.5-0.6 arcsec.

In addition, a small sample of 6 strongly lensed galaxies, observed with the integral field spectrograph SINFONI within previous programs and/or collected from the ESO archive, is included. This sample consists of sources part of galaxy-galaxy lensing systems or lensed by galaxy clusters. Three galaxies were observed as part of some of our previous programs: SDSS J114833+193003 (also known as the *Horseshoe*), MACS J0451+0006 (MACS0451) and SGAS J111124+140901 (SGAS). Unfortunately, due to scheduling constraints, we could not get the entire sample observed in all the three (J,H,K) required bands. Seeing-limited mode observations were performed with a PSF ranging between 0.4 to 0.9 arcsec. The SINFONI 0.125 arcsec x 0.25 arcsec pixel scale was adopted. We also include additional lensed galaxies observed with SINFONI in multiple bands and available on the ESO archive. In particular, we included A68/HLS115 and SDSS J0232-0323 (also know as CSWA64). This brings the total sample analyzed in this work to 35 galaxies. The complete list of targets with the observing log is reported in Table 4.1.

4.2.2 Data Reduction

The SINFONI data reduction, after the removal of cosmic rays from raw data using the “L.A.Cosmic” procedure (van Dokkum, 2001), involved the latest version of the ESO-SINFONI pipeline to perform the flat fielding, wavelength calibration and reconstruct a non-sky subtracted cube for each observation, in which the pixels were resampled to a symmetric angular size of 0.125” x 0.125”. We next implemented the sky subtraction technique from Davies (2007) to perform a better removal of the residual OH airglow emission lines from the data. We corrected for the atmospheric absorption and instrumental response using a telluric standard star, which also provides the flux calibration, before finally combining all the single observation blocks (OBs) to produce a final science cube.

The data obtained from KMOS were reduced with the latest available version of the KMOS pipeline provided by ESO. We implemented the avanced sky subtraction technique from Davies (2007) as well as the sky-stretch algorithm, which stretches the sky-cube in order to align the sky lines visible in it to those appearing in the object-cube. The stretching is a relatively high degree polynomial (whose order can be set by the user), and allows to remove the residuals from the first correction. The final datacubes were then reconstructed onto a 0.1” x 0.1” pixel scale (see. Chapter 2 for more details on cube reconstruction procedure).

To properly align and combine the single exposures within each OB, as well as the observations belonging to different OBs, three IFUs (i.e. one for each KMOS detector) were devoted to observe bright continuum sources; we exploited the relative position of these bright stars' centroids in each exposures to compute the shifts to apply to the scientific sources, having care to apply to each galaxy the offset computed from the star observed on the same detector. The final cubes have been created through a sigma-clipping average.

4.3 Analysis

4.3.1 Emission line fitting

We performed the emission line fitting on the original datacubes, which sample the image plane of each galaxy. We spatially smoothed the datacubes with a Gaussian kernel of $0.3"$ arcsec FWHM (below the average seeing of the observations, i.e. $\sim 0.5" - 0.6"$) to increase the signal to noise ratio (SNR) of the weakest emission lines that we aim to detect and map in our galaxies (e.g. [N II]$\lambda 6583$, [S II]$\lambda 6717, 6731$ and Hβ). The stellar continuum is often weak or even undetected in the large majority of our targets, thus we included only a power-law component to account for continuum emission in each band. All the emission lines of interest were fitted with single Gaussian components. The Hα, [N II] and [S II] lines were jointly fit by linking their velocity and width, as well for [O III] and Hβ; [O II] doublet is fitted with two Gaussian components. When available, the [S III] doublet is fitted with two Gaussian components linked in velocity and width as well. Moreover, the [O III]$\lambda\lambda 4959, 5007$ and [S III]$\lambda\lambda 9068, 9532$ doublets were fixed in flux ratios to their relative Einstein spontaneous transition coefficients. We choose to keep the fitting procedure within each band self-consistent: we do not link the line widths between different bands because of the different KMOS resolving powers (namely 3582, 4045 and 4227 in the center of YJ, H and K band respectively); velocities were not linked as well to avoid any systematic introduced by possible absolute calibration offsets between the three bands. The SNR was estimated for each emission line on the total integrated line flux. We note here that Hα and [O III]$\lambda 5007$ are not only always detected in the integrated spectrum, but even spatially resolved in more than 90% of the sample. Thanks to gravitational lensing magnification we were able to detect on single pixel basis even [N II] and Hβ in a large number of galaxies, allowing the application of different diagnostics to infer spatially resolved physical quantities like gas-phase metallicity. When also the [S II] doublet is detected and resolved, a larger number of diagnostics becomes available. In Table 4.1 the set of emission lines detected in each band (from the integrated spectra) is reported for each source in the sample.

After the fitting procedure is completed, all the emission line maps are mapped back into the Source Plane of the galaxy after converting them to surface brightness units, which is the physical quantity conserved by gravitational lensing.

4.3.2 Lens Modeling and Source Plane reconstruction

In order to reconstruct our emission line maps on the Source Plane, we have to rely on lens models that describe how the foreground mass (either a single galaxy or a cluster) has re-distributed the light from the background galaxy on the sky. As previously mentioned, our sample includes some strongly lensed galaxies observed with SINFONI: Horseshoe and CSWA64 are galaxy-galaxy lens systems, while MACS0451 is lensed by a foreground cluster. For the Horseshoe galaxy, which forms an almost complete Einstein ring on the image plane, we start from V-band HST observations and build our model assuming an elliptical power law with external shear. Following the forward modeling technique we create a galaxy in the source plane which we then lens into the image plane using a trial lens model, before comparing the results with the HST image. This procedure is repeated at each step of a MCMC analysis to find the best fit values for model parameters that reproduce HST data. The same technique is applied to model the CSWA64 lensed galaxy, using the available data from the ESI imager on KECK II telescope. From the resulting lens mass models we can compute the deflection maps that we subsequently use for source plane image reconstruction. These maps define the deflections ($\mathit{\Delta}$x,$\mathit{\Delta}$y) for a given pixel located at the (x,y) position in the image plane, that we can apply to calculate the exact position of that given pixel in the source plane. For MACS0451, which is lensed by a cluster, we use the multiply imaged system to constrain the model so that the multiple images all refer to the same position in the image plane. We assume a singular isothermal sphere mass profile with an elliptical power law with external shear for the cluster. We then use this model to create deflection maps which give the x and y deflections for every spaxel in the HST image.

For galaxies observed with KMOS, which belong to well studied clusters as part of the CLASH program (Postman et al., 2012), we exploit the already available deflection maps provided by the CLASH collaboration, based on assuming a Pseudo Isothermal Elliptical Mass Distributions for the galaxies and an analytical elliptical-NFW dark matter halo, primarily centered on the BCG(s) (Zitrin et al., 2015). Since the deflection maps are modeled from the HST images, we first align our SINFONI or KMOS surface brightness emission line maps to the HST images, by exploiting the H band continuum maps, and then rescale the IFU data to match the HST pixel size (i.e. 0.065"/pixel). In those cases for which we do not have any clear continuum detection in our datacubes, we align the emission peak of the strongest line observed in the H-band (i.e. Hα or [O III]) to the peak in the HST H-band image, hence assuming in these cases that the latter is dominated by emission lines. After applying the deflections provided by lensing models, we define a regular grid on the source plane whose pixel size is chosen to allow a proper sampling of the source plane PSF: for example, for KMOS data we choose to apply a resampling factor of 0.5 to the original HST pixel size, so that the final pixel size of our reconstructed images on the source plane is 0.032"/pixel (we recall the KMOS data is originally sampled on a 0.1"/pixel scale). We finally compute, at any given location on the source plane, the mean surface brightness of that area via nearest-neighbor interpolating the deprojected values, in order to reconstruct a complete and "continuous" source plane surface brightness map for each emission line of interest. An estimate of the total magnification factor μ is computed during the delensing procedure, by evaluating the ratio of the total Hα flux in the image plane to the total Hα flux in the source plane: these values are reported in Table 4.2.

The delensing procedure has a non negligible effect also on the size and shape of the PSF, which appears more sheared and stretched on the source plane. To take into account this effect we modeled the original PSF (both from KMOS and SINFONI) on the image plane from the observations of the standard stars; the average FWHM of our seeing-limited KMOS observations is ~ 0.5" – 0.6". We apply the deflection maps to the seeing limited PSF image to reconstruct the PSF shape on the source plane and fit an ellipse to properly model the de-projected PSF. The typical source plane resolution obtained for our sample is of the order of 1.5 – 2 kpc.

From now on we refer to the forthcoming analysis as conducted, except where noted otherwise, on source plane emission line maps, where the spatial distribution of physical properties in our galaxies can be related to proper physical distances, shapes and sizes, allowing the determination, for example, of meaningful metallicity gradients.

4.3.3 Stellar Mass and Star Formation Rate

Stellar masses and SFRs in our sample were derived as discussed in the following. As previously mentioned in Section 4.2, the galaxies observed with KMOS are distributed around the two clusters MS2137-2353 and RXJ2248, which are among the clusters observed as part of the HST-CLASH program. Photometric measurements were extracted from the HST images provided by the CLASH collaboration using SExtractor, to perform SED-fitting on the galaxies belonging to our sample. Stellar masses were then obtained using the high-z extension of the MAGPHYS program da Cunha et al.

(2015), assuming a Chabrier (2003) IMF and exploting the Bruzual & Charlot (2003) models. Similarly, for the Horseshoe, we used the available HST images in multiple bands to carry out the SED-fitting and derive the stellar mass. For the remaining four SINFONI galaxies we use the stellar masses provided in the literature, after a proper scaling (when needed) to the same IMF adopted by da Cunha et al. (2015). In detail, the stellar mass for MACS0451 is taken from Richard et al. (2011), SGAS from Wuyts et al. (2012), A68 from Sklias et al. (2014) and CSWA64 from Kostrzewa-Rutkowska et al. (2014). All the derived stellar masses take into account the magnification factor.

The total SFR is calculated using the extinction corrected total Hα emission flux, converted to SFR assuming the Kennicutt (1998) relation and applying a scaling factor of 1.7 to convert to a Chabrier (2003) IMF. Reddening correction have been obtained from the Balmer decrement assuming an intrinsic ratio of Hα/Hβ = 2.86 and a Cardelli et al. (1989) extinction law. For some of our galaxies Hβ is weakly detected on resolved spatial scales, therefore we cannot produce a reliable E(B-V) map to correct the Hα on a spaxel by spaxel basis. Therefore, we inferred a global E(B-V) value from the total Hα and Hβ fluxes and applied it to all spaxels, hence assuming that the extinction does not change dramatically across the galaxy. The resulting, de-lensed SFRs are reported in Table 4.2 in units of $M_{\odot}$ yr^{-1}. The SFR values of two galaxies, SGAS and A68, are missing, since we were not able to build reliable lens models for these objects. Although in theory we could compute the Source Plane SFR converting the one derived through the observed Hα emission flux by dividing it by the magnification factor provided by different works in literature, we prefer not to do so as we wish to keep our analysis the more self-consistent as possible. Additional care also has to be taken when computing the SFR and magnification for the Horseshoe galaxy. Our IFU observations of this object only encompasses the western arc, which however are not enough to sample the entire galaxy when re-constructed in the source plane and thus to compute the total SFR. Therefore, we use additional SINFONI observation of the Horseshoe, conducted in 2009, which samples both the western arc and the southern high surface brightness peak. Then, we perform the lensing analysis on the Hα emission line map from this SINFONI observations to compute the total SFR. However, we note that only K-band observations covering the full arc are available; therefore, for the rest of the current analysis, which depends on detecting multiple emission lines in different bands, we will use only the latest SINFONI multi-band observations (from 2013 − 2014) of the western arc of this system.

4.3.4 Metallicity determination

We derive the gas-phase metallicity using a diversity of calibrated diagnostics, thanks to the broad wavelength coverage of multiple emission lines. Since for the large majority of the sources in our sample we target, detect and spatially resolve at least Hα, [N II]λ6584, [O III]λ5007 and Hβ, a combination of such emission lines is used as the standard diagnostic to create the metallicity maps. In this work we exploit the strong-line calibrations presented in Chapter 3 (Curti et al. 2017, hereinafter C17), which redefine the diagnostics from Maiolino et al. (2008) to fully anchor them to the T_e-abundance scale defined in the local Universe by the SDSS galaxies. The R_3 (i.e. log([O III]λ5007/Hβ)) and N_2 (i.e. log([N II]λ6484/Hα)) indicators are jointly used to tightly constrain the metallicity value, by minimizing the chi-square defined as :

$$\chi^2 = \sum_i \frac{(F_{\mathrm{obs}_i} - R_i)^2}{\sigma^2_{\mathrm{obs}} + \sigma^2_{R_i}} \ , \tag{4.1}$$

where F_{obs_i} are the observed line ratio while R_i are the expected value, according to the C17 calibrations, at fixed metallicity. The uncertainty on the observed line ratio σ_{obs} and the intrinsic dispersion of each calibrated indicator σ_{R_i} are both taken into account in the procedure. Since R_3 and N_2 are both unaffected by dust attenuation, no reddening correction is required at this stage. An MCMC is run to sample the log(O/H) posterior distribution, whose median value is then assumed as the inferred metallicity and the 1σ interval define the associated uncertainties. When more emission lines become available (e.g. [O II]λ3727 for z> 2 galaxies, or when [S II]λ6716,6731 is detected and spatially resolved), we can exploit different diagnostics from C17 to further constrain the metallicity determination. A few z> 2 galaxies (e.g. GLASS_01845-99-99) are affected by very poor spatially resolved detection of the [N II]λ6584 line; in those cases, we use the [O II] doublet to infer the metallicity from a combination of the R_3 and the O_{32} (i.e. [O III]λ5007/[O II]λ3727) diagnostics. We note here that, if on one side increasing the number of involved diagnostics can reduce the spread of the log(O/H) distribution and allow us to obtain more accurate metallicity estimates, one the other it may introduce the uncertainties related to the extinction correction procedure, especially when dealing with the [O II]λ3727 doublet.

As already discussed in Section 1.3.1, whether the locally calibrated diagnostics are applicable to the high-redshift Universe is still a matter of great debate. Diagnostics which are expected to be little affected by the ionization conditions of the gas (see e.g. Dopita et al. 2016) have been suggested to be valuable for high-redshift galaxies, where strong variations in ionization parameter and excitation conditions have been invoked as the main drivers of the observed offset of high-z sources in the classical

BPT diagrams with respect to the local sequence (Kewley et al., 2013; Nakajima et al., 2013; Steidel et al., 2014; Kashino et al., 2016; Strom et al., 2017). However, since they usually involve the [N II]/[O II] or the [N II]/[S II] line ratios, they are strongly dependent on the assumed relation between the N/O ratio as a function of the oxygen abundance O/H, which is affected by a large scatter and whose evolution with cosmic time and/or dependence on galaxy mass is also indicated as a possible origin of the observed evolution of emission line ratios in high-z galaxies (Masters et al., 2014, 2016; Shapley et al., 2015). Within this context, we show in a companion paper (Williams et al., in prep., see also Sec. 4.6) that an increase in N/O at fixed O/H could indeed be responsible for the observed offset in the N2-BPT for some of the KLEVER galaxies. Strong-line indicators based only on alpha-elements (like oxygen) have also been suggested as good ones for high redshift studies since galaxies at z $\sim 1.5-2.5$ seem to show no appreciable offset from local trends in oxygen based diagnostic diagrams (e.g. R_{23} vs O_{32}, Shapley et al. 2015); however, the location on the abovementioned diagram could even be sensitive to a variation in the hardening of the radiation field at fixed metallicity rather than a variation in abundances (Strom et al., 2017). In any case, at redshifts ~ 1.5 (where the majority of KLEVER galaxies observed so far lie), the lack of the [O II] doublet in the NIR bands observable from KMOS prevents us from using purely oxygen diagnostics, thus forcing us to exploit the nitrogen-based ones. When this survey will be complete it will allow us to investigate the spatially resolved behavior of z ~ 2 galaxies on the R_{23} vs O_{32} diagram in a more statistically robust manner. Nevertheless, only a fully Te-based calibration of metallicity indicators at these redshifts would be the keystone to overcome potential discrepancies; unfortunately, just a handful of robust auroral line detections have been reported so far in high-z sources (e.g. Jones et al. 2015a; Sanders et al. 2016), due to the intrinsic observational challenges in detecting these faint emissions with current instrumentation. The advent of new ground-breaking facilities like the JWST will be crucial to tackle this issue definitely in the next few years. Therefore, at the present time any result involving gas-phase metallicity measurements from strong-line calibrations at high-z should always be interpreted with full awareness of these potential caveats.

We also emphasize here that all these strong-line calibrations are valid only if the gas is photoionized by stellar continuum, with no contribution to ionisation due to AGN or shocks. We checked the possible contamination from AGN or shocks in our sample in two different ways, which are described in more detail in Williams et al (in prep.) and that we briefly summarize here. First of all, we found no clear correlation between the most deviating pixels on BPT diagrams and their relative position with respect to the central regions of the galaxy. In other words, we could naively expect

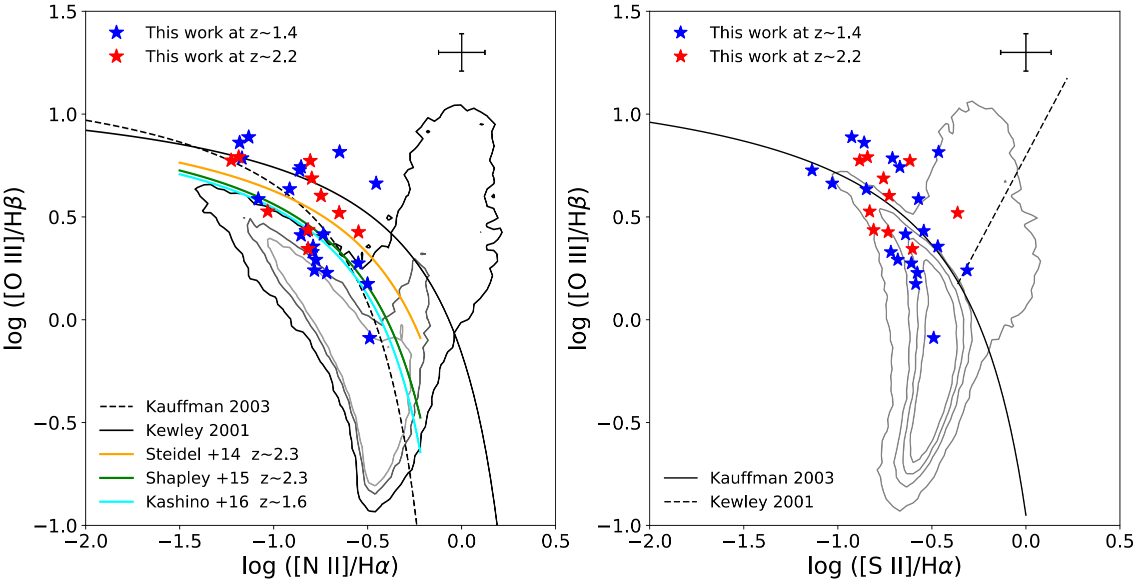

Figure 4.2: Global BPT diagrams for the KLEVER sample analysed in this work. In both panels the position of the z ∈ [1.2, 1.6] sources is marked with blue stars, while that of the z ∈ [2, 2.4] ones is marked with red stars. The theoretical demarcation line between the star forming locus and AGN/LINER galaxies from Kewley et al. 2001 and Kauffmann et al. 2003b are shown with solid and dashed black lines respectively, while the underlying grey contours encompass the distribution of SDSS galaxies. On the N2-BPT in the *left panel* a fit to the location of high redshift galaxies from the FMOS survey (Kashino et al. 2016, z ∼ 1.6), MOSDEF survey (Shapley et al. 2015, z ∼ 2.3) and KBSS survey (Steidel et al. 2014, z ∼ 2.3) is shown with cyan, green and orange lines respectively. The typical error on the emission line ratios is indicated in the upper right corner of each panel.

that those pixels which show the most AGN-like line ratios are located towards the center of the galaxy, if an AGN is the primary source of their ionisation, but this is not the case for our galaxies. Moreover, we find no significant fraction of deviating spaxels occupying the shock-like region of the [S II]-BPT, nor any clear trend between the observed BPT-offsets and velocity dispersion, as one would expect in case of shock-driven line ratios. Finally, we stacked the spectra from all the most deviating spaxels in both the [N II]- and [S II]-based BPT diagrams to look for clear spectral signatures of AGN or Wolf-Rayet contamination (like prominent He II λ4686 emission), but we did not find any evidence for that as well. Therefore, we conclude that the contribution from AGN or shocks is negligible in the majority of cases and that our metallicity determination based on emission line ratios is reliable for the purposes that we pursue in this work.

Galaxy	SFR(Hα) [$M_\odot yr^{-1}$]	log($M_\star/M_\odot$)	12 + log(O/H)	μ
Horseshoe	54.56 ± 12.0	10.18 ± 0.16	$8.48\ ^{+0.1}_{-0.11}$	9.5
MACSu	49.37 ± 2.16	9.5 ± 0.1	$8.22\ ^{+0.09}_{-0.12}$	11.7
MACSl	31.57 ± 2.16	9.28 ± 0.1	$8.22\ ^{+0.08}_{-0.1}$	11.7
CSWA	76.86 ± 1.03	9.4 ± 0.19	$8.45\ ^{+0.09}_{-0.12}$	12.6
sp1	36.28 ± 1.11	9.002 ± 0.092	$8.5\ ^{+0.11}_{-0.11}$	1.1
sp2	268.57 ± 1.32	10.29 ± 0.065	$8.33\ ^{+0.11}_{-0.12}$	1.2
sp3	59.82 ± 1.17	10.26 ± 0.075	$8.49\ ^{+0.1}_{-0.11}$	2.3
sp5	22.79 ± 0.47	9.632 ± 0.075	$8.38\ ^{+0.08}_{-0.11}$	1.7
sp6	34.71 ± 1.17	9.617 ± 0.065	$8.43\ ^{+0.08}_{-0.09}$	1.4
sp7	51.67 ± 0.59	9.957 ± 0.059	$8.53\ ^{+0.1}_{-0.12}$	1.3
sp13	3.79 ± 0.88	9.982 ± 0.0865	$8.18\ ^{+0.13}_{-0.11}$	13.9
sp14	1.93 ± 0.05	9.567 ± 0.04	$8.21\ ^{+0.16}_{-0.17}$	5.1
sp15	47.4 ± 0.69	9.982 ± 0.054	$8.42\ ^{+0.08}_{-0.09}$	2.1
ph2594	14.14 ± 0.56	9.682 ± 0.0475	$8.59\ ^{+0.11}_{-0.14}$	1.3
ph3729	13.92 ± 0.15	9.732 ± 0.1025	$8.45\ ^{+0.12}_{-0.13}$	1.3
ph3912	88.97 ± 3.87	9.292 ± 0.03	$8.16\ ^{+0.17}_{-0.14}$	1.1
ph6532	12.48 ± 0.34	9.607 ± 0.3425	$8.40\ ^{+0.11}_{-0.14}$	1.1
ph8073	58.16 ± 3.55	9.382 ± 0.2075	$8.34\ ^{+0.11}_{-0.12}$	1.0
GLASS_00093-99-99	54.92 ± 1.84	9.612 ± 0.1225	$8.34\ ^{+0.13}_{-0.13}$	1.6
R2248_LRb_p1_M3_Q4_58__2*	66.66 ± 5.16	–	$8.47\ ^{+0.11}_{-0.13}$	1.37
MUSE_SW_462-99-99	32.3 ± 1.31	10.34 ± 0.12	$8.48\ ^{+0.1}_{-0.12}$	3.17
R2248_LRb_p3_M4_Q3_93__1	165.87 ± 6.43	9.852 ± 0.08	$8.45\ ^{+0.09}_{-0.1}$	1.2
R2248_LRb_p3_M4_Q3_94__1	110.01 ± 17.74	9.762 ± 0.195	$8.48\ ^{+0.09}_{-0.1}$	1.2
GLASS_01845-99-99	71.22 ± 7.67	9.917 ± 0.115	$8.39\ ^{+0.14}_{-0.16}$	1.7
MUSE_SW_45-99-99	8.90 ± 1.37	8.397 ± 0.040	$8.37\ ^{+0.14}_{-0.17}$	1.7
MUSE_SW_461-99-99	23.81 ± 2.24	10.61 ± 0.105	$8.52\ ^{+0.1}_{-0.12}$	2.8
MUSE_NE_111-99-99*	117.93 ± 1.83	–	$8.34\ ^{+0.13}_{-0.17}$	1.9
GLASS_00800-99-99	0.69 ± 0.61	9.737 ± 0.13	$8.64\ ^{+0.07}_{-0.08}$	4.7
MUSE_NE_23-99-99	3.18 ± 1.97	9.882 ± 0.065	$8.52\ ^{+0.09}_{-0.1}$	2.4

Table 4.2: Global properties of the analyzed sample. The star formation rate in $M_\odot yr^{-1}$, the stellar mass and the metallicity derived from the integrated spectra with the C17 calibrations are reported for each source. In the last column the magnification factor is also reported, as estimated from the ratio between the image plane and source plane Hα fluxes.
Notes -* Stellar masses for R2248_LRb_p1_M3_Q4_58__2 and MUSE_NE_111-99-99 are missing at the time of writing.

4.4 Results

4.4.1 Global properties

We briefly discuss here the global properties of our sample by examining line ratios and physical quantities inferred from integrated spectra. We first show the position of our galaxies on the classical BPT diagrams in Fig 4.2: consistently with typical findings at these redshifts, they appear to be shifted from the tight sequence occupied by galaxies in the local Universe (encompassed by the grey contours as inferred from the SDSS survey). On the N2-BPT diagram, the offset is towards both higher [O III]/Hβ and [N II]/Hα, but their position is still broadly consistent, within the uncertainties, with belonging to the star forming locus as predicted by the theoretical dividing line from

Kewley et al. (2001). On the S2-BPT diagram our sample present a larger scatter around the theoretical dividing line, although the average offset is less prominent than in the N2-BPT diagram. For a more in-depth, spatially resolved analysis and discussion on the physical drivers of the BPT-offset for the KLEVER sample, we refer to Williams et al.(in prep); anyhow, a brief discussion on the main results, together with a list of spatially-resolved BPT diagrams for KLEVER galaxies, is reported in Section 4.6.

In the left panel of Figure 4.3 we plot the global SFR (as measured from Hα) as a function of stellar mass $M_\star$ for the sample analyzed in this work. For comparison, the star-forming Main Sequence (SFMS) at z = 1.4 and z = 2.2 (i.e. the mean values in the two redshift intervals probed by the KLEVER sample) from Speagle et al. (2014) and Whitaker et al. (2014) are shown as shaded regions and dashed lines respectively. Although Speagle et al. (2014) assume a Kroupa et al. (1993) IMF, converting to a Chabrier (2003) IMF introduce negligible effects. The grey shaded region represents instead the 1σ dispersion of the local SFMS from Speagle et al. (2014). Our sample of redshift-selected lensed galaxies analyzed in this work allow us to probe a lower range in stellar masses than typical mass-selected surveys, populating both the region below and, in particular, above the average SFMS for those masses at z$\sim 1.5-2$, with some galaxies which are approximately ten times more star forming than the average population at those epochs. The full KLEVER sample will comprise also a large number of more massive, unlensed sources from CANDELS fields, which are complementary to this sample for a full exploration of the Mass-SFR plane.

The right panel of Figure 4.3 shows instead the relation between stellar mass and oxygen abundance (the mass-metallicity relation, MZR) for our sample, derived through the simultaneous use of the R3 and N2 diagnostics from C17 calibrations as explained above, on the integrated emission line measurements. For comparison, the MZR derived from Andrews & Martini 2013 with the T_e method from stacked spectra in bins of stellar mass is shown with the green solid line, while in magenta we report the local MZR computed exploiting the Pettini & Pagel 2004 calibration of the O3N2 indicator. The grey shaded area encloses the 1σ spread of the median-MZR computed on SDSS galaxies with the C17 calibrations (see Sec. 3.7). For consistency, all the mass-metallicity relations shown here are based on the abundance scale defined by the T_e method. Consistently with typical findings at these redshifts, our sample is characterized by lower metallicities at fixed stellar mass with respect to the values predicted by the local MZR. In particular, the average offset from the local MZR is -0.26 and -0.30 dex for z $\sim$ 1.4 and z $\sim$ 2.2 galaxies respectively. A detailed study on the MZR within KLEVER will follow when the observations of the program are completed.

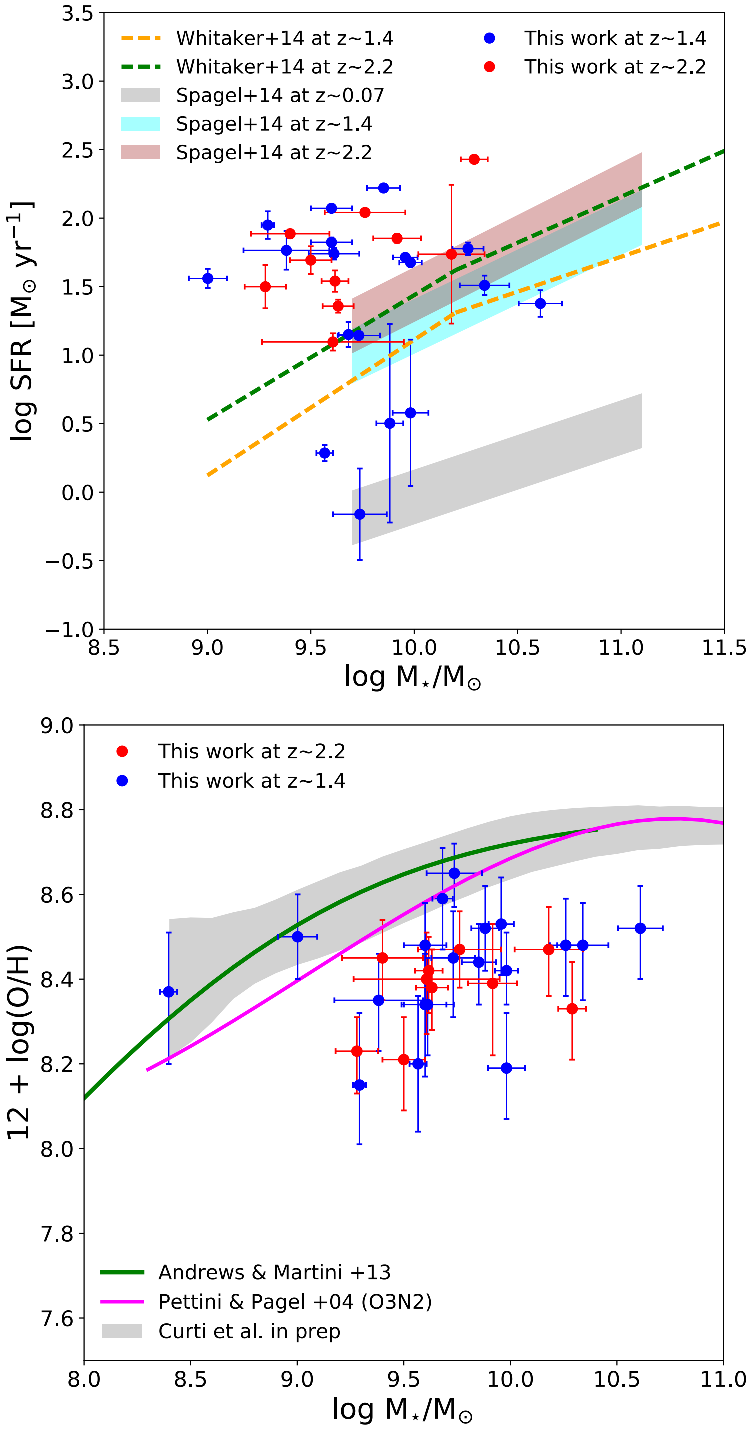

Figure 4.3: *Left Panel*: Global SFR as a function of stellar mass for the sample analysed in this work. Blue points indicate sources at $1.2 < z < 1.6$, while red points mark sources between $2 < z < 2.4$. The typical dispersion of the star-forming main sequence (SFMS) at redshift 0.07, 1.4 and 2.2 from Speagle et al. 2014 is represented by grey, cyan and brown shaded regions respectively. The fit to the SFMS at z = 1.4 and z = 2.2 from Whitaker et al. 2014 are also shown as green and orange dashed lines. *Right Panel*: Global relation between stellar mass and metallicity for our sample, derived with the C17 calibrations. For comparison, the local mass-metallicity relation (MZR) from Andrews & Martini 2013 derived with the T_e method from stacked spectra in bins of stellar mass is shown in green, while in magenta we report the local MZR computed exploiting the Pettini & Pagel 2004 calibration of the O3N2 indicator. The grey shaded region encloses the 1σ dispersion of the median-MZR computed on the SDSS sample with the C17 calibrations (see Sec. 3.7). All the metallicity measurements shown here are consistent with the abundance scale defined by the T_e method.

Galaxy	Resolved	Gradient (dex kpc^{-1})
Horseshoe	Yes	0.012 ± 0.027
MACSu	Yes	-0.005 ± 0.017
MACSl	Yes	-0.027 ± 0.017
CSWAu	Yes	0.021 ± 0.023
sp1	Yes	-0.006 ± 0.023
sp2	Yes	0.001 ± 0.038
sp3	Yes	0.016 ± 0.035
sp5	Marg	0.010 ± 0.092
sp6	Marg	0.062 ± 0.091
sp7	Yes	0.025 ± 0.036
sp14	Marg	0.041 ± 0.084
sp15	Yes	0.024 ± 0.014
ph2594	Marg	-0.038 ± 0.044
ph3729	Yes	0.007 ± 0.053
ph3912	Marg	-0.001 ± 0.077
ph6532	No	0.010 ± 0.015
ph8073	Yes	0.022 ± 0.059
GLASS_00093-99-99	Yes	0.038 ± 0.053
R2248_LRb_p1_M3_Q4_58__2	Yes	-0.005 ± 0.029
MUSE_SW_462-99-99_up	Yes	0.009 ± 0.077
MUSE_SW_462-99-99_low	Yes	0.010 ± 0.085
R2248_LRb_p3_M4_Q3_93__1	Yes	0.010 ± 0.023
R2248_LRb_p3_M4_Q3_94__1	Yes	0.045 ± 0.072
GLASS_01845-99-99	Yes	0.064 ± 0.11
MUSE_SW_45-99-99	No	0.047 ± 0.17
MUSE_SW_461-99-99	Yes	-0.031 ± 0.029
MUSE_NE_111-99-99	Marg	0.024 ± 0.096
GLASS_00800-99-99	Yes	-0.010 ± 0.057
MUSE_NE_23-99-99	No	0.00 ± 0.11

Table 4.3: Metallicity gradients with associated uncertainties for each galaxy derived from the source plane metallicity maps using the C17 metallicity calibrations. We also indicate to what degree each galaxy has been resolved following the criteria described in Section 4.4.2. “Resolved” indicates galaxies where the gradient is extracted out to a radius at least 2 times the size of the linear PSF, ’marginal’ where this radius is 1.5 to two times bigger and ’unresolved’ where it is less than 1.5 times bigger.

4.4.2 Spatially resolved metallicity maps and metallicity gradients

As previously stated, we compute the metallicity on a pixel by pixel basis from our delensed source plane emission line maps using a combination of the R_3 and N_2 indicators from C17 calibrations; moreover, for those galaxies having the required emission lines (i.e. [S II]λ6717,6731 and/or [O II]λ3727), detected and spatially resolved with enough SNR, we included more calibrated line ratios (like [O III]λ5007/[O II]λ3727) from C17 in our procedure to reduce the uncertainty in the metallicity measurement. As a general criteria, we impose a SNR threshold of 3 on the brightest emission lines for each band (i.e. Hα and [O III]λ5007) and of 2.5 on weakest emission lines (i.e. [N II]λ6584, Hβ, [S II]λ6717,6731 and [O II]λ3727). Galaxies with no spatially-resolved detection in at least [N II]λ6584 and/or Hβ are excluded from the forthcoming analysis.

To infer metallicity gradients we define the center of the galaxy as the peak of the H band continuum, or the peak of the Hα emission (hence at the peak of the SFR surface density) for galaxies with no continuum detection. Simply extracting the metallicity in circular annuli of increasing radius would not be valuable as we would be affected by the smearing effect of the distorted source plane PSF, especially at large distances from the center. Thus, to partially overcome this issue, we define a series of elliptical apertures according to shape of the source plane PSF, whose increasing radii are taken in steps of a fraction of the linear PSF size (defined as the geometric mean of the PSF ellipse, i.e. $r = \sqrt{x \times y}$, where x and y represent the FWHM along the major and minor axis respectively). From each annuli we then extract the average metallicity value; we note here that the result does not change significantly if we compute instead the average emission line ratios within each annulus and compute the metallicity from the diagnostics mentioned above. To avoid that the most external apertures are dominated by a few isolated pixels in the outskirts of the galaxy, we consider only apertures including a number of pixels covering at least the 10% of the total aperture area. We compute metallicity gradients by fitting a first order polynomial to the extracted metallicity values. The derived linear gradients for our sample are reported in Table 4.3.

A few galaxies in the sample show clear signatures of ongoing interaction. The delensed Hα map of MACS0451, for example, highlights what appears to be two separate peaks approximately $\sim$ 2 kpc apart. Further investigation conducted on the velocity field proves that this is most likely to be a galaxy pair system, as the two Hα peaks show separate rotation patterns. MUSE_SW_462-99-99 presents two clear separate peaks in the Hα emission line map as well; thus, we identify this as a pair of galaxies

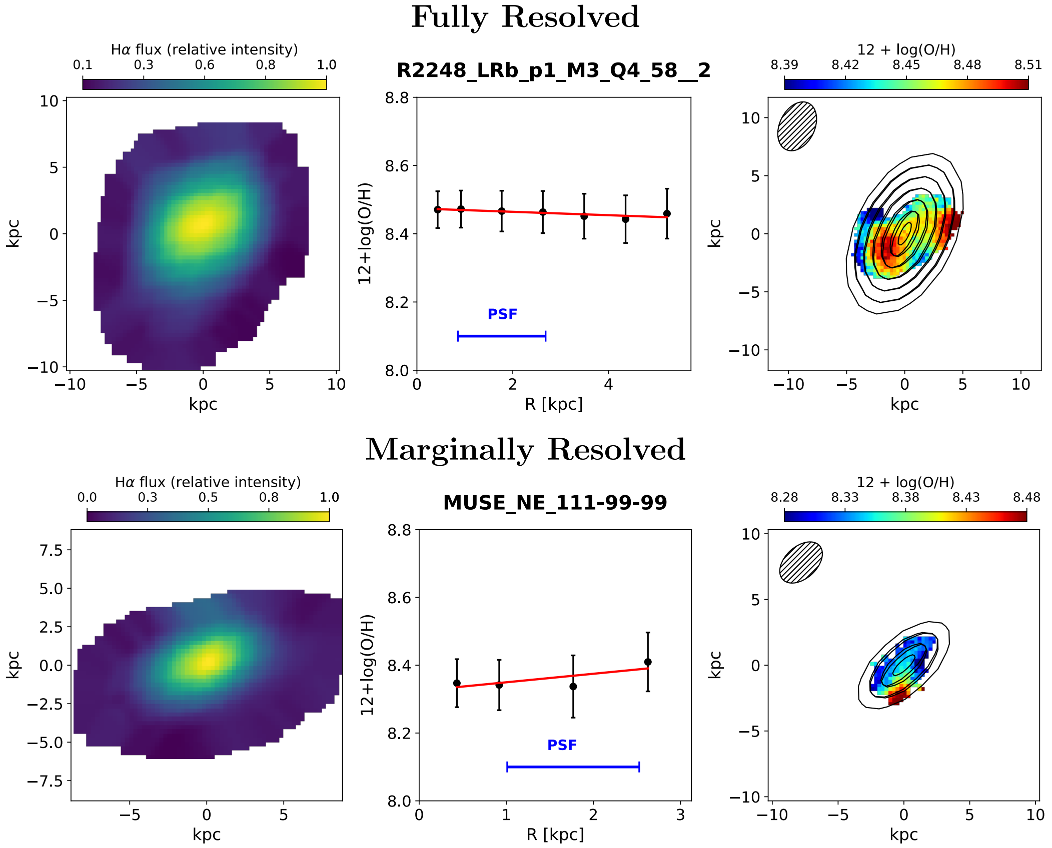

Figure 4.4: Two examples of metallicity gradients for KLEVER galaxies illustrating a fully resolved (*top* panel) and a marginal resolved (*bottom* panel) case. We show (*left*) the normalized Hα emission maps, (*middle*) the extracted metallicities at increasing radii across each galaxy, and the full metallicity map (*right*), derived using the C17 calibrations. In the *middle* panel the linear fit to the metallicity gradient (in red) and the linear size of the PSF (in blue) are also shown. The shaded black region in the *right* panel reproduce the shape and size of the PSF when mapped back into the source plane. The elliptical apertures used to derive the radial gradient overlay the 2D metallicity map.

too. For these systems, therefore, we compute two separate metallicity gradients, one for the *upper* and one for the *lower* region of the map. MUSE_SW_461-99-99 is also characterized by the presence of a separate Hα blob in the lower-right region of the map, which is not visible in the H-band HST image; since from the velocity diagram we can not definitively assess this as a merging system, we continue to analyze it a single system, however noting that it could host an interacting companion. Interestingly, the metallicity associated with the secondary Hα blob is significantly lower than that of the "core" galaxy, suggesting also that this could be due to an episode of accretion of pristine gas. This is possibly also the case for SP15, where the complex kinematics suggests a primary galaxy (associated with the Hα peak and with a clear velocity gradient) interacting with a fainter companion responsible for the redshifted Hα emission towards the north east. Also in this case, the 2D metallicity map is characterized by two regions of quite different average metallicities.

From the analysis of the source plane PSF we can set criteria to determine whether we are truly resolving the metallicity gradients or if we are affected by poor angular resolution. We claim that our gradients as fully resolved if can extract metallicities up to a radius at least twice the linear PSF size, while we consider them marginally resolved if the gradient is evaluated between 1.5 and 2 times the linear PSF. We finally classify them as unresolved if the gradient is computed within 1.5 times the linear PSF. We show an example of a resolved and marginally resolved metallicity gradient in Fig. 4.4, while the gradients and maps for the entire sample can be found in Fig. 4.8 of Appendix 4.5. The shape of the source plane PSF, as well as its linear size, are reported for each source to aid visualization.

The bulk of our galaxies show radial metallicity gradients fully consistent with being flat within their uncertainties. However, we note how the spatial distribution of metals in these galaxies is often asymmetric and characterized by the presence of irregular patterns . Therefore, although in a few cases a flat radial metallicity gradient is truly associated with a fairly homogeneous metallicity map, in most cases it is not indicative of a flat distribution but rather arises azimuthal averaging of regions with different metallicities, while a more chaotic pattern lies underneath. Therefore, we stress here that a flat radial gradient does not necessarily exclude the presence of strong spatial metallicity variations, which are indeed clearly visible in some of the 2D metallicity maps. In this sense, although azimuthally averaged gradients are still useful and commonly adopted as benchmark for theoretical predictions, only 2D resolved metallicity maps can provide the full characterization of spatial distribution of metals within a galaxy and provide key insights on the effect that physical processes occurring on local scales, such as gas infall and radial flows, have in shaping the formation of galaxy disks at these epochs. With the advent of an increasingly large number of spatially resolved observations, being able to reproduce the complex in metallicity distribution seen in many high redshift galaxies will represent the next goal for chemical evolution models and cosmological simulations.

4.4.3 Discussion

Evolution with redshift

We use our derived metallicity gradients to investigate their evolution across the cosmic time and compare the resulting trends with those predicted by chemical evolution models and simulations. In Fig. 4.5 we show a collection of radial metallicity gradients (in units of dex/kpc) from our sample and previous published works at high redshift (namely Yuan et al., 2011; Swinbank et al., 2012; Queyrel et al., 2012; Jones et al., 2013, 2015b; Stott et al., 2014; Troncoso et al., 2014; Leethochawalit et al., 2016; Wang

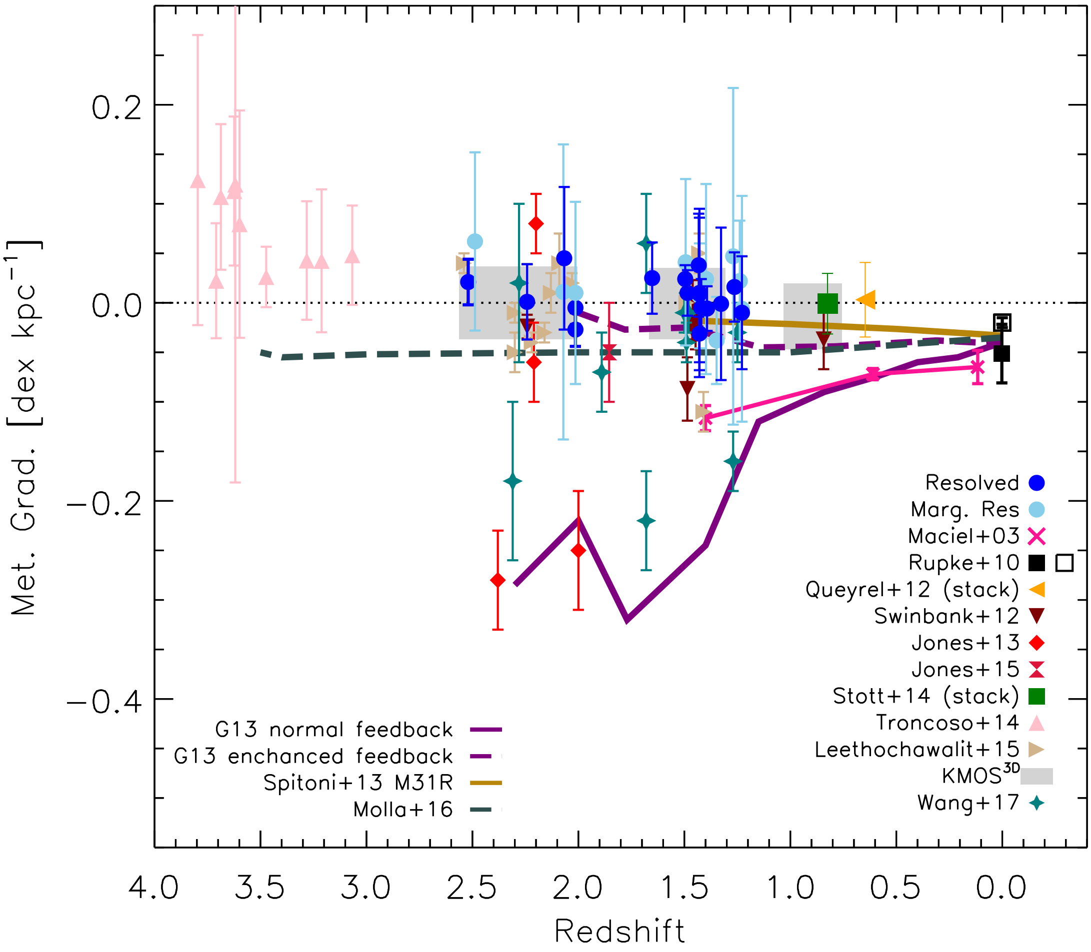

Figure 4.5: Metallicity gradients, derived for our sample of lensed galaxies using the C17 calibration, as a function of redshift; we distinguish between gradients which we claim to be resolved (blue circles) or marginally resolved (light blue circles). Some additional gradients from previous works on local and high-z galaxies (i.e. Maciel et al., 2003; Rupke et al., 2010b; Yuan et al., 2011; Swinbank et al., 2012; Queyrel et al., 2012; Jones et al., 2013; Stott et al., 2014; Troncoso et al., 2014; Leethochawalit et al., 2016; Wuyts et al., 2016; Wang et al., 2017) are included with different symbols/colors which are explained in the legend. The predictions from MUGS and MaGICC cosmological simulation reported in Gibson et al. (2013a), which tracks the evolution of a typical disc galaxy implementing two different feedback modes, are shown with a dashed purple line for the enhanced feedback scenario and with a straight purple line for the normal feedback scenario respectively. In orange, we show instead the predicted cosmic evolution of the metallicity gradient from the Spitoni et al. (2013) modeling of M31, while in dark-grey those from the chemical evolution models by Mollá et al. 2016a. Our results are consistent with little or no evolution of the metallicity gradients with redshift, in better agreement with predictions by simulations including an enchanced feedback mode.

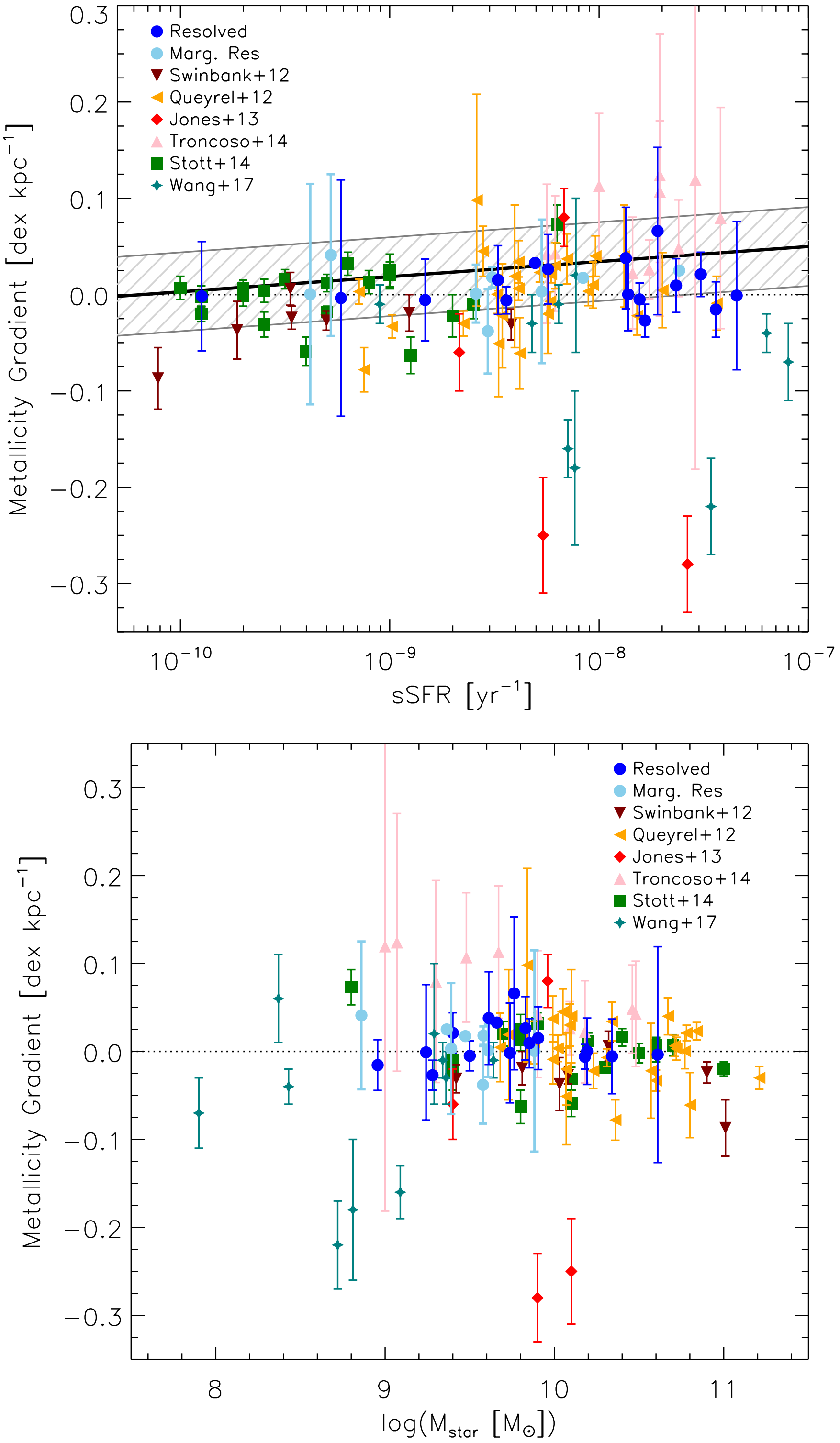

Figure 4.6: Metallicity gradients, derived using the C17 calibration for our lensed galaxies, as a function of global galaxy properties, in particular specific star formation rate (sSFR) (*Left Panel*) and stellar mass (*Right Panel*). The sample includes additional gradients from previous works on high-z sources; symbols and colors are the same as in Fig. 4.5. In the upper panel a linear fit to the data is shown in black, with 1σ uncertainty marked by the grey shaded region; the most deviating points from Wang et al. (2017) and Jones et al. (2013) have been excluded from the fit.

et al., 2017), plotted as a function of redshift. We show the gradients from KLEVER galaxies claimed as fully resolved with dark blue filled circles, while light blue circles instead represent the gradients which we deem to be only marginally resolved. For Queyrel et al. (2012) and Stott et al. (2014) measurements, we report only the average and 1σ dispersion in metallicity gradients from their samples. The grey shaded area represent instead the spread of the metallicity gradients reported from the KMOS^{3D} Survey (Wuyts et al., 2016) in 3 different redshift intervals. The average of local gradients (both for isolated and interacting systems) from Rupke et al. (2010b) and the trend of the Milky Way gradient evolution from Maciel et al. (2003) are also shown. The large majority of currently available results rely on a variety of different indicators for metallicity estimates: some are inferred only from nitrogen based diagnostics ([N II]/Hα in particular), some from purely oxygen based ones. Moreover, beside the fact that the metallicity gradients shown in Fig. 4.5 are obtained with different diagnostics, the latter are even sometimes based on different calibration methods. As previously discussed in Section 1.3.1, we here note that different calibration methods are sometimes defined on different metallicity scales: this means not only that the absolute metallicity estimates could disagree between various methods, but also that the dynamic range of possible values spanned by the calibration is often different. In general, theoretical calibrations provide a wider range of possible metallicity values with respect to T_e-based methods, even when considering the same set of strong-line ratios. Thus, although by definition every gradient estimate relies only on relative metallicity measurements, different diagnostics/calibrations can give rise, potentially, to a systematic offset in the slope of the inferred gradients. However this effect turns out to be very small in the majority of cases, thus our core results are not affected by the choice of the adopted metallicity calibration and the resulting abundance scale. Our results are in general consistent with previous investigations of metallicity gradients at these redshifts: despite the variety of observational set up, resolution, sample selection, metallicity calibration etc.. the bulk of observed star forming galaxies exhibit on average almost radially flat metal distributions between $1 < z < 2.5$.

We can compare this results with the predictions from cosmological hydrodynamical simulations presented in Gibson et al. (2013a), which traces the gas phase metallicity of disc galaxies from $z \sim 2$ to the present day under different feedback modes in the framework of the MUGS (Stinson et al., 2010) and MaGICC (Stinson et al., 2013) schemes. We show the evolutionary track for their simulated galaxy g15784 under both “normal” and “enhanced” feedback conditions. The “normal” feedback scenario, in which 10 to 40% of the energy from each supernova is used to heat the surrounding ISM, predicts steeper metallicity gradients at earlier redshifts (i.e. ~ -0.2dex/kpc) which become flatter over cosmic time. The totality of our measurements and even the largest part of those reported in the literature are inconsistent with this scenario, with just a few example of observed gradients that match its predictions at redhifts higher than 1.5 (Jones et al., 2013; Wang et al., 2017). The enhanced feedback scheme instead, where outflows re-distribute energy and re-cycle ISM material over larger galactic scales, with preferential re-accretion into the outer regions (i.e. metal re-cycling), is characterised by a milder evolution with a progressive (minimal) flattening of the metallicity gradients with increasing redshift. Our results, together with the majority of previous indications from the literature, seem to point towards this latter regime, which suggests that at high-z, stronger star formation feedback is in place causing flatter gradients due to rapid and efficient recycling of enriched gas and re-distribution of the ISM, which occurs on timescales shorter that those related to star formation and metal enrichment. In Fig 4.5 we also show the prediction for the metallicity gradient of M31 at different redshifts according to the Spitoni et al. (2013) chemical evolution model which assumes no gas threshold on star formation, an inside-out formation of the disk, constant star formation efficiency along the disk and radial gas flows. This model is entirely consistent with enhanced feedback simulation schemes in prescribing a mild steepening of the gradient with z, and nicely reproduces the trend followed by the majority of the currently available observations. Interestingly, a good matching between theoretical predictions and observed gradients can be achieved also by purely- or semi-analytical chemical evolution models (CEMs) which do not include any prescription about feedback processes mixing up the gas. The models from Mollá et al. (2016b), for example, assuming an inside-out disc growth, an ISM structured as a multiphase mix of diffuse gas and cold clouds and prescribing star formation efficiencies, stellar yields, gas infall rates and atomic to molecular hydrogen conversion factors, predict flat metallicity gradients at all redshifts within 2.5 times the effective radii in disc galaxies, with no assumption on radial gas mixing. Tidal and gravitational interactions can also strongly contribute to the flattening of the observed gradients. Among our galaxies, we also report a few examples of mildly positive, "inverted" metallicity gradients (e.g. SP6, SP7, R2248_LRb_p3_M4_Q3_94__1); previous claims of such gradients have been reported both at the same redshifts (Wuyts et al., 2016) and even at earlier epochs, mostly in seeing-limited data of unlensed galaxies (Cresci et al., 2010; Troncoso et al., 2014). They have been initially interpreted as evidence of inflows of pristine gas into the central regions of such galaxies, which both fuels new star formation episodes and dilutes the metallicity; an alternative explanation consist in considering these galaxies affected by strong feedback processes, driven by outflows that rain material from the inner regions back down in the outskirts of the galaxy (the so called 'galactic fountain' effect, Fraternali & Binney 2008; Werk et al. 2011): this effect, whose primary effect results into an average flattening of the abundance gradients, can even contribute to invert the gradient itself. However, the impact of these outflows does not seem to be powerful enough to represent the dominant contribution to such a flattening, since the measured yields are often too small (Cresci et al., 2010; Troncoso et al., 2014).

Correlation with stellar mass and SFR

Despite the lack of a clear trend in the behavior of metallicity gradients with redshift at these cosmic epochs, the sample is clearly affected by scatter in its distribution. We investigate and discuss here whether the metallicity gradients exhibit any particular correlation with global galaxy properties. starting with the SFR, as suggested by some recent investigations (e.g. Stott et al. 2014). As previously mentioned, simulations of the inside-out growth of galaxies predicts initial steep negative gradients which flatten at later times, whereas observed positive or flat gradients are predicted by simulations (e.g. Gibson et al. 2013a) as due to efficient re-accretion and gas mixing processes. In particular, the specific star formation rate (sSFR) is a measured quantity that holds information about galaxy star formation history: galaxies exhibiting high sSFR are thought to be in an early stage of their cosmic evolution, as they are constantly fuelled by inflowing gas into their central regions. One can expect thus that signatures of this process may show up also in the metallicity gradients. Stott et al. (2014) presented KMOS observations of star-forming galaxies at $z \sim 1$, combined with a collection of metallicity gradients from the literature, and find no clear correlation between metallicity gradients and stellar mass, but a positive correlation between metallicity gradients and sSFR. They show that galaxies with higher sSFR, which are possibly more subject to gas mixing and inflows, exhibit on average flatter or even positive metallicity gradients. Therefore, they suggest that the claims of positive, negative or flat metallicity gradients at different redshifts is actually driven by the different sSFR at these epochs. We can test this scenario exploiting the KLEVER metallicity gradients previously derived to extend the investigation towards higher specific star formation rates.

In the upper panel of Fig. 4.6 we plot the C17 metallicity gradients computed for our sample, along with gradients from previous works at $z \sim 1$ or higher (i.e. Swinbank et al., 2012; Queyrel et al., 2012; Jones et al., 2013; Troncoso et al., 2014; Stott et al., 2014)), as a function of sSFR. Fig. 4.6 shows that there is a high level of scatter in the observed trend. We attempt to fit a linear relation to quantify the level of correlation: this is shown with the black line, while the region including the 1σ uncertainty on the fit is indicated by the grey shaded region. We decided not to include the most steep gradients derived from Jones et al. (2013) and Wang et al. (2017) in the fit, which may constitute a different population of galaxies (or be affected by large uncertainties in the measured gradients due to low SNR, see also Sec. 5.4.4). The fit suggests that a mild correlation between gradients and the sSFR may be present, with higly star forming galaxies being characterized by flatter or positive gradients, although everything is still fully consistent with no correlation at all given the uncertainties. This is in contrast to what derived from the Stott et al. (2014) sample alone, where the slope of the relation has been found to be different from zero with a $\sim 3\sigma$ statistical significance. We note that both our study and their study do not include any local galaxy in the fit.

We investigate then whether our metallicity gradients correlates with total stellar mass in the lower panel of Fig. 4.6. The bulk of our galaxies, as well as those collected from the literature, shows no clear correlation with stellar mass. This result is thus consistent with previous claims (e.g. with the majority of KMOS^{3D} galaxies, Wuyts et al. 2016) and it is now starting to be extended also to the lower mass range probed by our sample of lensed sources. Wang et al. (2017) report a few examples of steep, negative gradients at low masses (i.e. $M_\star < 10^9 M_\odot$) from their HST grism spectroscopy survey of lensed galaxies, which deviate from the average trend of the rest of the sample. These represent the only available measured gradients so far for such low mass objects and, according to the authors, could be interpreted as a clue for the “downsizing” scenario of galaxy formation, where more massive galaxies evolve more rapidly and show therefore flatter gradients, being in a later phase of their disc assembly. However, a larger number of robust measurements at low masses is needed in order to carefully assess this picture, and forthcoming observations within the KLEVER program will contribute in increasing the statistics in this low mass regime.

Star formation rate density

We can extend the investigation on local scales by evaluating whether the SFR surface density ($\Sigma_{\rm SFR}$) correlates with metallicity on a spaxel by spaxel basis, exploiting the spatially revolved data of our survey. According to previous claims, inverted positive metallicity gradients could be ascribed to a fueling of pristine gas into the central region of galaxies that simultaneously promotes star formation and dilutes the metallicity (e.g. Cresci et al., 2010; Queyrel et al., 2012; Troncoso et al., 2014). Moreover, episodes of local accretion of metal poor gas could favor the formation of bright Hα regions associated with low metallicities and contribute explaining some of the complex morphologies seen in the metallicity maps. Recent cosmological simulations by Ceverino et al. (2016) show that in 50% of cases at redshifts lower than 4, pristine gas accretion from the cosmic web can give rise to the formation of local star-forming clumps and subsequent drop in metallicity ($\sim$ 0.3 dex) compared to the surrounding

ISM. They further assert that the accretion should be rapid enough to sustain such a metallicity drop, as the turbulence mixing would dissolve these features within a few disc dynamical timescales. In this picture, one would expect to find evidences of an anti-correlation between gas-phase metallicity and $\Sigma_{\rm sfr}$. We computed the $\Sigma_{\rm sfr}$ in our galaxies by dividing the SFR value in each spaxel by its area (expressed in kpc); this can be performed on the image plane maps, since flux surface density is conserved by gravitational lensing. Metallicities are computed for each spaxel in the image plane with the same procedure described in Section 4.3.4 adopting the C17 calibrations. We combine the results for all galaxies in the sample and show them in the $\Sigma_{\rm sfr}$-log(O/H) diagram in Fig. 4.7. The 2D histogram of the distribution of our points in the $\Sigma_{\rm sfr}$-log(O/H) plane is shown in a blue scale and overlayed in orange by the contours including 10%,50% and 75% of the distribution respectively. Purple points represent median $\Sigma_{\rm sfr}$ values with the associated dispersion in bins of log(O/H). Despite the relatively broad distribution, the existence of a mild trend can be assessed between the two quantities, with low metallicity spaxels that are characterized on average by higher $\Sigma_{\rm sfr}$ values and indirectly, by inverting the Schmidt-Kennicutt law, by a higher gas fraction. This imply that on local scales smooth gas inflow plays a role in triggering star formation while diluting the metal content of the ISM, although we do not find the observed anti-correlation to be strong as reported in previous studies of high redshift galaxies (e.g. Troncoso et al. 2014 at z ~ 3.4). This may suggest that at these epochs different mechanisms, occurring on shorter timescales than secular processes, largely contribute to the actual complexity seen in the 2D metallicity maps and may weaken the significance of the local correlation between star-formation and gas metallicity. We note of course that not all the points in this analysis are completely independent of each other due to the finite size of the PSF; thus, we can only qualitatively assess the presence of a trend between this two quantities: only the full KLEVER sample will allow a more statistically robust analysis of this correlation.

4.4.4 Conclusions

We have analysed a sample of gravitationally lensed galaxies between redshift $1.2 < z < 2.5$, observed with the SINFONI and KMOS IFUs in the framework of the KLEVER Survey. Our data provides spatially resolved information in the YJ, H and K bands, enabling us to map the almost full suite of rest-frame optical nebular emission lines. We exploit the lensing properties and a modeling of the PSF of these galaxies to obtain source plane metallicity maps with a typical resolution of $1-2$ kpc and extract radial metallicity gradients. The main conclusions drawn in this paper are summarized as follows.

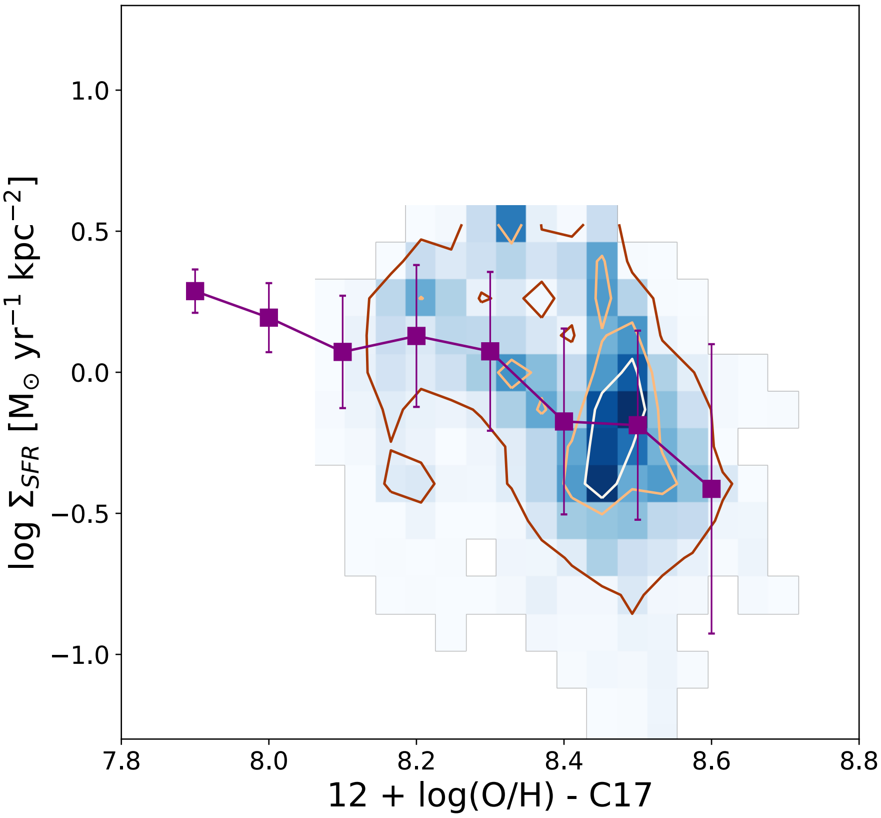

Figure 4.7: Distribution of the star formation rate surface density $\Sigma_{\rm sfr}$ against the C17 derived metallicity, combining all spaxels from all galaxies in our sample. In purple we show the median $\Sigma_{\rm sfr}$ in bins of log(O/H) and relative dispersions. The orange contours encompass the 10%, 50% and 75% of the sample respectively.

- The bulk of our galaxy sample present azimuthally averaged radial metallicity gradients fully consistent with being flat within the uncertainties. This is consistent with the majority of previous results reported in the literature which investigated metallicity gradients at z ~ 1 − 2. Comparison with cosmological simulations that explore the effect of different feedback modes suggest a scenario where efficient mixing processes, that redistribute a significant amount of gas over large scales, are in place. However, predictions from some analytical models which assumes fairly constant star formation spatial profiles and no prescriptions about gas flows can also reproduce the majority of the observed gradients. Some of our galaxies, showing a relatively homogeneous metal distribution across large spatial scales, seem to point towards this scenario of uniform disk mass assembly.

- We have found that, despite the apparent radial invariance, many of our galaxies exhibit complex and irregular patterns in the metallicity maps. This warns against using only radial gradients as constrains for galaxy evolution models. The complete information hold by full 2D metallicity maps can help to discriminate between different processes (galactic feedback, tidal interactions, local streams of pristine gas etc..) that contribute to shape the observed morphologies.

- We explored the correlation between the sSFR and metallicity gradients suggested by Stott et al. (2014), extending the relation towards the highest sSFRs probed by our sample. We find a trend in which galaxies with a higher sSFR exhibit flatter or more “positive” gradients, although this turns out to be not as tight as previously reported.
- We do not find in our sample any clear trend between metallicity gradients and stellar mass.
- We find evidence of a general spatial anti-correlation on local scales between metallicity and the SFR surface density, from the analysis of the full sample on a pixel by pixel basis. This result suggests that at least in some regions of our galaxies, smooth inflow of gas is active in diluting the metal content and boost star formation episodes. When this occur into the central regions, a flat or positive gradient arises.

Summarizing, our results confirm that the metal distribution in high-z galaxies is linked to their star formation activity, which however can not be the only driver of the observed shape of metallicity gradients. Mutual interactions between star formation and different processes involving efficient radial mixing driven by intense galactic feedback or merger events could strongly affect the complex morphology of the maps and the average radial flattening of the gradients that we see at these epochs. A more comprehensive and self-consistent view of spatially resolved metallicity properties in high-z galaxies will be possible as soon as new KLEVER observations are completed, comprising a larger sample spanning a wider range in stellar masses and star formation rates. The complexity revealed by current generation IFU instruments pave also the way for first JWST observations, that will offer in the near future the opportunity to probe the metal distribution in high redshfit galaxies with unprecedented detail, helping to discriminate between different theoretical predictions and setting new and tight constraint for numerical simulations and models.

4.5 Appendix A: Maps and gradients

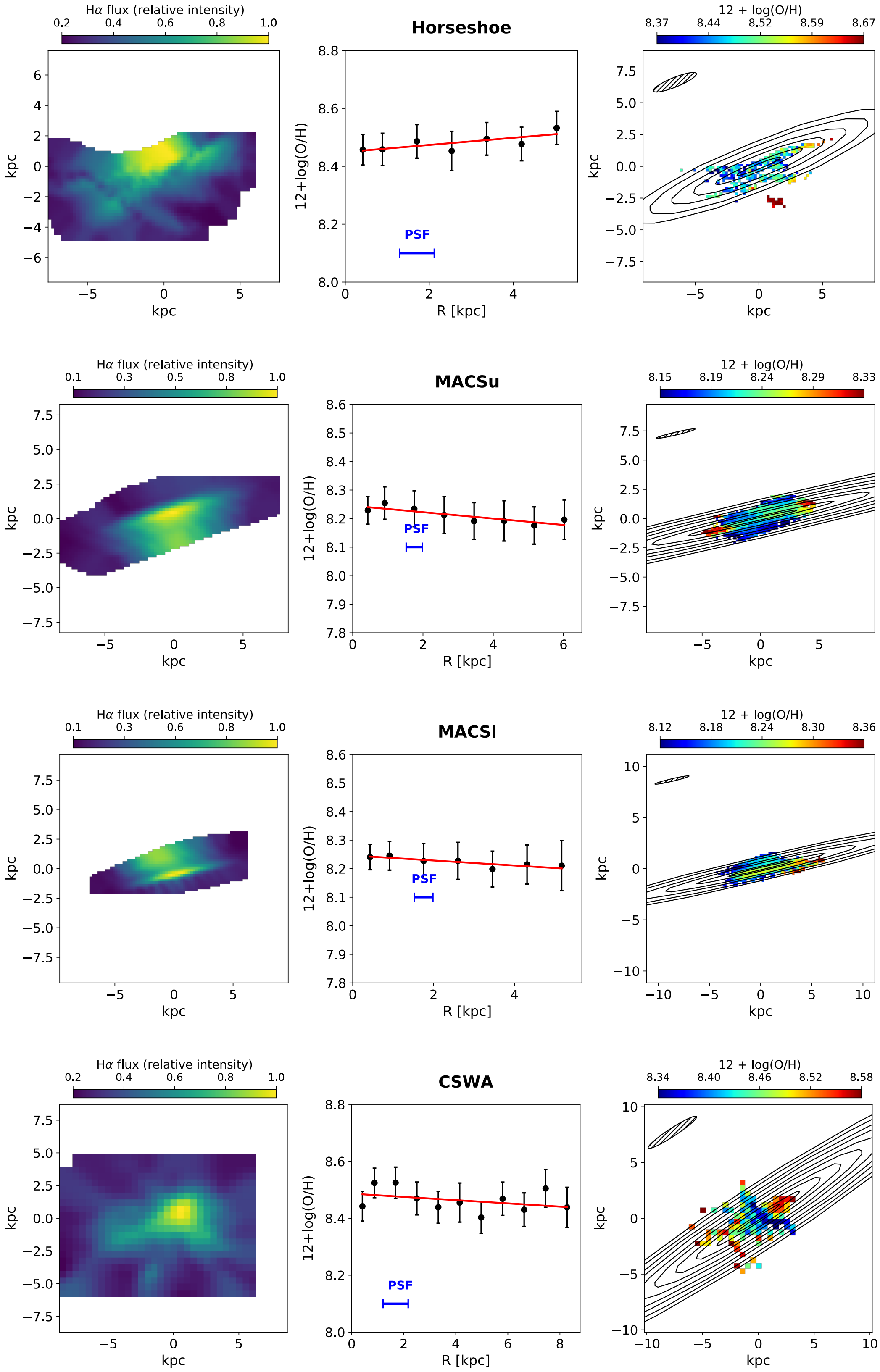

Figure 4.8: For each galaxy we show the normalized source plane Hα maps (*left*), the extracted metallicities at increasing radii across each galaxy (*middle*), and the full metallicity map derived using the C17 calibrations (*right*). In the *middle* panel the linear fit to the metallicity gradient (in red) and the linear size of the PSF (in blue) are also shown. The shaded black region in the *right* panel reproduce the shape and size of the PSF when mapped back into the source plane. The elliptical apertures used to derive the radial gradient overlay the 2D metallicity map.

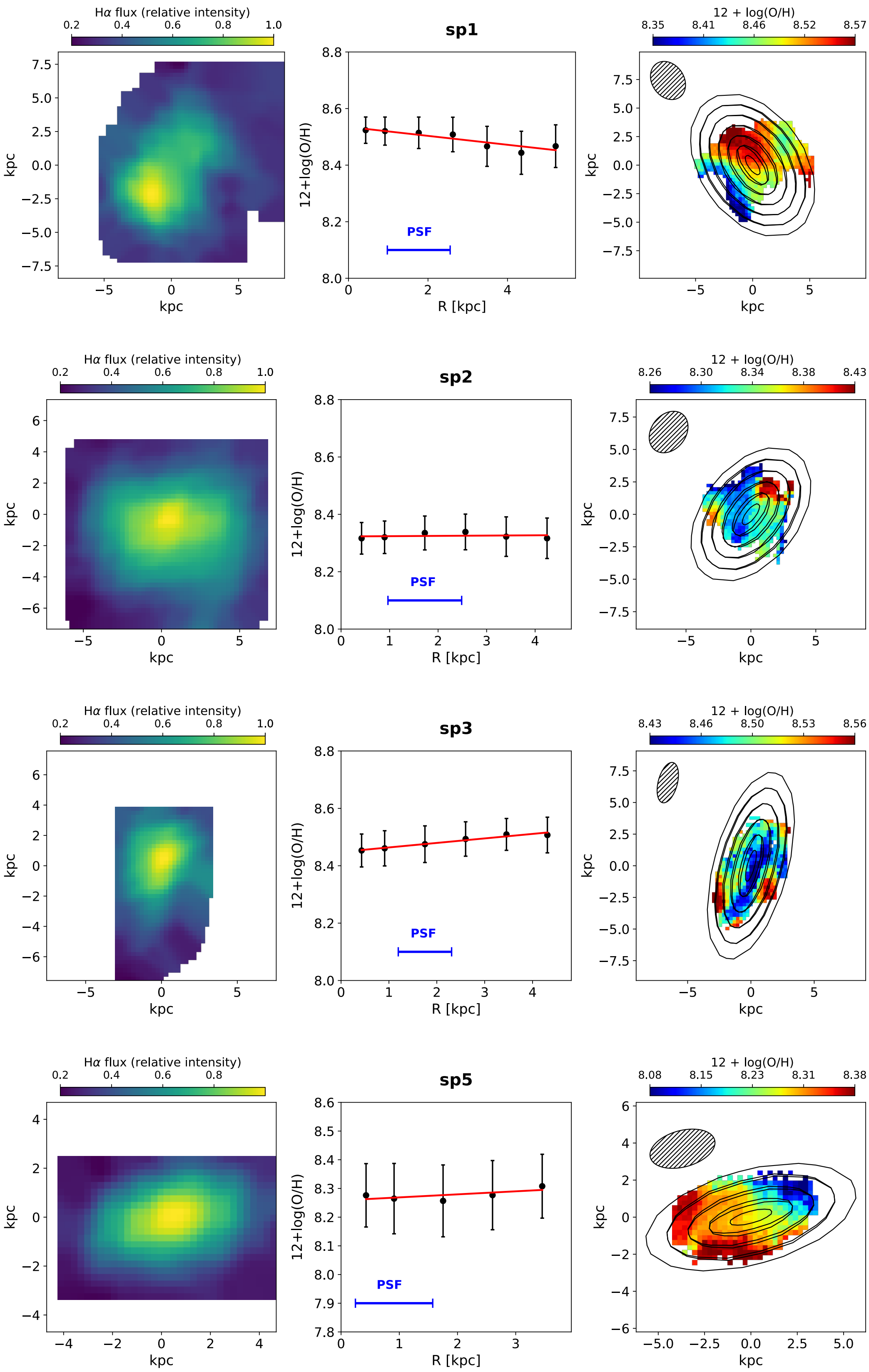
Hα flux (relative intensity)
0.2 0.4 0.6 0.8 1.0
kpc
sp1
12+log(O/H)
8.8 8.6 8.4 8.2 8.0
PSF
R [kpc]
12 + log(O/H)
8.35 8.41 8.46 8.52 8.57
sp2
8.26 8.30 8.34 8.38 8.43
sp3
8.43 8.46 8.50 8.53 8.56
sp5
8.6 8.5 8.4 8.3 8.2 8.1 8.0 7.9 7.8
8.08 8.15 8.23 8.31 8.38

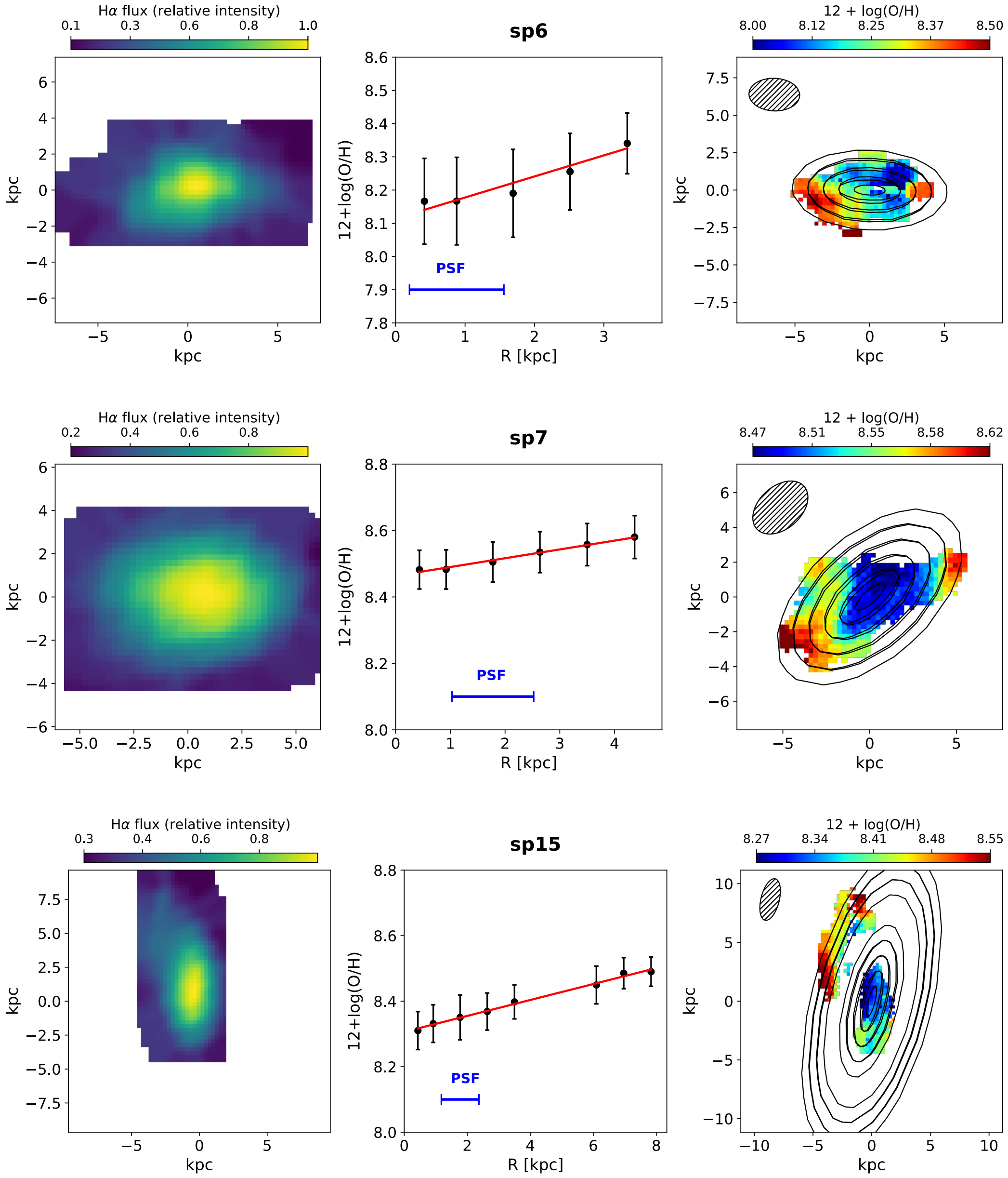
Hα flux (relative intensity)
0.1 0.3 0.6 0.8 1.0
kpc
sp6
12+log(O/H)
R [kpc]
PSF
12 + log(O/H)
8.00 8.12 8.25 8.37 8.50
Hα flux (relative intensity)
0.2 0.4 0.6 0.8
sp7
12 + log(O/H)
8.47 8.51 8.55 8.58 8.62
Hα flux (relative intensity)
0.3 0.4 0.6 0.8
sp15
12 + log(O/H)
8.27 8.34 8.41 8.48 8.55

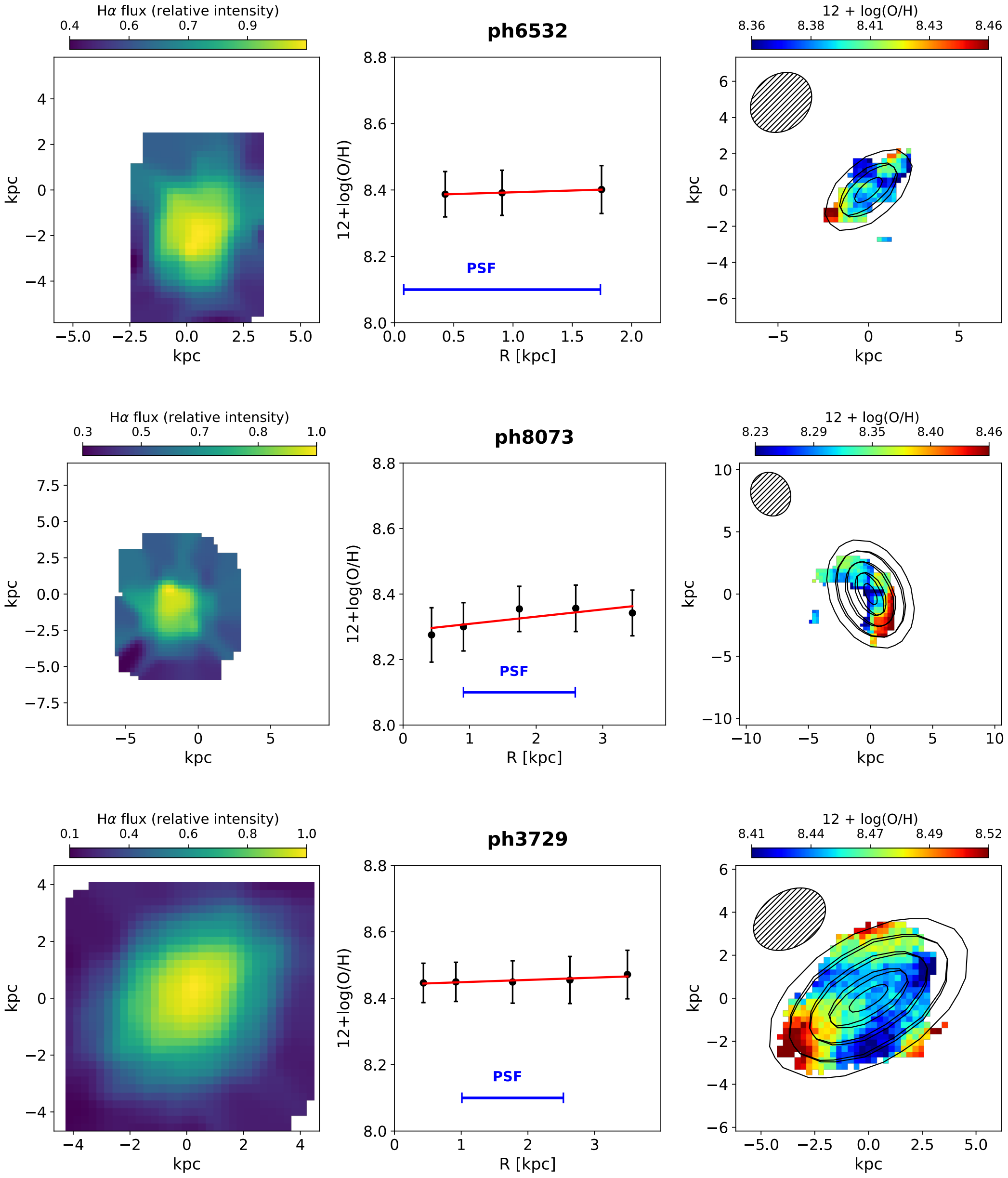
Hα flux (relative intensity)
0.4 0.6 0.7 0.9
kpc
kpc
ph6532
12+log(O/H)
PSF
R [kpc]
12 + log(O/H)
8.36 8.38 8.41 8.43 8.46
kpc
kpc
Hα flux (relative intensity)
0.3 0.5 0.7 0.8 1.0
ph8073
12 + log(O/H)
8.23 8.29 8.35 8.40 8.46
Hα flux (relative intensity)
0.1 0.4 0.6 0.8 1.0
ph3729
12 + log(O/H)
8.41 8.44 8.47 8.49 8.52

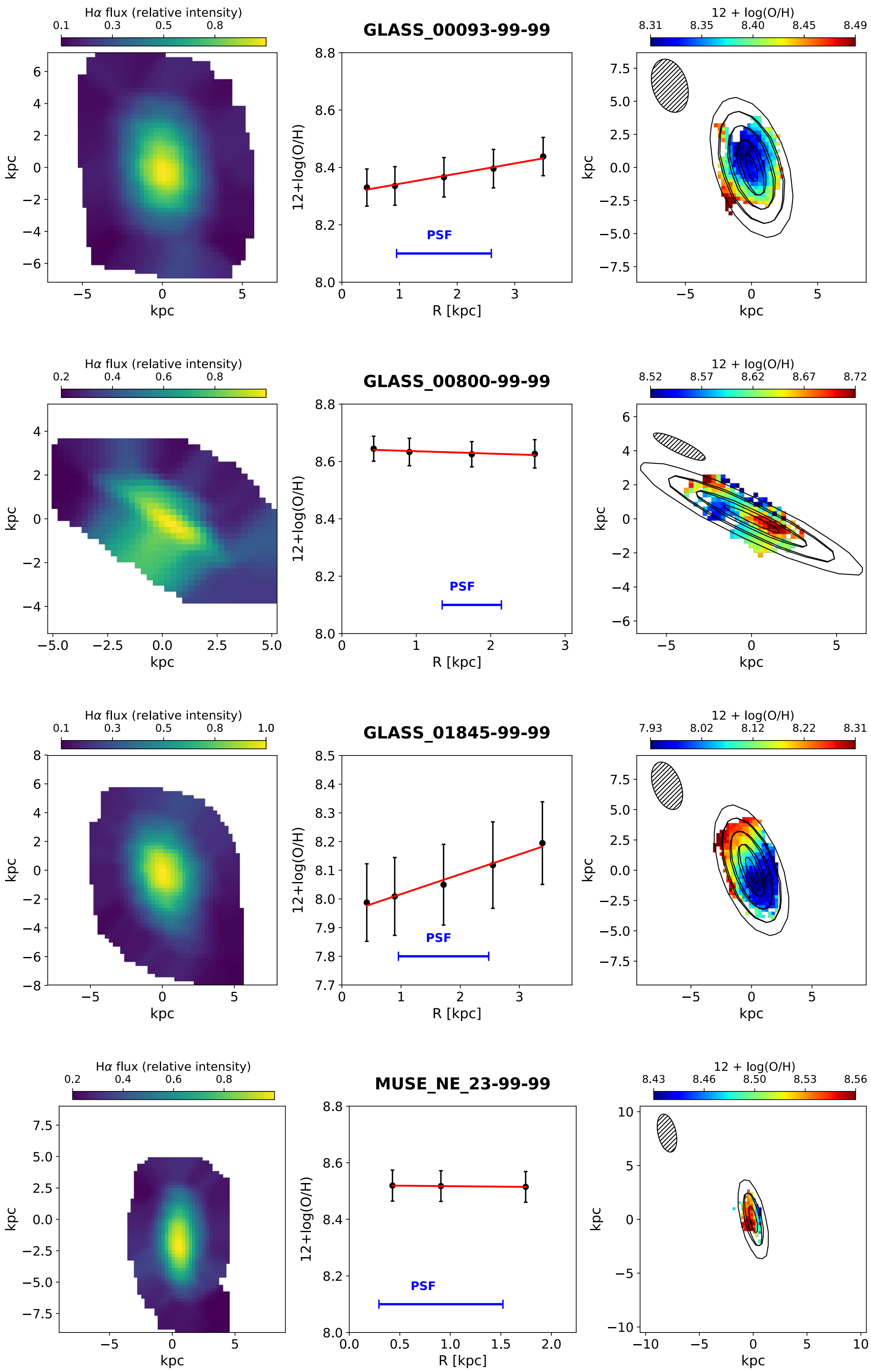
Hα flux (relative intensity)
0.1 0.3 0.5 0.8
kpc
GLASS_00093-99-99
12+log(O/H)
R [kpc]
PSF
12 + log(O/H)
8.31 8.35 8.40 8.45 8.49
Hα flux (relative intensity)
0.2 0.4 0.6 0.8
GLASS_00800-99-99
12 + log(O/H)
8.52 8.57 8.62 8.67 8.72
Hα flux (relative intensity)
0.1 0.3 0.5 0.8 1.0
GLASS_01845-99-99
12 + log(O/H)
7.93 8.02 8.12 8.22 8.31
Hα flux (relative intensity)
0.2 0.4 0.6 0.8
MUSE_NE_23-99-99
12 + log(O/H)
8.43 8.46 8.50 8.53 8.56

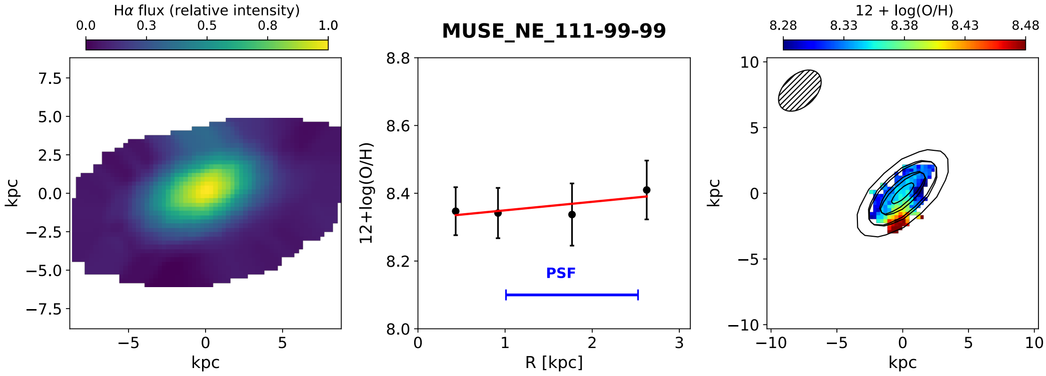

MUSE_NE_111-99-99

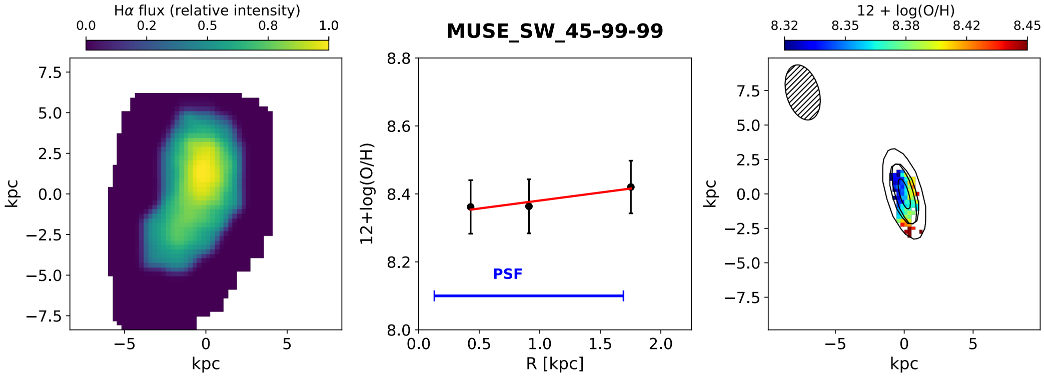

MUSE_SW_45-99-99

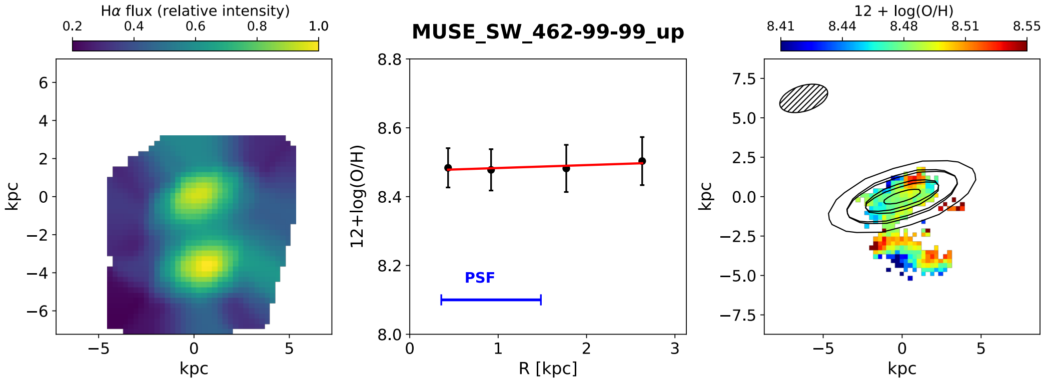

MUSE_SW_462-99-99_up

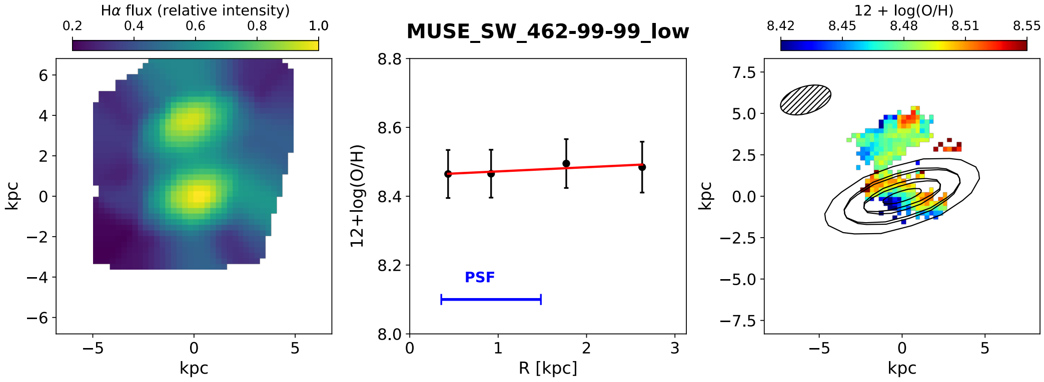

MUSE_SW_462-99-99_low

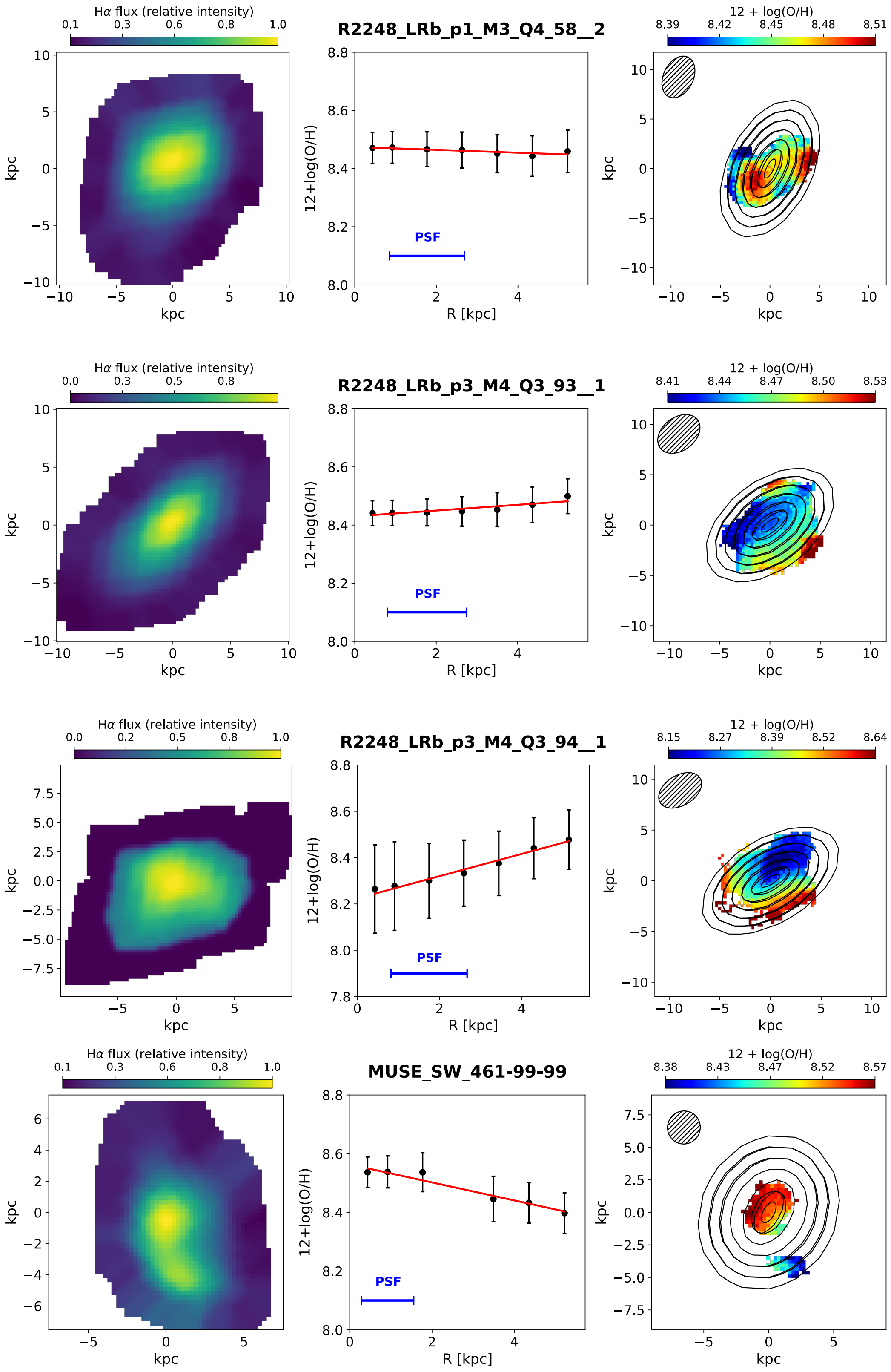
Hα flux (relative intensity)
0.1 0.3 0.6 0.8 1.0
R2248_LRb_p1_M3_Q4_58__2
12 + log(O/H)
8.39 8.42 8.45 8.48 8.51
PSF
12+log(O/H)
R [kpc]
kpc
Hα flux (relative intensity)
0.0 0.3 0.5 0.8
R2248_LRb_p3_M4_Q3_93__1
12 + log(O/H)
8.41 8.44 8.47 8.50 8.53
PSF
Hα flux (relative intensity)
0.0 0.2 0.5 0.8 1.0
R2248_LRb_p3_M4_Q3_94__1
12 + log(O/H)
8.15 8.27 8.39 8.52 8.64
PSF
Hα flux (relative intensity)
0.1 0.3 0.6 0.8 1.0
MUSE_SW_461-99-99
12 + log(O/H)
8.38 8.43 8.47 8.52 8.57
PSF

4.6 Appendix B: BPT diagrams of the KLEVER sample

In a companion paper of the KLEVER collaboration (Williams et al, in prep.), we investigated the main drivers of the observed offset of high-z galaxies in the classical BPT diagrams (see Sec. 1.1.3), trying to shed light on the different physical contributions at the origin of the evolution in the emission line ratios by exploiting the spatially resolved approach enabled by our data. In particular, exploiting the broad wavelength coverage of the survey (which map the entire set of rest-frame optical nebular lines from [O II]λ3727 to [S III]λ9530), we can assess the presence of possible correlations between the BPT offsets and the electron density, the ionization parameter and the level of nitrogen enrichment, which are derived by means of different nebular diagnostics. In particular, the electron density is inferred from the [S II]λ6717,6731 doublet, the ionization parameter from the [S III]λ9530/[S II]λ6717,6731 ratio (for z<2 galaxies) and from the [O III]λ5007/[O II]λ3727 ratio (for z>2 galaxies), while N/O is derived exploiting different calibrations of the [N II]λ6584/[O II]λ3727 and [N II]λ6584/[S II]λ6717,6731 diagnostics (e.g. Pérez-Montero & Contini 2009).

The analysis is conducted both on pixel basis in individual galaxies and globally, by combining the spatially resolved information from the entire sample.

More specifically, we find that:

- Only in a few individual galaxies the most deviating pixels from the star forming sequence are spatially located closer to the galaxy center, suggesting the contribution of an AGN to the ionization. On average, no clear correlation is found between the offset from the local sequence and the spatial postion within the galaxy (Fig. 4.9, panel a)

- We stacked the spectra of all the spaxels (from all galaxies in the sample) located above the classification dividing lines in the BPT diagrams, finding no evidence of prominent broad components in the He IIλ4686 emission line; this suggests that excitation by Wolf-Rayet stars is unlikely to contribute to the deviation of these spaxels on the BPT diagrams.

- Although the average density in the ISM of our high-z sample is higher than local galaxies, this parameter shows only mild correlation with the location of the most deviating spaxels on the BPT diagrams (Fig. 4.9, panel b), suggesting that gas density (hence gas pressure) can not be ascribed as the main driver of the observed offsets from the star-forming sequence.

- The ionization parameter U is generally enhanced in high-z galaxies relative to local ones, but it follows the same distribution observed locally between ionization parameter, EW(Hα) (a proxy of the age of the stellar population) and R_{23} parameter (proxy of metallicity). In some galaxies however, the deviation from the star-forming sequence clearly correlates with an increase in the ionization parameter, suggesting that in these systems the observed offset can be largely ascribed to variations in this quantity (as largely predicted also in the literature, see e.g. Strom et al. 2017). On average, a clear trend in which the highest [O III]λ5007/Hβ measured in the sample are associated to the highest U values is visible (Fig. 4.9, panel c).

- The level of nitrogen enrichment (as measured from N/O) strongly correlates with the deviations from the star-forming sequence on the [N II]-BPT diagram in many of our galaxies, as is clearly visible on the global diagram (Fig. 4.9, panel d); this suggests that an increase in the relative nitrogen abundance plays a role in driving the observed ratios towards higher [N II]/Hα values; moreover, this trend is confirmed when considering the relative nitrogen enrichment relative to the local O/H vs N/O relation. However, the deviations on the [S II]-BPT diagram are not clearly correlated with this parameter. In addition, further care is needed in the interpretation of this results, since we infer N/O from a diagnostic involving the [N II]λ6584 emission line which may introduce spurious correlations; fully independent confirmations are thus required.

In conclusion, we suggest that none of this processes is likely to be the main and unique driver of the observed evolution in line-ratios, but that multiple effects (mainly related to increased U and N/O) may play a role at the same time, with relative contributions that can significantly change from galaxy to galaxy.

In the following, we report all the spatially resolved versions of BPT diagrams for our sample, color-coded by different physical parameters, namely electron density, ionization parameter and nitrogen-to-oxygen abundance. For a more in-depth discussion on their physical interpretation we refer to Williams et al (in prep.).

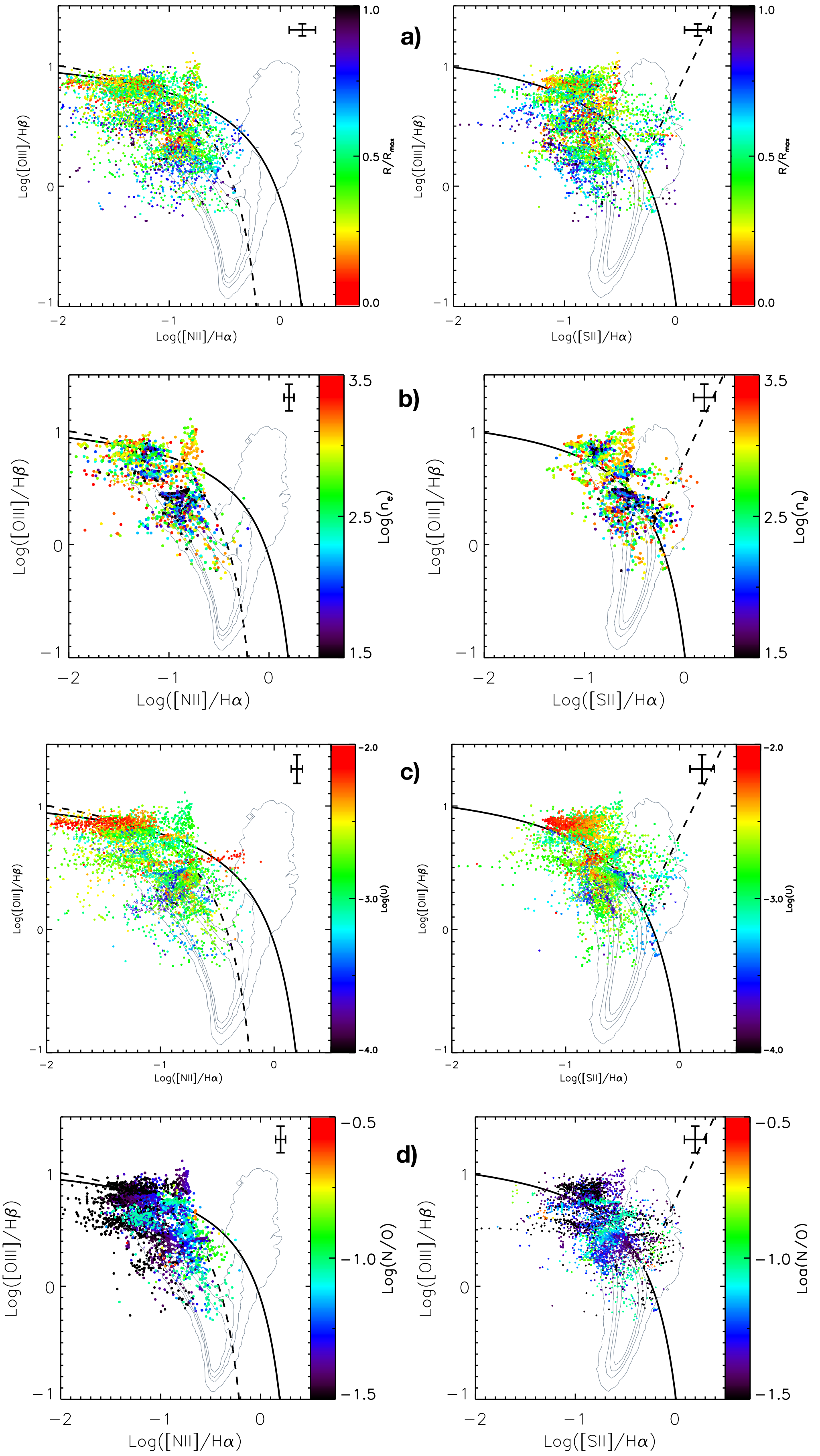

Figure 4.9: Spatially resolved BPT diagrams for the global KLEVER sample, obtained combining all the spaxels from individual galaxies. In each panel, the points are color-coded according to different properties, namely the radial distance from the center (a), the electron density (b), the ionization parameter (c) and the N/O ratio (d).

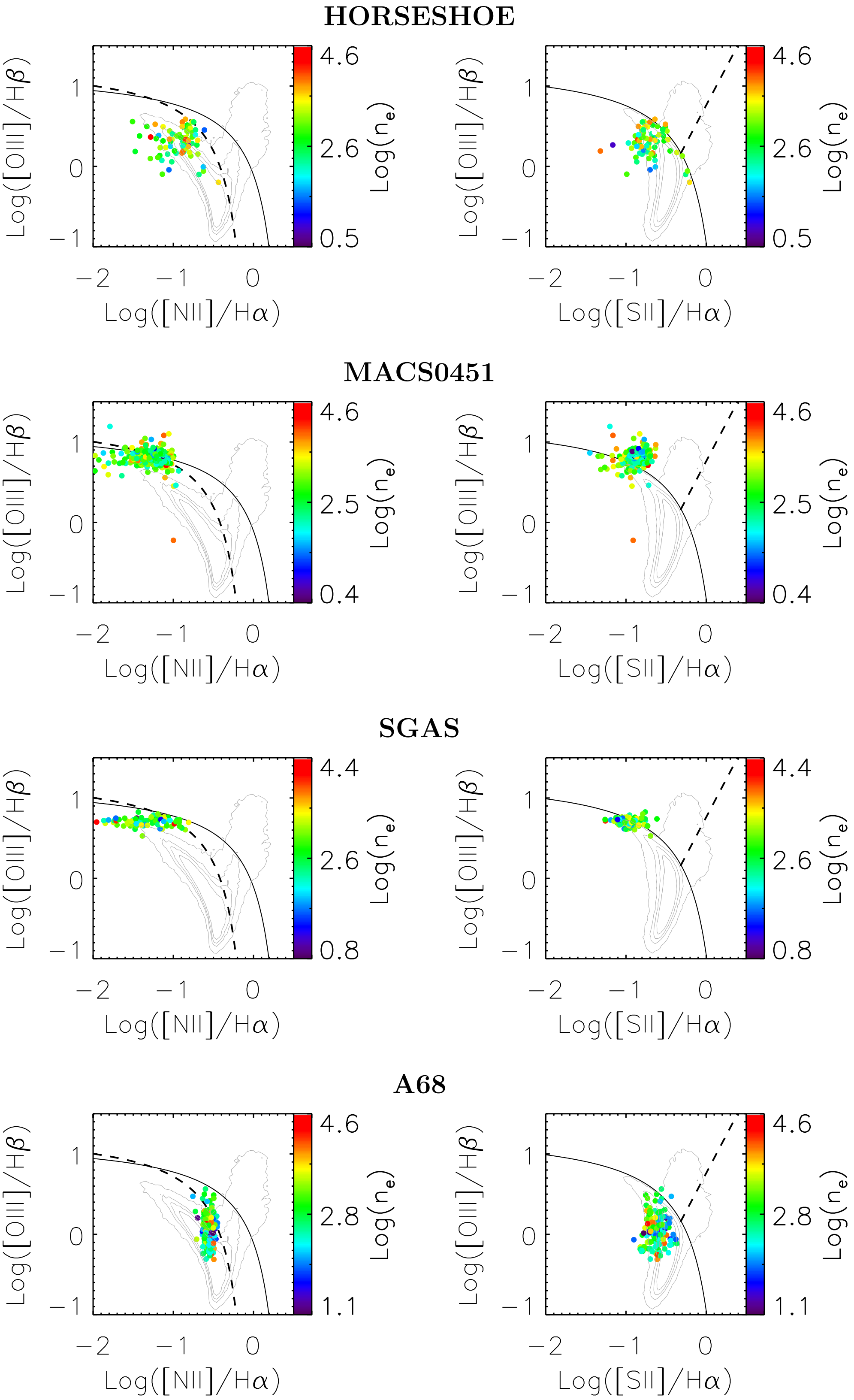

Figure 4.10: Spatially resolved [N II]-BPT (*left*) and [S II]-BPT (*right*) diagrams, where each point represents an individual pixel, color-coded by the electron density n_e, as inferred from the [S II] doublet. The grey contours indicate the location of the SDSS (local) galaxies and the black lines show the AGN-SF theoretical dividing lines by Kewley et al. 2001 and Kauffmann et al. (2003b) respectively.

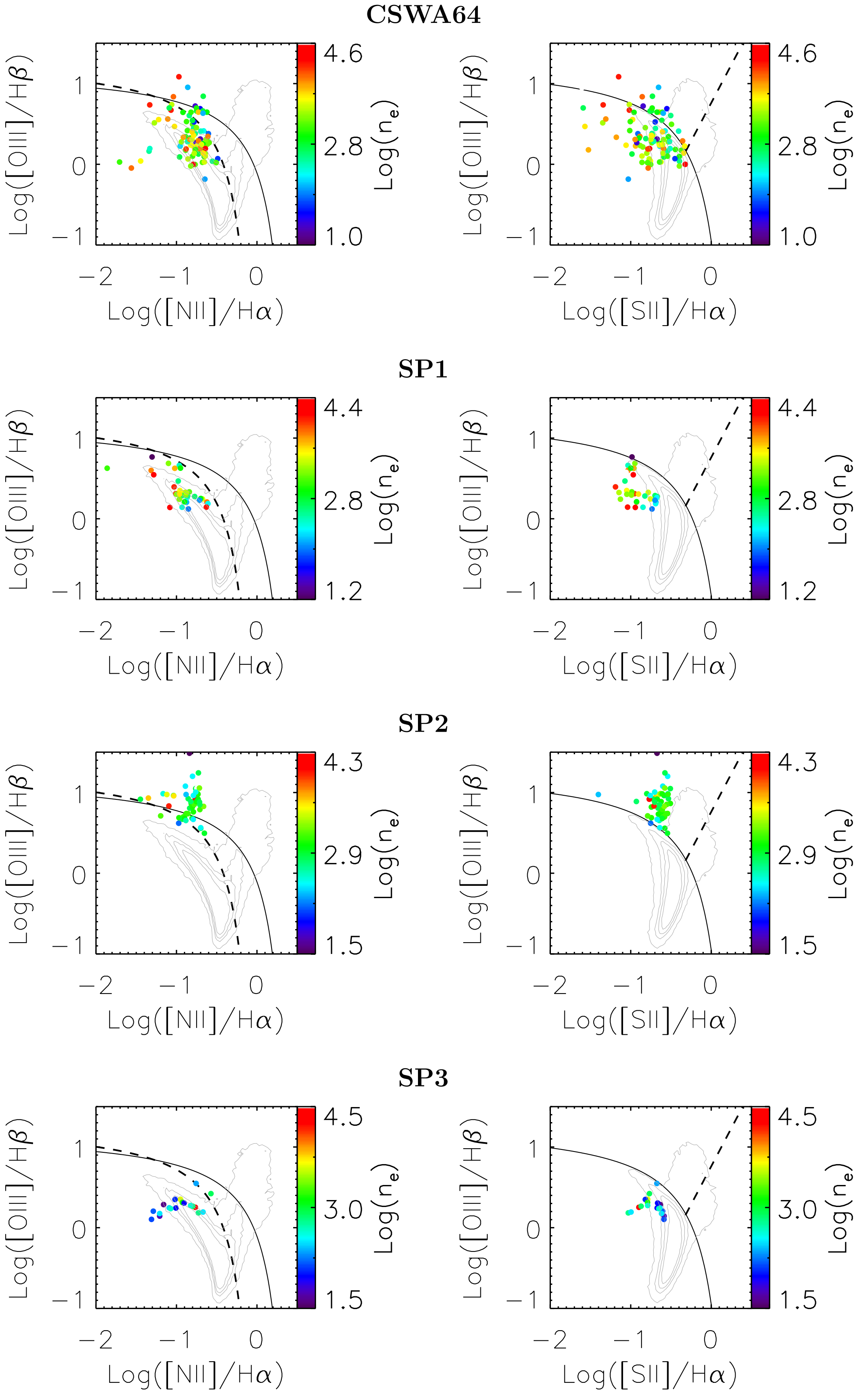
CSWA64
SP1
SP2
SP3
Log([OIII]/Hβ)
Log([NII]/Hα)
Log([SII]/Hα)
Log(n_e)
1
0
−1
−2
4.6
2.8
1.0
4.4
1.2
4.3
2.9
1.5
4.5
3.0

SP5

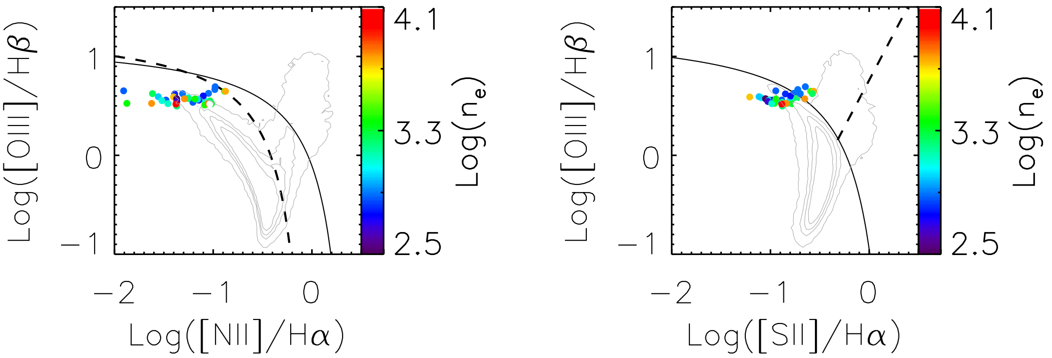

SP6

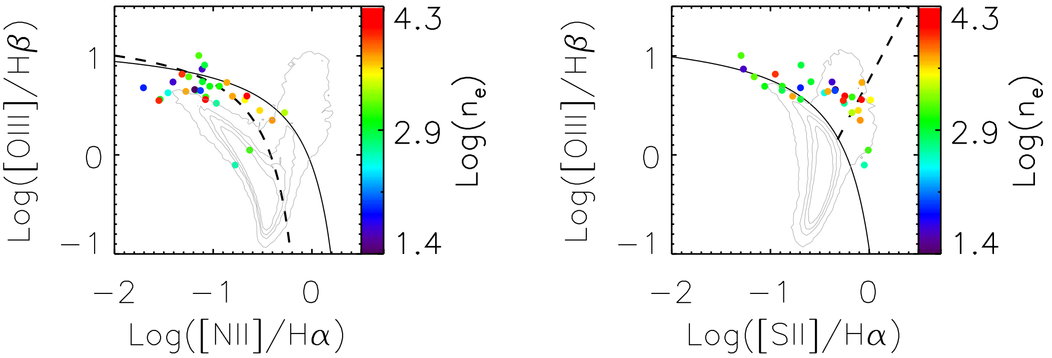

SP7

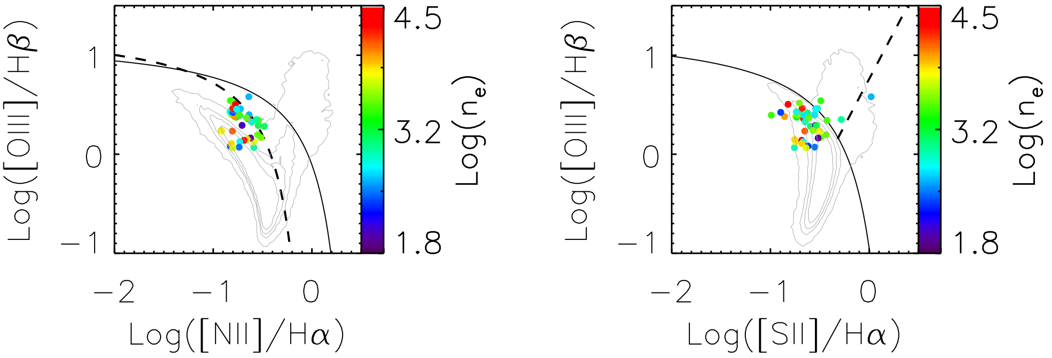

SP13

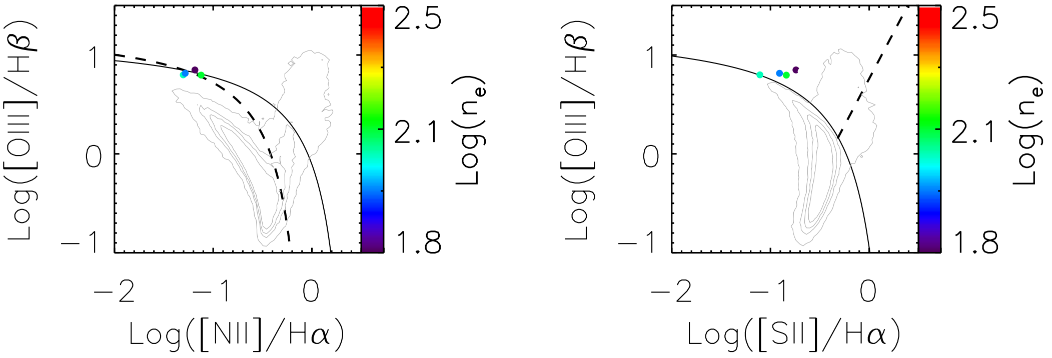

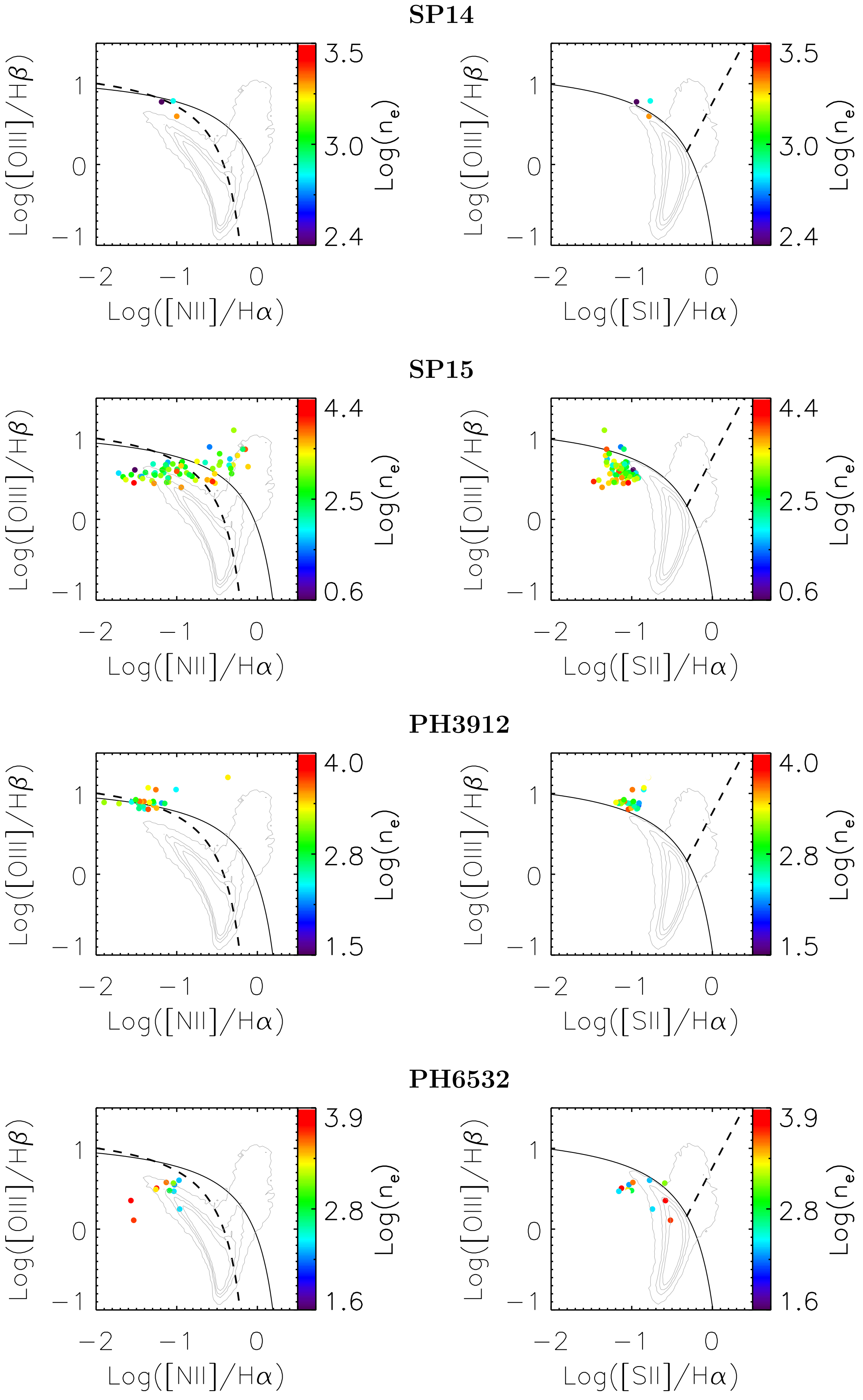
SP14
Log([OIII]/Hβ)
Log([NII]/Hα)
Log([SII]/Hα)
Log(n_e)
3.5
3.0
2.4
SP15
4.4
2.5
0.6
PH3912
4.0
2.8
1.5
PH6532
3.9
2.8
1.6
−2
−1
0
1

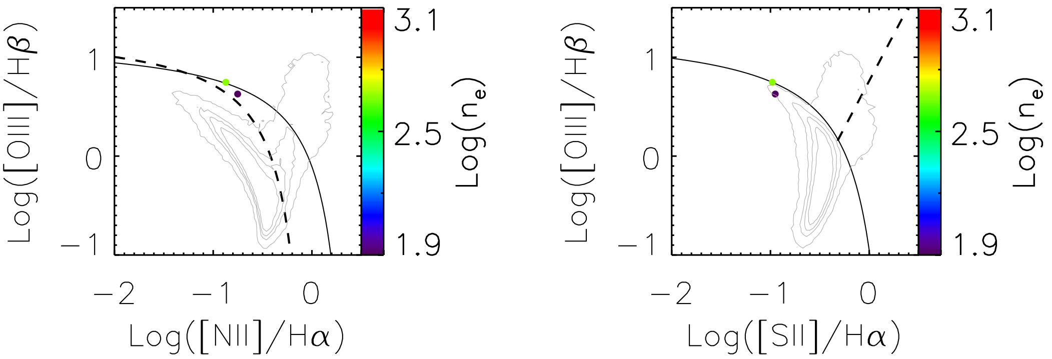

PH8073

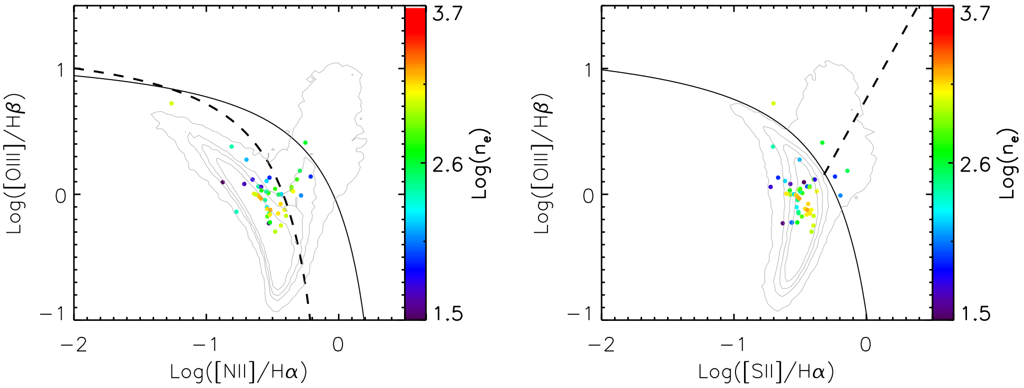

GLASS_00800-99-99

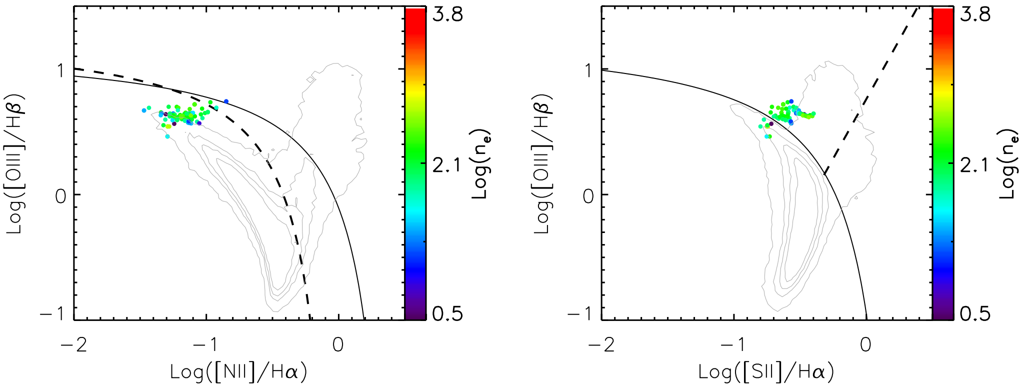

MUSE_NE_111-99-99

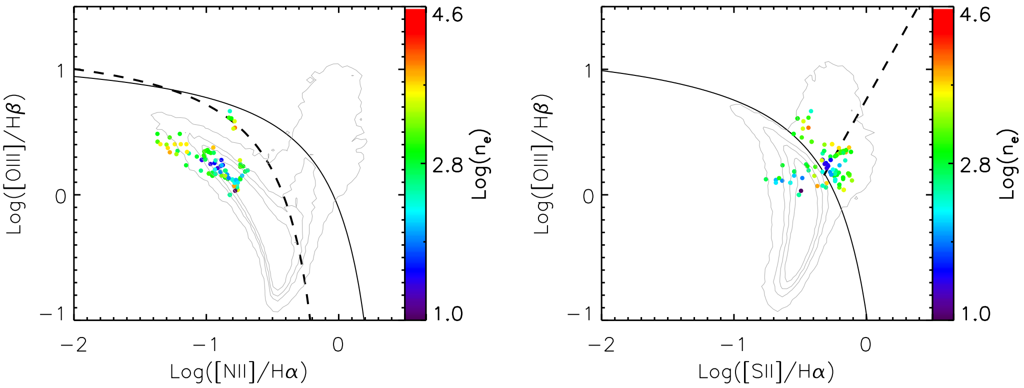

MUSE_SW_461-99-99

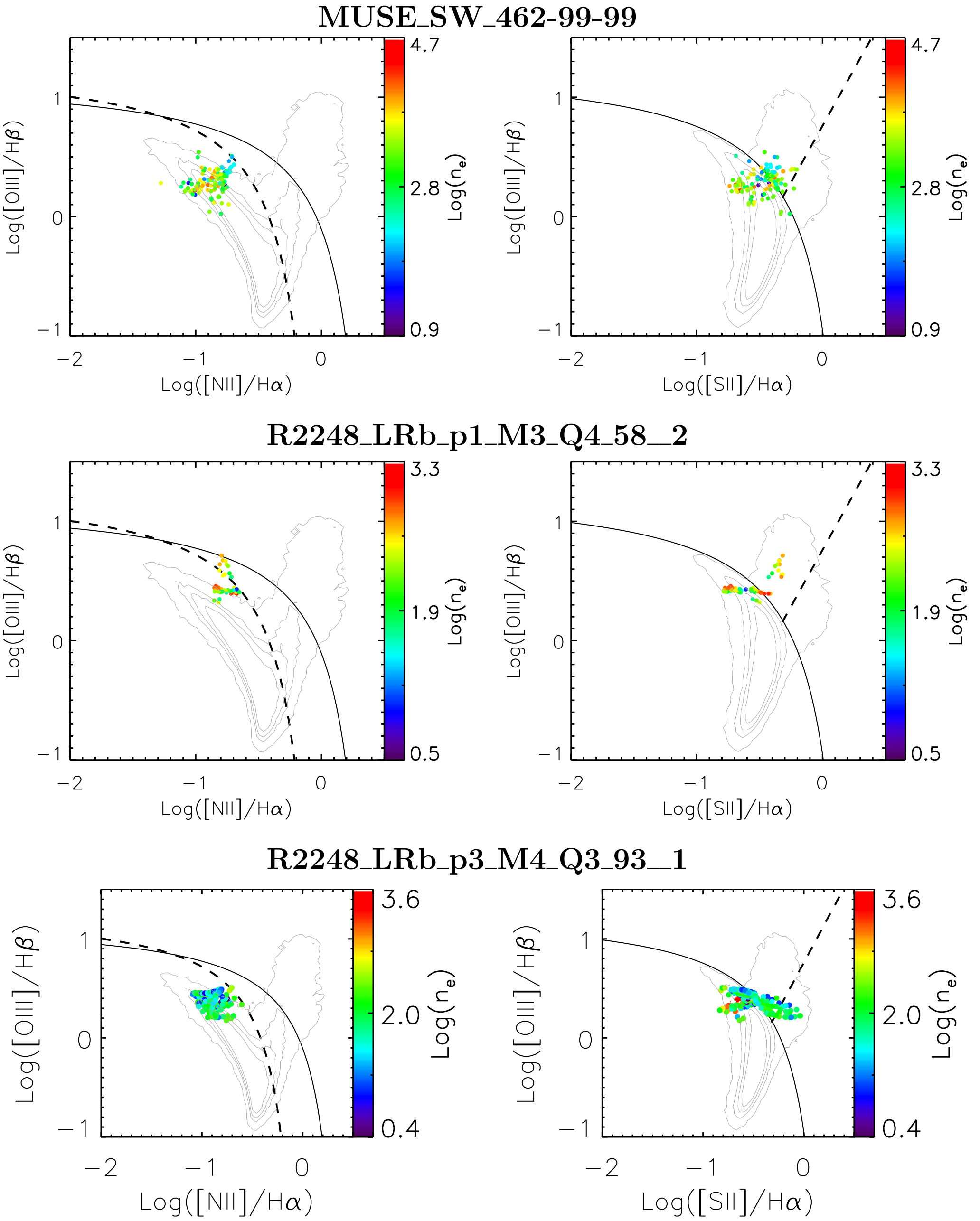

MUSE_SW_462-99-99

R2248_LRb_p1_M3_Q4_58__2

R2248_LRb_p3_M4_Q3_93__1

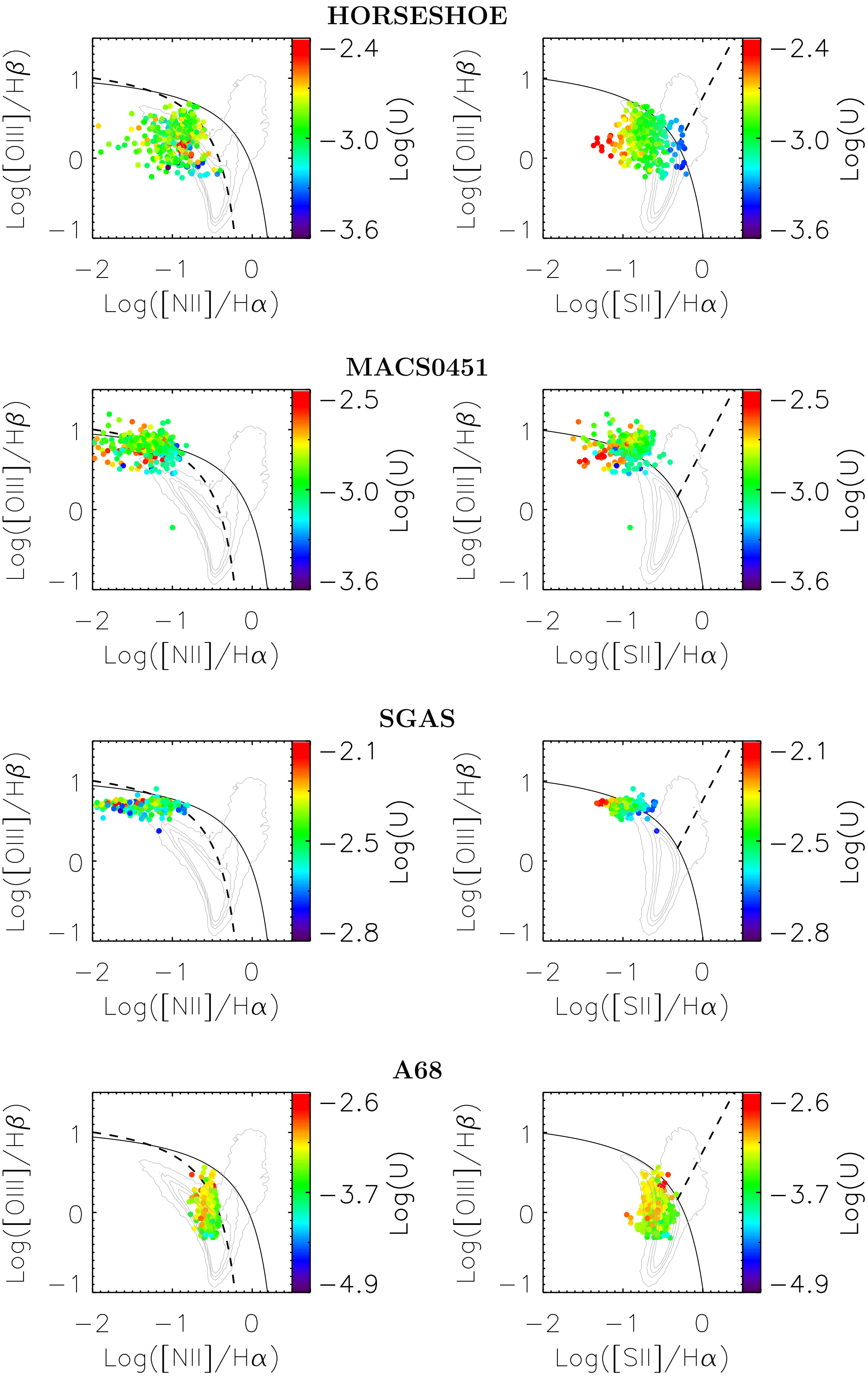

Figure 4.11: Spatially resolved [N II]-BPT (*left*) and [S II]-BPT (*right*) diagrams, where each point represents an individual pixel, color-coded by the ionization parameter, as inferred from the [S III]/[S II] or [O III]/[O II] ratios. The grey contours indicate the location of the SDSS (local) galaxies and the black lines show the AGN-SF theoretical dividing lines by Kewley et al. 2001 and Kauffmann et al. (2003b) respectively.

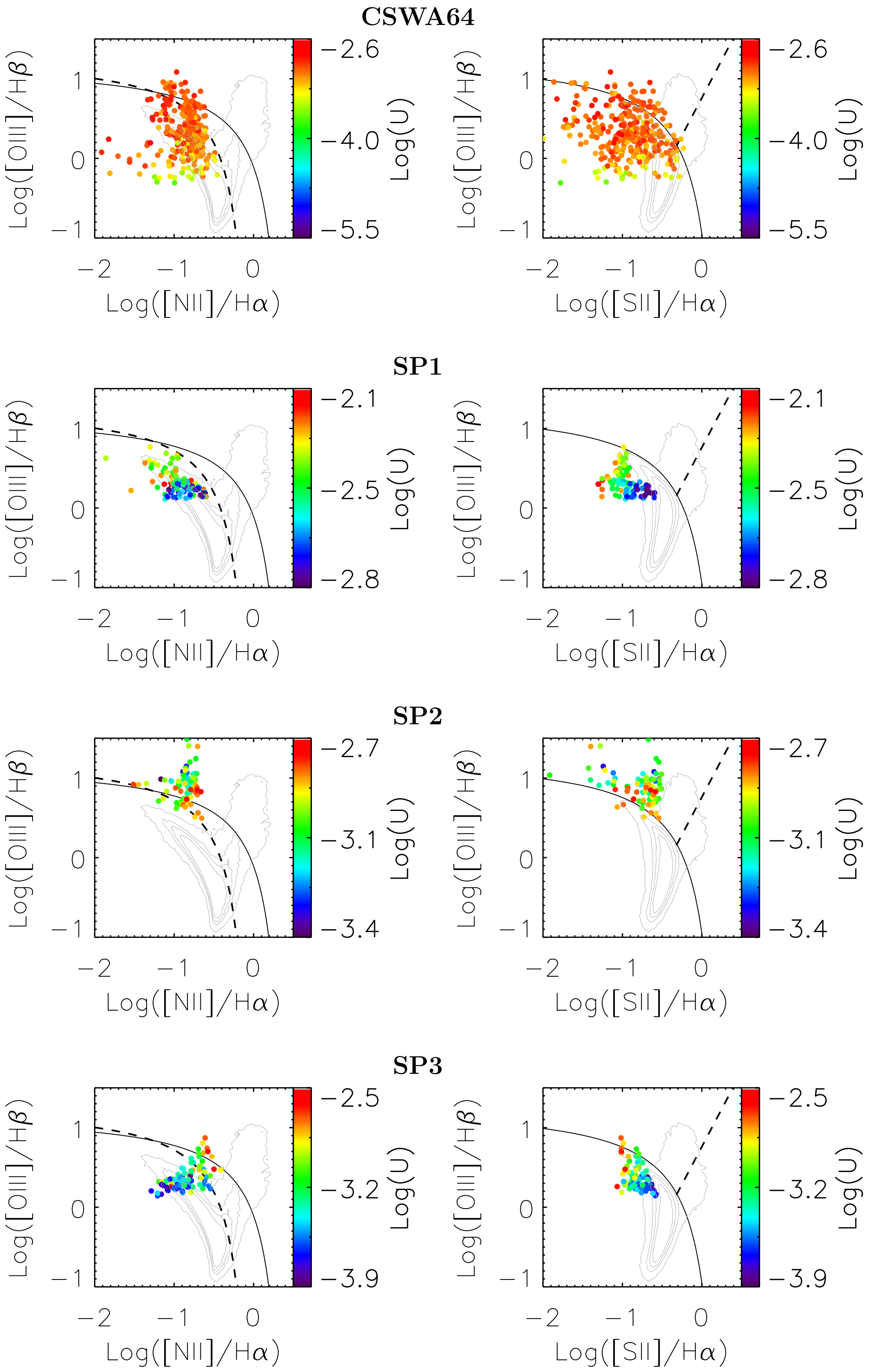
CSWA64
SP1
SP2
SP3
Log([OIII]/Hβ)
Log([NII]/Hα)
Log([SII]/Hα)
Log(U)
−2.6
−4.0
−5.5
−2.1
−2.5
−2.8
−2.7
−3.1
−3.4
−2.5
−3.2
−3.9
1
0
−1
−2
−1
0

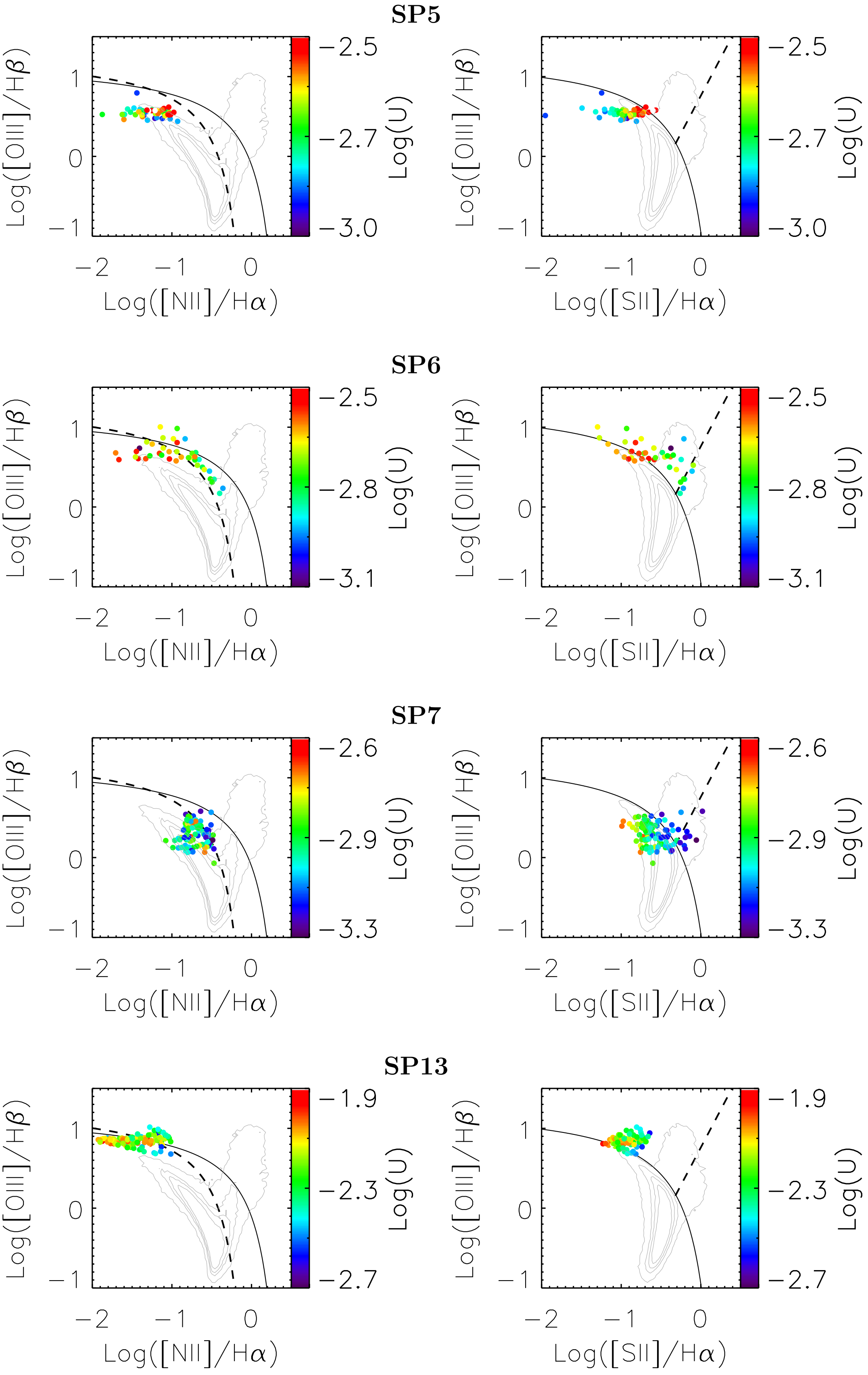
SP5
Log([OIII]/Hβ)
1
0
−1
−2
−1
0
Log([NII]/Hα)
Log([SII]/Hα)
Log(U)
−2.5
−2.7
−3.0
SP6
Log(U)
−2.5
−2.8
−3.1
SP7
Log(U)
−2.6
−2.9
−3.3
SP13
Log(U)
−1.9
−2.3
−2.7

SP14

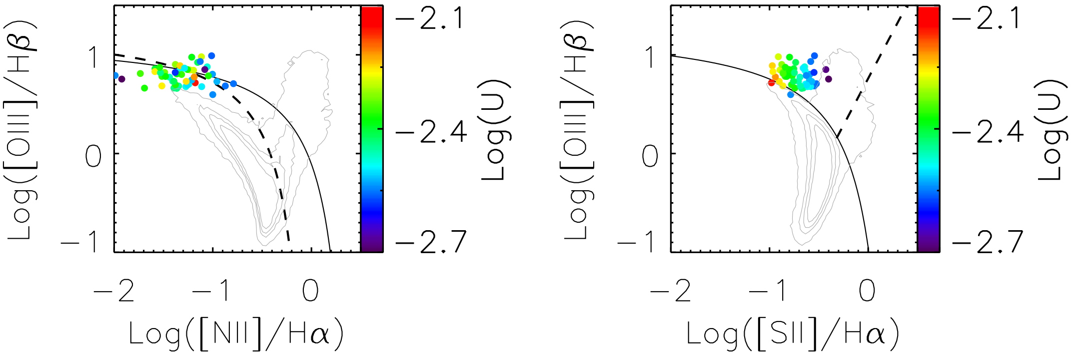

SP15

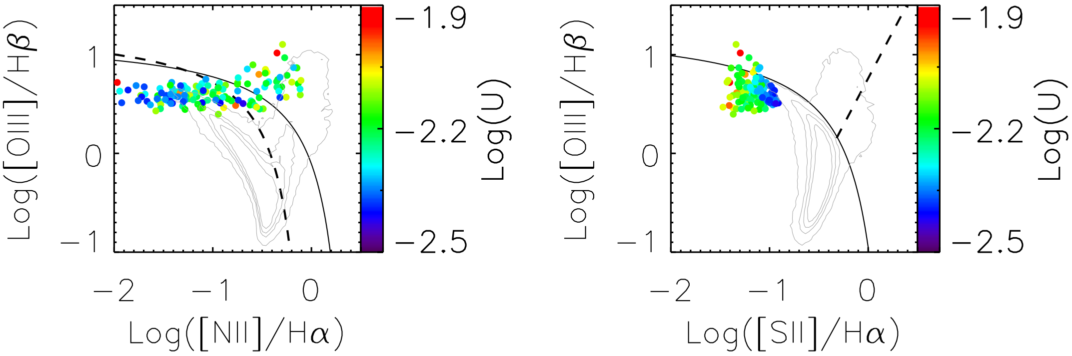

PH2594

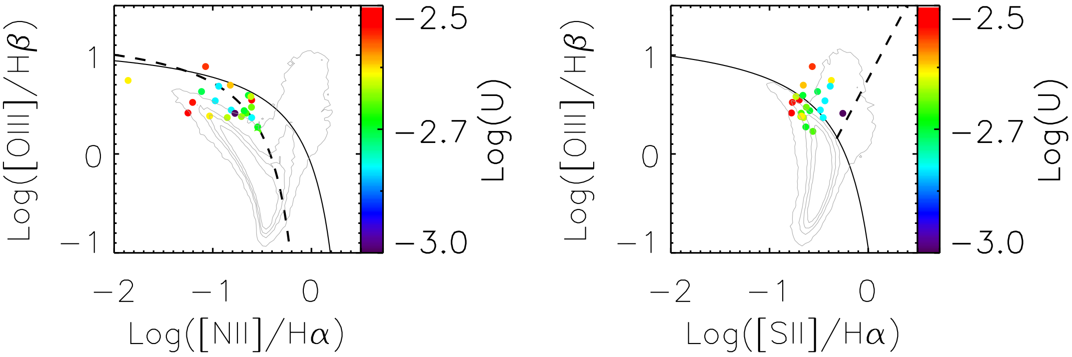

PH3729

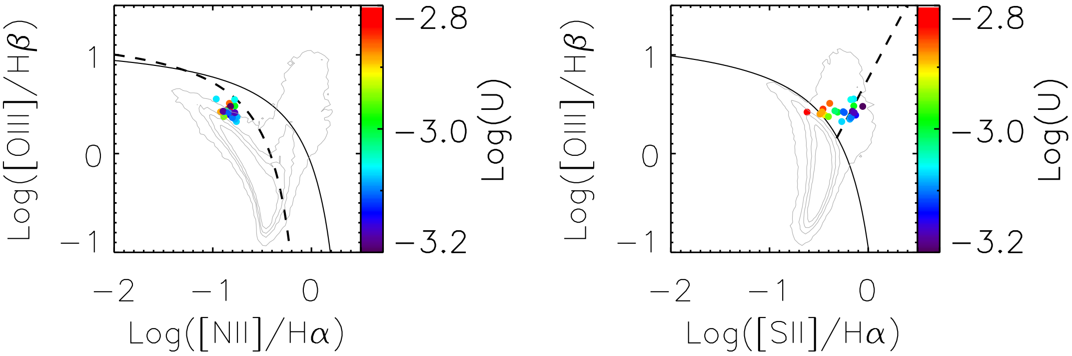

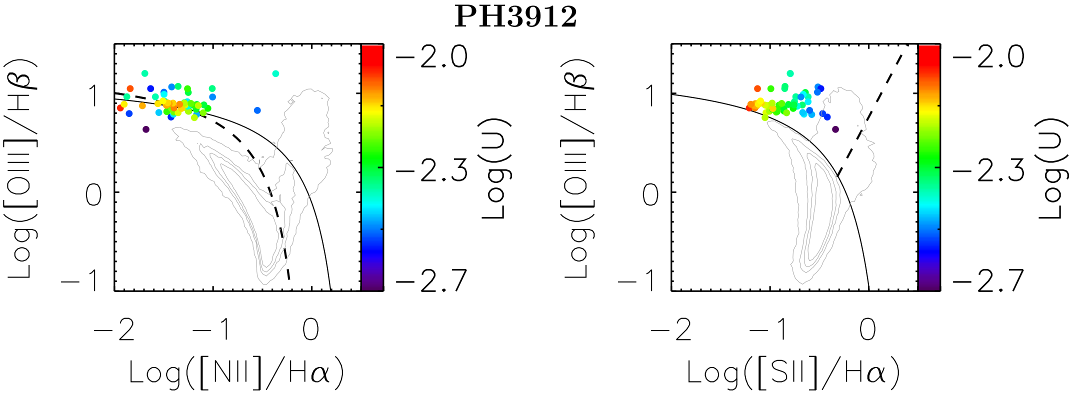
PH3912

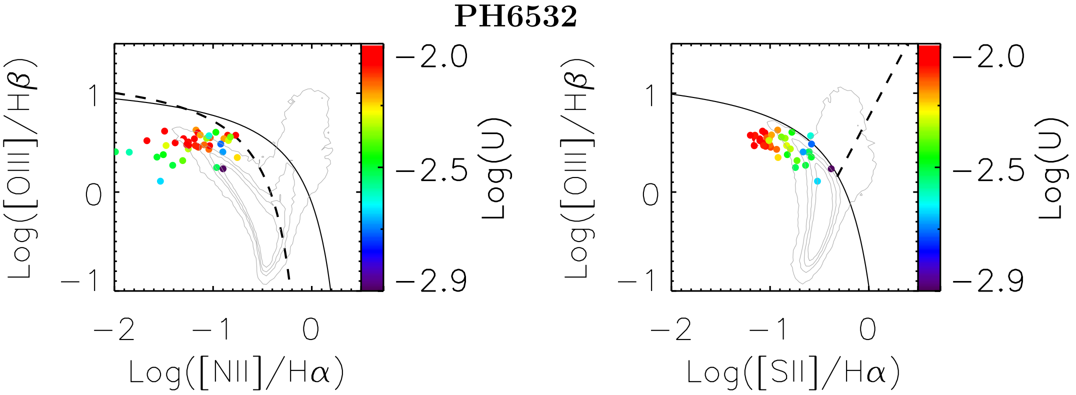
PH6532

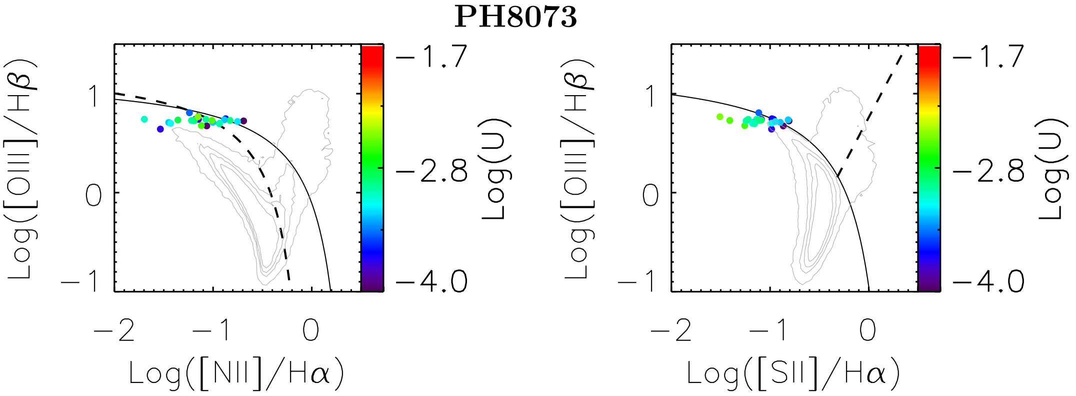
PH8073

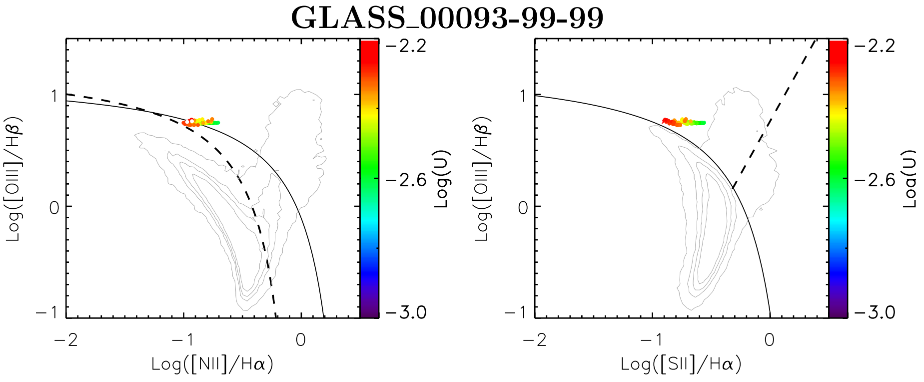
GLASS_00093-99-99

R2248_LRb_p3_M4_Q3_94__1

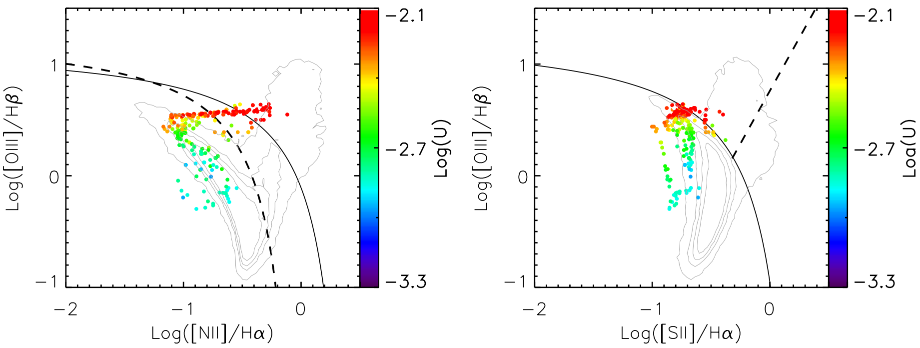

GLASS_00800-99-99

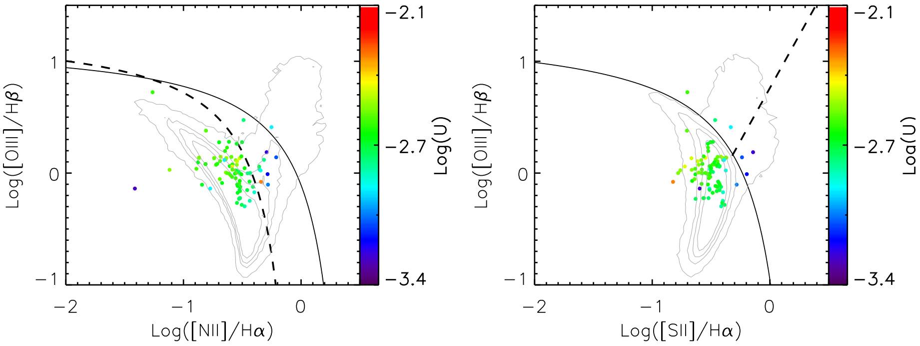

MUSE_NE_23-99-99

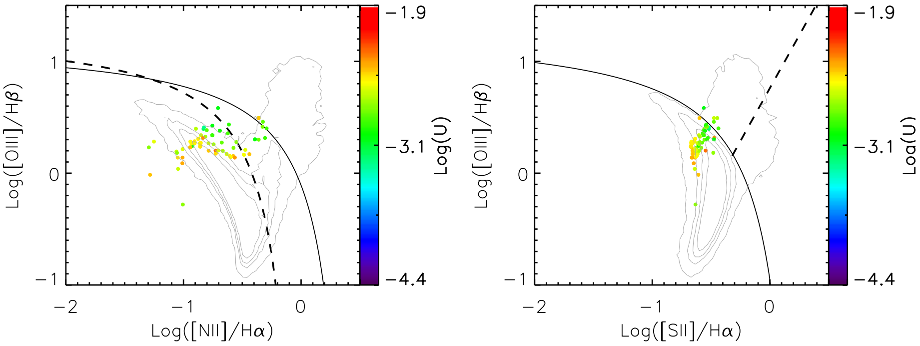

MUSE_NE_111-99-99

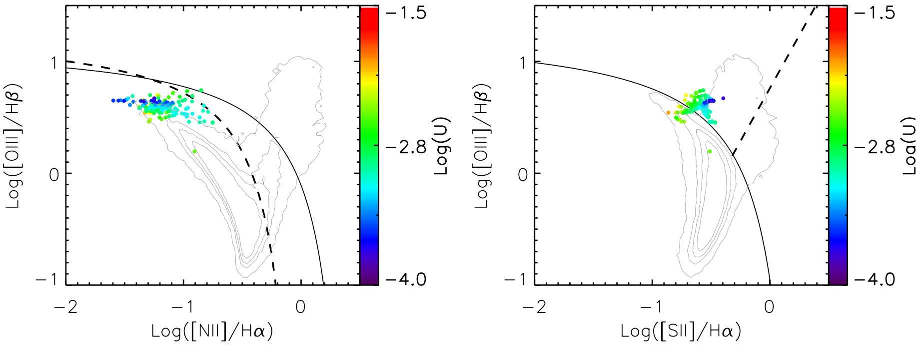

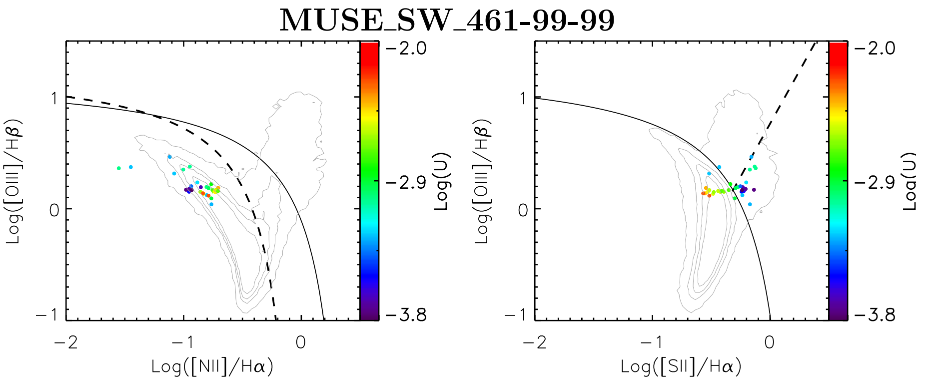
MUSE_SW_461-99-99
Log([OIII]/Hβ)
Log([NII]/Hα)
Log([SII]/Hα)
Log(U)
−2.0
−2.9
−3.8
1
0
−1
−2
−1
0

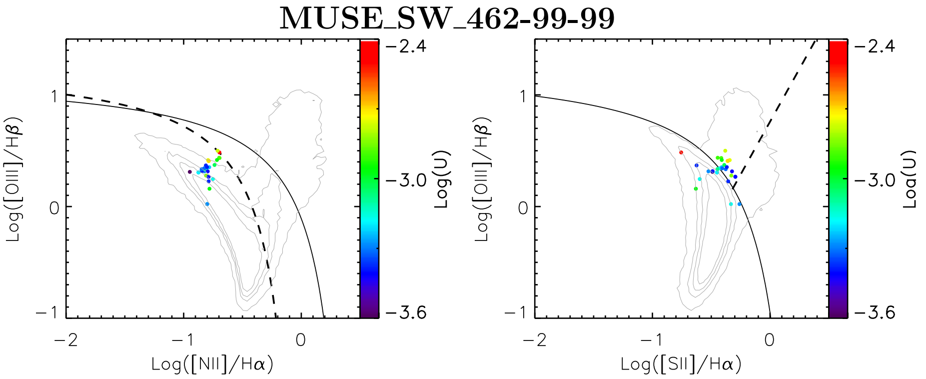
MUSE_SW_462-99-99
Log([OIII]/Hβ)
Log([NII]/Hα)
Log([SII]/Hα)
Log(U)
−2.4
−3.0
−3.6
1
0
−1
−2
−1
0

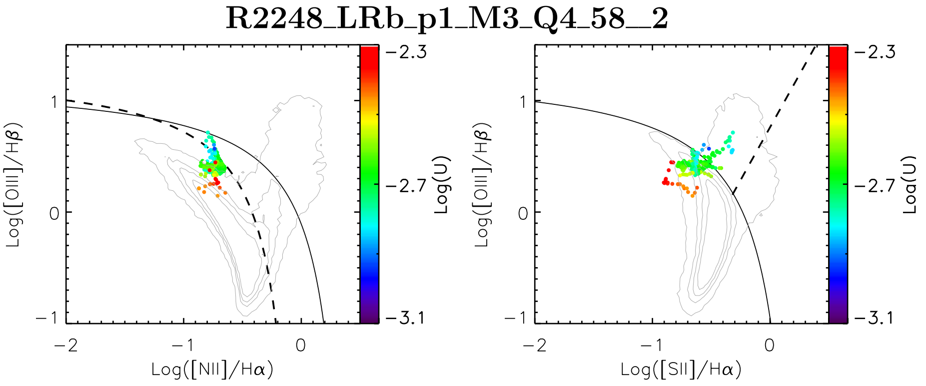
R2248_LRb_p1_M3_Q4_58__2
Log([OIII]/Hβ)
Log([NII]/Hα)
Log([SII]/Hα)
Log(U)
−2.3
−2.7
−3.1
1
0
−1
−2
−1
0

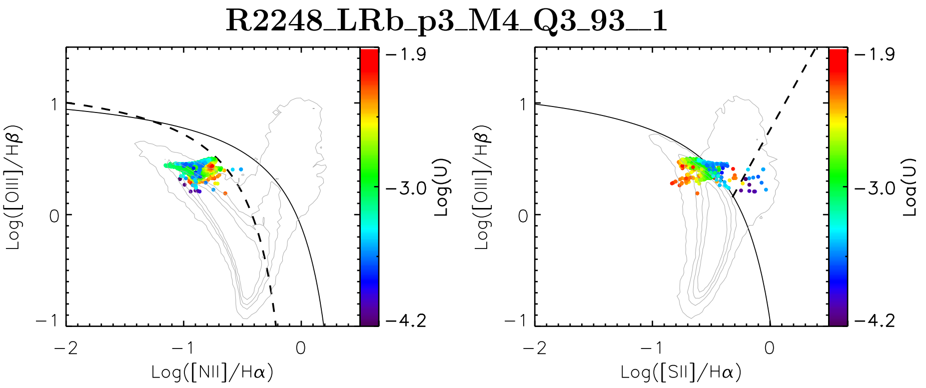
R2248_LRb_p3_M4_Q3_93__1
Log([OIII]/Hβ)
Log([NII]/Hα)
Log([SII]/Hα)
Log(U)
−1.9
−3.0
−4.2
1
0
−1
−2
−1
0

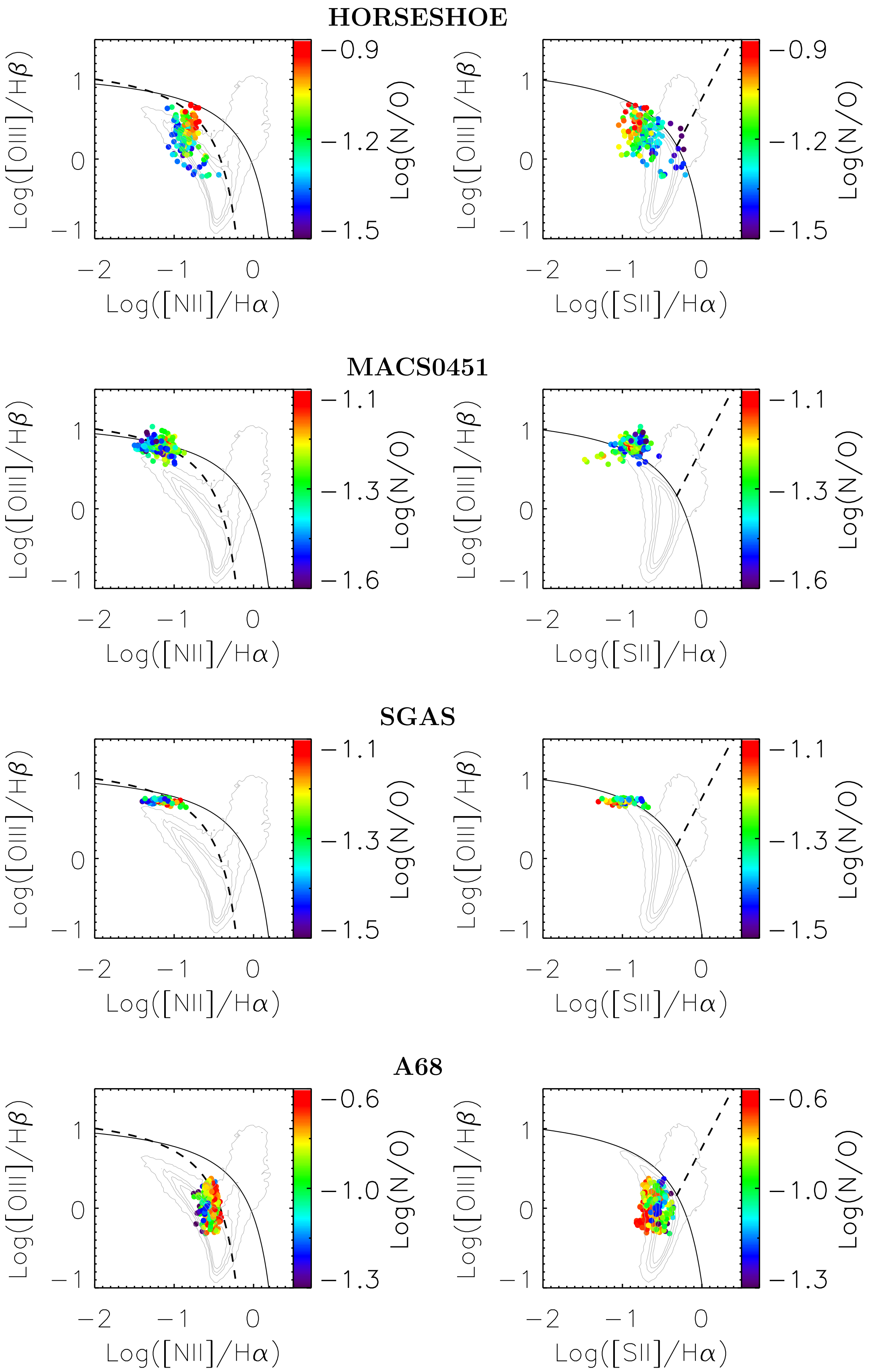

Figure 4.12: Spatially resolved [N II]-BPT (*left*) and [S II]-BPT (*right*) diagrams, where each point represents an individual pixel, color-coded by the N/O abundance ratio, as inferred from the [N II]/[S II] and [N II]/[O II] diagnostics. The grey contours indicate the location of the SDSS (local) galaxies and the black lines show the AGN-SF theoretical dividing lines by Kewley et al. 2001 and Kauffmann et al. (2003b) respectively.

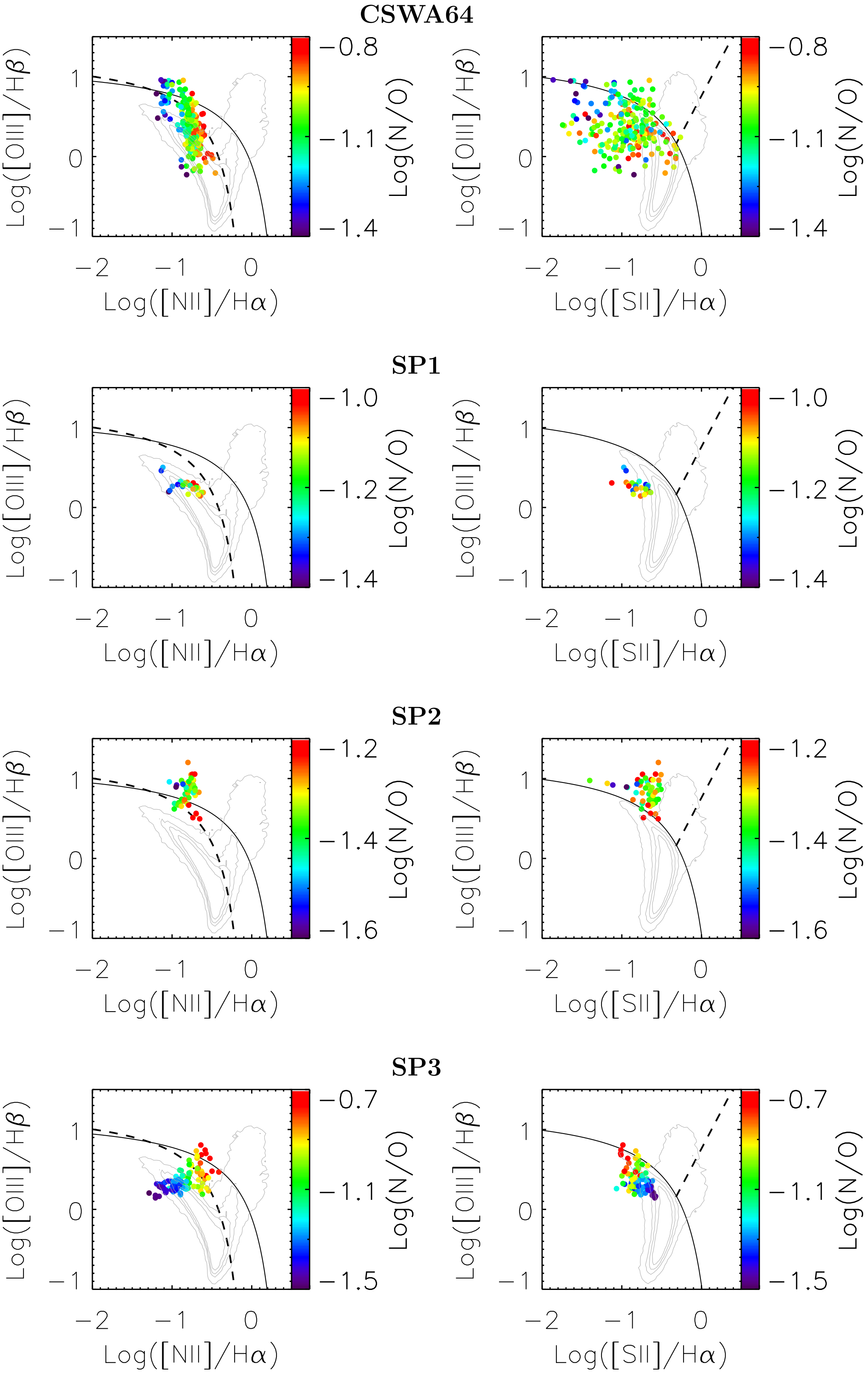
CSWA64
SP1
SP2
SP3
Log([OIII]/Hβ)
Log([NII]/Hα)
Log([SII]/Hα)
Log(N/O)
−2
−1
0
1
−0.8
−1.1
−1.4
−1.0
−1.2
−1.4
−1.2
−1.4
−1.6
−0.7
−1.1
−1.5

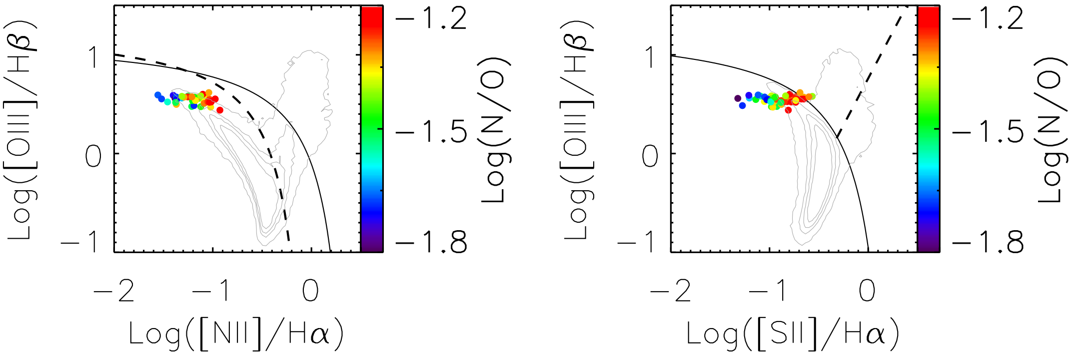

SP5

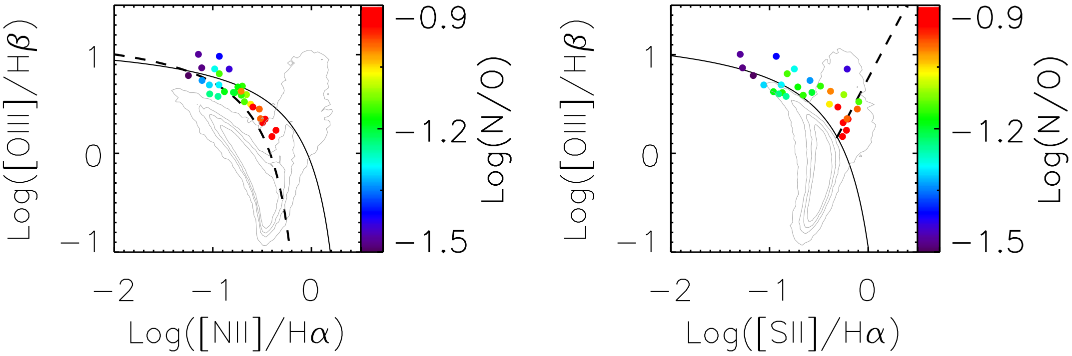

SP6

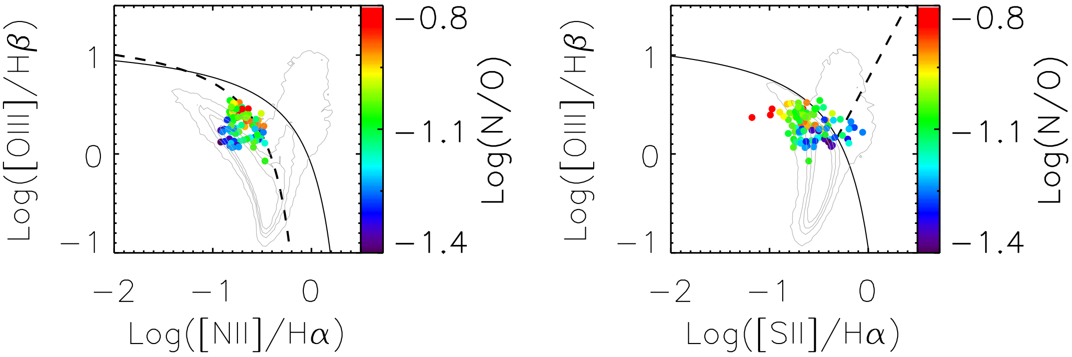

SP7

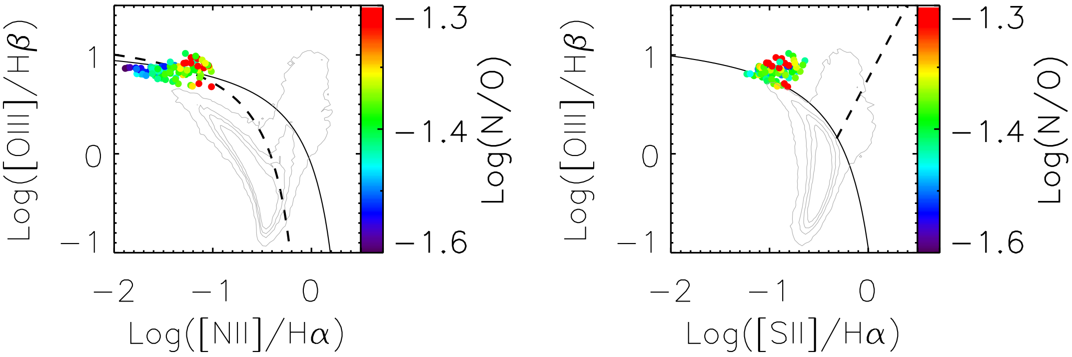

SP13

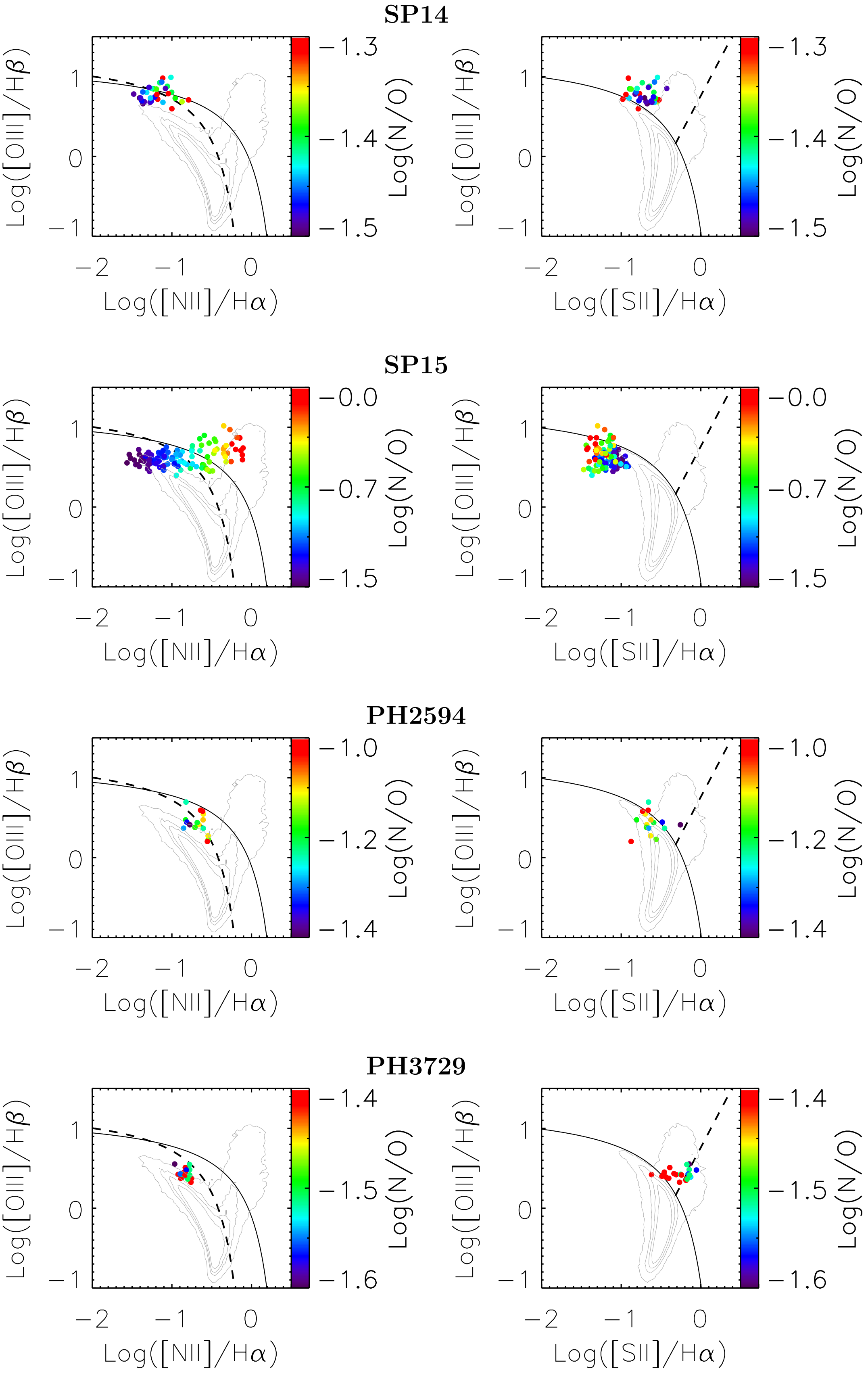
SP14
Log([OIII]/Hβ)
Log([NII]/Hα)
Log([SII]/Hα)
Log(N/O)
−1.3
−1.4
−1.5
SP15
−0.0
−0.7
−1.5
PH2594
−1.0
−1.2
−1.4
PH3729
−1.4
−1.5
−1.6
1
0
−1
−2
−1
0

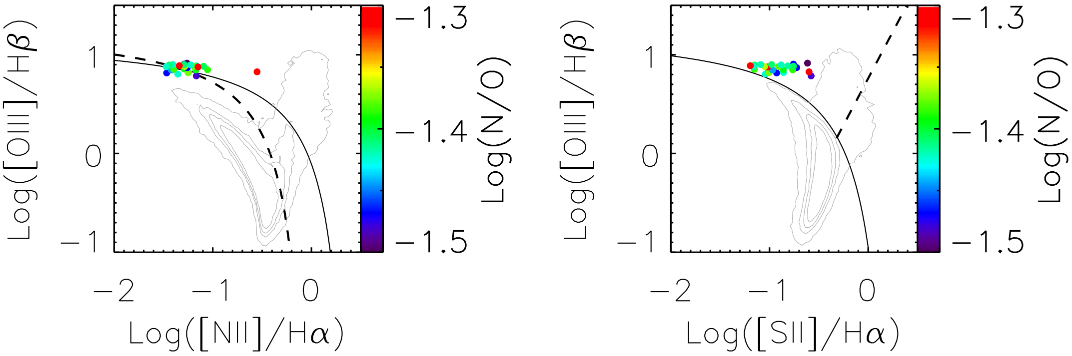
PH3912

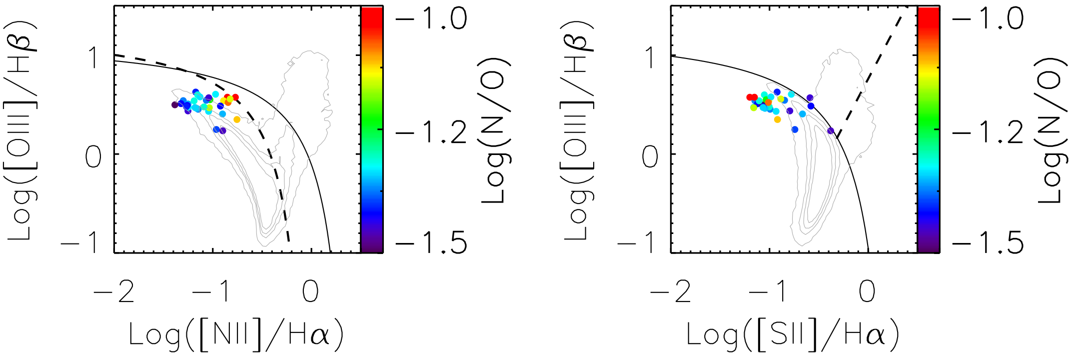
PH6532

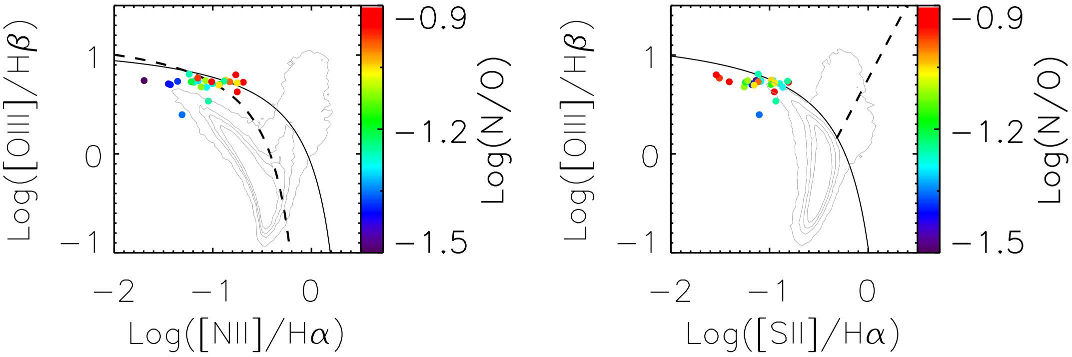
PH8073

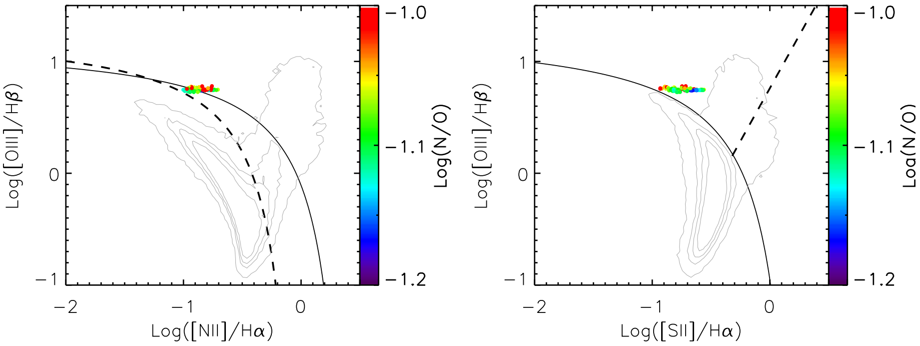
GLASS_00093-99-99

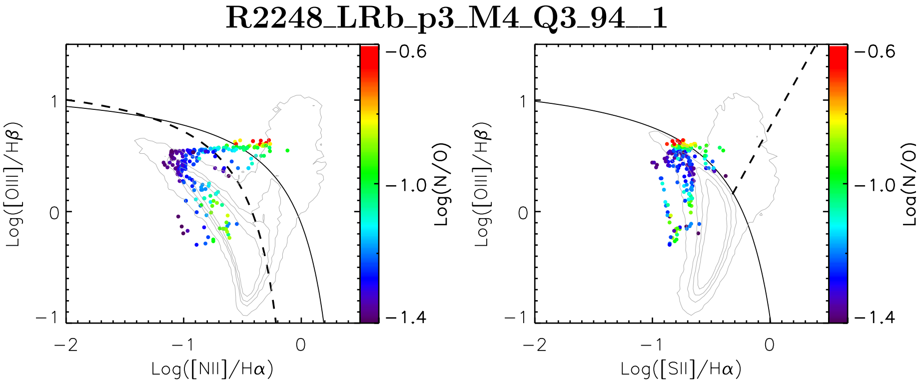
R2248_LRb_p3_M4_Q3_94__1
Log([OIII]/Hβ)
1
0
−1
−2
−1
0
Log([NII]/Hα)
Log([SII]/Hα)
−0.6
−1.0
−1.4
Log(N/O)

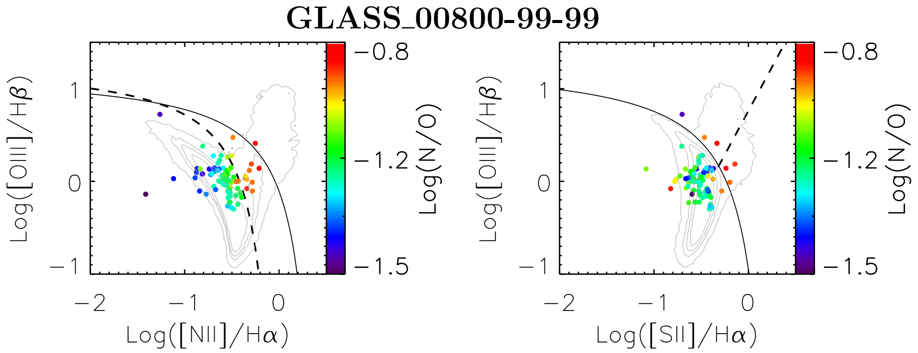
GLASS_00800-99-99
Log([OIII]/Hβ)
1
0
−1
−2
−1
0
Log([NII]/Hα)
Log([SII]/Hα)
−0.8
−1.2
−1.5
Log(N/O)

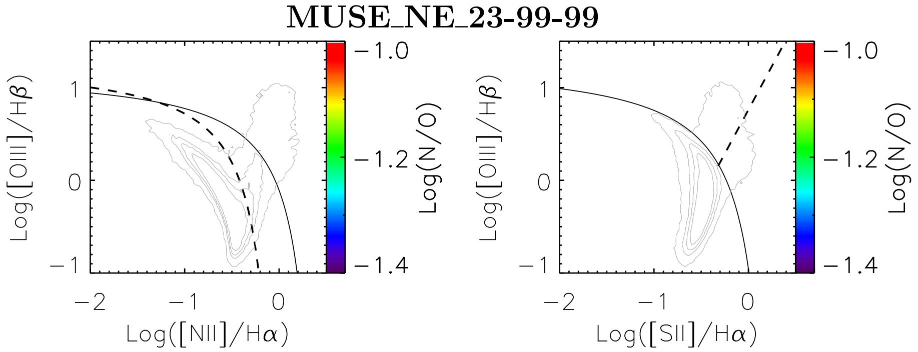
MUSE_NE_23-99-99
Log([OIII]/Hβ)
1
0
−1
−2
−1
0
Log([NII]/Hα)
Log([SII]/Hα)
−1.0
−1.2
−1.4
Log(N/O)

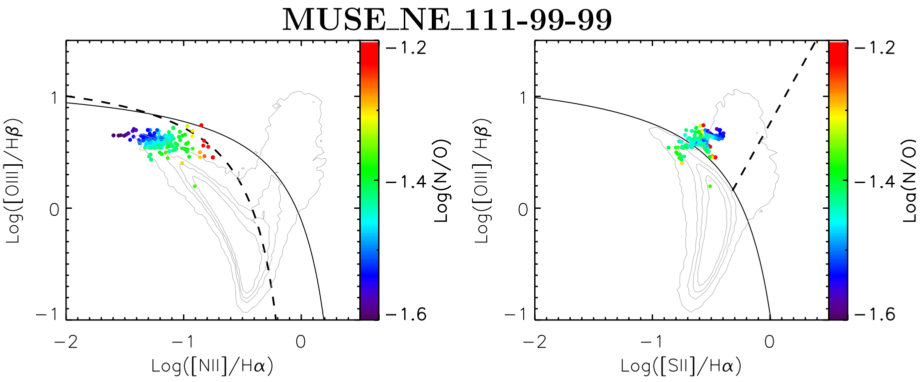
MUSE_NE_111-99-99
Log([OIII]/Hβ)
1
0
−1
−2
−1
0
Log([NII]/Hα)
Log([SII]/Hα)
−1.2
−1.4
−1.6
Log(N/O)

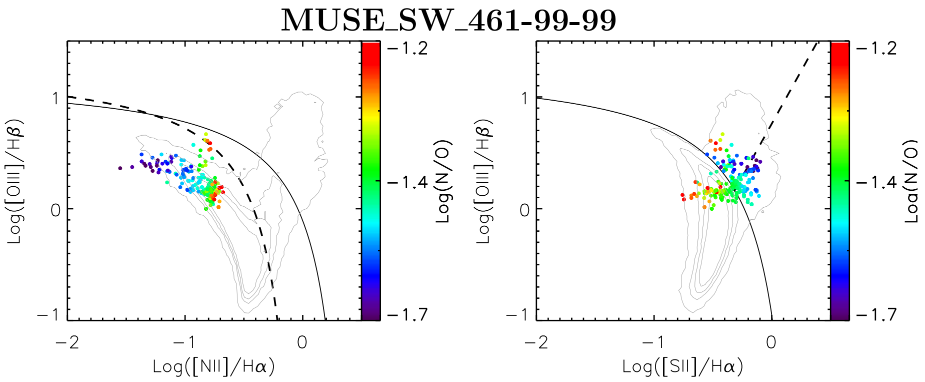
MUSE_SW_461-99-99

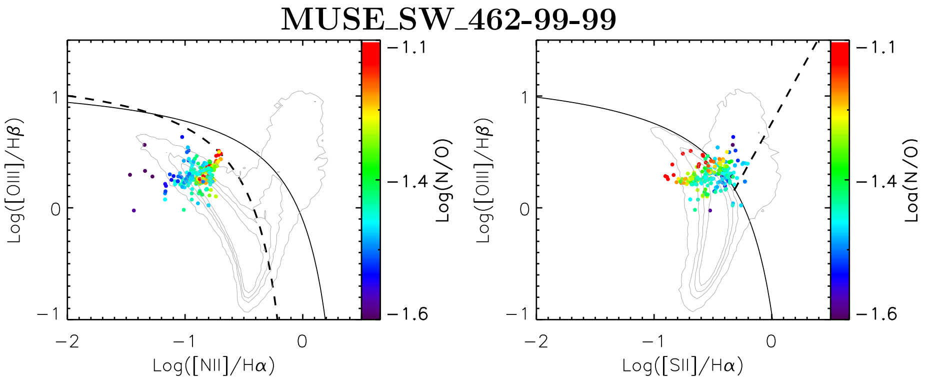
MUSE_SW_462-99-99

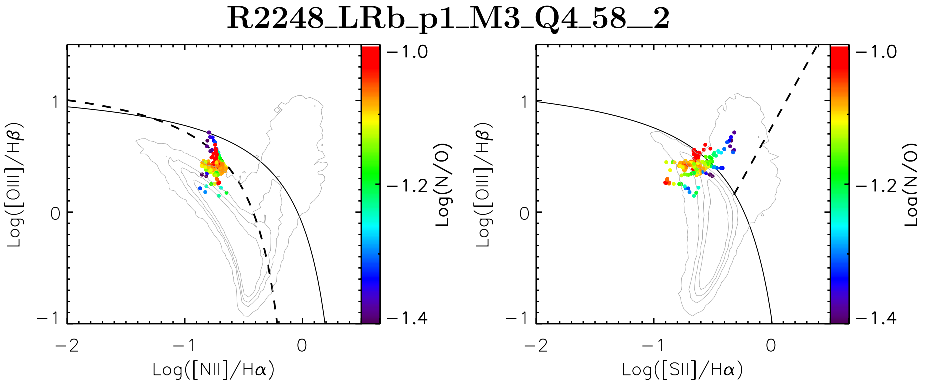
R2248_LRb_p1_M3_Q4_58__2

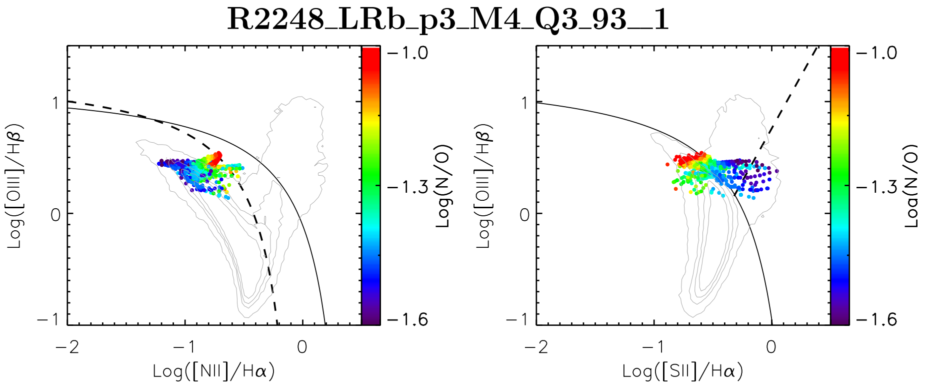
R2248_LRb_p3_M4_Q3_93__1

5

An ARGOS view of gravitationally lensed galaxies

We present the results from the first observations conducted at the LBT with the near-infrared imager and spectrograph LUCI, assisted by the ARGOS adaptive optics facility. This Chapter partially reproduce the draft of a paper submitted to Astronomy and Astrophysics as: Perna,M., Curti,M. et al., *LBT/ARGOS adaptive-optics observations of lensed galaxies at* $z\sim 2.5$ (2017, A&A, submitted).
These observations were obtained in the framework of the commissioning phase of the Adaptive Optics module ARGOS. I led the target selection, the preparation of AO observations and spectroscopic masks and the data analysis regarding the metallicity and ionization properties of the sample. Part of the data presented in the following have been obtained during two commissioning runs carried out in 2016, which I personally attended.

5.1 Introduction

The history of baryonic assembly in galaxies is governed by complex interactions between different astrophysical processes. The accretion of cool gas through cosmological infall of pristine and recycled material regulates both the star formation and the growth of the central supermassive black hole (SMBH) in the host galaxy. Galactic-scale outflows associated with stellar activity and SMBH accretion, depositing energy and momentum to the surrounding medium, are expected to affect the physical and dynamical conditions of infalling gas and the formation of new stars, preventing massive galaxies to overgrow and producing the red colors of ellipticals (see Somerville & Davé 2015 for a recent review).

Most star-forming galaxies (SFGs) and active galactic nuclei (AGNs) show evidence of powerful, galaxy-wide outflows. Spatially resolved optical, infrared and mm spectroscopic studies are revealing the extension, the morphology and the energetics related to the ejected multiphase material, both in the local Universe (e.g. Rupke & Veilleux 2013; Harrison et al. 2014; Arribas et al. 2014; Cicone et al. 2014; Feruglio et al. 2015) and at high redshift (e.g. Brusa et al. 2015; Förster Schreiber et al. 2014; Genzel et al. 2014; Harrison et al. 2012; Perna et al. 2015). In order to understand the physical processes responsible for the outflows and the long-term effects they may have on the global baryon cycle, host galaxy and outflow properties have been studied looking for causal relationships.

In AGN-dominated systems, outflow energetics seems to be related to the AGN power: faster and powerful winds are preferentially found in more luminous, massive and fast accreting nuclei (e.g. Cicone et al. 2014; Carniani et al. 2015; Fiore et al. 2017; Perna et al. 2017). AGN-driven outflow properties have been also related to star formation rate (SFR) in the host galaxy, in order to test the impact of these winds on the state of star forming gaseous clouds, but contrasting results have been found (e.g. Balmaverde et al. 2016; Lanzuisi et al. 2017; Mullaney et al. 2015; Wylezalek & Zakamska 2016).

SF-driven winds have also been investigated and several authors found that the incidence of outflows increases with the SFR (e.g. Rubin et al. 2014; Cicone et al. 2016). In SF-dominated systems, the effects of outflows can also be probed studying the relationships between SFR, stellar mass and gas-phase metallicity (Mannucci et al., 2010; Tremonti et al., 2004), because of the interconnection between accretion/ejection of material to/into the ISM and the physical conditions regulating the formation of new stars (e.g. Davé et al. 2011b; Lilly et al. 2013). In particular, the spatial distribution of the heavy elements abundances within a galaxy, keeping track of the effects of outflows, can constrain the baryonic assembly history (e.g. Gibson et al. 2013a).

Lensed galaxies and quasars offer a wealth of information to study galaxy evolution at redshift $1.5-3$, i.e. at the peak of star formation and AGN activity: magnification effect increases up to factors of tens the apparent size on the sky and the total flux of lensed sources. Ionized gas emission lines can be therefore used to characterize the internal kinematics and metallicity gradients on scales as small as 100 parsec, especially when exploiting the correction provided by adaptive optics (AO; e.g. Jones et al. 2010b, 2013; Leethochawalit et al. 2016; Shirazi et al. 2014; Stark et al. 2008; Wisnioski et al. 2015). In particular, the study of gravitationally lensed systems represents an ideal strategy to characterise the less massive systems at z$\sim$ 2.

In this chapter we present kinematic and chemical analysis of the first combined LUCI and ARGOS observations of five bright lensed galaxies at redshift z$= 2.0-2.7$.

LUCI is an infrared multi-mode instrument installed at the Large Binocular Telescope (LBT) which can work with the wide field "seeing enhancer" ARGOS facility (see Chapter 2); detailed discussion of the general performances provided by ARGOS, both in terms of spectroscopic and imaging capabilities, are discussed in Rabien et al., in prep. The selected arcs have been chosen on the basis of their observability during the scheduled ARGOS commissioning runs and the presence of bright proximate tip-tild guide stars. These systems are characterized by SFR in the range between 10 and 400 $M_\odot$/yr, and low stellar masses, in the range of $9.1 < \log(M_{star}/M_\odot) < 10.5$. All but one galaxy (J1343+4154) are therefore above the main sequence in SFR-$M_\star$ plane at z~ 2 (e.g. Whitaker et al. 2014; see Tab. 5.1). We characterize the physical properties of the lensed galaxies by combining the results we obtained by high spectral and angular resolution ARGOS data analysis with the available multiwavelength information, comprising recent lens modelling presented by Jones et al. (2013); Leethochawalit et al. (2016); Shirazi et al. (2014); Johnson et al. (2017a).

5.2 Observing strategy

The near-infrared (NIR) spectroscopic data presented in this chapter have been obtained in single and binocular mode with the two NIR multi-object spectrographs LUCI1&2, mounted on the Large Binocular Telescope (LBT) on Mount Graham, Arizona, USA.

The observations have been conducted during the commissioning of the Advanced Rayleigh guided star Ground Layer Adaptive optics System (ARGOS) facility (Rabien et al., 2010; Busoni et al., 2015). ARGOS is a multi-laser guide stars ground layer adaptive optics system, capable to correct for the ground layer turbulence above the two 8.4 LBT mirrors and provide an effective seeing improvement of a factor of $\sim 2-3$ over a 4x4 arcmin field of view Orban de Xivry et al. (2015). ARGOS is designed for operation with both LUCI multi-object spectrographs and NIR imagers: with the binocular operation mode, it is possible to obtain simultaneous acquisitions with identical or independent instrument configurations for the two LBT mirrors (e.g. taking for a given target the spectra in two bands), significantly reducing the time needed for an observing program.

The targets were originally selected according to their visibility, lensing magnification, redshift (in order to ensure the presence of the emission lines of interest in the proper wavelength range) and presence of a nearby suitable star for tip-tilt correction in the field. The spectroscopic masks to be installed into LUCI for observations were designed exploiting the Lucifer Mask Simulator (LMS) software, which implement the

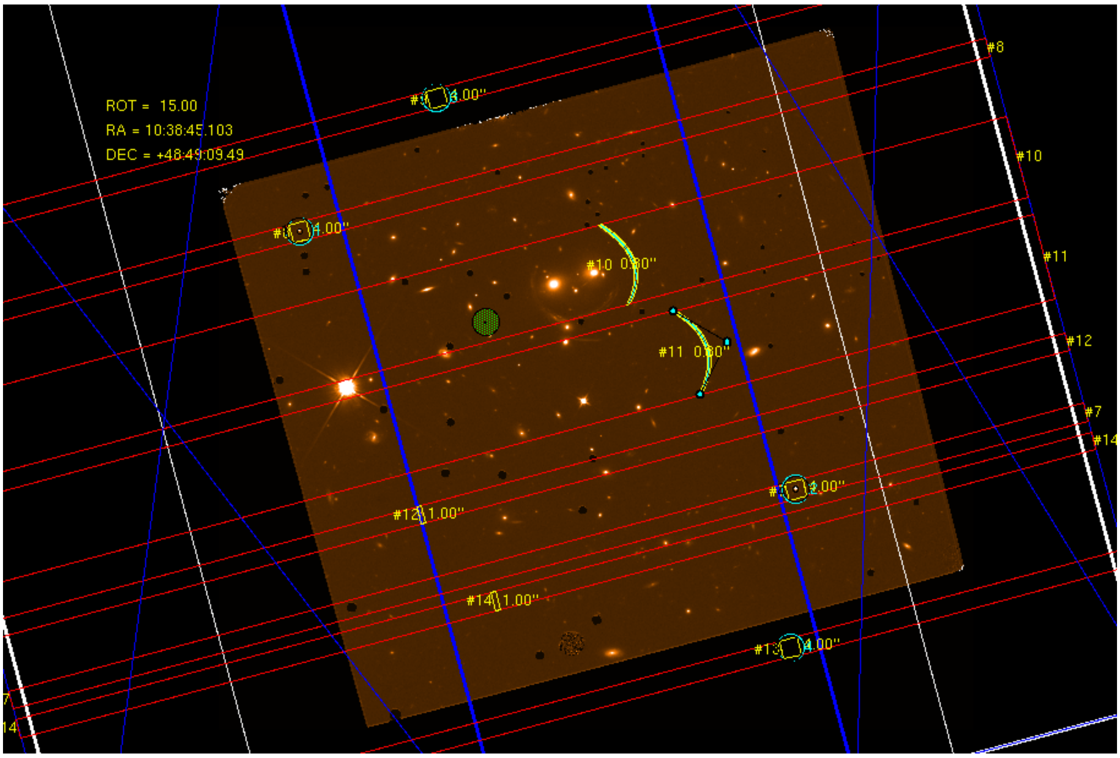

Figure 5.1: Spectroscopic mask created with the Lucifer Mask Simulator (LMS) for the observations of J1038. Slits labeled #10 is the curved slit designed to follow the entire arc-like shape of the target on the sky. The slit is exactly replicated (#11) in a nearby empty region of the field to perform the nodding between the A and B position of the acquisition sequence. The 4x4 arcsec^2 square slits target the reference stars for initial mask alignment, while an 1" wide slit (#12) is placed (and replicated, #14) on a bright continuum source to aid the offsets execution and verify the correct alignment between the two positions of the pattern. Horizontal red lines encloses the region of the detector where the spectra of the different targets are dispersed. The green circle mark the centre of the field of view.

possibility to generate curved slits; in this way we could precisely reproduce the shape of the lensed arc on the sky in order to obtained resolved properties of the galaxy along the entire slit. Up to 20 MOS-slits can be positioned and at least 3 reference stars are required for mask alignment and to derive the exact dithering pattern during the sequence of acquisitions. Our masks were designed to conduct MOS observations based on a 'A-B-A-B' sequence, in a way similar to a classical *nodding* strategy even if, in our case, nodding does not occur along the same slit but between two different slits. This means that, in practice, the curved slits for lensed arcs were manually replicated in two different positions of the mask in order to take a spectrum of the scientific object in every frame, while taking a spectrum of a blank sky position at the same time (see Fig. 5.1). This allowed to avoid losing time in acquiring dedicated sky frames. B-frames are then subtracted from A-frames to perform the sky background subtraction, which is crucial for every observation in the near-infrared (see Sec. 5.3 for details on data reduction). Since our scientific targets are intrinsically faint in each single exposure their spectrum is completely dominated by sky lines, thus we put a 1"-wide slit on two (or more) bright stars within the field, to be sure that the mask was properly aligned at each step of the dithering pattern by checking the presence of the continuum emission of the stellar spectrum in these "reference slits". The maximum offset that can be performed in order not to loose the tip-tilt star acquisition by the ARGOS system is of the order of 20"; when inside this range, offsets between the two different positions of the observing pattern can be automatically performed by the software while keeping the AO loop closed.

For each lensed galaxy, 0.25" (i.e. 2-pixel slit, sampling limit of the N3.75 camera) or 0.5" wide curved-slits, matching the arc's geometry on the sky, have been designed on the basis of available high resolution HST images. When the systems were not covered by HST observations, LUCI/ARGOS images have been obtained and used to define the slit. All but one target were observed in one or two filters (H or K), depending on the spectroscopic redshift. For J0022+1431 (J0022 hereinafter), a lensed system at z$\sim$ 2.7, we used a clear filter to detect Hα line at 2.45μm: in this wavelength region the K filter transmission is very low, as the line is expected where the thermal continuum contribution is significant. For all but one target, we used the combination of the G210 grating and the N3.75 camera, for nominal resolutions of R$\sim$ 5000 and 5900 for H and K bands respectively, and a pixel scale of 0.12"/pixel. The G150 grating, with a nominal R of $\sim$ 4150 for the K-band, was used for J13432. The targets were acquired with dithered 150s observations. The HST/LUCI images on our targets, with the curved slits superimposed, are show in Fig. 5.2, while the main information regarding the observations for each object are reported in Table 5.1.

5.3 Data reduction

Near-infrared multi-object spectroscopic data have been reduced with a custom set of routines (courtesy of M. Perna) and optimized to reduce LUCI observations with curved slit MOS configuration. The main steps of the data reduction are briefly summarized in the following, as well as illustrated by some simple sketches in Fig. 5.3. After the removal of cosmic rays using the L.A. Cosmic procedure (van Dokkum, 2001), we corrected for the non-linear response of the detector following the prescriptions described in the LUCI User Manual. We separated the frames belonging to the A and the B positions respectively using a dedicated slit with a star devoted to trace the position of each frame on the detector y-axis (the spatial direction; the spectral direction is along the horizontal axis; see Fig. 5.3, step 1). We measured the reference star position using the spatial profile constructed integrating the stellar continuum within a 100 pixel sky-line free interval along the x-axis. From a Gaussian fit of the

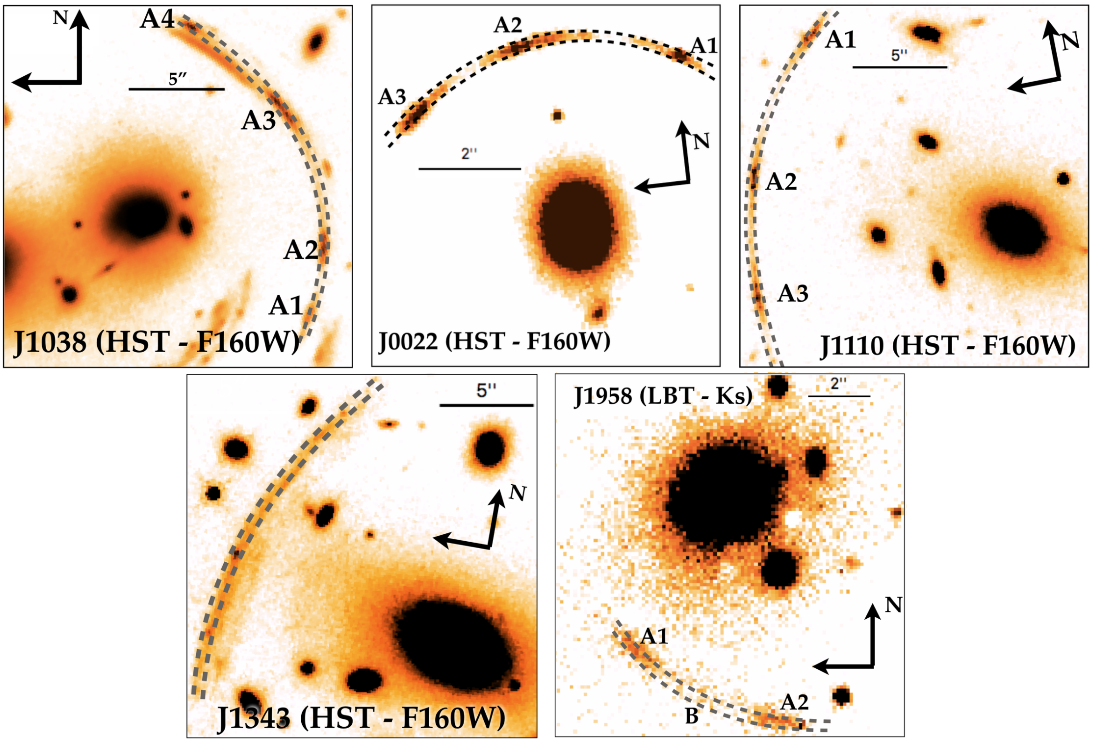

Figure 5.2: Infrared HST and LBT/ARGOS images of the galaxy sample studied in this work. Scalebars and target names are labeled in each figure. We labeled the lensed galaxy components according to the definitions proposed throughout the work. For each cut-out, we show with dotted curves the curved slit we defined for observing the target.

spatial profile we then derived the star position (from the Gaussian centre) and the spatial resolution (from the FWHM) associated with the individual frame. Then, we extracted from the MOS image the A and B 2-dimensional spectra slices within the edges of the curved slits, taking into account the dithering pattern (Fig. 5.3, step 2).

We corrected the curvature of the 2D spectra by performing a rectification so that the spatial and spectral channels were all aligned in dispersion and spatial pixel space (Fig. 5.3, 3rd panel). This step is based on the identification of individual bright sky emission lines, which can be reliably used to trace the variations in the spectral dispersion pixel scale along the Y axis. Due to grating instability during the acquisition of subsequent frames, we referred all the rectified spectra for a given instrument configuration to the spectral dispersion pixel scale of the first scientific frame.

We removed the sky lines and background emission by subtracting the 2D frames of the B dither position from the A dither position (and viceversa), pairing subsequent frames (Fig. 5.3, step 4). We coadded all the A sky-subtracted spectra and all the B sky-subtracted spectra separately. Finally, after a wavelength calibration performed using OH sky lines, we combined the A and B spectra.

Flux calibrations were performed using the 2MASS magnitudes of the reference stars. For J1038+4849 (J1038 hereinafter) and J0022 we used emission line fluxes

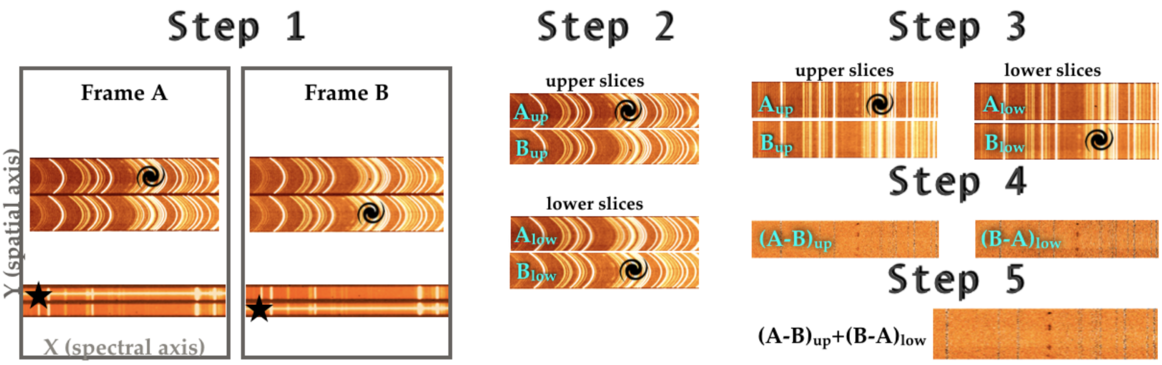

Figure 5.3: Sketch to illustrate some of the steps of the data reduction (see Sect. 5.3 for the complete data reduction procedure used in this work). For clarity, the diagram show a set of just two subsequent frames. The first two panels show a sketch of a 150s exposure through a MOS mask designed to observe a science target and a reference star with two dither positions. The panels display the 2D spectra obtained from the two curved slitlets (in the upper side), dedicated to the science target, and two long-slits (in the lower part), to allocate the reference star spectrum. The extended structures observed in the upper spectra, due to sky emission lines, highlight the strong distorsion caused by the curved slitlets. In the first panel (frame A) the target and the reference star are in the relative upper positions: J1038+4849 Hα emission line blobs can be distinguished in the figure (in the vicinity of the spiral symbol), as well as the stellar continuum (next to the star symbol). In the second panel (frame B) the objects are in the relative lower positions. The insets in the Step 2 show the extracted slices from the upper and lower positions, distinguishing between A and B spectra. These 2D spectra are then displayed in the Step 3 part of the diagram, after the rectification. Step 4 shows the A-B and B-A results for both upper and lower slices (the colorbars here are inverted for a better visual inspection of the Hα knots). Finally, Step 5 shows the final 2D spectrum obtained from the combine of the Step 4 intermediate products.

derived from IFU spectroscopic data published by Jones et al. (2013) (for J1038) and long-slit spectra by Finkelstein et al. (2009) (for J0022) to test the reliability of our calibration: a very good agreement (within 20%) has been found comparing integrated emission line fluxes from the same images covered by their observations.

In Table 1 we reported the information about median spatial resolutions derived from the observations. We note that spatial resolutions lower than the ones reported in the table have been usually measured in individual frames, i.e. FWHM values as small as 0.25 – 0.30". In this work, however, we decided to use the entire set of frames to gain higher signal-to-noise spectra; as a result, the final angular resolution is slightly larger.

The final 2D spectra we obtained from the data reduction are reported in Fig. 5.4, 5.6, 5.7 and 5.9. In the next sections we briefly discuss the general spectroscopic analysis.

Galaxy properties and observations log

Name (1)	z (2)	Coordinates (3)	log($M_\star$) (4)	SFR (5)	Dates (6)	Band (7)	slit width (8)	TOT (9)	seeing (10)	FWHM (11)	resolution (12)
J1038	2.197	10:38:42 +48:49:19	$9.1^{+0.2}_{-0.1}$	40 ± 2	03/2017	H	0.3"	4h 20m	1.0"	0.52"	1.0 kpc
						K		3h 47m	1.0"	0.43"	0.8 kpc
J1958	2.225	19:58:35 +59:50:59	9.9 ±0.1	250^{+71}_{-142}	05/2017	H	0.3"	30m	1.18"	0.50"	0.6 kpc
						K		27m	1.03"	0.32"	0.4 kpc
J0022	2.735	00:22:41 +14:31:14	$10.5^{+0.5}_{-0.6}$	390 ± 20	10/2016	(K)	0.3"	1h 30m	1.04"	0.43"	0.9 kpc
J1110	2.480	11:10:16 +64:59:17	9.5 ± 0.4	15^{+15}_{-4}	05/2016	K	0.5"	1h 20m	0.98"	0.41"	0.9 kpc
J1343	2.092	13:43:36 +41:54:29	10.0 ± 0.3	12 ± 11	05/2016	K	0.5"	35m	0.97"	0.41"	0.7 kpc

Table 5.1: Column (1): lensed galaxy name as reported in the paper. Column (2): spectroscopic redshift. Column (3): Coordinates of the lensed sources (RA and Dec). Column (4): stellar masses for J1038 from Jones et al. 2013, J0022 from Shirazi et al. 2014, J1343 from Saintonge et al. 2013, J1110 from Johnson et al. 2017a, with nominal correction from a Chabrier to a Salpeter IMF when required. Stellar mass of J1958 from this work (see Sect. 5.4.3). Column (5): SFR from the Hα flux corrected for extinction and lensing magnification using Kennicutt 1998 relation (J1958 and J1343 from Leethochawalit et al. 2016); J0022 from Shirazi et al. (2014), using the Hβ flux). SFR of J1110 from the value reported inJohnson et al. 2017a and obtained by SED fitting analysis, nominally corrected from a Chabrier to a Salpeter IMF. Column (6): observing dates (MM/YYYY). Column (7): LUCI filters; for J0022, we used a clear filter to detect Hα line redshifted at 2.45μm. Column (8): curved slit width. Column(9): Total on source integration time. Column (10): seeing as measured by the DIMM station. Column(11): spatial FWHM obtained integrating the reference star flux within a 100 px interval along the X axis. Column (12): estimate of the spatial resolution in the source plane. For J1038, J0022 and J1110 we used the values derived by Jones et al. 2013,Shirazi et al. 2014 and Johnson et al. (2017a), respectively, which refer to the A2 knots.

5.4 Analysis

5.4.1 Emission line fitting

Figures 5.4, 5.6, 5.7 and 5.9 show the one-dimensional integrated rest frame spectra, extracted in $7-18$" apertures, according to the presence of distinct blobs and extended arc-like emission line systems along the spatial direction in the 2D spectra. The aperture tracing along the dispersion axis, for each lensed galaxy, has been performed using the relative "reference star" as a guide and applying the same tracing to the target spectra.

For each source, we defined the systemic redshift from the best fitting solution which give the wavelengths of narrow components of the detected rest-frame emission lines in the integrated spectra. Spectral fit have been performed following the prescriptions described in Brusa et al. (2015). We used Levenberg-Markwardt least-squares fitting code MPFITFUN (Markwardt, 2009) to reproduce simultaneously all the detected optical emission lines with Gaussian profiles. Because of the presence of asymmetric line profiles, different sets of Gaussian profiles have been used to reproduce the emission lines in J1958+5950 (J1958 hereinafter) and J1038. For each set of Gaussians, we imposed the following constraints: the wavelength separation between emission lines is constrained in accordance to atomic physics; the relative flux of the single components of the [N II]λ6548,6584 and [O III]λ4959,5007 doublets is fixed to 2.99. We excluded from the fit the regions where significant sky-subtraction residuals downgrade the emission line profiles (e.g. Fig. 5.4, gray shaded area).

5.4.2 Kinematics

To better characterize the kinematic properties of our targets, we used the a non-parametric approach, which does not depend on the number of Gaussian components used to fit the emission lines. Non-parametric velocities are obtained measuring the velocity v at which a given fraction of the total best-fit line flux is collected using a cumulative function, for the best fit [O III]λ5007 and/or Hα line profiles, depending of the wavelength coverage of our observations. The zero point velocity is defined adopting the systemic redshift derived from the integrated spectra. In particular, we define V10 and V90 as the velocity corresponding to 10% and 90% of the flux (the former being always negative, the latter positive), and W80 (i.e. the line width defined as the difference between the velocity at 90% and 10% of the cumulative flux) is closely related to the velocity dispersion for a Gaussian velocity profile, and is therefore indicative of the line widths, while maximum velocities are mostly used to constrain outflow kinematics when prominent line wings are found (e.g. Cresci et al. 2015; Cano-Díaz et al. 2012; Perna et al. 2017). The velocity corresponding to the peak of the flux density (V_{peak}) is used instead as a kinematic tracer for rotating disk emission in the host galaxy.

5.4.3 Source properties

SDSS J1038

SDSS J1038+4849 is a lensed system associated with a relatively poor group of galaxies at z~ 0.45, dominated by two luminous elliptical galaxies. Belokurov et al. (2009) and Bayliss et al. (2011) identified four major rings systems associated with background galaxies at redshift 0.80, 0.97, 2.20 and 2.78 respectively. This system is also known as the *Cheshire cat* (from Lewis Carroll's famous novel *Alice's Adventures in Wonderland*, 1866) gravitational lens because of the smiling cat-like appearance defined by the spatial configuration of the foreground and background lensed galaxies.

Archival observations taken with HST WFC3 using the F390W, F110W and F160W filters are available for this target. Part of the extended arc structure has been already observed with the NIR integral field spectrograph OSIRIS at Keck II and K-band

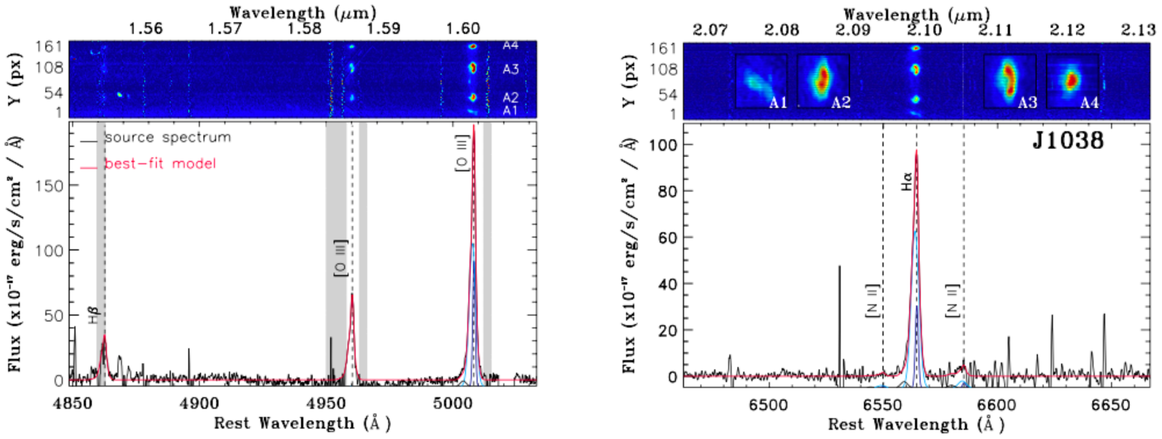

Figure 5.4: Integrated H-band (*left panel*) and K-band (*right panel*) spectra of J1038. Superimposed on the spectra are the best-fitting components, with arbitrary normalization to aid visualization; the red solid curve shows the best-fitting sum of all components. The dotted lines mark the wavelengths of the most prominent emission lines. The regions excluded from the fit, corresponding to the brightest sky lines, are marked as shaded grey areas. For each spectrum, the upper part of the panel shows the observed 2D spectrum (blue to red colors represent increasing fluxes). Labels in the 2D spectra locate the regions from which we obtained the 1D integrated spectra associated with the different knots. In the K-band spectra, we also show a zooom-in portion of the 2D spectrum, associated with the four different Hα knots. The features at ~ 1.558μm in the H-band 2D spectrum are associated with some persistences of the LUCI's detector.

spectroscopic results have been presented by Jones et al. (2013). ARGOS observations cover entirely the arc associated with the galaxy at z = 2.20 and previously observed with Keck II. Figure 5.4 shows the integrated spectrum around the Hβ+[O III] and Hα+[N II] lines, redshifted in H- and K-band respectively. As mentioned in the previous section, we fitted all the emission lines simultaneously using atomic physics constrains and the same kinematic components for each set of Gaussian profiles. Because of the presence of strong sky line residuals affecting the blue wing of the Hβ, we constrained the amplitude ratio of the different Gaussian sets to be the same for the two Balmer lines.

HST images shows that this arc-like structure is composed of multiple overlapping arcs and knots. Three luminous knots are easily distinguishable (A2, A3 and A4 in Fig. 5.2), and a fainter image (A1) can be identified at the lower end of the arc. All these knots are seen in ARGOS spectra, especially in [O III] and Hα lines (see Fig. 5.4, top panels). A3 is the more elongated structure and presents two small sub-systems both in HST images and NIR 2D spectra, with the northest one showing greater extension at shorter wavelengths. The same sub-systems may be tentatively recognized also in A2 and A4 images (see the insets in the top right panel), but with blueish extension in the south sub-components. These kinematically resolved shapes in [O III] and Hα line knots in 2D spectra may suggest that A2, A3 and A4 are different images of the same physical region, with A3 inverted with respect to the others (see e.g. Johnson

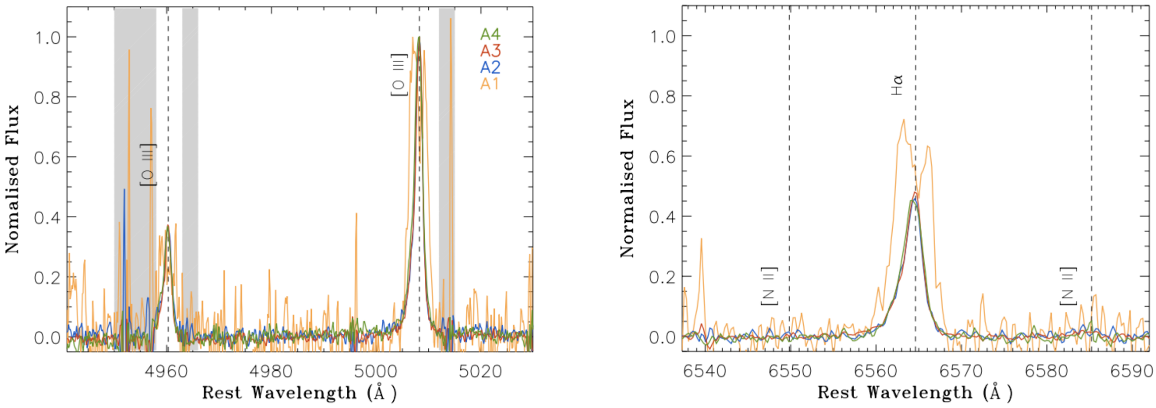

Figure 5.5: J1038 integrated spectra of the four bright knots, color-coded as labeled in the left panel. Grey shaded regions mark the wavelength ranges mostly affected by sky-line residuals and that have been excluded from the spectral fit. To facilitate the comparison, we normalized the fluxes so that the intensity of the [O III] line is unity for each integrated spectrum.

et al. 2017b for an analogue configuration in a different lensed galaxy). The shape of A1 is instead quite different; this image is likely part of the same lensed galaxy but, if lying outside the caustic region, could not be multiply imaged. Finally, we also note the presence of a small faint knot between the A2 and A3 images, noticeable in the [O III]λ5007 emission line and fairly resolved in Hα, blueshifted with respect to the bulk of the doubly ionised emission.

To assess if these blobs are related or not to the same emitting regions, as a first step, we compared their one-dimensional integrated spectra. We reported in Fig. 5.5 the spectra extracted from the regions in the proximity of brightest knots associated with [O III]λ5007 and Hα (we consider the regions within 5σ contours; see labels in 2D spectra, Fig. 5.4). We also extracted the spectrum from the fainter blob (A1) considering the regions within 2σ contour levels. The spectral analysis revealed that A2, A3 and A4 are characterised by similar kinematic properties, with W80 = 150 km/s. The spectrum associated with A1, although affected by lower S/N, is instead significantly different: broad (W80 ≈ 220 km/s), double peaked profiles are recognized in the more prominent emission lines. Moreover, we notice that the values of the [O III]/Hα and [O III]/Hβ line ratios are consistent, given the observational uncertainties, for A2, A3, and A4, while A1 shows significantly different line ratios. This supports our interpretation that A1 might not be a counter-image of the source plane region responsible for the A2, A3 and A4 knots on the image plane, but rather a different emitting region (e.g. associated with a merging companion, see also Jones et al. 2013).

SDSS J1958

SDSS J1958+5950, the giant arc at redshift z = 2.225, is lensed by a rich galaxy cluster at redshift z = 0.24, discovered by Stark et al. (2013). This source does not have HST

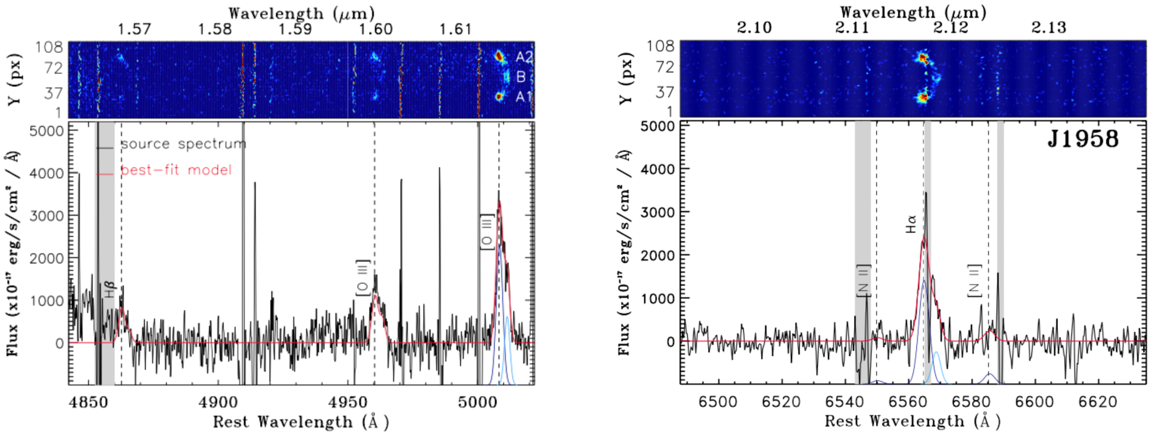

Figure 5.6: Same as Fig. 5.4 for J1958.

images available; we obtained ARGOS image in Ks-band in the commissioning night of May 19th 2016, using LUCI 1, with a total integration time of 74 minutes (Fig. 5.2). The system is comprised of three images and extends over ≥ 5" .

Figure 3 (bottom panels) shows the integrated spectra around the Hβ+[O III] and Hα+[N II] lines, detected in the H- and K-band respectively. Because of the low S/N and the presence of intense sky lines in the proximity of Balmer lines, we constrained, also for this target, the relative amplitudes of Gaussian profiles used to fit the Hβ and Hα lines. The best-fit shows the presence of two distinct Gaussian components in each emission line. These components are also easily visible in the 2D spectra (insets in the bottom panels of Fig. 5.6). As for the targets previously presented, we compared the spectra of A1 and A2 images and proved that they are reasonably related to the same emitting region in the source plane. The central image (B), barely distinguishable in the Ks-band LBT image, appears instead redshifted by ≈ 180 km/s. From the kinematical analysis of the [O III] emission, we infer that the peak-to-peak velocity amplitude between the A1, A2 images and the central B knot is ≈ 200 km/s, while maximum velocities vary by a factor of two: this may indicative of the presence of two different lensed galaxies caught during an ongoing interaction (fully consistent with recent findings from IFU observations, Leethochawalit et al. 2016), rather than an induced motion within the galaxy's gravitational potential.

J0022

J0022+1431 was discovered by Allam et al. (2007), from visual inspection of an SDSS imaging data catalog of candidate interacting/merging galaxy pairs. Follow-up imaging and spectroscopy revealed that this system, dubbed the 8 o'clock arc, is associated with a bright Lyman break galaxy at z = 2.73 strongly lensed by a z = 0.38 red galaxy. The system has been observed with HST/NICMOS (using the F110W and F160W filters; see

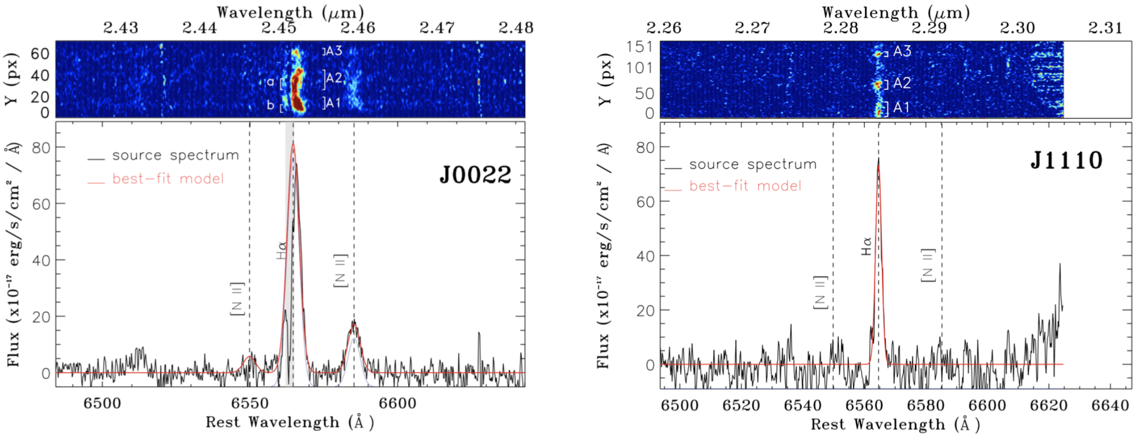

Figure 5.7: K-band spectra for J0022 (*left panel*) and J1110 (*right panel*) respectively. See Fig. 5.4 for details.

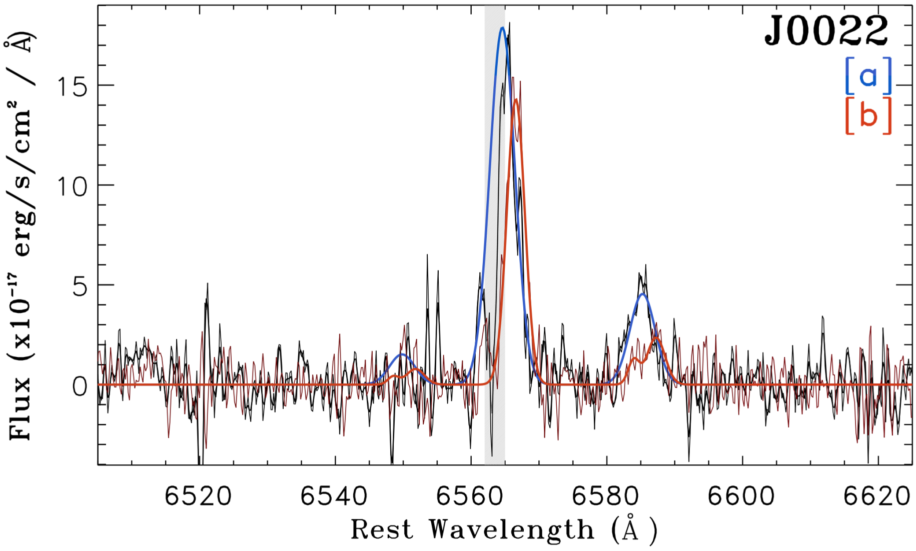

Figure 5.8: J0022 spectra around the Hα+[N II] lines, extracted from the a and b regions defined along the curved-slit (see Fig. 5.7, left panel). The spectra and best-fit models reproducing the line profiles are color-coded according to the labels in the figure.

Fig. 5.2), and with HST/WFPC2 (F450W, F606W, F814W). Long-slit spectroscopic follow-up observations have also been obtained covering part of the elon- gated structure with Keck LRIS (optical) and Gemini NIRI (NIR; Finkelstein et al. 2009), and with VLT/X-Shooter (UV to NIR; Dessauges-Zavadsky et al. 2010, 2011). Integral field NIR spectroscopic data have been obtained at VLT/SINFONI, mapping for the first time the entire extension of the arc in H-band (Shirazi et al., 2014). The study of the most prominent optical emission lines of J0022 has been limited by observational constrains: [O III]λ5007 line fall outside the H band ($\lambda_{obs} \sim 1.87\mu$m), while the H$\alpha$ is redshifted at $\sim 2.45\mu$m in the proximity of a strong atmospheric sky-line.

In Figure 5.7 (left panel) we show the LBT/ARGOS integrated spectrum over the entire curved-slit, with our best-fit model overimposed. The presence of bad sky-line residuals strongly affect the blue wing of the Hα line. The LBT/ARGOS 2D spectrum of J0022 shows the presence of a prominent knot in the lower part and a fainter one in the central part of the slit, connected by an extended arc; an additional knot is fairly distinguishable in the upper part. Overall, the elongated structure and the three images can be related to the arc shown in the HST image. The Hβ flux map of the arc obtained by (Shirazi et al., 2014) using the IFU instrument SINFONI shows relative fluxes between the three images which are very similar to those observed in the LBT/ARGOS spectrum. Therefore, differential slit losses are not at the origin of the non-perfect match between F160W image and 2D spectrum (especially regarding the A1 image intensity). As for J1038, we compared the integrated spectra extracted from the three different knots and derived consistent non-parametric measurements, with W80 ≈ 235 km/s and V10 ≈ -100 km/s. This allows us to asses that the images can be related to a unique emitting region in the source plane, confirming the previous results based on the analysis of the faint Hβ line (Shirazi et al., 2014).

The bad sky-line residuals affecting the blue wing of the Hα line do not allow a reliable kinematic analysis along the Y axis. The presence of distinct kinematic components is, however, notable from the 2D spectrum in Fig. 5.7, showing blueish emission lines in the region between A1 and A2. In order to quantify the kinematic variations along the curved-slit we extracted two additional spectra from y=[26-36], corresponding to the central part of the arc, and from y=[5-12], where more prominent Balmer emission is detected; the derived best fit models reproducing the spectra are shown in Fig. 5.8. The observed significant differences are mostly due to the emission line shift between the two spectra, with ΔV peak ≈ 90 km/s. Possible interpretations for this velocity shift may be the presence of strong outflows or, alternatively, of a merger; the former hypothesis is consistent with previous findings from UV rest-frame (Finkelstein et al., 2009; Dessauges-Zavadsky et al., 2010) and NIR IFU (Shirazi et al., 2014) spectroscopy.

J1110

J111020.0+645950.8 (J1110 hereinafter) is a giant arc at z = 2.48 lensed by a galaxy cluster at redshift 0.66. It was discovered as part of the CASSOWARY survey (Stark et al., 2013) and is composed by three main images (A1, A2 and A3; Fig. 1) covering ~ 17" on the sky. Archival HST/WFC3 (UVIS and IR) images reveal the presence of bright emission knots within the three overlapping images. Johnson et al. (2017b) identified the same individual clumps within the three images and confirmed that are associated with the same emitting region in the source plane.

In Figure 5.7 (right panel) we show the LBT/ARGOS integrated spectrum over

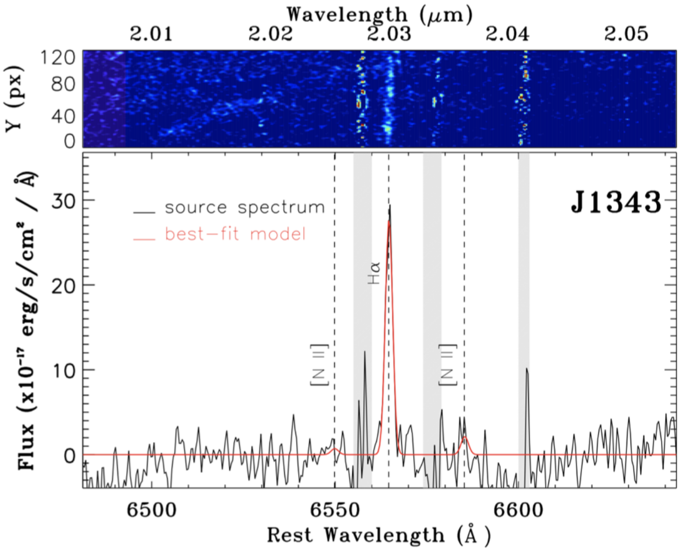

Figure 5.9: K-band spectra for J1343. See Fig. 5.4 for details.

the entire curved-slit, with superimposed best-fit model. The Hα emission line is well reproduced with a single narrow Gaussian profile. However, the 2D spectrum shows more complex kinematics, with different knots elongated along the velocity axis. As for J1038, we derived a kinematic map of the Hα emission line analysing 1D spectra extracted along the Y axis. The variations observed in the non-parametric measurements are much smaller than the ones revealed in the previously analyzed sources; on the basis of this consideration we may exclude a significant contribution of mergers or outflows in the observed kinematics.

J1343

SDSS J1343+4155 (J1343) was reported for the first time by Diehl et al. (2009); the arc is lensed by a rich galaxy cluster at z ~ 0.42 with a bright central luminous red galaxy. Archival HST/FWC3 (UVIS and IR) images reveal the presence of bright emission knots within a 20" elongated arc (Fig. 5.2).

The Hα spatial distribution in ARGOS 2D spectrum (Fig. 5.9) well reproduces the clumpy structure observed in HST images. The integrated spectrum reveals the possible presence of [N II]λ6584 emission line (detected at ~ 2σ level); line features are narrow and symmetric, with W80 ≈ 120 km/s. The Hα emission line seems to show a shallow velocity gradient along the spatial dimension of the curved-slit. IFU OSIRIS observations of J1343 have been recently reported by Leethochawalit et al. (2016), which classified this galaxy as a rotationally supported system, consistently with our LUCI observations.

5.4.4 Diagnostic diagrams and chemical abundances

BPT diagram

In Fig. 5.10 we show the BPT diagram for the two sources observed in both H- and K-band, thus with detected and measured [O III]λ5007/Hβ and [N II]λ6584/Hα emission line ratios. For each source, we report both the flux ratios derived from the individual images along the arcs and the one measured from the total integrated spectra shown in Fig. 5.4. The theoretical, redshift-dependent dividing lines, used to separate purely star-forming galaxies from AGN-like sources, are drawn for z = 0 and z= 2.2 with the solid and dashed curve respectively, according to Eq. 1 of Kewley et al. (2013). Due to the large uncertainties affecting the flux ratios, we can not completely exclude the presence of an AGN contribution to the ionization in these sources, neither can we distinguish between possibly different ionization states between the different knots associated to a given galaxy, since all of them appear consistent within the errors. We note, however, that the observed, large [O III]λ5007/Hβ ratios are consistent with values usually reported for high redshift galaxies in the literature at z ~ 2 (e.g.Steidel et al. (2014); Shapley et al. (2015); see also Sec. 1.1.3), and could be attributed to more extreme ISM conditions than seen in the global spectra of local galaxies, rather than AGN ionisation. The concomitant presence of asymmetric emission line profiles in our two lensed galaxies, possibly associated with a merger (J1958) and the presence of outflows (J1038) fits with this scenario.

For J1038, we also estimated the diagnostic ratios possibly associated with outflowing gas for the integrated spectrum and the A2, A3 and A4 knots. Outflow emission has been measured from the v< −50 km/s fluxes, i.e. considering only the blue asymmetric extension of the line profiles (the maximum redshift velocity is ≈ 50 km/s; see Fig. 5). We note that the flux ratios associated with outflows are shifted to higher [N II]λ6584/Hα. This is generally observed in SF-driven (e.g. Ho et al. 2014; Newman et al. 2012) and AGN-driven (e.g. Perna et al. 2017) outflows and is interpreted as due to shock excitation (e.g. Allen et al. 2008). On the basis of these arguments, we argue that the observed asymmetric line profiles are due to SF-driven outflows.

The three sources observed only in the K band are characterized by [N II]λ6584/Hα ratios comparable to those of J1038 and J1958 (see Table 5.2). Also in this case, therefore, we can not completely rule out the presence of AGNs in these systems, from only N2-based considerations. We note, however, that at low masses, i.e. log(M$_\star$ ≤ 10.5, the effect of AGN contribution to the ionization is expected to be limited (e.g. Wuyts et al. 2016; Genzel et al. 2014; Leethochawalit et al. 2016).

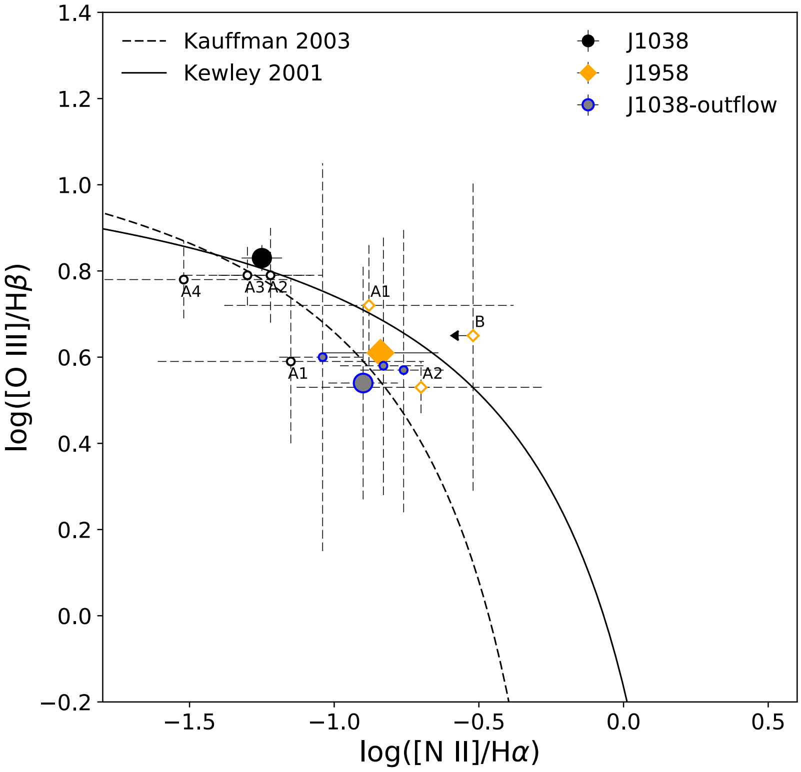

Figure 5.10: BPT diagram for the two sources with both [O III]λ5007/Hβ and [N II]λ6584/Hα detection. Black dots refer to J1038 flux ratios; orange diamonds refer to J1958 measurements. For each object, we report the ratios derived for each knot associated with the arc structure (i.e. A1, A2, A3 and A4 for J1038; A1, A2 and B for J1958). For J1038, for which we have indication for the presence of warm outflows, we reported the flux ratios associated with the high velocity gas emission for the A2, A3 and A4 images (small dots circled in blue) and for the total integrated spectrum (large black dot circled in blue; see text for details). The lines drawn in the figure display the theoretical curves used to separate HII -like ionized regions from galaxies containing AGNs, from Kewley et al. 2001 (dashed line) and Kauffmann et al. 2003b (solid curve) respectively.

Gas-phase metallicity

We can estimate the gas-phase metallicity in our sample of lensed galaxies, because we have shown that the emission lines originate predominantly from star forming regions with negligible contribution from AGNs or shocks. To estimate the metallicities, we used the N2 ([N II]λ6584/Hα) and, when available, the R3 ([O III]λ5007/Hβ) diagnotic ratios, assuming the Te-based calibration from Curti et al. (2017) (see Chapter 3). When both line ratios are available, they are jointly used to put tighter constrains on metallicity, by minimizing the χ^2 in the N2 and R3 calibrations simultaneously, taking into account both measurement errors and dispersion of each calibration. We run an MCMC to generate a posterior probability distribution for log(O/H), whose median and 1σ intervals are then assumed as the inferred metallicity and its uncertainties respectively (see also Sec. 3.7). Since both indicators involve lines close in wavelength, they are unaffected by nebular attenuation. We note here that this

Source	log([O III]λ5007/Hβ)	log(N II]λ6584/Hα)	12+log(O/H) N2 (C17)	12+log(O/H) N2 + R3 (C17)	12 + log(O/H) N2 (M08)
J1038 A1	0.59 ± 0.19	-1.15 ± 0.46	$8.33^{+0.37}_{-0.48}$	$8.30^{+0.22}_{-0.37}$	$8.42^{+0.54}_{-0.63}$
J1038 A2	0.79 ± 0.11	-1.22 ± 0.18	$8.3^{+0.25}_{-0.3}$	$8.21^{+0.18}_{-0.19}$	$8.33^{+0.35}_{-0.37}$
J1038 A3	0.79 ± 0.07	-1.3 ± 0.22	$8.27^{+0.26}_{-0.36}$	$8.15^{+0.21}_{-0.2}$	$8.26^{+0.36}_{-0.47}$
J1038 A3 (low)	0.59 ± 0.01	-1.7 ± 0.2	$7.95^{+0.34}_{-0.27}$	$8.06^{+0.28}_{-0.43}$	$7.9^{+0.40}_{-0.32}$
J1038 A3 (centre)	0.68 ± 0.01	-1.2 ± 0.1	$8.31^{+0.2}_{-0.23}$	$8.27^{+0.08}_{-0.11}$	$8.35^{+0.27}_{-0.29}$
J1038 A3 (top)	0.74 ± 0.01	-1.5 ± 0.1	$8.12^{+0.22}_{-0.26}$	$8.14^{+0.13}_{-0.28}$	$8.1^{+0.27}_{-0.34}$
J1038 A4	0.78 ± 0.09	-1.52 ± 0.36	$8.08^{+0.38}_{-0.43}$	$8.04^{+0.3}_{-0.29}$	$8.07^{+0.54}_{-0.48}$
J1038 A2A3A4	0.83 ± 0.03	-1.25 ± 0.07	$8.29^{+0.17}_{-0.2}$	$8.18^{+0.11}_{-0.11}$	$8.31^{+0.23}_{-0.26}$
J1958 A1	0.72 ± 0.14	-0.88 ± 0.5	$8.48^{+0.4}_{-0.45}$	$8.24^{+0.23}_{-0.22}$	$8.58^{+0.43}_{-0.59}$
J1958 A2	0.53 ± 0.06	-0.7 ± 0.43	$8.56^{+0.33}_{-0.35}$	$8.37^{+0.12}_{-0.19}$	$8.73^{+0.28}_{-0.51}$
J1958 B	0.65 ± 0.36	< -0.52[a]	< 8.67	$8.27^{+0.33}_{-0.27}$	< 8.91
J1958 A1A2	0.61 ± 0.03	-0.84 ± 0.2	$8.49^{+0.33}_{-0.25}$	$8.34^{+0.09}_{-0.11}$	$8.63^{+0.38}_{-0.36}$
J0022	–	-0.63 ± 0.05	$8.61^{+0.2}_{-0.16}$	–	$8.82^{+0.21}_{-0.21}$
J0022 A1	–	-0.72 ± 0.05	$8.56^{+0.16}_{-0.15}$	–	$8.73^{+0.22}_{-0.2}$
J0022 A2	–	-0.6 ± 0.09	$8.63^{+0.26}_{-0.17}$	–	$8.84^{+0.19}_{-0.26}$
J0022 A3	–	-0.48 ± 0.26	$8.69^{+0.2}_{-0.29}$	–	$8.95^{+0.11}_{-0.47}$
J0022 a	–	-0.74 ± 0.12	$8.55^{+0.3}_{-0.19}$	–	$8.71^{+0.31}_{-0.29}$
J0022 b	–	-0.56 ± 0.12	$8.64^{+0.25}_{-0.2}$	–	$8.88^{+0.16}_{-0.3}$
J1110	–	< -0.79[a]	< 8.52	–	< 8.68
J1343	–	-1.1 ± 0.95	$8.36^{+0.52}_{-0.65}$	–	$8.41^{+0.60}_{-0.82}$

Table 5.2: Emission line ratios and metallicities for our sample of lensed sources. Oxygen abundances are inferred from the N2 and R3 indicators following the Curti et al. 2017(C17) and Maiolino et al. 2008(M08) calibrations. In the (N2+R3) column, both diagnostics are used simultaneously to better constrain the metallicity estimate (see text for details).

Notes - [a]: from a 3σ upper limit on the undetected [N II] line.

approach provide more accurate (i.e. with lower uncertainties) metallicity estimates than using the direct combination of the two line ratios as a single diagnostic (i.e. O3N2=([O III]λ5007/Hβ)/([N II]λ6584/Hα)) in the majority of cases, although the metallicities measured with the two methods are fully consistent between each other within the errors. The derived metallicities are reported in Table 5.2.

J1038 is the source with highest SNR and has been observed in both H and K bands. If we consider the brightest and more resolved image of the source, A3, and extract individual spectra requiring a minimum SNR of 2 for the [N II]λ6584 detection, we can obtain three spectra, associated with the upper and lower blobs (see Fig. 5.4) and the fainter central region respectively. We fitted these spectra using the same constrain introduced in Sect. 5.4.1 and derived the line ratio to estimate the metallicity within different regions in the galaxy. Given that the Balmer decrement Hα/Hβ obtained from the integrated spectrum seems to be consistent with the absence of dust-extinction, and that the Hβ line is affected by strong sky line residuals at shorter wavelengths, we used the theoretical ratio of 2.87 predicted by case B recombination to infer the [O III]λ5007/Hβ ratios from a re-scaling of the Hα fluxes[1]. Our metallicity

---

[1] The metallicity estimates derived using the measured log([O III]/Hβ) are consistent with those obtained from the 'corrected' flux ratios within the uncertainties, although associated with larger

measurements for this source are consistent with those reported by Jones et al. (2013) for the central regions in the reconstructed source image plane. We however note here that, despite the larger SNR in our spectra with respect to those reported in Jones et al. (2013), we do not detect any apparent radial trend in the metallicity of J1038. Moreover, even using the same set of calibrations (i.e. from Maiolino et al. 2008), our estimates are not consistent with the large range of metallicities found analysing Keck spectra, with 12+log(O/H) between 8.1 and 9.0 (see Tab. 5.2, last column). A possible cause lies in the low SN of the faint emission lines used: for example, the [N II]$\lambda6584$ line is detected in A2 with a significance of 2σ (1σ) in the LBT/ARGOS (Keck) integrated spectrum.

In Tab. 5.2 we also reported the estimates derived from the flux ratios previously computed for the integrated spectra over the different images along the arcs for all our targets. The metallicities inferred from the combination of N2 and R3 diagnostics are in good agreement with those derived from the N2 only.

The large uncertainties due to the low SNR in the detected emission lines and the intrinsic scatter in the metallicity calibrations do not allow to unveil the possible presence of different gas-phase metallicity conditions in spatially resolved regions and between the different arc images. According to the measured errors, however, available data are constraining metallicity variations to values lower than ≈ 0.15 dex. Larger time investment is required to spatially resolve the metallicity in these systems.

The metallicity estimates derived for this sample of lensed galaxies are in agreement with those generally reported for low-mass systems at z$\sim$ 2 (e.g. Erb 2006; Mannucci et al. 2010; Cresci et al. 2010; Wuyts et al. 2016). In the upper panel of Fig. 5.11 we show the mass-metallicity relation combining our results with those derived from stacked spectra analysis and reported by Erb (2006),Wuyts et al. (2014) and Steidel et al. (2014). For consistency, all the metallicity measurements from previous works have been re-derived according to the Curti et al. (2017) calibration of the N2 indicator. The redshift evolution of the mass-metallicity relation is highlighted in the figure by showing the best-fit curve obtained by Andrews & Martini (2013) from Te measurements on stacked spectra (in narrow mass bins) of SDSS galaxies. Moreover, the 1σ dispersion in bins of stellar mass of the local MZR derived with Curti et al. (2017) calibrations (Sec.3.7) are enclosed by the grey contours.

In the bottom panel of Fig. 5.11 we report the 2D projection of the fundamental metallicity relation by Mannucci et al. (2009) (i.e. 12+ log(O/H) as a function of $\mu_{0.32} = \log(M_\star) - 0.32\log(\mathrm{SFR})$). In this plot, metallicities are computed using the Maiolino et al. (2008) calibration of the N2 diagnostic, for consistency with Mannucci

---

scatter.

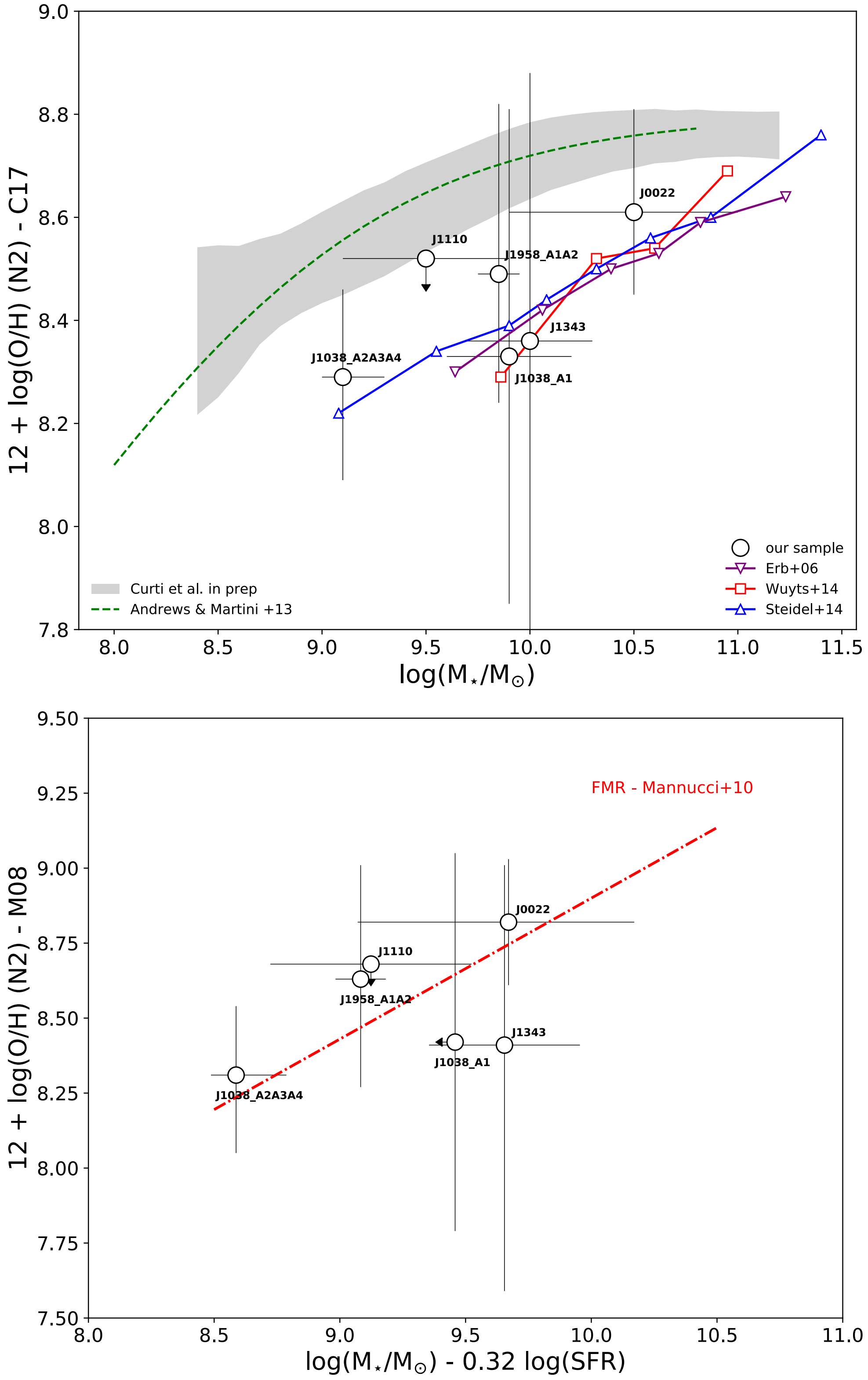

Figure 5.11: *Upper Panel*: Mass-metallicity relation (MZR) for our sample. The metallicities are derived exploiting the Curti et al. 2017(C17) calibration of the N2 indicator. Previous N2-based metallicities from the literature are plotted with different color/symbols as reported in the legend. The grey shaded are encompass the 1σ of the median MZR for SDSS galaxies, as derived from the C17 calibrations (see Sec. 3.7). The Te-based MZR from staked spectra in bins of stellar mass from Andrews & Martini 2013 is also shown with the dashed green line.
Bottom Panel: Oxygen abundance as a function of μ_{32}, according to the Mannucci et al. 2010 2D-projection of minimum scatter of the FMR. Metallicities are derived, for consistency, with the Maiolino et al. 2008 (M08) calibrations.

et al. (2010). Our results are in fair agreement, within the uncertainties, with the absence of any redshift evolution of the relation at these epochs (see e.g. Belli et al. (2013); Christensen et al. (2012); Cresci et al. (2012)), although a couple of points (i.e. J1038_A1 and J1343) appear to lie more than 0.1 dex below the metallicity value predicted by the FMR.

5.5 Conclusions

We analyzed the rest-frame optical spectra of five lensed galaxies at z~ 2.5, observed with the near-infared spectrograph LUCI at the LBT, assisted with the laser guide star adaptive optics system ARGOS. The entire extension of the on-sky arc-like shapes of these lensed systems was covered thanks to spectroscopic masks designed with curved slits. Thanks to the seeing improvement provided the AO-module ARGOS, near infrared spectra with high spectral (~ 50 km/s) and spatial (0.4") resolution have been obtained to cover the [N II]$\lambda6584$ + Hα complex, redshifted into the K-band. For two out of five sources, we also obtained H-band spectra, covering the [O III]$\lambda5007$ and Hβ emission lines. We combined the spatially resolved information from our spectra with available data and lens modelling from the literature to constrain the properties of the ionized gas in our targets. In particular, we find the following key results:

- We find strongly disturbed kinematics in the ISM component of the lensed galaxy J1038. Broad and asymmetric line profiles, with W80 as high as $\sim 150 \div 300$ km/s and V10 $\approx -100 \div -200$ km/s, have been detected over the entire extension of the arc-like structure. In Jones et al. (2013) and Leethochawalit et al. (2016), this target has been interpreted as an undergoing merger, with the A1 and A2 knots associated with the two different galaxy companions. Our analysis shows that A1 image can be actually associated with a different emitting region in the source plane, but that the disturbed kinematics and diagnostic line ratios observed in the other images can be reasonably related with a different physical origin. We suggest the presence of SF-driven outflow in this galaxy.

- The spatially resolved non-parametric velocity measurements along the arc of J1958 reveal the presence of two distinct, spatially separated kinematic components, suggesting the presence of two approaching galaxies in this system. The source plane reconstruction presented by Leethochawalit et al. (2016) confirm our results.

- From the analysis of the BPT diagram, we did not find any strong evidence for AGN activity in these systems. Even the outflowing component of J1038 shows line ratios compatible with ionization due to HII regions, revealing its possible nature of star formation-driven outflow.

- Assuming that the observed emission lines are mostly due to star formation activity, we derived gas-phase metallicity estimates using the N2 and R3 diagnostics. We found values that are consistent with what is generally observed in low-mass systems at these redshifts. The average offset of our targets from the local mass-metallicity relation is ~ 0.25 dex. The lensed galaxies analyzed in this work are consistent, within the errors, with the local FMR.
- The low spectral SNR does not allow us to infer clear spatially resolved metallicity information along the slit. On the basis of our measurements, however, we assess that the metallicity variations in our targets should be less than ≈ 0.15 dex.

The near-infrared spectra analyzed in this Chapter represent the first scientific demonstration of the spectroscopic capabilities that can be achieved with the ARGOS facility in combination with LUCI. Kinematics and ionized gas properties within the individual images of lensed systems have been easily recognized thanks to the achieved high spectral and angular resolutions provided by the AO correction in combination with the use of narrow, curved-shape slits. In order to better constrain gas-phase metallicities within high-z galaxies, high S/N spectra are required. The simultaneous use of both LUCI instruments in binocular mode is already reducing by nearly a factor of two the time needed to complete most of the spectroscopic observing programs; the full exploitation of the ARGOS correction in binocular mode will even more boost the telescope efficiency in the near future, providing a powerful way to improve our knowledge on galaxy evolution.

6

Conclusions and future prospects

In this thesis we addressed some of the currently most debated topics related to the chemical evolution of star forming galaxies throughout the epochs, by means of statistically robust analysis of large samples of local galaxies and of near-infrared, spatially resolved spectroscopy of high-redshift sources.

In Chapter 3 we revisited some of the most common methods for metallicity determination based on strong emission lines, exploiting a novel approach based on stacking the spectra of SDSS star-forming galaxies according to their position on the [O III]λ5007/Hβ vs[O III]λ3727/Hβ diagram, i.e. assuming that galaxies with such similar strong-line ratios are characterized by similar metallicities. The stacking procedure allowed us to detect the extremely faint, metallicity-sensitive auroral lines (e.g. the [O III]λ4363 and the [O II]λ7320, 7330) required to measure the electron temperatures of the different ionization zones and apply the T_e-method to measure the oxygen abundances from our composite spectra. In this way, we could provide a new calibration of the strong-line metallicity diagnostics which is fully based on the T_e-abundance scale, descends from the analysis of global galaxy spectra and covers the entire metallicity range spanned by the SDSS galaxies.

Our set of calibrations deviates both from empirical ones based on HII regions and from calibrations based on prediction from photoionization models, especially in the high metallicity regime where the highest oxygen abundances inferred from our stacked spectra are of the order of ~ 1.4 times the solar abundance. Classical empirical calibrations obtained from HII regions, on the other hand, generally show lower metallicities for fixed line ratios, probably due to the fact that the calibrating sample somehow biased towards HII regions of high excitation conditions, in order to ensure auroral line detection at high metallicity.

When applied individually to the sample of local SDSS galaxies, this set of calibrated diagnostics provides consistent results, with metallicity estimates differing on average by only 0.04 dex; this allow, in principle, to compare abundances obtained involving lines at different wavelengths, which results extremely useful at higher redshifts, where galaxies are often observed at different epochs and in different spectral bands. The use of such calibrations for high-redshift studies however, should always follow a careful evaluation of the systematics that may be introduced by the application of a given diagnostic to objects characterized by different physical properties from those of the calibrating sample. Whether the locally calibrated diagnostics are truly reliable for measuring metallicity of high-redshift galaxies, in fact, is still matter of debate.

Meanwhile, some more interesting results emerged from the analysis of the composite spectra. We found evidence for contamination of the [O III]λ4363 auroral line in high-metallicity stacks, probably due to emission in [Fe II] lines. As this is one of the crucial lines for the application of the T_e method, we recommend attention in using this line as electron temperature diagnostic when detected in high-metallicity galaxy spectra. However, we also show that, in the high metallicity regime (i.e. $12 + \log(O/H) \gtrsim 8.4$), the O^+ ion dominates the relative contribution to the total oxygen abundance; therefore, we suggest that the [O II]λ7320, 7330 auroral doublet become the most sensitive probe to the global metallicity, while [O III]λ4363 can be used to infer the correction ($\approx 30\%$, or even less) provided by the O^{++} species to the dominant O^+ ionization state. From electron temperatures measured by means of different auroral line detections in our stacked spectra, we analyzed the relations between electron temperatures of different ionization zones, finding discrepancies both between temperatures tracing the same ionization region as well as between temperatures associated to different regions. Our stacks in fact, does not follow the t_2-t_3 relation predicted from photoionization models, nor the one empirically derived from measurements on individual HII regions. However, the temperatures measured from our stacks are better represented by a relation that directly correlates auroral and nebular line fluxes (the so-called *ff-relations*). Exploiting the direct detection of the [O II]λ7320, 7330 auroral doublet in all of our composite spectra, we provided a new relation (the ff_{O2}-relation) for the prediction the expected flux of this auroral line given a combination of strong-line ratios. This new relation can be used to correct for the unseen O^{++} ionization state when the relative auroral line is undetected.

Finally, we derived a new MZR and FMR in the local Universe, by applying the new set of calibrations to the mother SDSS sample. This represent preliminary work: an in-depth analysis of their properties will be conducted in the near future.

We then moved to the high redshift Universe, to investigate the ISM properties in high-redshift galaxies and how their metal content is linked to their star formation history. In Chapter 4, we analyzed a sample of high-redshift (i.e. $1.2 < z < 2.5$) gravitationally lensed galaxies, in the framework of the ESO Large Programme KLEVER.

Combining integral field spectroscopy from KMOS with the increased sensitivity and resolution provided by gravitational lensing, we could investigate in detail the physical properties of the ionized gas in our sample on spatially resolved basis. Moreover, the large spectral coverage of the survey allows to map the almost entire set of optical rest-frame nebular diagnostics (from [O II]$\lambda3727$ to [S III]$\lambda9530$), which could be used to tightly constrain the inferred physical quantities. Chapter 4 is focused in particular on assessing the properties and the cosmic evolution of metallicity gradients. By modeling the lensing effect, we obtained de-projected source plane metallicity maps with typical spatial resolutions of 1-2 kpc, exploiting the new calibrations presented in the previous chapter; we then extracted radial metallicity gradients by full taking into account the PSF distortions introduced by the de-lensing procedure. The bulk of our galaxy sample present azimuthally-averaged radial metallicity gradients fully consistent with being flat within the uncertainties, similarly to the majority of previous literature results which investigated metallicity gradients at z $\sim 1-2.5$ and with no clear evidence of redshift evolution. From a theoretical point of view, this could be representative of a scenario where efficient mixing processes, that redistribute a significant amount of gas over large scales, are in place, as predicted by many recent cosmological simulations. However, despite the apparent radial invariance of the metallicity gradients, the presence of irregular patterns and metallicity variations in the resolved 2D metallicity maps warns against the use of azimuthally-averaged radial gradients as the only observable to constrain galaxy evolution models and simulations. Only the complete information hold by the full bidimensional maps in fact can help to discriminate how different physical mechanisms related to gas flows and radial mixing processes locally contribute in shaping the observed complex morphologies.

We also investigated the presence of possible correlations between the metallicity gradients and intrinsic galaxy properties. We reported a tentative correlation between the presence of gradients and the star formation activity in galaxies, as parametrized by the sSFR, in the sense that galaxies with a higher sSFR exhibit flatter or inverted gradients. On the contrary, we did not find in our sample any clear trend between metallicity gradients and stellar mass, like previously reported in the literature for very low mass systems. On local scales, we found qualitative evidence of a general spatial anti-correlation on local scales between metallicity and the SFR surface density, as previously claimed by different works conducted on samples of high-redshift sources. This suggests that, at least in some regions of our galaxies, smooth inflow of gas is active in diluting the metal content and boost star formation episodes. When occurring into the central regions, this generates a flat or positive gradient.

By fully taking advantage of the broad spectral coverage provide by the KLEVER survey, we also investigated the processes responsible for the observed offset of high-z galaxies in the classical BPT diagrams, trying to disentangle the different physical contributions at the origin of the evolution in the emission line ratios, in a spatially resolved manner. In particular, we assessed the presence of possible correlations between the BPT offsets and the electron density, the ionization parameter and the level of nitrogen enrichment. We suggest that each of these processes may play a role in driving the observed evolution in line-ratios, with relative contributions that may change from galaxy to galaxy.

The study of galaxy properties at high redshift conducted with ground-based spectroscopy can largely benefit from the increased spatial resolution provided by the adaptive optics correction of the atmospheric turbulence, thus representing a strong scientific case for the development of new AO-facilities. Indeed, the forthcoming generation of extremely large telescopes (ELTs) will be intrinsically designed to exploit AO-assisted instrumentation. In Chapter 5, we presented the first spectroscopic observations conducted at the LBT with the NIR imager and spectrograph LUCI, assisted by the laser guide stars ground-layer adaptive optics system ARGOS. We observed a small sample of z$\sim$ 2 strongly lensed objects, by means of curved-slit multi-object spectroscopy that allowed us to cover the full extension of the arc-like shapes of these systems on the sky. Thanks to the seeing improvement provided by ARGOS, which shrink the PSF-size to get better coupling with the slit, we could obtain NIR observations characterized by a spectral resolution of $\sim$ 50 km/s and spatial resolution of $\sim$ 0.4”; this allowed us to resolve several, separated emitting regions along these systems. Our observation was mainly conducted in the K band, to cover the [N II]λ6584 + Hα complex; for two out of five sources we also obtained H-band spectra, aimed at detecting the [O III]λ5007 + Hβ emission lines.

The kinematic analysis of our sources revealed disturbed motions in many of them, with velocity dispersions up to $\sim$ 300 km/s. We could also confirm that two of our galaxies are undergoing merging systems, as previously claimed by different IFU studies reported in the literature. Analyzing the ionized gas properties from the inferred emission line ratios, we did not find any strong evidence for AGN activity in these systems according to their position on the BPT diagrams. Assuming therefore that the observed emission lines are mostly due to star formation activity, we derived gas-phase metallicity from the calibrated diagnostics presented in Chapter 3, finding that the inferred metallicities are consistent with those generally observed in low-mass systems at these redshifts. The lensed galaxies analyzed in this work are also consistent, within the uncertainties, with the predictions from the local FMR.

6.1 Future work

Most of the work presented in this thesis can be subject of further development: some ideas about future prospects are discussed in the following.

- The new MZR and FMR derived in Sec. 3.7 will be subject of a detailed analysis. In particular we will explore the effects introduced on the relation by the choice of different abundances diagnostics, which can change how tight the secondary dependence on SFR manifests in different mass regimes. The new M-Z-SFR framework obtained would represent a valuable benchmark to compare forthcoming studies on high-redshift galaxies; in this sense, a comprehensive and consistent assessment of the evolution of the MZR, pursued by compiling the available emission line measurements in the literature and consistently re-deriving the metallicities with the new calibrations, is already in progress.

- Exploiting the spatially resolved data from the KLEVER survey (which is expected to be completed by fall 2018), we could investigate the relation between stellar mass surface density, star formation rate density and metallicity on local kpc scales for the very first time at high redshift, using the variety of different metallicity diagnostics provided by the large spectral coverage of the program. Such relations have been already assessed in the local Universe by integral-field spectroscopic surveys like CALIFA and MANGA, but a full characterization of their properties is missing at earlier epochs; indeed, this would represent a strong testbed for predictions from numerical chemical evolution models and hydrodynamical simulations applied to spatially resolved regions of high redshift sources, to understand to what extent the relations holding on local scales drive the well-known scaling relations observed for galaxy integrated properties.

- The first attempt to study the chemical abundances in the KLEVER sample concerned the shape of radial gradients in the oxygen abundance. As it is well known however, studying the relative abundance of different species that are released into the ISM on different time-scales provides key and complementary information on the gas flow and star formation history of a galaxy with respect to measuring the abundances of individual elements. This is usually done by inferring the nitrogen-to-oxygen abundance ratio (N/O), which is often derived exploiting a calibration of the [N II]λ6584/[O II]λ3727 and/or the [N II]λ6584/[S II]λ6717,6731 ratios. We will investigate the spatial distribution of the N/O in our high-z sources and assess the position of our spatially resolved regions in the N/O vs O/H diagram, to search for evidences of a possible cosmic evolution.

- In this respect, in addition to the well known calibrations of these two diagnostics, a new T_e-based calibration can be obtained from our composite spectra, exploiting the detection of the [N II]λ5755 auroral line (as well as the [S II]λ4070) to infer the electron temperature associated to the N^+ region and, therefore, “directly” measuring the N^+/O^+ abundance ratio, which can be assumed as a tracer for N/O giving the similar ionization potentials of the O^+ and N^+ species.

- Given the broad wavelength coverage of the survey, many different metallicity diagnostics, based on different calibration methods, can be used to characterize the chemical abundances maps in our sample. We will conduct an extensive comparison between different metallicity estimates on pixel by pixel basis, searching for possible correlations between the observed discrepancies in metallicity determination and other physical properties. For example, from the preliminary analysis of a small sample of galaxies with spatially resolved [S III] emission, we found that regions with different metallicity predictions from T_e-based and theoretical calibrations seems to be associated with an increased ionization parameter, as inferred from the distribution of the [S III]/[S II] diagnostic ratio.

- As soon as the KLEVER survey will be completed, the increased statistics in $z > 2$ sources will allow us to investigate the position of our galaxies in the alpha-elements based diagnostic diagrams like R_{23} vs O_{32}; in fact, given the small offsets observed in such diagrams from integrated spectra of high-redshift galaxies, these has been recently suggested as the more robust to be calibrated as metallicity indicators.

- A complete kinematic characterization of the KLEVER sample will be provided. This will follow from the proper reconstruction of the source plane velocity and velocity dispersion maps of lensed galaxies, that will be used to quantify the degree of rotational support in these systems and to address the systematics introduced in the determination of metallicity gradients due to beam-smearing effects related to disc inclination. Moreover, we will carefully evaluate the presence of broad components in the emission line profiles of our sample, to search evidences of (star-formation-driven) outflows in the ionized gas.

- A multi-wavelength follow-up program of KLEVER galaxies is also expected. We will propose ALMA observations to map the distribution of cold molecular gas in our galaxies. We will also exploit the already available MUSE data of the KLEVER fields, to probe the UV-rest frame spectra of our galaxies and compare the UV-diagnostics of the ISM with the rest-frame optical ones obtained from the NIR observations.

- Within the commissioning phase of ARGOS, the system will be thoroughly tested for binocular-mode operations and made available for the community hopefully by fall 2018. Meanwhile, we will obtain new AO-assisted observations aimed both at improving the quality of the already available spectra and at increasing the size of the analyzed galaxy sample. At the time of writing, two more strongly lensed arc-like systems (known as CL2244 and SDSS J0143+1607) are already under observations; as opposed to the targets which have been observed so far, no observations with any other AO-facility are reported in the literature, but only longslit observations in seeing-limited mode. For CL2244 in particular, the absence of bright stars in the proximity of the target prevented any AO observation from being performed till now, even with laser guide stars AO systems. The unique combination of LUCI wide field of view and ARGOS GLAO correction allowed us to design a mask configuration suitable for including a relatively bright ($R = 16$) tip-tilt star in the field and plan an AO-assisted observation of this target for the first time ever.

In conclusion, the work presented in this dissertation can be seen as a first step for future larger investigations on the chemical evolution of star forming galaxies. The advent in the nearby future of new generation space- and ground-based instruments like NIRSPEC on the JWST and MOONS on the VLT will completely revolutionize our view of the high-redshift Universe, thanks to the unprecedented improvements provided both in the sensitivity and statistical robustness of the observations.

For example, the high multiplexing capabilities of MOONS would finally bring to a fully T_e-based calibration of metallicity diagnostics in the high-redshift Universe, which could be in principle obtained following a similar approach to that presented in Chapter 3; in fact, the large statistics provided in terms of high-redshift spectra would allow to stack hundreds of thousands spectra of galaxies at $z \sim 1.5$ and even up to $z \sim 2.7$, where the detection of [O II] and [O III] lines will still be guaranteed given the spectral range covered by the instrument. Furthermore, JWST will push forward this limit by exploring the epochs beyond the cosmic noon, to shade light on the interplay between the processes responsible for the assembly and chemical characterization of early galaxies.

Bibliography

Abazajian K. N., et al., 2009, ApJS, 182, 543

Aggarwal K. M., Keenan F. P., 1999, ApJS, 123, 311

Allam S. S., Tucker D. L., Lin H., Diehl H. T., Annis J., Buckley-Geer E. J., Frieman J. A., 2007, ApJLett, 662, L51

Allen G. E., Houck J. C., Sturner S. J., 2008, in AAS/High Energy Astrophysics Division #10. p. 31.09

Allende Prieto C., Lambert D. L., Asplund M., 2001, ApJLett, 556, L63

Alloin D., Collin-Souffrin S., Joly M., Vigroux L., 1979, A&A, 78, 200

Andrews B. H., Martini P., 2013, ApJ, 765, 140

Arribas S., Colina L., Bellocchi E., Maiolino R., Villar-Martín M., 2014, A&A, 568, A14

Baldwin J. A., Phillips M. M., Terlevich R., 1981, PASP, 93, 5

Balmaverde B., et al., 2016, A&A, 585, A148

Barrera-Ballesteros J. K., et al., 2016, MNRAS, 463, 2513

Bayliss M. B., Hennawi J. F., Gladders M. D., Koester B. P., Sharon K., Dahle H., Oguri M., 2011, ApJS, 193, 8

Belfiore F., et al., 2015, MNRAS, 449, 867

Belfiore F., et al., 2016, MNRAS, 461, 3111

Belfiore F., et al., 2017, preprint, (`arXiv:1703.03813`)

Belli S., Jones T., Ellis R. S., Richard J., 2013, ApJ, 772, 141

Belokurov V., Evans N. W., Hewett P. C., Moiseev A., McMahon R. G., Sanchez S. F., King L. J., 2009, MNRAS, 392, 104

Berg D. A., Croxall K. V., Skillman E. D., Pogge R. W., Moustakas J., Groh-Johnson M., 2015, preprint, (`arXiv:1501.02270`)

Binette L., Matadamas R., Hägele G. F., Nicholls D. C., Magris C. G., Peña-Guerrero M. Á., Morisset C., Rodríguez-González A., 2012, A&A, 547, A29

Blanc G. A., Kewley L., Vogt F. P. A., Dopita M. A., 2015, ApJ, 798, 99

Blanton M. R., Moustakas J., 2009, ARA&A, 47, 159

Bothwell M. S., Maiolino R., Kennicutt R., Cresci G., Mannucci F., Marconi A., Cicone C., 2013, MNRAS, 433, 1425

Bothwell M. S., Maiolino R., Cicone C., Peng Y., Wagg J., 2016, preprint, (`arXiv:1606.04102`)

Bresolin F., 2011, ApJ, 730, 129

Bresolin F., Schaerer D., González Delgado R. M., Stasińska G., 2005, A&A, 441, 981

Bresolin F., Gieren W., Kudritzki R.-P., Pietrzyński G., Urbaneja M. A., Carraro G., 2009, ApJ, 700, 309

Bresolin F., Kennicutt R. C., Ryan-Weber E., 2012, ApJ, 750, 122

Bresolin F., Kudritzki R.-P., Urbaneja M. A., Gieren W., Ho I., Pietrzynski G., 2016, preprint, (`arXiv:1607.06840`)

Brinchmann J., Charlot S., White S. D. M., Tremonti C., Kauffmann G., Heckman T., Brinkmann J., 2004, MNRAS, 351, 1151

Brown J. S., Martini P., Andrews B. H., 2016, preprint, (`arXiv:1602.01087`)

Brusa M., et al., 2015, preprint, (`arXiv:1503.01783`)

Bruzual G., Charlot S., 2003, MNRAS, 344, 1000

Bundy K., et al., 2015, ApJ, 798, 7

Busoni L., et al., 2015, in Adaptive Optics for Extremely Large Telescopes IV (AO4ELT4). p. E92

Calzetti D., Kinney A. L., Storchi-Bergmann T., 1994, ApJ, 429, 582

Calzetti D., Armus L., Bohlin R. C., Kinney A. L., Koornneef J., Storchi-Bergmann T., 2000, ApJ, 533, 682

Campbell A., Terlevich R., Melnick J., 1986, MNRAS, 223, 811

Cano-Díaz M., Maiolino R., Marconi A., Netzer H., Shemmer O., Cresci G., 2012, A&A, 537, L8

Cappellari M., Emsellem E., 2004, PASP, 116, 138

Cardelli J. A., Clayton G. C., Mathis J. S., 1989, ApJ, 345, 245

Carniani S., et al., 2015, preprint, (`arXiv:1506.03096`)

Carniani S., et al., 2016, preprint, (`arXiv:1604.04290`)

Carton D., et al., 2015, MNRAS, 451, 210

Cenarro A. J., Cardiel N., Gorgas J., Peletier R. F., Vazdekis A., Prada F., 2001, MNRAS, 326, 959

Ceverino D., Sánchez Almeida J., Muñoz Tuñón C., Dekel A., Elmegreen B. G., Elmegreen D. M., Primack J., 2016, MNRAS, 457, 2605

Chabrier G., 2003, PASP, 115, 763

Chiappini C., Matteucci F., Romano D., 2001, ApJ, 554, 1044

Christensen L., et al., 2012, MNRAS, 427, 1953

Cicone C., et al., 2014, A&A, 562, A21

Cicone C., Maiolino R., Marconi A., 2016, A&A, 588, A41

Cid Fernandes R., Stasińska G., Mateus A., Vale Asari N., 2011, MNRAS, 413, 1687

Cowie L. L., Barger A. J., Songaila A., 2015, preprint, (`arXiv:1512.00017`)

Cresci G., Mannucci F., Maiolino R., Marconi A., Gnerucci A., Magrini L., 2010, Nature, 467, 811

Cresci G., Mannucci F., Sommariva V., Maiolino R., Marconi A., Brusa M., 2012, MNRAS, 421, 262

Cresci G., et al., 2015, ApJ, 799, 82

Cresci G., Vanzi L., Telles E., Lanzuisi G., Brusa M., Mingozzi M., Sauvage M., Johnson K., 2017, preprint, (`arXiv:1704.08367`)

Croom S. M., et al., 2012, MNRAS, 421, 872

Cullen F., Cirasuolo M., McLure R. J., Dunlop J. S., Bowler R. A. A., 2014, MNRAS, 440, 2300

Curti M., Cresci G., Mannucci F., Marconi A., Maiolino R., Esposito S., 2017, MNRAS, 465, 1384

Daddi E., et al., 2007, ApJ, 670, 156

Davé R., Oppenheimer B. D., Finlator K., 2011a, MNRAS, 415, 11

Davé R., Finlator K., Oppenheimer B. D., 2011b, MNRAS, 416, 1354

Davé R., Rafieferantsoa M. H., Thompson R. J., Hopkins P. F., 2017, MNRAS, 467, 115

Davies R. I., 2007, MNRAS, 375, 1099

Davies R., Kasper M., 2012, ARA&A, 50, 305

Davies R. I., et al., 2013, A&A, 558, A56

Dayal P., Ferrara A., Dunlop J. S., 2013, MNRAS, 430, 2891

De Robertis M. M., Dufour R. J., Hunt R. W., 1987, JRASC, 81, 195

De Rossi M. E., Theuns T., Font A. S., McCarthy I. G., 2015, preprint, (`arXiv:1506.02772`)

Dessauges-Zavadsky M., D'Odorico S., Schaerer D., Modigliani A., Tapken C., Vernet J., 2010, A&A, 510, A26

Dessauges-Zavadsky M., Christensen L., D'Odorico S., Schaerer D., Richard J., 2011, A&A, 533, A15

Diehl H. T., et al., 2009, ApJ, 707, 686

Dopita M. A., Koratkar A. P., Evans I. N., Allen M., Bicknell G. V., Sutherland R. S., Hawley J. F., Sadler E., 1996, in Eracleous M., Koratkar A., Leitherer C., Ho L., eds, Astronomical Society of the Pacific Conference Series Vol. 103, The Physics of Liners in View of Recent Observations. p. 44

Dopita M. A., Sutherland R. S., Nicholls D. C., Kewley L. J., Vogt F. P. A., 2013, ApJS, 208, 10

Dopita M. A., Kewley L. J., Sutherland R. S., Nicholls D. C., 2016, Ap&SS, 361, 61

Edmunds M. G., Pagel B. E. J., 1978, MNRAS, 185, 77P

Ellison S. L., Patton D. R., Simard L., McConnachie A. W., 2008, ApJLett, 672, L107

Erb D., 2006, in American Astronomical Society Meeting Abstracts. p. 925

Erb D. K., Shapley A. E., Pettini M., Steidel C. C., Reddy N. A., Adelberger K. L., 2006, ApJ, 644, 813

Esposito S., et al., 2010, in Adaptive Optics Systems II. p. 773609, doi:10.1117/12.858194

Esposito S., et al., 2011, in Astronomical Adaptive Optics Systems and Applications IV. p. 814902 (`arXiv:1203.2761`), doi:10.1117/12.898641

Esteban C., Peimbert M., García-Rojas J., Ruiz M. T., Peimbert A., Rodríguez M., 2004, MNRAS, 355, 229

Esteban C., Bresolin F., Peimbert M., García-Rojas J., Peimbert A., Mesa-Delgado A., 2009, ApJ, 700, 654

Esteban C., García-Rojas J., Carigi L., Peimbert M., Bresolin F., López-Sánchez A. R., Mesa-Delgado A., 2014, MNRAS, 443, 624

Falcón-Barroso J., Sánchez-Blázquez P., Vazdekis A., Ricciardelli E., Cardiel N., Cenarro A. J., Gorgas J., Peletier R. F., 2011, A&A, 532, A95

Ferland G. J., et al., 2013, RMXAC, 49, 137

Ferland G. J., Henney W. J., O'Dell C. R., Peimbert M., 2016, RMXAC, 52, 261

Feruglio C., et al., 2015, A&A, 583, A99

Field G. B., Goldsmith D. W., Habing H. J., 1969, in Bulletin of the American Astronomical Society. p. 240

Filippenko A. V., Terlevich R., 1992, ApJLett, 397, L79

Finkelstein S. L., Papovich C., Rudnick G., Egami E., Le Floc'h E., Rieke M. J., Rigby J. R., Willmer C. N. A., 2009, ApJ, 700, 376

Fiore F., et al., 2017, A&A, 601, A143

Förster Schreiber N. M., et al., 2014, ApJ, 787, 38

Fraternali F., Binney J. J., 2008, MNRAS, 386, 935

Fu J., et al., 2013, MNRAS, 434, 1531

Fumagalli M., Fossati M., Hau G. K. T., Gavazzi G., Bower R., Sun M., Boselli A., 2014, MNRAS, 445, 4335

García-Rojas J., Esteban C., 2007, ApJ, 670, 457

Garnett D. R., 1992, AJ, 103, 1330

Gazak J. Z., et al., 2015, ApJ, 805, 182

Genzel R., et al., 2014, ApJ, 796, 7

Gibson B. K., Courty S., Cunnama D., Mollá M., 2013a, Asociacion Argentina de Astronomia La Plata Argentina Book Series, 4, 57

Gibson B. K., Pilkington K., Brook C. B., Stinson G. S., Bailin J., 2013b, A&A, 554, A47

Guo Y., et al., 2016, ApJ, 822, 103

Harrison C. M., et al., 2012, MNRAS, 426, 1073

Harrison C. M., Alexander D. M., Mullaney J. R., Swinbank A. M., 2014, MNRAS, 441, 3306

Ho I.-T., et al., 2014, MNRAS, 444, 3894

Ho I.-T., Kudritzki R.-P., Kewley L. J., Zahid H. J., Dopita M. A., Bresolin F., Rupke D. S. N., 2015, MNRAS, 448, 2030

Hunt L., Dayal P., Magrini L., Ferrara A., 2016, MNRAS, 463, 2020

Izotov Y. I., Stasińska G., Meynet G., Guseva N. G., Thuan T. X., 2006, A&A, 448, 955

Johnson T. L., et al., 2017a, ApJ, 843, 78

Johnson T. L., et al., 2017b, ApJLett, 843, L21

Jones T. A., Swinbank A. M., Ellis R. S., Richard J., Stark D. P., 2010a, MNRAS, 404, 1247

Jones T., Ellis R., Jullo E., Richard J., 2010b, ApJLett, 725, L176

Jones T., Ellis R. S., Richard J., Jullo E., 2013, ApJ, 765, 48

Jones T., Martin C., Cooper M. C., 2015a, preprint, (`arXiv:1504.02417`)

Jones T., et al., 2015b, AJ, 149, 107

Kashino D., et al., 2016, preprint, (`arXiv:1604.06802`)

Kauffmann G., et al., 2003a, MNRAS, 341, 33

Kauffmann G., et al., 2003b, MNRAS, 346, 1055

Kennicutt Jr. R. C., 1998, ARA&A, 36, 189

Kennicutt R. C., Evans N. J., 2012, ARA&A, 50, 531

Kennicutt Jr. R. C., Bresolin F., Garnett D. R., 2003, ApJ, 591, 801

Kewley L. J., Dopita M. A., 2002, ApJS, 142, 35

Kewley L. J., Ellison S. L., 2008, ApJ, 681, 1183

Kewley L. J., Dopita M. A., Sutherland R. S., Heisler C. A., Trevena J., 2001, ApJ, 556, 121

Kewley L. J., Groves B., Kauffmann G., Heckman T., 2006, MNRAS, 372, 961

Kewley L. J., Rupke D., Zahid H. J., Geller M. J., Barton E. J., 2010, ApJLett, 721, L48

Kewley L. J., Maier C., Yabe K., Ohta K., Akiyama M., Dopita M. A., Yuan T., 2013, ApJLett, 774, L10

Kimura M., et al., 2010, preprint, (`arXiv:1006.3102`)

Kobulnicky H. A., Kewley L. J., 2004, ApJ, 617, 240

Kobulnicky H. A., Kennicutt Jr. R. C., Pizagno J. L., 1999, ApJ, 514, 544

Köppen J., Hensler G., 2005, A&A, 434, 531

Kostrzewa-Rutkowska Z., Wyrzykowski Ł., Auger M. W., Collett T. E., Belokurov V., 2014, MNRAS, 441, 3238

Kroupa P., Tout C. A., Gilmore G., 1993, MNRAS, 262, 545

Kudritzki R.-P., Ho I.-T., Schruba A., Burkert A., Zahid H. J., Bresolin F., Dima G. I., 2015, MNRAS, 450, 342

Lanzuisi G., et al., 2017, A&A, 602, A123

Le Borgne D., Rocca-Volmerange B., Prugniel P., Lançon A., Fioc M., Soubiran C., 2004, A&A, 425, 881

Lee H., Skillman E. D., Cannon J. M., Jackson D. C., Gehrz R. D., Polomski E. F., Woodward C. E., 2006, ApJ, 647, 970

Leethochawalit N., Jones T. A., Ellis R. S., Stark D. P., Richard J., Zitrin A., Auger M., 2016, ApJ, 820, 84

Lequeux J., Peimbert M., Rayo J. F., Serrano A., Torres-Peimbert S., 1979, A&A, 80, 155

Liang Y. C., Hammer F., Yin S. Y., Flores H., Rodrigues M., Yang Y. B., 2007, A&A, 473, 411

Lilly S. J., Carollo C. M., Pipino A., Renzini A., Peng Y., 2013, ApJ, 772, 119

Liu X., Shapley A. E., Coil A. L., Brinchmann J., Ma C.-P., 2008, ApJ, 678, 758

López-Sánchez Á. R., Dopita M. A., Kewley L. J., Zahid H. J., Nicholls D. C., Scharwächter J., 2012, MNRAS, 426, 2630

Lotz J. M., et al., 2017, ApJ, 837, 97

Luridiana V., Morisset C., Shaw R. A., 2012, in IAU Symposium. pp 422–423, doi:10.1017/S1743921312011738

Luridiana V., Morisset C., Shaw R. A., 2015, A&A, 573, A42

Maciel W. J., Costa R. D. D., Uchida M. M. M., 2003, A&A, 397, 667

Madau P., Dickinson M., 2014, ARA&A, 52, 415

Maiolino R., et al., 2008, A&A, 488, 463

Mannucci F., et al., 2009, MNRAS, 398, 1915

Mannucci F., Cresci G., Maiolino R., Marconi A., Gnerucci A., 2010, MNRAS, 408, 2115

Marino R. A., et al., 2012, ApJ, 754, 61

Marino R. A., et al., 2013, A&A, 559, A114

Markwardt C. B., 2009, in Bohlender D. A., Durand D., Dowler P., eds, Astronomical Society of the Pacific Conference Series Vol. 411, Astronomical Data Analysis Software and Systems XVIII. p. 251 (`arXiv:0902.2850`)

Masters D., et al., 2014, ApJ, 785, 153

Masters D., Faisst A., Capak P., 2016, preprint, (`arXiv:1605.04314`)

Matteucci F., 1986, MNRAS, 221, 911

McGaugh S. S., 1991, ApJ, 380, 140

McKee C. F., Ostriker J. P., 1977, ApJ, 218, 148

McLean I. S., et al., 2012, in Ground-based and Airborne Instrumentation for Astronomy IV. p. 84460J, doi:10.1117/12.924794

Menzel D. H., Aller L. H., Hebb M. H., 1941, ApJ, 93, 230

Mollá M., Díaz A. I., 2005, MNRAS, 358, 521

Mollá M., Cavichia O., Costa R. D. D., Maciel W. J., Gibson B. K., Díaz A. I., 2016b, preprint, (`arXiv:1612.03064`)

Mollá M., Díaz A. I., Ascasibar Y., Gibson B. K., Cavichia O., Costa R. D. D., Maciel W. J., 2016a, preprint, (`arXiv:1612.03348`)

Moustakas J., Kennicutt Jr. R. C., 2006, ApJS, 164, 81

Moustakas J., Kennicutt Jr. R. C., Tremonti C. A., Dale D. A., Smith J.-D. T., Calzetti D., 2010, ApJS, 190, 233

Moustakas J., et al., 2011, preprint, (`arXiv:1112.3300`)

Mullaney J. R., et al., 2015, MNRAS, 453, L83

Nagao T., Maiolino R., Marconi A., 2006, A&A, 459, 85

Nakajima K., Ouchi M., Shimasaku K., Hashimoto T., Ono Y., Lee J. C., 2013, ApJ, 769, 3

Newman S. F., et al., 2012, ApJ, 761, 43

Newville M., Stensitzki T., Allen D. B., Ingargiola A., 2014, LMFIT: Non-Linear Least-Square Minimization and Curve-Fitting for Python

Nicholls D. C., Dopita M. A., Sutherland R. S., 2012, ApJ, 752, 148

Nicholls D. C., Dopita M. A., Sutherland R. S., Kewley L. J., Palay E., 2013, ApJS, 207, 21

Noeske K. G., et al., 2007, ApJLett, 660, L47

Orban de Xivry G., et al., 2015, in Adaptive Optics for Extremely Large Telescopes IV (AO4ELT4). p. E72

Pagel B. E. J., Edmunds M. G., Blackwell D. E., Chun M. S., Smith G., 1979, MNRAS, 189, 95

Pagel B. E. J., Simonson E. A., Terlevich R. J., Edmunds M. G., 1992, MNRAS, 255, 325

Palay E., Nahar S. N., Pradhan A. K., Eissner W., 2012, MNRAS, 423, L35

Peimbert M., 1967, ApJ, 150, 825

Peimbert M., Peimbert A., 2014, in Revista Mexicana de Astronomia y Astrofisica Conference Series. pp 137–137

Peimbert M., Peimbert A., Esteban C., García-Rojas J., Bresolin F., Carigi L., Ruiz M. T., López-Sánchez A. R., 2007, in Guzmán R., ed., Revista Mexicana de Astronomia y Astrofisica Conference Series Vol. 29, Revista Mexicana de Astronomia y Astrofisica Conference Series. pp 72–79 (`arXiv:astro-ph/0608440`)

Peimbert A., Peimbert M., Delgado-Inglada G., García-Rojas J., Peña M., 2014, RMXAC, 50, 329

Peng Y., Maiolino R., Cochrane R., 2015, Nature, 521, 192

Pérez-Montero E., 2014, MNRAS, 441, 2663

Pérez-Montero E., Contini T., 2009, MNRAS, 398, 949

Perna M., et al., 2015, A&A, 583, A72

Perna M., Lanzuisi G., Brusa M., Cresci G., Mignoli M., 2017, A&A, 606, A96

Pettini M., Pagel B. E. J., 2004, MNRAS, 348, L59

Pilkington K., et al., 2012, MNRAS, 425, 969

Pilyugin L. S., 2005, A&A, 436, L1

Pilyugin L. S., 2007, MNRAS, 375, 685

Pilyugin L. S., Grebel E. K., 2016, MNRAS, 457, 3678

Pilyugin L. S., Thuan T. X., 2005, ApJ, 631, 231

Pilyugin L. S., Thuan T. X., Vílchez J. M., 2006a, MNRAS, 367, 1139

Pilyugin L. S., Vílchez J. M., Thuan T. X., 2006b, MNRAS, 370, 1928

Pilyugin L. S., Mattsson L., Vílchez J. M., Cedrés B., 2009, MNRAS, 398, 485

Pilyugin L. S., Vílchez J. M., Cedrés B., Thuan T. X., 2010a, MNRAS, 403, 896

Pilyugin L. S., Vílchez J. M., Thuan T. X., 2010b, ApJ, 720, 1738

Pilyugin L. S., Vílchez J. M., Mattsson L., Thuan T. X., 2012a, MNRAS, 421, 1624

Pilyugin L. S., Grebel E. K., Mattsson L., 2012b, MNRAS, 424, 2316

Poggianti B. M., et al., 2016, AJ, 151, 78

Postman M., et al., 2012, ApJS, 199, 25

Queyrel J., et al., 2012, A&A, 539, A93

Rabien S., et al., 2010, in Adaptive Optics Systems II. pp 77360E–77360E–12, doi:10.1117/12.857210

Rahimi A., Kawata D., Allende Prieto C., Brook C. B., Gibson B. K., Kiessling A., 2011, MNRAS, 415, 1469

Renzini A., Peng Y.-j., 2015, ApJLett, 801, L29

Ricciardelli E., Vazdekis A., Cenarro A. J., Falcón-Barroso J., 2012, MNRAS, 424, 172

Richard J., Jones T., Ellis R., Stark D. P., Livermore R., Swinbank M., 2011, MNRAS, 413, 643

Rodighiero G., et al., 2011, ApJLett, 739, L40

Rosales-Ortega F. F., Díaz A. I., Kennicutt R. C., Sánchez S. F., 2011, MNRAS, 415, 2439

Rosati P., et al., 2014, The Messenger, 158, 48

Rubin K. H. R., Prochaska J. X., Koo D. C., Phillips A. C., Martin C. L., Winstrom L. O., 2014, ApJ, 794, 156

Rupke D. S. N., Veilleux S., 2013, ApJLett, 775, L15

Rupke D., Kewley L., Barnes J., 2010a, in Smith B., Higdon J., Higdon S., Bastian N., eds, Astronomical Society of the Pacific Conference Series Vol. 423, Galaxy Wars: Stellar Populations and Star Formation in Interacting Galaxies. p. 355

Rupke D. S. N., Kewley L. J., Chien L.-H., 2010b, ApJ, 723, 1255

Saintonge A., et al., 2013, ApJ, 778, 2

Salim S., et al., 2007, ApJS, 173, 267

Salim S., Lee J. C., Ly C., Brinchmann J., Davé R., Dickinson M., Salzer J. J., Charlot S., 2014, preprint, (`arXiv:1411.7391`)

Salpeter E. E., 1955, ApJ, 121, 161

Sánchez-Blázquez P., et al., 2006, MNRAS, 371, 703

Sánchez S. F., et al., 2012, A&A, 538, A8

Sánchez S. F., et al., 2013, A&A, 554, A58

Sánchez S. F., et al., 2014, A&A, 563, A49

Sanders R. L., et al., 2015a, preprint, (`arXiv:1509.03636`)

Sanders R. L., et al., 2015b, ApJ, 799, 138

Sanders R. L., et al., 2016, preprint, (`arXiv:1606.04107`)

Sanders R. L., Shapley A. E., Zhang K., Yan R., 2017, preprint, (`arXiv:1708.04625`)

Schawinski K., et al., 2014, MNRAS, 440, 889

Shapley A. E., Steidel C. C., Erb D. K., Reddy N. A., Adelberger K. L., Pettini M., Barmby P., Huang J., 2005, ApJ, 626, 698

Shapley A. E., et al., 2015, ApJ, 801, 88

Sharples R., et al., 2013, The Messenger, 151, 21

Shirazi M., Vegetti S., Nesvadba N., Allam S., Brinchmann J., Tucker D., 2014, MNRAS, 440, 2201

Skillman E. D., 1989, ApJ, 347, 883

Sklias P., et al., 2014, A&A, 561, A149

Somerville R. S., Davé R., 2015, ARA&A, 53, 51

Speagle J. S., Steinhardt C. L., Capak P. L., Silverman J. D., 2014, ApJS, 214, 15

Spitoni E., Matteucci F., Marcon-Uchida M. M., 2013, A&A, 551, A123

Stahler S. W., Palla F., 2005, The Formation of Stars

Stark D. P., Swinbank A. M., Ellis R. S., Dye S., Smail I. R., Richard J., 2008, Nature, 455, 775

Stark D. P., et al., 2013, MNRAS, 436, 1040

Stasińska G., 2002, ArXiv Astrophysics e-prints, pp 115–170

Stasińska G., 2005, A&A, 434, 507

Stasińska G., 2006, A&A, 454, L127

Stasińska G., 2007, preprint, (`arXiv:0704.0348`)

Steidel C. C., et al., 2014, ApJ, 795, 165

Steidel C. C., Strom A. L., Pettini M., Rudie G. C., Reddy N. A., Trainor R. F., 2016, ApJ, 826, 159

Stetson P. B., 1987, PASP, 99, 191

Stinson G. S., Bailin J., Couchman H., Wadsley J., Shen S., Nickerson S., Brook C., Quinn T., 2010, MNRAS, 408, 812

Stinson G. S., Brook C., Macciò A. V., Wadsley J., Quinn T. R., Couchman H. M. P., 2013, MNRAS, 428, 129

Storchi-Bergmann T., Calzetti D., Kinney A. L., 1994, ApJ, 429, 572

Stott J. P., et al., 2014, MNRAS, 443, 2695

Strom A. L., Steidel C. C., Rudie G. C., Trainor R. F., Pettini M., Reddy N. A., 2017, ApJ, 836, 164

Sutherland R. S., Dopita M. A., 1993, ApJS, 88, 253

Swinbank A. M., Sobral D., Smail I., Geach J. E., Best P. N., McCarthy I. G., Crain R. A., Theuns T., 2012, MNRAS, 426, 935

Tremonti C. A., et al., 2004, ApJ, 613, 898

Troncoso P., et al., 2014, A&A, 563, A58

Vazdekis A., Sánchez-Blázquez P., Falcón-Barroso J., Cenarro A. J., Beasley M. A., Cardiel N., Gorgas J., Peletier R. F., 2010, MNRAS, 404, 1639

Vazdekis A., Ricciardelli E., Cenarro A. J., Rivero-González J. G., Díaz-García L. A., Falcón-Barroso J., 2012, MNRAS, 424, 157

Veilleux S., Osterbrock D. E., 1987, in Lonsdale Persson C. J., ed., NASA Conference Publication Vol. 2466, NASA Conference Publication.

Vila Costas M. B., Edmunds M. G., 1993, MNRAS, 265, 199

Vilchez J. M., Esteban C., 1996, MNRAS, 280, 720

Vincenzo F., Belfiore F., Maiolino R., Matteucci F., Ventura P., 2016, MNRAS,

Wang X., et al., 2017, ApJ, 837, 89

Werk J. K., Putman M. E., Meurer G. R., Santiago-Figueroa N., 2011, ApJ, 735, 71

Whitaker K. E., et al., 2014, ApJ, 795, 104

Wisnioski E., et al., 2015, ApJ, 799, 209

Wu Y.-Z., Zhang S.-N., 2013, MNRAS, 436, 934

Wuyts E., Rigby J. R., Sharon K., Gladders M. D., 2012, ApJ, 755, 73

Wuyts E., et al., 2014, ApJLett, 789, L40

Wuyts E., et al., 2016, preprint, (`arXiv:1603.01139`)

Wylezalek D., Zakamska N. L., 2016, MNRAS, 461, 3724

Yabe K., et al., 2015, PASJ, 67, 102

Yin S. Y., Liang Y. C., Zhang B., 2007, in Ho L. C., Wang J.-W., eds, Astronomical Society of the Pacific Conference Series Vol. 373, The Central Engine of Active Galactic Nuclei. p. 686 (`arXiv:astro-ph/0701234`)

Yoachim P., Roškar R., Debattista V. P., 2010, ApJLett, 716, L4

York D. G., et al., 2000, AJ, 120, 1579

Yuan T.-T., Kewley L. J., Swinbank A. M., Richard J., Livermore R. C., 2011, ApJLett, 732, L14

Yuan T.-T., Kewley L. J., Rich J., 2013, ApJ, 767, 106

Zahid H. J., Kewley L. J., Bresolin F., 2011, ApJ, 730, 137

Zahid H. J., Bresolin F., Kewley L. J., Coil A. L., Davé R., 2012, ApJ, 750, 120

Zahid H. J., Dima G. I., Kudritzki R.-P., Kewley L. J., Geller M. J., Hwang H. S., Silverman J. D., Kashino D., 2014a, ApJ, 791, 130

Zahid H. J., et al., 2014b, ApJ, 792, 75

Zaritsky D., Kennicutt Jr. R. C., Huchra J. P., 1994, ApJ, 420, 87

Zhang K., et al., 2016, preprint, (`arXiv:1612.02000`)

Zitrin A., et al., 2015, ApJ, 801, 44

da Cunha E., et al., 2015, ApJ, 806, 110

van Dokkum P. G., 2001, PASP, 113, 1420

van Zee L., Salzer J. J., Haynes M. P., O'Donoghue A. A., Balonek T. J., 1998, AJ, 116, 2805

Acknowledgements

Ringrazio in primo luogo Filippo Mannucci, per la sua guida, le promesse mantenute, le critiche sempre costruttive e la considerazione che nei miei confronti non ho mai sentito venire meno. Grazie di cuore anche a tutto il gruppo extragalattico di Arcetri e in particolare a Giovanni Cresci e Alessandro Marconi, per i suggerimenti, gli scambi di idee, il sostegno, l'incrollabile entusiasmo e i momenti più leggeri e divertenti (e per il Messico!). Grazie a Simone Esposito, per avermi dato la possibilità concreta di restare a Firenze per il Dottorato; e grazie a Lorenzo Busoni, Tommaso Mazzoni, Marco Bonaglia per avermi introdotto ai segreti dell'ottica adattiva ed avermi accompagnato in un'esperienza unica come quella di una notte di osservazioni ad uno dei telescopi più grandi del mondo.

Un ringraziamento doveroso a Roberto Maiolino, per l'opportunità concessami di trascorrere otto mesi nel suo gruppo di ricerca a Cambridge, un'esperienza di crescita sia personale che professionale. Grazie a tutti i ragazzi conosciuti sulle rive a volte grigie ma affascinanti del *River Cam* dove, seppur per pochi mesi, mi sono sentito pienamente come a casa: Davide, Alberto, Francesco, Andrea, Manuela, Ciro, Andrin, James, Rob, Ricardo, Ricardo, Matt. Grazie speciale a Stefano e Valentina, per la gentilezza e l'ospitalità.

Penso di poter dire, senza timore di smentita, che questo percorso sarebbe stato infinitamente più duro e pesante senza i miei compagni di viaggio del bunker di "Arcetraz"; grazie ragazzi, per l'insostituibile fonte di supporto, la condivisione e il senso di famiglia, i confronti, le risate genuine, la leggerezza (e il caffè!) che hanno fatto di Arcetri il miglior posto di lavoro che si potesse desiderare: Giacomo, Antonio, Greta, Claudia, Eleonora (e Yuri!), Tommaso, Barbara, Susanna, Sara, Teresa, Luca, Matilde, Laura. Un piccolo pezzo del mio cuore vi appartiene.

Un pensiero per tutte le persone che ho avuto modo e fortuna di conoscere durante le mie peregrinazioni negli ultimi tre anni: colleghi, collaboratori, semplici ragazzi all'inseguimento di un sogno, ognuno di voi una tessera che contribuisce a comporre il mosaico di questa splendida esperienza.

Grazie al mio gruppo di amici "storici" fiorentini, una certezza inalterata dallo scorrere del tempo.

Grazie infinite ai miei genitori, per l'incondizionato sostegno e l'affetto in questi tre(nta) anni.

E, sopra ogni altra cosa, Marta, grazie per aver restituito un senso a tante cose: sei il colore che rende unico e vivo un disegno altrimenti in bianco e nero. Questo lavoro di tesi (finalmente!) finisce qui, ma tanti nuovi capitoli di un libro tutto nostro restano da scrivere, insieme.